

**DESIGN OF A TEST FIXTURE FOR ROTATIONAL CORE LOSSES IN
ELECTRICAL MACHINE LAMINATIONS**

Natheer Alatawneh

A Thesis

In the Department

of

Electrical and Computer Engineering

Presented in Partial Fulfillment of the Requirements

For The Degree Of

Doctor of Philosophy (Electrical and Computer Engineering) at

Concordia University

Montreal, Quebec, Canada

© Natheer Alatawneh, 2012

CONCORDIA UNIVERSITY
SCHOOL OF GRADUATE STUDIES

This is to certify that the thesis prepared

By: Natheer Alatawneh

Entitled: Design of a Test Fixture for Rotational Core Losses in Electrical Machine Laminations

and submitted in partial fulfillment of the requirements for the degree of

Doctor of Philosophy (Electrical and Computer Engineering)

complies with the regulations of the University and meets the accepted standards with respect to originality and quality.

Signed by the final examining committee:

<u>Dr. Andreas K. Athienitis</u>	Chair
<u>Dr. Iqbal Husain</u>	External Examiner
<u>Dr. Marius Paraschivoiu</u>	External to Program
<u>Dr. L. A. C. Lopes</u>	Examiner
<u>Dr. Sheldon S. Williamson</u>	Examiner
<u>Dr. P. Pillay</u>	Thesis Supervisor

Approved by

Dr. W. E. Lynch

Chair of Department or Graduate Program Director

Date: _____ Dr. Robin A. L. Drew

Dean, Faculty of Engineering and Computer Science

ABSTRACT

Design of a Test Fixture for Rotational Core Losses in Electrical Machine Laminations

Natheer Alatawneh, Ph.D.

Concordia University, 2012

In recent years, several methods and devices have been proposed to measure rotational core losses. Technically, it is still a challenge to realize both high and uniform magnetic flux density within a wide area of the sample under test. Because of that, importance has been placed on the development of magnetizing circuits which are capable of performing 2-D rotating field tests.

In this work, a novel design of a magnetizing circuit is presented, simulated, and implemented practically to obtain a uniform rotating flux density inside the test sample. This magnetizing circuit is based on an electromagnetic Halbach array. The new test fixture is suitable for the measurement of rotational core loss, and capable of measuring pulsating loss in different directions within the specimen. Measurements were carried out on five silicon steel circular samples of 20 cm diameter. These samples are: M15 gauge 29, M19 gauge 29, M19 gauge 24, M36 gauge 29, and M36 gauge 26.

This work describes the influence of different flux patterns on core loss estimation, where three different machines, induction, BLDCM, and SRM are simulated to calculate the zones of rotating flux density in the stator cores of these machines. Experimental tests are executed, and the percentage error made by assuming all flux is pulsating is calculated.

Core loss differences in electrical machine laminations have been noticed under rotating field in the case of clockwise (CW) and counterclockwise (CCW) direction excitation. Experimental results manifest that the anisotropy of the magnetic material is attributed mainly to the asymmetry in the CW and CCW rotational core losses, where the permeability varies significantly when the direction of rotating field is reversed. A study on three different types of machines at different frequencies show the importance of considering the direction of rotating field during the machine efficiency estimation.

The negative power in rotational core loss which was reported in some laboratories has been addressed and interpreted according to the dynamic hysteresis loop behavior. The negative power which appears in one loss component is caused by the reversal of the field direction which can be realized from the interfered dynamic hysteresis loop, while the negative value in the total rotational loss originates in the sensors misalignment.

The reason behind the unusual shape of the hysteresis loop under rotating field observed in the literature is revealed, where the harmonics under rotating field is responsible for the change in the hysteresis loop shape from the well known shape under pulsating field. The results show also that the behavior of the minor loop under rotating fields differs from its behavior under pulsating fields. The minor loop under rotating fields moves outside the major loop at saturation, while it is confined inside the major loop under pulsating fields. The effect of harmonics on core losses under a rotating field is estimated and compared with losses under pulsating fields.

ACKNOWLEDGMENTS

I would like to thank my supervisor Prof. Pragasen Pillay not only for his guidance in the research work, but also for his important role in my life during the past four years. Prof. Pillay reconstructed my academic character and taught me how to be a successful professor in the future. I learnt how to push the students gracefully and effectively, be kind and assertive at the same time, provide the students with the advice they need in a tactful and professional way, and give the students the opportunity to express their ideas and thoughts freely which launches a fruitful dialogue. I will never forget this experience and I will present it as a model for my students in the future.

Words fail me to express my deepest feelings of gratitude to my parents, Mr. Ahmad Alatawneh and Mrs. Amina Almalty for their unconditional support during my whole life.

I thank my lovely wife Jamila for her support and patience throughout this project. She is the best example of a supportive wife, and she is the source of my happiness in this life.

I would like to thank and acknowledge the support of the Natural Sciences & Engineering Research Council of Canada and Hydro-Québec for this work.

This work was supported in part by the R&D program of the NSERC Chair entitled, “Energy efficiency in electrical machines for small renewable energy production systems” established in 2009 at Concordia University.

TABLE OF CONTENTS

List of Figures	xi
List of Tables	xxxvii
1. Introduction.....	1
1.1 Motivation and Aim of the Work.....	1
1.2 Core Losses in AC Machines.....	2
1.3 Methods and Apparatus for Measuring Rotational Core Losses	3
1.3.1 Method	3
1.3.2 Apparatus	5
1.4 Techniques for Measuring Components of the Magnetic Flux Density (B), and the Magnetic Field Strength (H).	7
1.4.1 Methods of Measuring the Magnetic Flux Density (B)	7
1.4.2 Methods of Measuring the Magnetic Field Strength (H).....	10
1.5 Conclusion	13
2. Design Considerations	14
2.1 Introduction.....	14

2.2	Halbach Array Design.....	14
2.2.1	Halbach Array Principle.....	14
2.2.2	Choosing Size and Number of Poles.....	16
2.3	The Electromagnetic Halbach Array.....	23
2.4	Sample Shape Design	26
2.5	Simulation Results	32
2.6	The New Test Fixture Structure.....	35
2.7	Validation.....	41
2.8	Conclusion	43
3.	Basic Measurements	45
3.1	Introduction.....	45
3.2	The Measurement Set-up	45
3.3	Data Extraction and Loss Evaluation.....	47
3.4	Experimental Results	48
3.4.1	Signals Obtained from the Coil Sensors	49
3.4.2	Rotational Core Losses under Circular Excitation.....	52

3.4.3	Rotational Core Losses Compared with Pulsating Losses	59
3.4.4	Rotational and Pulsating Core Loss Measurements with Reference to the Permeability Asymmetry	65
3.5	Conclusion	67
4.	The Impact of Rotating Field on Core Loss Estimation	72
4.1	Introduction.....	72
4.2	Methodology to Determine Flux Patterns in Electrical Machines	72
4.3	Simulation Results	77
4.4	Experimental Results	80
4.5	Error Estimation.....	87
4.6	Discussion	101
4.7	Conclusion	102
5.	Rotational Core Loss Measurements in Clockwise and Counterclockwise Directions	103
5.1	Introduction.....	103
5.2	The Inconsistency between the CW and CCW Rotational Core Losses.....	103
5.3	Results and Discussion	107

5.4	Permeability Asymmetry in CW and CCW Directions	122
5.5	The Influence on Rotating Machines	128
5.5.1	Simulations	128
5.5.2	Experimental Results	130
5.6	Conclusion	146
6.	Specific Phenomena Associated with Rotational Core Loss Measurements	147
6.1	The Negative Power in the Rotational Core Loss Measurements.....	147
6.1.1	Introduction.....	147
6.1.2	Results and Discussion	147
6.1.3	Conclusion	162
6.2	The Minor Hysteresis Loop under Rotating Magnetic Fields.....	163
6.2.1	Introduction.....	163
6.2.2	Fundamentals of Minor Loop Generation.....	163
6.2.3	Measurements and Results.....	166
6.2.4	Further Discussion	185
6.2.5	Conclusion	186

7. Conclusions and Recommendations	187
7.1 Conclusions.....	187
7.2 Recommendations and Proposed Future Research	189
7.3 Contribution	191
7.3.1 Journal Papers	191
7.3.2 Conference Papers	192
References.....	193
Appendix.....	200

LIST OF FIGURES

Fig. 1.1 : Stator tooth and two slots of stator yoke in AC machine	2
Fig. 1.2: The structure of vertical yoke tester	6
Fig. 1.3: Different shapes of samples with their corresponding magnetizing circuits (a) Square (b) Hexagonal (c) Circular.	7
Fig. 1.4: Needle method for measuring flux density in the sample	8
Fig. 1.5: The operation principle of Hall Effect sensor.	9
Fig. 1.6: Rogowski-Chattock potentiometer (RCP).....	10
Fig. 1.7: Tangential coil placed on sample surface.....	12
Fig. 2.1: Circular Halbach design of 8 cylindrical magnets which produces one sided flux in the y-axis. (a) circuit design (b) simulation result.	15
Fig. 2.2: Poles around the central air gap.....	16
Fig. 2.3: Simulation showing resultant of two orthogonal equal vectors of 8-pole Halbach array producing 45° direction flux.	19
Fig. 2.4: Simulation showing resultant of two orthogonal equal vectors of 16-pole Halbach array producing 45° direction flux.....	19

Fig. 2.5: Simulation showing resultant of two orthogonal equal vectors of 32-pole Halbach array producing 45° direction flux.....	19
Fig. 2.6: The magnetic flux density profile along the x-axis of the sample in 8-pole circuit.	20
Fig. 2.7: The magnetic flux density profile along the x-axis of the sample in 16-pole circuit.	20
Fig. 2.8: The magnetic flux density profile along the x-axis of the sample in 32-pole circuit.	21
Fig. 2.9: The 2-D flux density distribution of the sample in an 8-pole circuit.	21
Fig. 2.10: The 2-D flux density distribution of the sample in a 16-pole circuit.	22
Fig. 2.11: The 2-D flux density distribution of the sample in a 32-pole circuit.	22
Fig. 2.12: The produced flux density in the gap of the Halbach array with different poles.	23
2.13: The flux direction in each pole of a 16-pole Halbach array to produce a uni-directional flux. (a) In x-axis. (b) In y-axis.	24
Fig. 2.14: Simulations of resultant vector produces a net flux at different angles, with flux paths in the top pole at (a) 0° (b) 45° (c) 60°	25

Fig. 2.15: Different shapes of samples with their corresponding magnetizing circuits (a) Square with SRSST (b) Hexagonal with HRSST (c) Circular with RRSST (d) Circular with Halbach array.....	27
Fig. 2.16: The flux density distribution of different sample shapes with the corresponding 3D mesh surfaces (a) Square (b) Hexagonal (c) Circular using RRSST (d) Circular using the Halbach array.	29
Fig. 2.17: Standard deviation profile of the flux density distribution for the square sample.	30
Fig. 2.18: Standard deviation profile of the flux density distribution for the hexagonal sample.	31
Fig. 2.19: Standard deviation profile of the flux density distribution for the circular sample using RRSST.	31
Fig. 2.20: Standard deviation profile of the flux density distribution for the circular sample using the Halbach array.	32
Fig. 2.21: The magnetic flux density profile in the x - z plane along the axis of the circuit, using M19 Silicon steel gauge 24.	33
Fig. 2.22: The flux density distribution within the sample of M19 Silicon steel gauge 24 in x - z plane.	34

Fig. 2.23: The magnetic flux density profile in x - z plane along the axis of the circuit. Test of three samples with different gauges.	34
Fig. 2.24: (a) The 3D design of the circuit frame using <i>AutoCAD</i> . (b) The frame disc made of Cast Acrylic. (c) The Cover.	36
Fig. 2.25: (a) Photograph of a pole with wound interleaved coils in x and y directions. (b) Laminations collected to form a pole designed by Auto Cad. (c) A complete set of 16 poles.	37
Fig. 2.26: The position of \mathbf{B} coils wound around the sample. (a) Drawing design. (b) Real picture.	39
Fig. 2.27: (a) \mathbf{H} coil for measurement in y direction. (b) \mathbf{H} coil for measurement in x direction. (c) Positions of \mathbf{H} coil. (d) Real picture of tangential \mathbf{H} coil wound on Plexiglas former.	40
Fig. 2.28: Photograph of the Halbach magnetizing circuit.	41
Fig. 2.29: (a) 280 turns Epstein frame. (b) 352 turns Epstein frame.	42
Fig. 2.30: The pulsating core losses in M19G24 at 1 kHz.	43
Fig. 3.1: The test bench schematic diagram.	46
Fig. 3.2: The measurement system at Concordia University.	46

Fig. 3.3: The instantaneous output voltage signals at 60 Hz obtained from the surface coils in the x -direction (v_{Hx}), and y -direction (v_{Hy}).	49
Fig. 3.4: The instantaneous values of the magnetic field strength at 60 Hz in the x -direction (Hx), and y -direction (Hy).	50
Fig. 3.5: The instantaneous output voltage signals at 60 Hz obtained from the \mathbf{B} coils in the x -direction (v_{Bx}), and y -direction (v_{By}).	50
Fig. 3.6: The instantaneous values of the magnetic flux density at 60 Hz in the x -direction (Bx), and y -direction (By).	50
Fig. 3.7: The instantaneous output voltage signals at 1 kHz obtained from the surface coils in the x -direction (v_{Hx}), and y -direction (v_{Hy}).	51
Fig. 3.8; The instantaneous values of the magnetic field strength at 1 kHz in the x -direction (Hx), and y -direction (Hy).	51
Fig. 3.9: The instantaneous output voltage signals at 1 kHz obtained from the \mathbf{B} coils in the x -direction (v_{Bx}), and y -direction (v_{By}).	51
Fig. 3.10: The instantaneous values of the magnetic flux density at 1 kHz in the x -direction (Bx), and y -direction (By).	52
Fig. 3.11: Rotational core losses at 1 kHz in the five samples.	54
Fig. 3.12: A comparison of M19 steel with different gauges at 1 kHz.	54

Fig. 3.13: The core losses at 1 kHz of three different samples (M15, M19, and M36) with the same gauge (Gauge 29).....	55
Fig. 3.14: Rotational core losses at 400 Hz in the five samples.	55
Fig. 3.15: The core losses at 400 Hz of three different samples (M15, M19, and M36) with the same gauge (Gauge 29).....	56
Fig. 3.16: A comparison of M19 steel with different gauges at 400 Hz.....	56
Fig. 3.17: Rotational core losses at 60 Hz in the five samples.	57
Fig. 3.18: The core losses at 60 Hz of three different samples (M15, M19, and M36) with the same gauge (Gauge 29).....	57
Fig. 3.19: A comparison of M19 steel with different gauges at 60 Hz.....	58
Fig. 3.20: The total rotational core loss at 60 Hz, in M36 steel Gauge 29, with the corresponding x and y components, P_x and P_y respectively.	58
Fig. 3.21: The rotational core losses (P_{rot}) compared with pulsating losses in x and y directions, P_{hx} and P_{hy} , respectively. For M19G24 at 60 Hz.....	61
Fig. 3.22: The rotational core losses (P_{rot}) compared with pulsating losses in x and y directions, P_{hx} and P_{hy} , respectively. For M36G29 at 60 Hz.....	61
Fig. 3.23: The difference between rotational core loss and average pulsating core losses, for M19G24 and M36G29 at 60 Hz.....	62

Fig. 3.24: The rotational core losses (P_{rot}) compared with pulsating losses in x and y directions, P_{hx} and P_{hy} , respectively. For M19G24 at 400 Hz.....	62
Fig. 3.25: The rotational core losses (P_{rot}) compared with pulsating losses in x and y directions, P_{hx} and P_{hy} , respectively. For M36G29 at 400 Hz.....	63
Fig. 3.26: The difference between rotational core loss and average pulsating core losses, for M19G24 and M136G29 at 400 Hz.....	63
Fig. 3.27: The rotational core losses (P_{rot}) compared with pulsating losses in x and y directions, P_{hx} and P_{hy} , respectively. For M19G24 at 1 kHz.....	64
Fig. 3.28: The rotational core losses (P_{rot}) compared with pulsating losses in x and y directions, P_{hx} and P_{hy} , respectively. For M36G29 at 1 kHz.....	64
Fig. 3.29: The difference between rotational core loss and average pulsating core losses, for M19G24 and M136G29 at 1 kHz.....	65
Fig. 3.30: The dynamic hysteresis loops in the x and y directions for M15G29 sample under 1.3T rotating field with (a) 60 Hz (b) 400 Hz (c) 1 kHz.....	68
Fig. 3.31: The dynamic hysteresis loops B_x-H_x and B_y-H_y measured in the x and y directions, respectively, for M15G29 sample under 1.3T pulsating field, with (a) 60 Hz. (b) 400 Hz. (c) 1 kHz.	69
Fig. 3.32: The relative permeability as a function of magnetic flux density for M15G29 sample. Where μ_{xp} , μ_{yp} , μ_{xr} , and μ_{yr} refer to the relative permeability in the x -direction	

under pulsating field, y -direction under pulsating field, x -direction under rotating field, and y -direction under rotating field, respectively, with (a) 60 Hz. (b) 400 Hz. (c) 1 kHz.	70
Fig. 4.1: Flux paths distributions in for FEA of (a) 2-pole IM (b) 2-pole BLDCM (c) 6-4 SRM.	75
Fig. 4.2: Flux density locus of (a) Circular rotating field (b) Elliptical rotating field (c) Pulsating field.	75
Fig. 4.3: Flowchart for determination of the flux patterns.	76
Fig. 4.4: The aspect ratio distribution in the stator of a 2-pole induction machine.	78
Fig. 4.5: The aspect ratio distribution in the stator of a 2-pole BLDCM.	78
Fig. 4.6: The aspect ratio distribution in the stator of a 6-4 SRM.	78
Fig. 4.7: Percentages of the aspect ratio out of the total area of the stator in a 2-pole induction machine.	79
Fig. 4.8: Percentages of the aspect ratio out of the total area of the stator in a 2-pole BLDCM.	79
Fig. 4.9: Percentages of the aspect ratio out of the total area of the stator in a 6-4 SRM.	79

Fig. 4.10: The loci of flux density with different aspect ratios (From 0 to 1) at 60 Hz for M36G29.....	81
Fig. 4.11: The loci of flux density with different aspect ratios (From 0 to 1) at 400 Hz for M36G29.....	81
Fig. 4.12: The loci of flux density with different aspect ratios (From 0 to 1) at 1 kHz for M36G29.....	82
Fig. 4.13: The rotational core losses with different aspect ratios compared with pulsating loss (aspect ratio=0) at 60 Hz for M36G29.	84
Fig. 4.14: The rotational core losses with different aspect ratios compared with pulsating loss (aspect ratio=0) at 60 Hz for M19G24.	84
Fig. 4.15: The rotational core losses with different aspect ratios compared with pulsating loss (aspect ratio=0) at 400 Hz for M36G29.	85
Fig. 4.16: The rotational core losses with different aspect ratios compared with pulsating loss (aspect ratio=0) at 400 Hz for M19G24.	85
Fig. 4.17: The rotational core losses with different aspect ratios compared with pulsating loss (aspect ratio=0) at 1 kHz for M36G29.	86
Fig. 4.18: The rotational core losses with different aspect ratios compared with pulsating loss (aspect ratio=0) at 1 kHz for M19G24.	86

Fig. 4.19: The percentage of relative error in the rotational core losses at 60 Hz for M36G29.....	89
Fig. 4.20: The percentage of relative error in the rotational core losses at 60 Hz for M19G24.....	90
Fig. 4.21: The percentage of relative error in the rotational core losses at 400 Hz for M36G29.....	90
Fig. 4.22: The percentage of relative error in the rotational core losses at 400 Hz for M19G24.....	91
Fig. 4.23: The percentage of relative error in the rotational core losses at 1 kHz for M36G29.....	91
Fig. 4.24: The percentage of relative error in the rotational core losses at 1 kHz for M19G24.....	92
Fig. 4.25: The percentage errors associated with considering the rotational core losses in the stator of a 2-pole induction machine using M36G29 laminations at 60 Hz.	92
Fig. 4.26: The percentage errors associated with considering the rotational core losses in the stator of a 2-pole induction machine using M19G24 laminations at 60 Hz.	93
Fig. 4.27: The percentage errors associated with considering the rotational core losses in the stator of a 2-pole induction machine using M36G29 laminations at 400 Hz.	93

Fig. 4.28: The percentage errors associated with considering the rotational core losses in the stator of a 2-pole induction machine using M19G24 laminations at 400 Hz.	93
Fig. 4.29: The percentage errors associated with considering the rotational core losses in the stator of a 2-pole induction machine using M36G29 laminations at 1 kHz.	94
Fig. 4.30: The percentage errors associated with considering the rotational core losses in the stator of a 2-pole induction machine using M19G24 laminations at 1 kHz.	94
Fig. 4.31: The percentage errors associated with considering the rotational core losses in the stator of a 2-pole BLDCM using M36G29 laminations at 60 Hz.	94
Fig. 4.32: The percentage errors associated with considering the rotational core losses in the stator of a 2-pole BLDCM using M19G24 laminations at 60 Hz.	95
Fig. 4.33: The percentage errors associated with considering the rotational core losses in the stator of a 2-pole BLDCM using M36G29 laminations at 400 Hz.	95
Fig. 4.34: The percentage errors associated with considering the rotational core losses in the stator of a 2-pole BLDCM using M19G24 laminations at 400 Hz.	95
Fig. 4.35: The percentage errors associated with considering the rotational core losses in the stator of a 2-pole BLDCM using M36G29 laminations at 1 kHz.	96
Fig. 4.36: The percentage errors associated with considering the rotational core losses in the stator of a 2-pole BLDCM using M19G24 laminations at 1 kHz.	96

Fig. 4.37: The percentage errors associated with considering the rotational core losses in the stator of a 6-4 SRM using M36G29 laminations at 60 Hz.	96
Fig. 4.38: The percentage errors associated with considering the rotational core losses in the stator of a 6-4 SRM using M19G24 laminations at 60 Hz.	97
Fig. 4.39: The percentage errors associated with considering the rotational core losses in the stator of a 6-4 SRM using M36G29 laminations at 400 Hz.	97
Fig. 4.40: The percentage errors associated with considering the rotational core losses in the stator of a 6-4 SRM using M19G24 laminations at 400 Hz.	97
Fig. 4.41: The percentage errors associated with considering the rotational core losses in the stator of a 6-4 SRM using M36G29 laminations at 1 kHz.	98
Fig. 4.42: The percentage errors associated with considering the rotational core losses in the stator of a 6-4 SRM using M19G24 laminations at 1 kHz.	98
Fig. 4.43: Flowchart of determination the all over error in the machine when considering the effect of rotating field compared with considering the whole flux pulsating.	99
Fig. 5.1: The misalignment of B coil during the threading process.	105
Fig. 5.2: Twisting terminals of H coil sensor.	106
Fig. 5.3: Rotational core losses in M36G29 sample at 1 kHz, in CW and CCW directions.	110

Fig. 5.4: Rotational core losses in M36G29 sample at 400 Hz, in CW and CCW directions.....	110
Fig. 5.5: Rotational core losses in M36G29 sample at 60 Hz, in CW and CCW directions.....	111
Fig. 5.6: Percentage of error between rotational core losses in CW and CCW directions for M36G29 sample.....	111
Fig. 5.7: Rotational core losses in M19G24 sample at 1 kHz, in CW and CCW directions.....	112
Fig. 5.8: Rotational core losses in M19G24 sample at 400 Hz, in CW and CCW directions.....	112
Fig. 5.9: Rotational core losses in M19G24 sample at 60 Hz, in CW and CCW directions.....	113
Fig. 5.10: Percentage of error between rotational core losses in CW and CCW directions for M19G24 sample.....	113
Fig. 5.11: Rotational core losses in M15G29 sample at 1 kHz, in CW and CCW directions.....	114
Fig. 5.12: Rotational core losses in M15G29 sample at 400 Hz, in CW and CCW directions.....	114

Fig. 5.13: Rotational core losses in M15G29 sample at 60 Hz, in CW and CCW directions.....	115
Fig. 5.14: Percentage of error between rotational core losses in CW and CCW directions for M15G29 sample.....	115
Fig. 5.15: The x -component measured dynamic hysteresis loops in CW and CCW directions for M36G29 sample under 1.3T rotating field with 1 kHz.....	116
Fig. 5.16: The y -component measured dynamic hysteresis loops in CW and CCW directions for M36G29 sample under 1.3T rotating field with 1 kHz.....	116
Fig. 5.17: The x -component measured dynamic hysteresis loops in CW and CCW directions for M36G29 sample under 1.3T rotating field with 400 Hz.....	117
Fig. 5.18: The y -component measured dynamic hysteresis loops in CW and CCW directions for M36G29 sample under 1.3T rotating field with 400 Hz.....	117
Fig. 5.19: The x -component measured dynamic hysteresis loops in CW and CCW directions for M36G29 sample under 1.3T rotating field with 60 Hz.....	118
Fig. 5.20: The y -component measured dynamic hysteresis loops in CW and CCW directions for M36G29 sample under 1.3T rotating field with 60 Hz.....	118
Fig. 5.21: The x -component measured dynamic hysteresis loops in CW and CCW directions for M19G24 sample under 1.2T rotating field with 1 kHz.....	119

Fig. 5.22: The y -component measured dynamic hysteresis loops in CW and CCW directions for M19G24 sample under 1.2T rotating field with 1 kHz.	119
Fig. 5.23: The x -component measured dynamic hysteresis loops in CW and CCW directions for M19G24 sample under 1.3T rotating field with 400 Hz.	120
Fig. 5.24: The y -component measured dynamic hysteresis loops in CW and CCW directions for M19G24 sample under 1.3T rotating field with 400 Hz.	120
Fig. 5.25: The x -component measured dynamic hysteresis loops in CW and CCW directions for M19G24 sample under 1.3T rotating field with 60 Hz.	121
Fig. 5.26: The y -component measured dynamic hysteresis loops in CW and CCW directions for M19G24 sample under 1.3T rotating field with 60 Hz.	121
Fig. 5.27: The total rotational core loss under CW rotating field at 60 Hz, in M15 steel Gauge 29, with the corresponding x and y components, P_x and P_y respectively.	124
Fig. 5.28: The total rotational core loss under CCW rotating field at 60 Hz, in M15 steel Gauge 29, with the corresponding x and y components, P_x and P_y respectively.	124
Fig. 5.29: The relative permeability in the x direction as a function of magnetic flux density for M15G29 sample under CW and CCW rotating field with 60 Hz.	125
Fig. 5.30: The relative permeability in the y direction as a function of magnetic flux density for M15G29 sample under CW and CCW rotating field with 60 Hz.	126

Fig. 5.31: The relative permeability in the x direction as a function of magnetic flux density for M15G29 sample under CW and CCW rotating field with 400 Hz.....	126
Fig. 5.32: The relative permeability in the y direction as a function of magnetic flux density for M15G29 sample under CW and CCW rotating field with 400 Hz.....	127
Fig. 5.33: The relative permeability in the x direction as a function of magnetic flux density for M15G29 sample under CW and CCW rotating field with 1 kHz.....	127
Fig. 5.34: The relative permeability in the y direction as a function of magnetic flux density for M15G29 sample under CW and CCW rotating field with 1 kHz.....	128
Fig. 5.35: The aspect ratio distribution in the stator of a 2-pole BLDCM, where the two mesh elements facing each other are shown at points (a) and (b)	129
Fig. 5.36: The flux density waveforms (B_x and B_y) in two mesh elements located exactly at the tooth roots of BLDCM. (a) At mesh element located at point a. (b) At mesh element located at point b. Referral points are depicted in Fig. 5.35.	129
Fig. 5.37: The rotational core losses in the CCW direction with different aspect ratios compared with pulsating loss (aspect ratio=0) at 60 Hz for M36G29.....	130
Fig. 5.38: The rotational core losses in the CCW direction with different aspect ratios compared with pulsating loss (aspect ratio=0) at 400 Hz for M36G29.....	131
Fig. 5.39: The rotational core losses in the CCW direction with different aspect ratios compared with pulsating loss (aspect ratio=0) at 1 kHz for M36G29.....	131

Fig. 5.40: Flowchart of determination the all over error in the machine when considering the effect of rotating field compared with considering the whole flux pulsating. 135

Fig. 5.41: The power loss distribution in [W/kg] considering the rotational core losses in the stator of a 2-pole IM using M36G29 laminations at 60 Hz, and under a CW rotating field. 136

Fig. 5.42: The power loss distribution in [W/kg] considering the rotational core losses in the stator of a 2-pole IM using M36G29 laminations at 60 Hz, and under a CCW rotating field. 136

Fig. 5.43: The power loss distribution in [W/kg] considering the rotational core losses in the stator of a 2-pole IM using M36G29 laminations at 400 Hz, and under a CW rotating field. 137

Fig. 5.44: The power loss distribution in [W/kg] considering the rotational core losses in the stator of a 2-pole IM using M36G29 laminations at 400 Hz, and under a CCW rotating field..... 137

Fig. 5.45: The power loss distribution in [W/kg] considering the rotational core losses in the stator of a 2-pole IM using M36G29 laminations at 1 kHz, and under a CW rotating field. 138

Fig. 5.46: The power loss distribution in [W/kg] considering the rotational core losses in the stator of a 2-pole IM using M36G29 laminations at 1 kHz, and under a CCW rotating field. 138

Fig. 5.47: The power loss distribution in [W/kg] considering the rotational core losses in the stator of a 2-pole BLDCM using M36G29 laminations at 60 Hz, and under a CW rotating field.....	139
Fig. 5.48: The power loss distribution in [W/kg] considering the rotational core losses in the stator of a 2-pole BLDCM using M36G29 laminations at 60 Hz, and under a CCW rotating field.....	139
Fig. 5.49: The power loss distribution in [W/kg] considering the rotational core losses in the stator of a 2-pole BLDCM using M36G29 laminations at 400 Hz, and under a CW rotating field.....	140
Fig. 5.50: The power loss distribution in [W/kg] considering the rotational core losses in the stator of a 2-pole BLDCM using M36G29 laminations at 400 Hz, and under a CCW rotating field.....	140
Fig. 5.51: The power loss distribution in [W/kg] considering the rotational core losses in the stator of a 2-pole BLDCM using M36G29 laminations at 1 kHz, and under a CW rotating field.....	141
Fig. 5.52: The power loss distribution in [W/kg] considering the rotational core losses in the stator of a 2-pole BLDCM using M36G29 laminations at 1 kHz, and under a CCW rotating field.....	141

Fig. 5.53: The power loss distribution in [W/kg] considering the rotational core losses in the stator of a 6-4 SRM using M36G29 laminations at 60 Hz, and under a CW rotating field. 142

Fig. 5.54: The power loss distribution in [W/kg] considering the rotational core losses in the stator of a 6-4 SRM using M36G29 laminations at 60 Hz, and under a CCW rotating field. 142

Fig. 5.55: The power loss distribution in [W/kg] considering the rotational core losses in the stator of a 6-4 SRM using M36G29 laminations at 400 Hz, and under a CW rotating field. 143

Fig. 5.56: The power loss distribution in [W/kg] considering the rotational core losses in the stator of a 6-4 SRM using M36G29 laminations at 400 Hz, and under a CCW rotating field. 143

Fig. 5.57: The power loss distribution in [W/kg] considering the rotational core losses in the stator of a 6-4 SRM using M36G29 laminations at 1 kHz, and under a CW rotating field. 144

Fig. 5.58: The power loss distribution in [W/kg] considering the rotational core losses in the stator of a 6-4 SRM using M36G29 laminations at 1 kHz, and under a CCW rotating field. 144

Fig. 6.1: The total rotational core loss at 60 Hz, in M36 steel Gauge 26, with the corresponding x and y components, P_x and P_y respectively. 152

Fig. 6.2: The total rotational core loss at 400 Hz, in M36 steel Gauge 26, with the corresponding x and y components, P_x and P_y respectively.	152
Fig. 6.3: The total rotational core loss at 1 kHz, in M36 steel Gauge 26, with the corresponding x and y components, P_x and P_y respectively.	153
Fig. 6.4: The pulsating losses in x and y directions at 60 Hz for M36G26.....	153
Fig. 6.5: The dynamic hysteresis loops (B_x - H_x) for the pulsating loss component in y direction at 60 Hz for M36G26. The loops are drawn at flux density level of 1T, 1.1T, 1.2T, and 1.3T.....	154
Fig. 6.6: The dynamic hysteresis loops (B_y - H_y) for the pulsating loss component in y direction at 60 Hz for M36G26. The loops are drawn at flux density level of 1T, 1.1T, 1.2T, and 1.3T.....	154
Fig. 6.7: The dynamic hysteresis loop for the y -component measured in the CW direction for M36G26 sample under 1.1T rotating field with 60 Hz.	155
Fig. 6.8: The dynamic hysteresis loop for the y -component measured in the CW direction for M36G26 sample under 1.2T rotating field with 60 Hz.	155
Fig. 6.9: The dynamic hysteresis loop for the y -component measured in the CW direction for M36G26 sample under 1.3T rotating field with 60 Hz.	156
Fig. 6.10: The dynamic hysteresis loop for the y -component measured in the CW direction for M36G26 sample under 1.4T rotating field with 60 Hz.....	156

Fig. 6.11: The dynamic hysteresis loop for the x -component measured in the CW direction for M36G26 sample under 1.1T rotating field with 60 Hz.....	157
Fig. 6.12: The dynamic hysteresis loop for the x -component measured in the CW direction for M36G26 sample under 1.2T rotating field with 60 Hz.....	157
Fig. 6.13: The dynamic hysteresis loop for the x -component measured in the CW direction for M36G26 sample under 1.3T rotating field with 60 Hz.....	158
Fig. 6.14: The dynamic hysteresis loop for the x -component measured in the CW direction for M36G26 sample under 1.4T rotating field with 60 Hz.....	158
Fig. 6.15: The position of \mathbf{B} coils wound around the sample. (a) The original position. (b) The position after a deflection of 10° in the CW direction.	159
Fig. 6.16: Rotational core losses in M36G26 sample before and after the \mathbf{B} coil deflection. Measurements are under the CW rotating field at 60 Hz.....	159
Fig. 6.17: The measured x and y loss components of rotational core losses in the CW direction for M36G26 sample with 60 Hz. The loss components at which \mathbf{B} coils were in their original right position P_x -Original and P_y -Original are compared with loss components after the deflection of the \mathbf{B} coil.	160
Fig. 6.18: The dynamic hysteresis loop for the y -component measured in the CW direction for M36G26 sample under 1.1T rotating field with 60 Hz after the \mathbf{B} coils deflection.....	160

Fig. 6.19: The dynamic hysteresis loop for the y -component measured in the CW direction for M36G26 sample under 1.2T rotating field with 60 Hz after the \mathbf{B} coils deflection..... 161

Fig. 6.20: The dynamic hysteresis loop for the y -component measured in the CW direction for M36G26 sample under 1.3T rotating field with 60 Hz after the \mathbf{B} coils deflection..... 161

Fig. 6.21: The dynamic hysteresis loop for the y -component measured in the CW direction for M36G26 sample under 1.4T rotating field with 60 Hz after the \mathbf{B} coils deflection..... 162

Fig. 6.22: The result of the flux density from the addition of the fundamental of 1T peak value and a third harmonic of a peak of 0.3 T, where both the fundamental and the harmonic are in-phase. 165

Fig. 6.23: The result of the flux density from the addition of the fundamental of 1T peak value and a third harmonic of a peak of 0.3 T, where the third harmonic is 180° lagging..... 165

Fig. 6.24: The result of the flux density from the addition of the fundamental of 1T peak value and a third harmonic of a peak of 0.3 T, where the third harmonic is 90° leading..... 166

Fig. 6.25: The flux density waveform of 1.3T and 60 Hz fundamental component with a third harmonic B_x , and the corresponding magnetic field strength waveform H_x for a M36G29 sample under a pulsating field.	168
Fig. 6.26: The flux density waveform of 1.3T and 60 Hz fundamental component with a third harmonic B_y , and the corresponding magnetic field strength waveform H_y for a M36G29 sample under a pulsating field.	168
Fig. 6.27: The dynamic hysteresis loops for a M36G29 sample under a pulsating field of 1.3T and 60 Hz fundamental component with a third harmonic. (a) In the x -direction. (b) In the y -direction.	169
Fig. 6.28: The dynamic hysteresis loops for a M36G29 sample under a pulsating field of 1.3T and 400 Hz fundamental component with a third harmonic. (a) In the x -direction. (b) In the y -direction.	169
Fig. 6.29: The flux density waveforms B_x and B_y of 1.0T and 60 Hz fundamental component with a third harmonic for a M36G29 sample under rotating field.	172
Fig. 6.30: The magnetic field strength waveforms H_x and H_y associated with the flux density waveforms B_x and B_y in Fig. 6.29 for a M36G29 sample under rotating field.	172
Fig. 6.31: (a) Locus of magnetic field strength for H_x and H_y waveforms in Fig. 6.30. (b) Locus of magnetic flux density for B_x and B_y waveforms in Fig. 6.29.	173

Fig. 6.32: The dynamic hysteresis loop in the x -direction for a M36G29 sample under a rotating field of 1T and 60 Hz fundamental component with a third harmonic.	173
Fig. 6.33: The dynamic hysteresis loop in the y -direction for a M36G29 sample under a rotating field of 1T and 60 Hz fundamental component with a third harmonic.	174
Fig. 6.34: The dynamic hysteresis loop in the x -direction for a M36G29 sample under a rotating field of 1.1T and 60 Hz fundamental component with a third harmonic.	174
Fig. 6.35: The dynamic hysteresis loop in the y -direction for a M36G29 sample under a rotating field of 1.1T and 60 Hz fundamental component with a third harmonic.	175
Fig. 6.36: The dynamic hysteresis loop in the x -direction for a M36G29 sample under a rotating field of 1.2T and 60 Hz fundamental component with a third harmonic.	175
Fig. 6.37: The dynamic hysteresis loop in the y -direction for a M36G29 sample under a rotating field of 1.2T and 60 Hz fundamental component with a third harmonic.	176
Fig. 6.38: The dynamic hysteresis loop in the x -direction for a M36G29 sample under a rotating field of 1.3T and 60 Hz fundamental component with a third harmonic.	176
Fig. 6.39: The dynamic hysteresis loop in the y -direction for a M36G29 sample under a rotating field of 1.3T and 60 Hz fundamental component with a third harmonic.	177
Fig. 6.40: The dynamic hysteresis loop in the x -direction for a M36G29 sample under a rotating field of 1T and 400 Hz fundamental component with a third harmonic.	177

Fig. 6.41: The dynamic hysteresis loop in the y -direction for a M36G29 sample under a rotating field of 1T and 60 Hz fundamental component with a third harmonic.	178
Fig. 6.42: The dynamic hysteresis loop in the x -direction for a M36G29 sample under a rotating field of 1.1T and 400 Hz fundamental component with a third harmonic.	178
Fig. 6.43: The dynamic hysteresis loop in the y -direction for a M36G29 sample under a rotating field of 1.1T and 400 Hz fundamental component with a third harmonic.	179
Fig. 6.44: The dynamic hysteresis loop in the x -direction for a M36G29 sample under a rotating field of 1.2T and 400 Hz fundamental component with a third harmonic.	179
Fig. 6.45: The dynamic hysteresis loop in the y -direction for a M36G29 sample under a rotating field of 1.2T and 400 Hz fundamental component with a third harmonic.	180
Fig. 6.46: The dynamic hysteresis loop in the x -direction for a M36G29 sample under a rotating field of 1.3T and 400 Hz fundamental component with a third harmonic.	180
Fig. 6.47: The dynamic hysteresis loop in the y -direction for a M36G29 sample under a rotating field of 1.3T and 400 Hz fundamental component with a third harmonic.	181
Fig. 6.48: The dynamic hysteresis loop in the y -direction under a rotating field of 1.43T peak	181
Fig. 6.49: A comparison between core losses obtained by: (a) Rotating field with a third harmonic. (b) Purely circular rotating field created by fundamentals. (c) Circular rotating	

field created by only third harmonics. (d) The algebraic sum of losses obtained in (b) and (c). Tests performed under fundamental frequency of 60 Hz for a M36G29 sample..... 183

Fig. 6.50: A comparison between core losses obtained by: (a) Rotating field with a third harmonic. (b) Purely circular rotating field created by fundamentals. (c) Circular rotating field created by only third harmonics. (d) The algebraic sum of losses obtained in (b) and (c). Tests performed under fundamental frequency of 400 Hz for a M36G29 sample.... 184

Fig. 6.51: A comparison between core losses obtained by: (a) Rotating field with a third harmonic. (b) Pulsating field with a third harmonic in x -direction. (c) Pulsating field with a third harmonic in y -direction. (d) The algebraic sum of losses obtained in (b) and (c). Tests performed under fundamental frequency of 60 Hz for a M36G29 sample..... 184

Fig. 6.52: A comparison between core losses obtained by: (a) Rotating field with a third harmonic. (b) Pulsating field with a third harmonic in x -direction. (c) Pulsating field with a third harmonic in y -direction. (d) The algebraic sum of losses obtained in (b) and (c). Tests performed under fundamental frequency of 400 Hz for a M36G29 sample.... 185

LIST OF TABLES

Table 2.1 : Standard deviation for flux density distribution in each sample in three circuits of different poles.	18
Table 2.2: Standard Deviation (SD) for each sample shape	29
Table 2.3: The flux density in samples with different gauges.	35
Table 2.4: Correlation coefficients of pulsating core losses.	43
Table3.1: A comparison between rotational and pulsating core losses in the x and y directions at different frequencies in [W/kg]	71
Table 3.2: The percentage permeability difference between the x and y directions	71
Table 4.1: Geometrical dimensions of the 2-pole induction machine in [mm].	74
Table 4.2: Geometrical dimensions of the 2-pole BLDC machine in [mm].....	74
Table 4.3: Geometrical dimensions of the 6-4 SRM in [mm].	74
Table 4.4: Aspect ratios of flux density loci and the corresponding phase shift between the input signals.	80
Table 4.5: Error percentages in the three different types of machines.	100
Table 5.1: The percentage permeability difference between the x and y directions in the case of CW and CCW rotating field	125

Table 5.2: Power loss in the three different machine types using M36G29 laminations with CW and CCW rotating field	145
Table 6.1: Power loss in the M36G29 lamination at 60 Hz and 400 Hz produced by pulsating fields with and without the third harmonic component.....	170
Table 6.2: Power loss in the M36G29 lamination at 60 Hz and 400 Hz produced by rotating fields with and without the third harmonic component.....	182

1. INTRODUCTION

1.1 Motivation and Aim of the Work

The need for testing magnetic materials used in electric machine laminations and measurements under rotating field is derived from the developments in efficient machine design. Industrial sectors will not be able to develop to their full potential without associated developments in measurement, testing and related disciplines. Despite the considerate work done in the core loss estimation and measurement equipment as well as modeling with the aid of powerful computers, the machine designers still suffer from inaccurate prediction of the total core loss in machines. Correction factors between (1.5-2) are applied to match the simulations results to the experimental data [1]. Many experts attributed the discrepancy between measured and simulated values to the ignorance of rotational core losses, and claimed that the rotating fields produce a remarkable portion of core loss [2], [3], [4], [5].

The lack of rotational core loss data and the vague understanding of rotating field behavior in the machine laminations were the initial motivation of this research. The absence of agreed standards of testing equipment and measuring methods urged the authors to design a new test fixture to overcome the problems in current fixture designs [6].

This work is expected to increase the understanding of the rotating field performance in rotating machine laminations, in order to progress to a rigid model of rotational core loss, which is capable of predicting the total core loss in machine cores.

1.2 Core Losses in AC Machines

Core losses can form 15-25 % of the total losses in conventional electrical machines operating with 50/60 Hz sinusoidal supply, depending on the type and quantity of magnetic materials [7]. Core loss consists of hysteresis loss and eddy current loss, and constitutes a much higher fraction in novel or high speed machines.

Characterization of flux patterns in the stator yoke of AC machines shows that many different flux trajectories appear in different zones in the stator core. It can be observed from Fig. 1.1 that the flux trajectory is almost circular at the roots of stator teeth, and elliptical at the back of the slots. But, the flux is pulsating in the stator teeth and along the back of the stator yoke [8] and [9]. In the three-phase T-joint transformers, the rotating flux occurs at the corners and at the joint area between the middle limb and the yoke [10].

In 1896 [11], Baily first investigated the hysteresis loss in steel exposed to magnetic rotating fields.

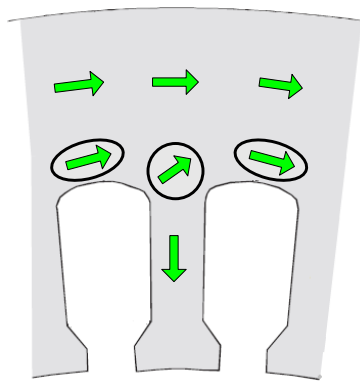


Fig. 1.1 : Stator tooth and two slots of stator yoke in AC machine

1.3 Methods and Apparatus for Measuring Rotational Core Losses

1.3.1 Method

There are several methods available in the literature which predict rotational core losses in machine laminations [12]. Depending on their principle techniques of calculating the losses, these methods can be categorized as follows:

A. Torque-Metric Method (Bailey's Method)

In this method, the testing sample which is a disc of magnetic material is mounted on a spindle and is placed in a horizontal plane containing an applied field [13]. The work done in one complete rotation represents the rotational losses per cycle, and the torque is measured by using a mechanical torque meter. The advantages of the Torque-Metric method are the direct reading of the torque due to the rotational losses and the ability to do measurements under a high flux density, where the difficulty of torque meter construction appears as a major shortcoming [14].

B. Thermal Method

The thermal method usually uses either thermocouples [15] or thermistors placed on the sample surface to determine the rate of change of the temperature dT/dt , this quantity is proportional to the dissipated power in the sample:

$$P = c_p \frac{dT}{dt} \quad (1.1)$$

Where c_p is the specific heat per unit mass.

The problems with the thermocouple are its low output voltage signal and the need for careful installation, calibration, and isolation against noise and electromagnetic interference. The disadvantage of thermistors is the need of supplying them by a stable current source, since they are considered active devices. Thermistors utilize a few percent of measured power, where an error correction should be taken into account [16]. By using the thermal method, localized measurement of core losses in T-joints transformers is available [17].

C. Field-metric Method

In this method, the rotational core loss figure is extracted from the measured data of flux density \mathbf{B} (inside the sample), and the magnetic field strength \mathbf{H} (at the surface of the sample, and not inside as some assumed). Then, the rotational core loss in the sample can be derived by using Poynting theorem as seen in [18], which yields:

$$P = \frac{1}{T\rho} \int_T (H_x \frac{dB_x}{dt} + H_y \frac{dB_y}{dt}) dt \quad (1.2)$$

Where, H_x , H_y , B_x , and B_y are the measured components of the magnetic field strength and the flux density in x and y directions respectively. T is the time period and ρ is the mass density of the material.

The advantage of this method is the high accuracy of results, but with many difficulties in setup manufacturing, sensor installation, and calibration.

The field-metric method is seen to be the most convenient and reliable method [19], and it will be used in this work.

D. Watt-Metric Method

This method is used to measure rotational core losses with a vertical yoke single sheet tester. In this case the flux is kept in the magnetic media where there is no air gap between yoke poles and the testing sample, and H is determined from the magnetizing current by using Ampere's law. This method is preferable because of simplicity, but the vague magnetic path causes inaccurate measurements. To reduce this error, more attention is paid to the sample's shape and yoke structure [20].

1.3.2 Apparatus

Rotational core losses are measured with different core loss measurement apparatus, and they are normally not identical. Each apparatus has its own properties. Lamination manufacturers tend to measure core losses more rapidly, while machine designers tend to require more accuracy. It is necessary to understand the difference among different measurement apparatus.

In general, rotational core loss apparatus can be classified as follows:

A. Torque Magnetometer

The testing sample which is a disc of magnetic material is mounted on a spindle and is placed in a horizontal plane containing an applied field. The work done in one complete

rotation represents the rotational losses per cycle. The torque can be read directly due to the rotational losses, and there is ability to do measurements under a high flux density. The difficulty of the torque magnetometer construction is appeared as a major shortcoming [14].

B. Vertical yoke tester

Two perpendicular U-shaped yokes are placed in the x and y directions, exciting coils wound around the yokes arms, and the sample closes the magnetic circuit for both directions. The rotational core loss is evaluated by the field-metric method or Watt-metric method [21]. The main problem in this system is the low flux density in the middle of the sample where the measurements are done, which reaches around 0.2 T, because of high leakage fluxes between the x and y yokes [14]. See Fig. 1.2.

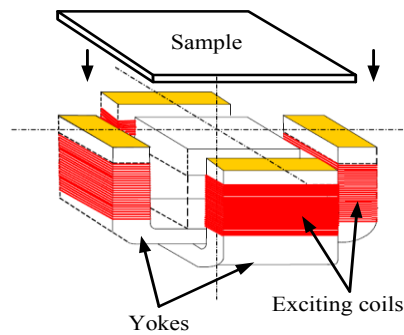


Fig. 1.2: The structure of vertical yoke tester [22].

C. Rotational single sheet tester (RSST)

The rotational single sheet testers (RSST) are classified according to the sample shape, while basically fall into three types: square, hexagonal and circular. Fig. 1.3 illustrates

these test fixtures. The problem in all these designs is that the main flux is distorted due to the closeness of poles, for example in square samples the x -direction flux is affected by y -poles where they attract the main flux and that increases the flux leakage.

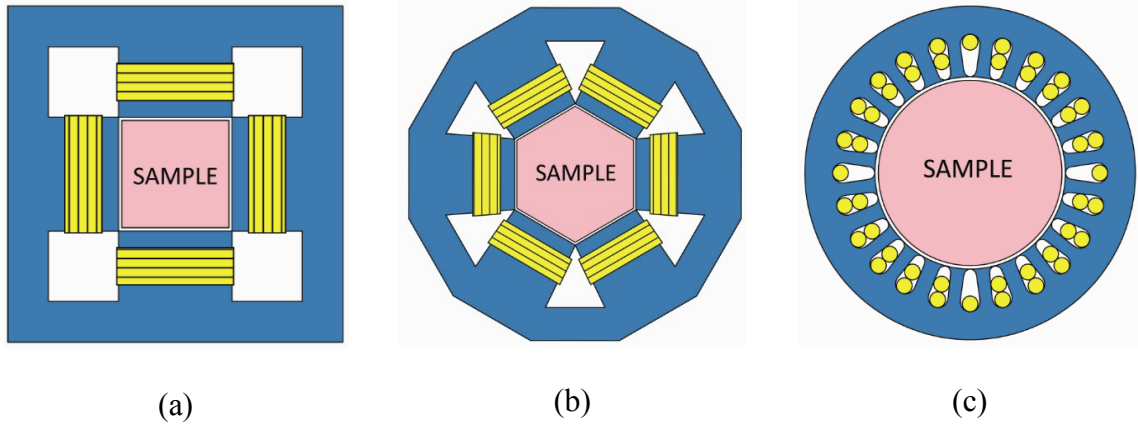


Fig. 1.3: Different shapes of samples with their corresponding magnetizing circuits
(a) Square (b) Hexagonal (c) Circular.

1.4 Techniques for Measuring Components of the Magnetic Flux Density (B), and the Magnetic Field Strength (H).

1.4.1 Methods of Measuring the Magnetic Flux Density (B)

A. Search coil method (Induction coil sensor)

The search coil operating principle is based on Faraday's law, where the flux density signal can be calculated by:

$$B = \int \frac{v_B}{N_B A_B} dt \quad (1.3)$$

Where, v_B is the terminal induced voltage of the search coil, N_B is the coil turn's number, and A_B is the cross sectional area of the coil. Because of the lack of the uniformity of the flux density over the whole sample, the coils are threaded in small holes in the middle of the sample in a small area called the measuring area. The disadvantage of this method is a reduction of the magnetic quality of the sample because of the holes, in addition to the difficulty of drilling micro holes [23].

B. Needle or Tip method

Two needle tips are placed on the sample surface with a distance (l) apart between them, as shown in Fig. 1.4.

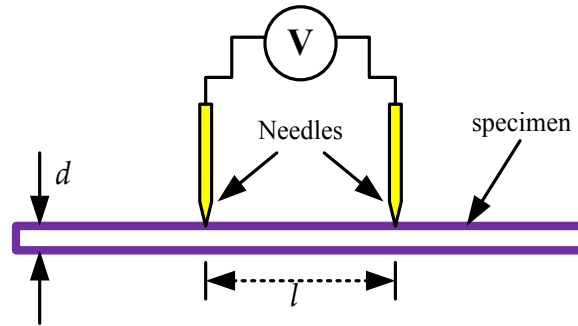


Fig. 1.4: Needle method for measuring flux density in the sample

The measured voltage can be obtained from Faraday- Maxwell's equation [24]:

$$v = \oint E \cdot dl = - \iint \frac{\partial B}{\partial t} \cdot dA \quad (1.4)$$

$$v = -\frac{1}{2} \oint_{A_n} \frac{dB}{dt} \cdot dA_n = -\frac{1}{2} \cdot l \cdot d \cdot \frac{dB}{dt} \quad (1.5)$$

Where E is the electric field, v is the measured voltage between the tips, A_n is the cross sectional area of the sample bordered by the tips, (l) is the distance between the tips, and (d) is the sample thickness. The disadvantage of needle method is the low voltage produced which is easily affected by noise [25], and also the need to remove the insulation surface which usually coats the laminations [26].

C. Hall element

The hall-effect phenomenon occurs when a conductor with a thickness (d) carries a current (i) and subjected to magnetic field B , an electromotive force (e_H) appears between points a and b as shown in Fig. 1.5, and can be given by:

$$e_H = R_H \cdot \frac{i \cdot B}{d} \quad (1.6)$$

Where d is the thickness of Hall element. R_H is the Hall coefficient, depending on the material properties, and can be determined experimentally [27].

The Hall effect method is not common in measurements of rotational core losses, because of the difficulty of installation within the experimental setup [28].

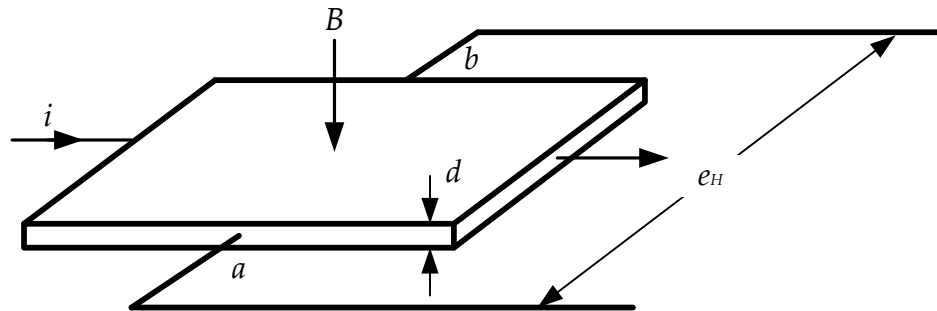


Fig. 1.5: The operation principle of Hall Effect sensor.

1.4.2 Methods of Measuring the Magnetic Field Strength (H)

A. Magnetization current method or direct method

The magnetic field strength (H) can be calculated directly by using Ampere's law:

$$H = \frac{N.i}{l_m} \quad (1.7)$$

Where N is the turn's number of the excitation coil, (i) is the current, and l_m is mean length of the magnetic path. To obtain accurate results by this technique, the magnetic path l_m should be clear and well defined, and the potential drop should be completely on the sample. Because of that, additional corrections should be scheduled, and it is rarely used in rotational losses measurements [29].

B. Rogowski-Chattock potentiometer (RCP) or The magnetic potentiometer

The form of RCP basically consists of a coil wound on a non-magnetic material core, and bent in order to place the coil's end-faces in such away butted against the specimen, as shown in Fig. 1.6 [30].

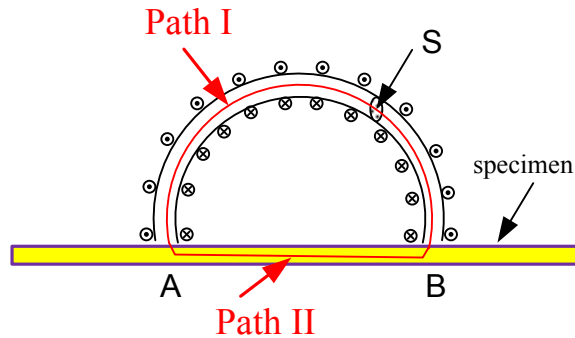


Fig. 1.6: Rogowski-Chattock potentiometer (RCP).

The operating principle of RCP is based on Ampere's law, where the magnetomotive force (*mmf*) between points A and be B can be found by taking the integrals along the paths I and II:

$$mmf(A) - mmf(B) = \int_{II} \mathbf{H}_{II} \cdot d\mathbf{l}_{II} = \int_I \mathbf{H}_I \cdot d\mathbf{l}_I \quad (1.8)$$

Where, (*dl*) is a line element of the path.

But, the flux enclosed by the coil is given by:

$$\Phi = \mu_o \cdot n^* \cdot S \int_I \mathbf{H}_I \cdot d\mathbf{l}_I \quad (1.9)$$

Where, *n** is the number of turns per unit length, and *S* is the cross sectional area of the coil. Recall that due the absence of current, the line integrals of **H** between points A and be B along any path are equal:

$$\int_{II} \mathbf{H}_{II} \cdot d\mathbf{l}_{II} = \int_I \mathbf{H}_I \cdot d\mathbf{l}_I \quad (1.10)$$

And since the *H_{II}* is assumed to be constant and homogenous,

$$\mathbf{H}_{II} \cdot L_{AB} = \int_I \mathbf{H}_I \cdot d\mathbf{l}_I \quad (1.11)$$

$$\mathbf{H}_{II} \cdot L_{AB} = \frac{\Phi}{\mu_o \cdot n^* \cdot S} \quad (1.12)$$

$$\Phi = \mu_o \cdot n^* \cdot S \cdot \mathbf{H}_{II} \cdot L_{AB} \quad (1.13)$$

Therefore, the induced voltage by the RCP is given by:

$$e(t) = \frac{d\Phi}{dt} = \mu_o \cdot n^* \cdot S \cdot L_{AB} \cdot \frac{dH_{II}}{dt} \quad (1.14)$$

The factor $(n^* \cdot S \cdot L_{AB})$ can be determined by calibration in a known field, and then the term $\frac{dH_{II}}{dt}$ can be found.

Measurement errors occur because the output signal is relatively small, difficulty in installing the end-faces exactly in close contact with the specimen plane, the non-uniformity in the winding (n^* will not be constant) [31], and also the misalignments of the coils in the x and y -axis [32].

C. Tangential (Flat) coil method

A multi-turn coil is wound on a non-magnetic material, and placed directly on the sample surface, as illustrated in Fig. 1.7. The induced voltage between the coil terminals is described by applying Faraday's law as:

$$v_H = -N \frac{d\Phi}{dt} = -N A_H \mu_o \frac{dH_s}{dt} \quad (1.15)$$

Where N is the number of turns on the former, Φ is the flux linked through the coil, A_H is the cross sectional area of the coil, and H_s represents the field strength at the surface of the sample [30].

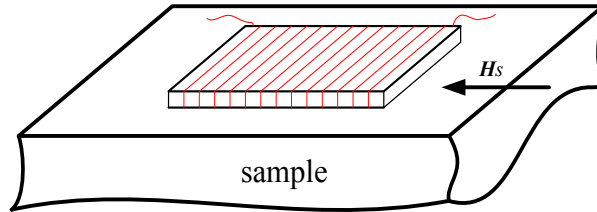


Fig. 1.7: Tangential coil placed on sample surface.

To obtain a reliable output signal from this sensor, the coil thickness should be as thin as possible to pick up the tangential component of \mathbf{H} exactly on the sample's surface; at the same time decreasing the coil thickness affects the output voltage level (thinner coil means lower voltage level). As a consequence, special attention should be paid to the coil dimension design and manufacturing process [33]. In many apparatus' designs, two orthogonal coils are wound on the same rectangular former [34]; in this case, the inner coil will be some distance from the sample surface because of the outer wound coil, and this creates additional errors. To overcome this problem, a two-coil system was proposed [35], and also a multi H-coil system had been suggested to find the tangential component of \mathbf{H} by extrapolating the coils' output signals [33].

1.5 Conclusion

In recent years, several methods and devices have been proposed to measure rotational core losses. Methods for measuring rotational core losses are discussed. The field-metric method is seen to be the most convenient and reliable method, where it will be used in this work. Techniques for measuring components of the magnetic flux density (\mathbf{B}) and the magnetic field strength (\mathbf{H}) are presented. In this work, a search coil method will be used for measuring \mathbf{B} , and tangential coil method for measuring \mathbf{H} .

2. DESIGN CONSIDERATIONS

2.1 Introduction

Recently, considerable attention has been focused on development of magnetizing circuit for the measurement of rotational core losses [36]. Technically, it is still a challenge to realize both high and uniform magnetic flux density within a wide area of the sample under testing. Because of that, importance is placed on developing fixtures which are capable of performing 2-D rotating field tests [37]. In the previous measurement apparatus designs, analysis of the flux density distributions in the sample show that the main flux was distorted due to the closeness of the magnetizing circuit poles, for example in a square sample, the x -direction flux is affected by y -poles where they attract the main flux which increases the flux leakage [38].

In this chapter, a new concept based on the Halbach principle is proposed to produce a rotating field in the sample. Extensive simulations are performed to study the magnetic field distribution in the sample using the new model design compared with the previous designs. The novel design of the magnetizing circuit is prototyped, operated using dSPACE, and validated successfully.

2.2 Halbach Array Design

2.2.1 Halbach Array Principle

In general, the Halbach array is an arrangement of permanent magnets in a special orientation that have the ability to create a one-sided flux of magnetization while

canceling it on the other side [39] and [40]. In the circular format, the magnets are arranged in predetermined angles in a circular frame where the flux is confined entirely within the frame [41]. As an example, Fig. 2.1 (a) shows an 8-pole Halbach circular design where 8 permanent magnets are arranged in specific angles, *i.e.* arrows show the flux directions. The total magnetic flux is confined within the frame and is directed entirely in one direction in the air gap at the center. Fig. 2.1 (b) shows the simulation of this format arrangement. The magnets used in this simulation are cylindrical in shape.

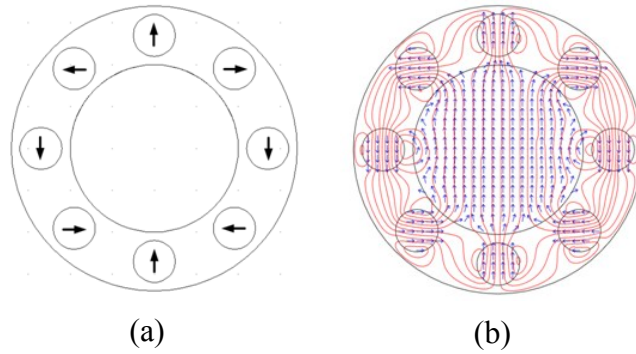


Fig. 2.1: Circular Halbach design of 8 cylindrical magnets which produces one sided flux in the y-axis. (a) circuit design (b) simulation result.

Of importance in the design is the determination of the deflection angles of the magnets to enhance the flux in only one direction in the air gap. The deflection angle δ can be calculated as:

$$\delta = 2 \times \frac{360^\circ}{\text{number of poles}} \quad (2.1)$$

2.2.2 Choosing Size and Number of Poles

The size of poles can be determined by considering the sample dimensions, and the air gap in the fixture, as shown in Fig. 2.2. Then equation (2.2) can be used to calculate the pole radius r_2 .

$$\frac{\sin \theta}{2 \times r_2} = \frac{\sin \alpha}{r_1 + r_2} \quad (2.2)$$

where

r_1 is the sample radius plus the air gap length.

r_2 is the pole radius.

θ is the central angle whose sides pass through centers of two adjacent poles.

α is equal to $\alpha = (\pi - \theta)/2$.

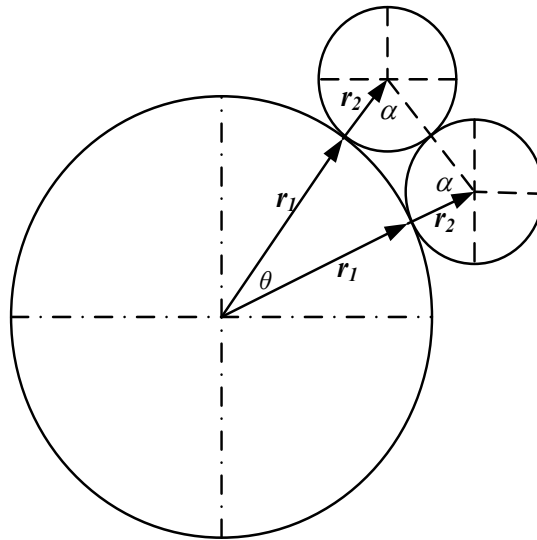


Fig. 2.2: Poles around the central air gap.

The number of poles in the magnetic array is an important factor which determines the flux density level and the homogeneity of the magnetic flux inside the sample. In this design, poles are arranged in a circular path to develop a one-sided flux direction in any desired direction.

Simulations are performed to examine the most suitable number of poles for a circular sample of 20 cm diameter, and 1 cm air gap. These include 8, 16, and 32 pole circuits. The geometrical shapes and dimensions (Figs. 2.3, 2.4, and 2.5) are designed according to the equations (2.1) and (2.2). The flux lines are shown at an angle of 45° .

Figs. 2.6, 2.7, and 2.8 show the magnetic flux density profile along the x -axis of the sample in the three circuits of different pole numbers. A large pole number requires more work in prototyping. Results illustrate that the flux variation within the sample in the 8-pole circuit happens not only at the edges but also in the middle of the sample, with a standard deviation of 0.0247. In the 16-pole design the variation is limited and appears at edges, with a standard deviation of 0.0209, where the flux density distribution is considered to be more homogeneous. With the 32-pole design, the variation in the flux is the least. The results are presented in Table 2.1. As a consequence, by increasing the number of poles, the variability of the magnetic field inside the sample decreases, and the flux density distribution becomes more homogeneous. To compromise between the prototyping effort and flux uniformity distribution, the 16-pole design was chosen. The 2-D flux density distributions of the same sample for the three different circuits are shown in Figs. 2.9, 2.10, 2.11.

Table 2.1 : Standard deviation for flux density distribution in each sample in three circuits of different poles.

Number of poles	Standard Deviation
8 poles circuit	0.0247
16 poles circuit	0.0209
32 poles circuit	0.0059

The reason for the reduction in the flux density distribution is explained from the fundamental Halbach equation. Dr. Halbach described the magnetic field inside the cylindrical array by the following equation [42]:

$$B_o = B_r \ln \left[\frac{r_o}{r_i} \right] \frac{\sin \left[\frac{2\pi}{m} \right]}{\left[\frac{2\pi}{m} \right]} \quad (2.3)$$

B_o is the field produced inside the working aperture. B_r is the remanence of the magnetic field of the permanent magnet material. r_i and r_o are the inside and outside radii of the magnet array, respectively. m is number of segments used.

By using equation (2.3), with many poles of different dimensions designed according to equation (2.2), and a constant magnetization (M) = 1170 [kA/m], the field produced inside the gap is illustrated in Fig. 2.12. By increasing the number of poles, the pole dimensions become smaller, and the flux density inside the array decreases.

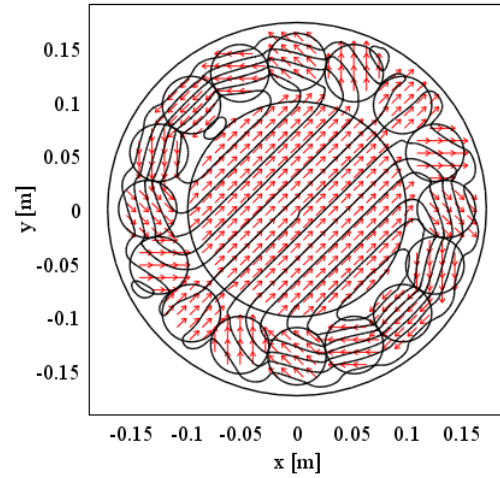
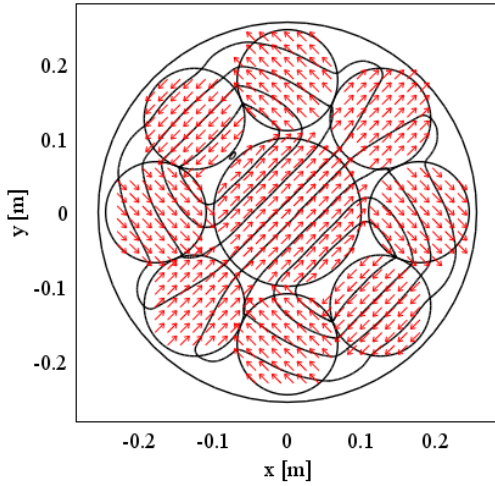


Fig. 2.3: Simulation showing resultant of two orthogonal equal vectors of 8-pole Halbach array producing 45° direction flux.

Fig. 2.4: Simulation showing resultant of two orthogonal equal vectors of 16-pole Halbach array producing 45° direction flux.

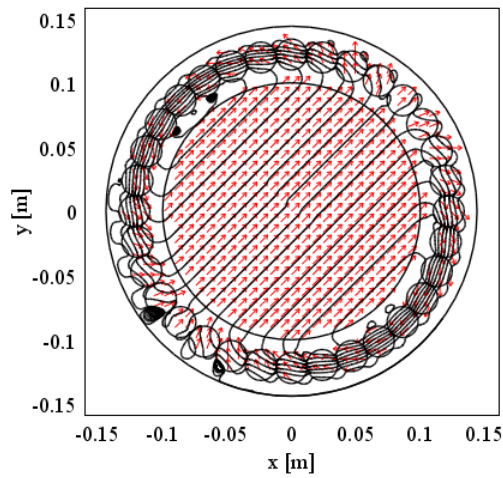


Fig. 2.5: Simulation showing resultant of two orthogonal equal vectors of 32-pole Halbach array producing 45° direction flux.

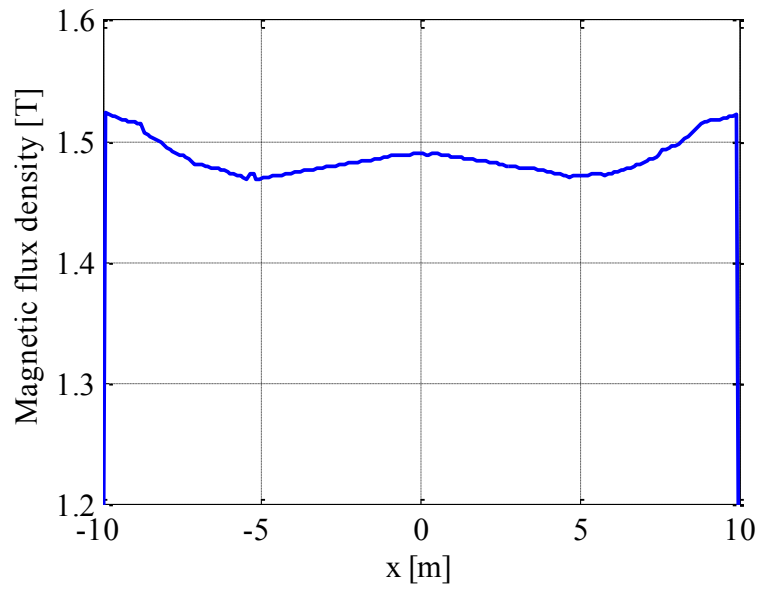


Fig. 2.6: The magnetic flux density profile along the x -axis of the sample in 8-pole circuit.

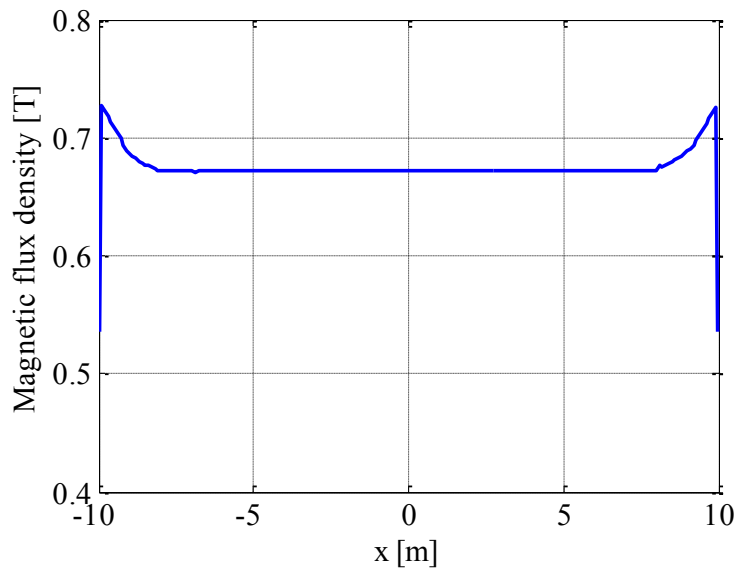


Fig. 2.7: The magnetic flux density profile along the x -axis of the sample in 16-pole circuit.

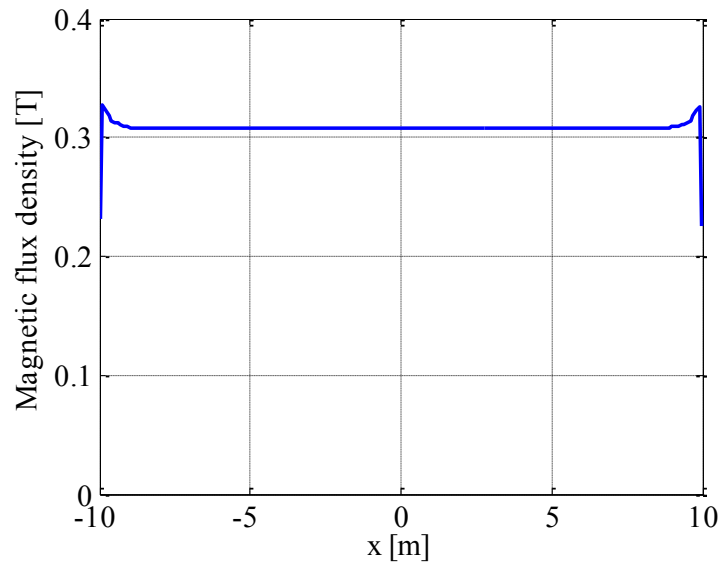


Fig. 2.8: The magnetic flux density profile along the x -axis of the sample in 32-pole circuit.

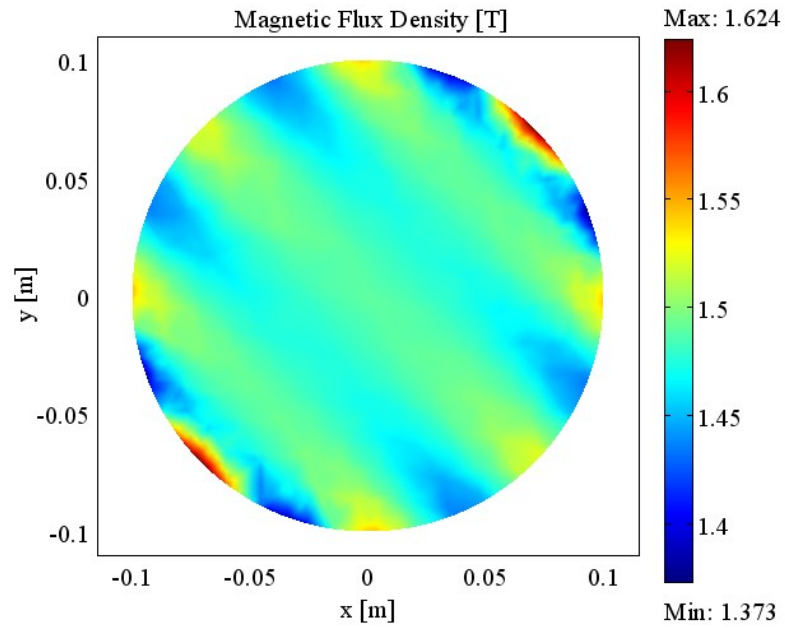


Fig. 2.9: The 2-D flux density distribution of the sample in an 8-pole circuit.

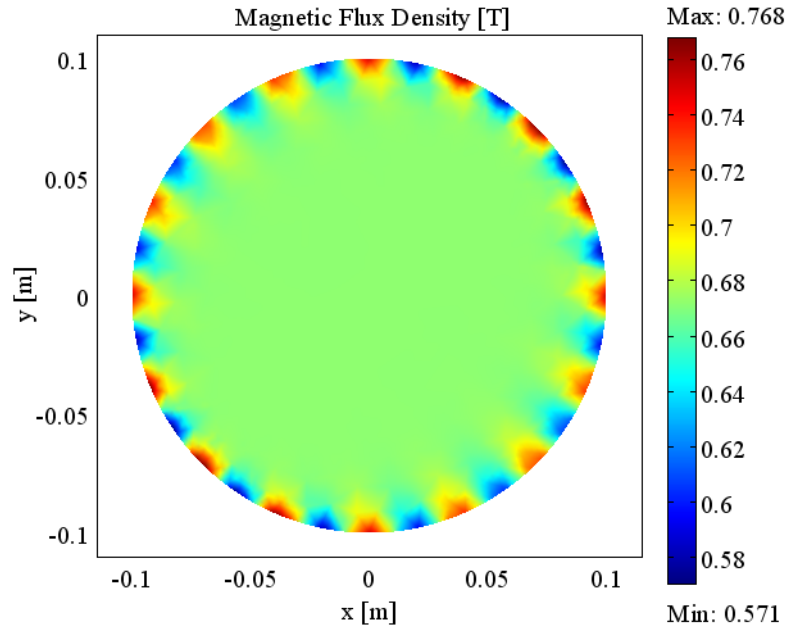


Fig. 2.10: The 2-D flux density distribution of the sample in a 16-pole circuit.

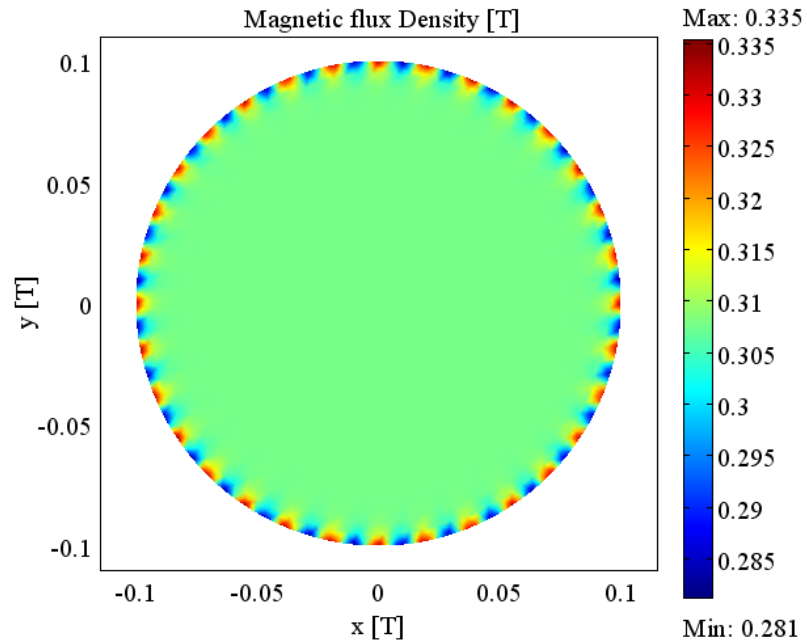


Fig. 2.11: The 2-D flux density distribution of the sample in a 32-pole circuit.

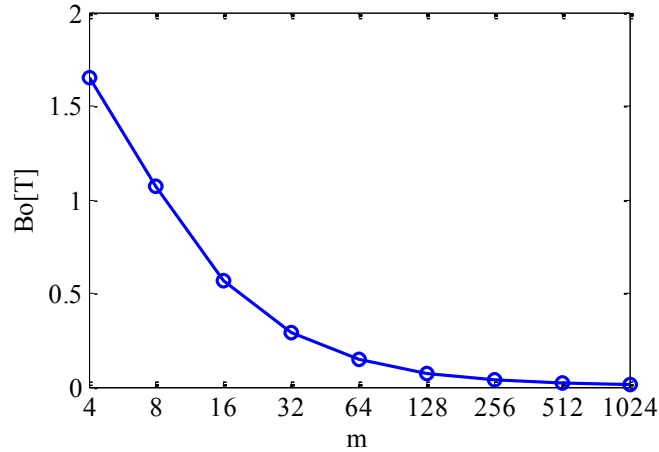


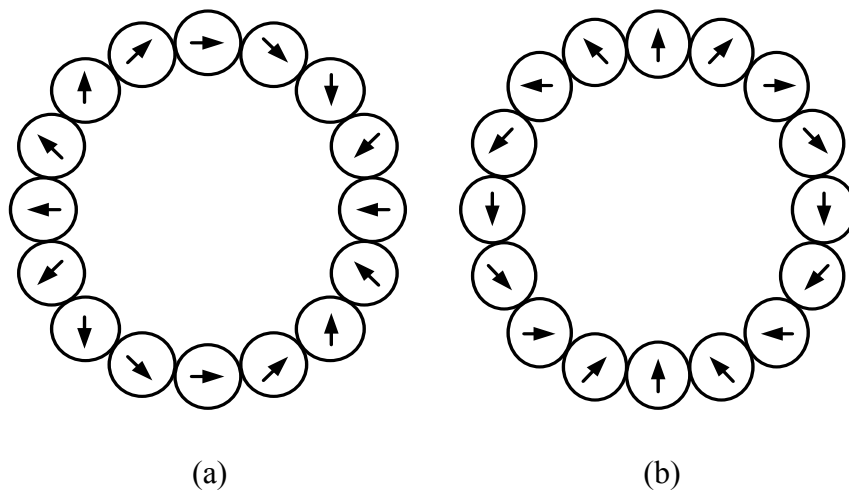
Fig. 2.12: The produced flux density in the gap of the Halbach array with different poles.

2.3 The Electromagnetic Halbach Array

Recently, many industrial applications have shown a strong interest in the PM Halbach array because of its attractive features. It has been used effectively in PM motor designs [43]. To date the Halbach array is known and presented using permanent magnets. In this new design, the magnetizing circuit is based on an electromagnetic system which is used to establish the Halbach pattern; electromagnets are used instead of permanent magnets, where coils are wrapped around magnetic cores in order to generate the flux. By using electromagnets, a controllable array in field magnitude and in signal shape is obtained. It also allows for a more compact sized array by using the same core for two different directions of electromagnets. This is the first application of an electromagnetic Halbach array for material testing.

Consider the 16-pole circuit, where the arrangement of the poles in the frame is in Fig. 2.14 (a), where a deflection of angle δ ($\delta=45^\circ$) is applied on each pole with respect to the

previous one. This electromagnetic Halbach array generates a flux density in the x -axis in the left direction. The same idea can be applied on the y -axis array as shown in Fig. 2.14 (b), where the net flux in the gap goes in the positive y -direction. If both arrays are combined by wrapping two coils on the same core (each coil is related to a different array), and both arrays are excited with the same input signals, then the result of the two perpendicular equal vectors is a resultant at 45° . The flux direction inside the sample can be varied in many ways: (a) Rotating the poles, which is not preferable, since it is difficult and not practical to move them mechanically. (b) Changing the amplitudes of the input signals, where the difference between the two magnitudes gives an ability to control the resultant. The simulations of both arrays for resultant vectors at 0° , 45° , and 60° are performed, where the flux paths through the whole circuit and the top pole are shown in Fig. 2.15.



2.13: The flux direction in each pole of a 16-pole Halbach array to produce a uni-directional flux. (a) In x -axis. (b) In y -axis.

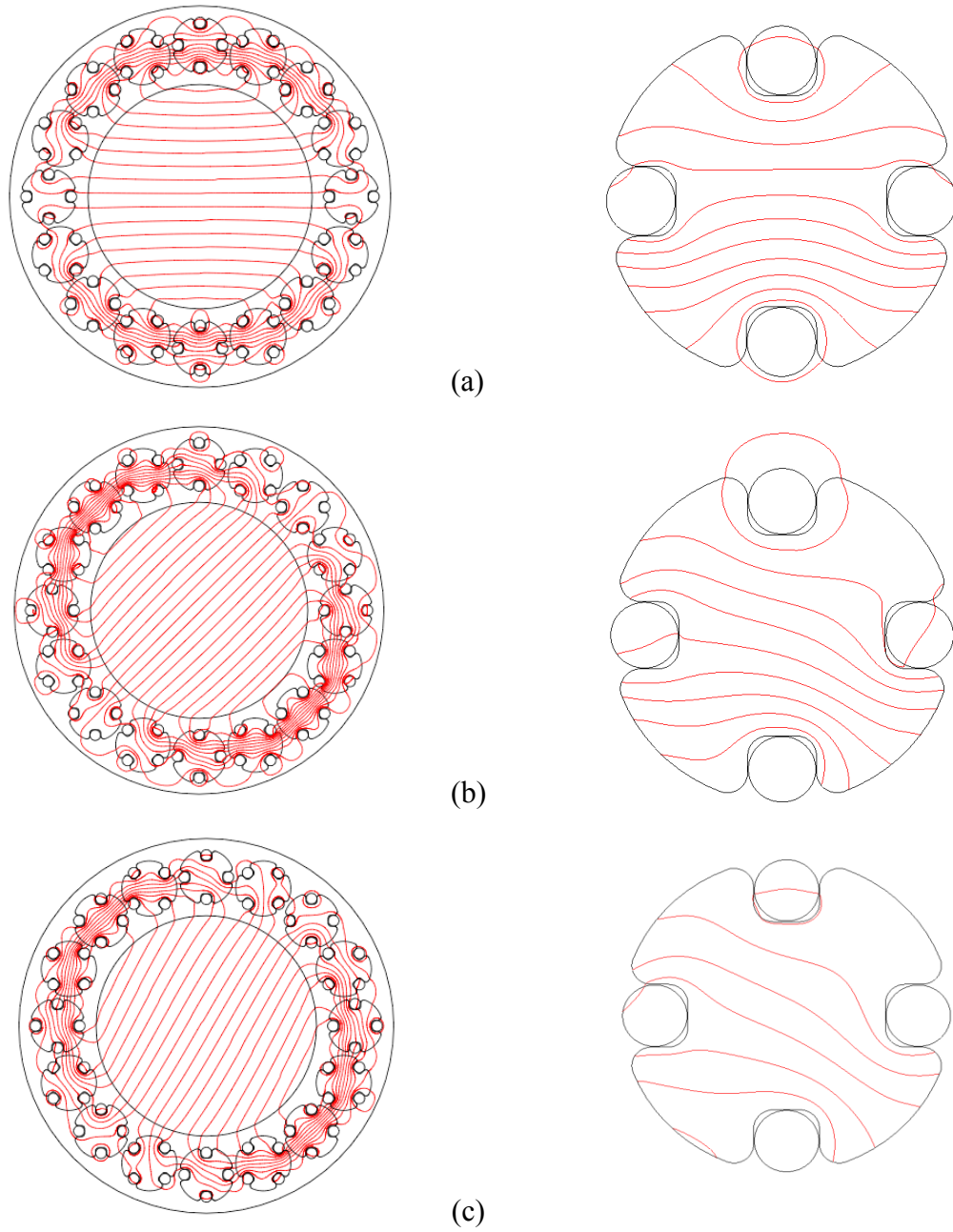


Fig. 2.14: Simulations of resultant vector produces a net flux at different angles, with flux paths in the top pole at (a) 0° (b) 45° (c) 60°

2.4 Sample Shape Design

The sample shape is an important factor to achieve uniformity and homogeneity in magnetic field distribution inside the sample. The most commonly used is the square, since it is easy to design and control its corresponding magnetic circuit. A hexagon is proposed in [44], and a circular shape is used in [45]. Each shape is suitable to a particular yoke or test frame. The square sample is used in the square rotational single sheet tester (SRSST), the hexagonal sample in the hexagonal rotational single sheet tester (HRSST), and the circular sample in the round rotational single sheet tester (RRSST) as shown in Fig. 2.15 (a), (b), and (c) respectively. In the RRSST, the core is similar to the stator of an induction machine, which can be excited by two-phases arranged orthogonally or by three-phases in order to create the rotating field. Two phases are used here to reduce the power supply requirement [46].

In all these designs the main flux experiences distortion due to the proximity of the poles. For example in the square sample the x -direction flux is affected by y -poles where they attract the flux which increases the flux leakage and causes non-uniform magnetization within the sample especially at the sample edges. The new design overcomes this problem, where the principle of magnetizing circuit construction is different, and there are no adjacent poles affecting the main flux. In this new design of an electromagnetic Halbach array, 16 poles are arranged in a circular path to develop one flux direction in the x -axis and another along the y -axis, see Fig. 2.15 (d). The vector summation of these two orthogonal fluxes allows rotational flux.

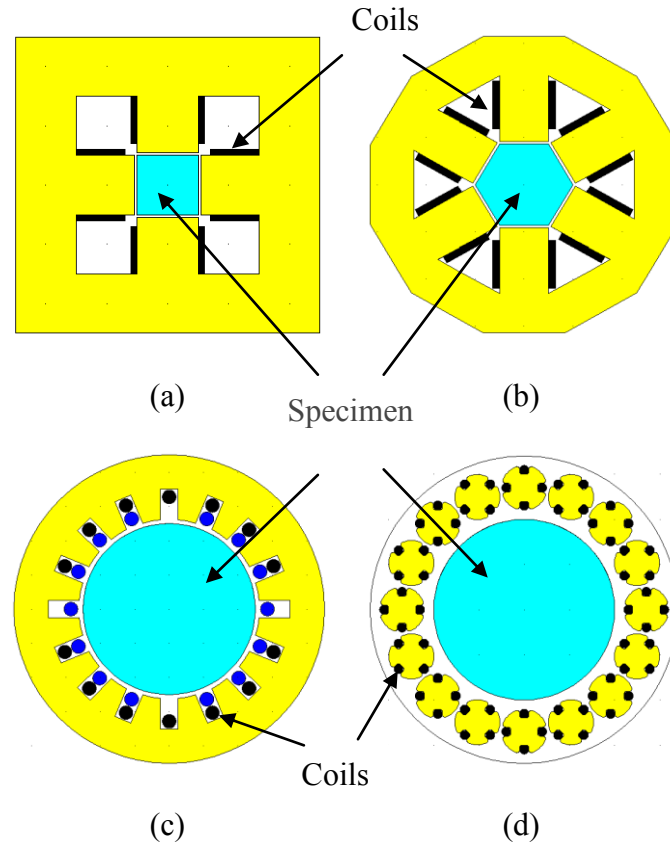


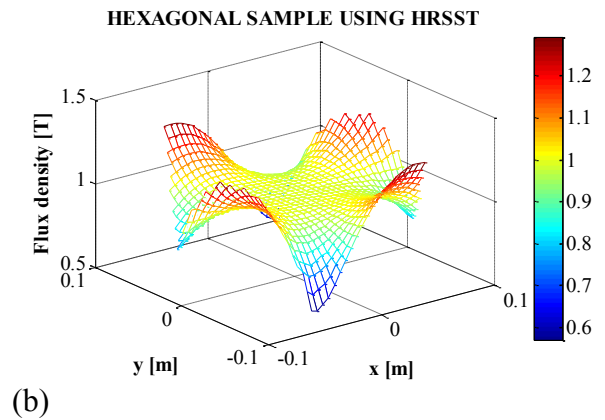
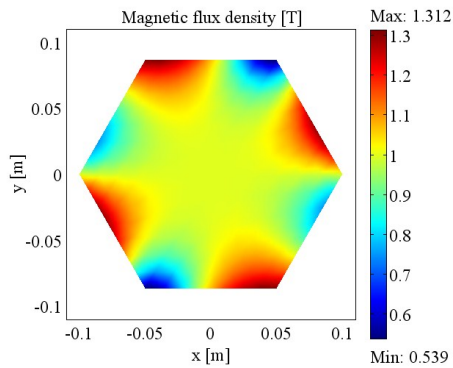
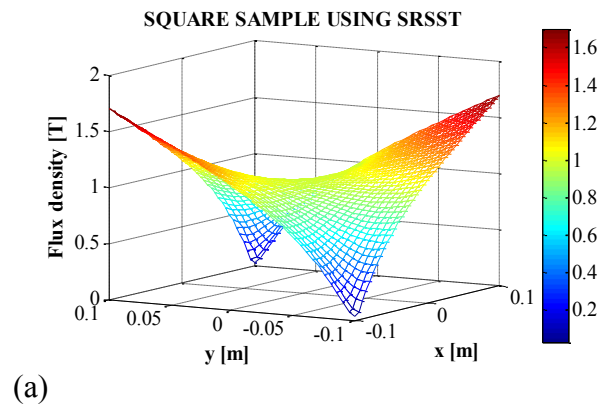
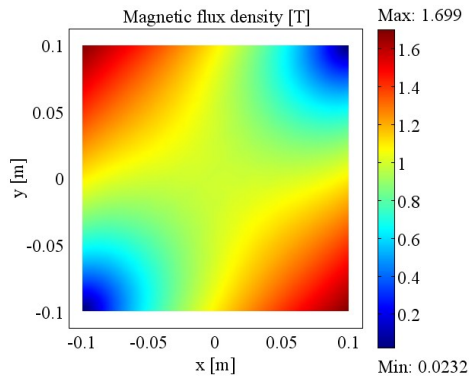
Fig. 2.15: Different shapes of samples with their corresponding magnetizing circuits
 (a) Square with SRSST (b) Hexagonal with HRSST (c) Circular with RRSST (d) Circular with Halbach array.

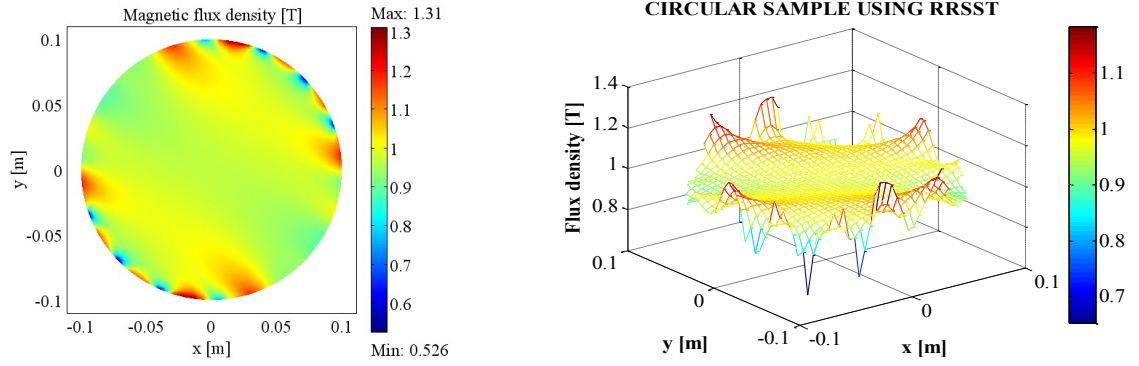
The three sample shapes (square, hexagonal, and circular) are simulated in 2-D under a constant flux density which is appropriate to obtain a 1T flux density level inside the sample with a direction of 45° using their corresponding magnetizing circuits. The flux density distribution within the samples is compared to determine the most appropriate shape to be used in test. Moreover, the circular sample is simulated using the new Halbach magnetizing circuit. The color maps of the flux density distribution and 3D mesh surfaces for the three different shapes are seen in Fig. 2.16.

Standard deviation (SD) is used as a criterion to determine the variability of the magnetic field inside the samples. The standard deviation is given by:

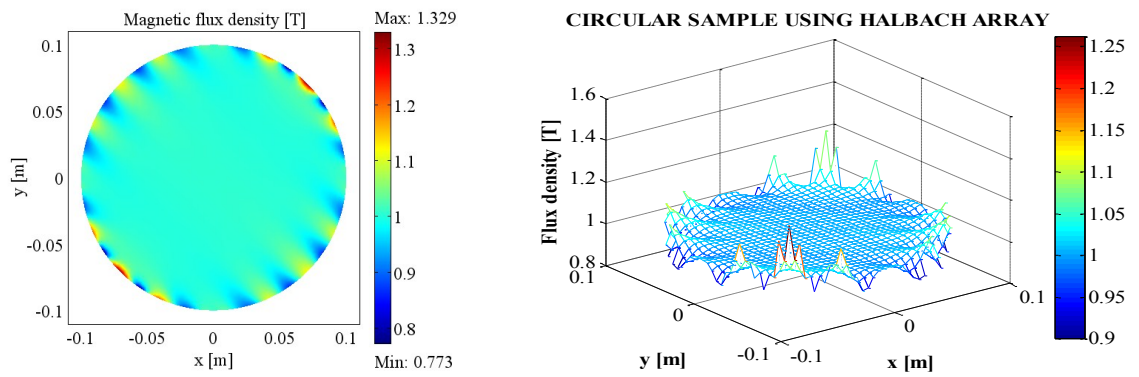
$$SD = \sqrt{\frac{1}{n} \sum_{i=1}^n (x_i - \bar{x})^2} \quad (2.4)$$

Where n is the number of samples in the specimen, x_i is the value of the flux density at each sample i , and \bar{x} is the flux density average of all samples. The results are presented in Table 2.2, where the circular sample tested by the Halbach array circuit has the lowest SD, which makes it the best shape to be used in test, since it achieves the best homogeneity of the flux density distribution.





(c)



(d)

Fig. 2.16: The flux density distribution of different sample shapes with the corresponding 3D mesh surfaces (a) Square (b) Hexagonal (c) Circular using RRSST (d) Circular using the Halbach array.

Table 2.2: Standard Deviation (SD) for each sample shape

Sample Shape	Standard Deviation
Square	0.31756
Hexagonal	0.11340
Circular using RRSST	0.07248
Circular using Halbach array	0.04831

To provide more accurate and reliable results of the field distribution within the sample, the standard deviation profile is estimated for a complete rotation of the flux density vector. Figs. 2.17, 2.18, 2.19, and 2.20 show the standard deviation profile of the flux density distribution over 360 degrees of rotation for the square sample, hexagonal sample, circular sample using RRSST, and for the circular sample using the Halbach array, respectively. The circular sample under test using Halbach array achieves the lowest SD in all directions of rotation, where the variation alternates between 0.046705 to 0.043498. On the other hand, the square sample has the highest SD and also the highest variation with changing the flux direction which is basically a result of asymmetry of the reluctance in the magnetizing circuit.

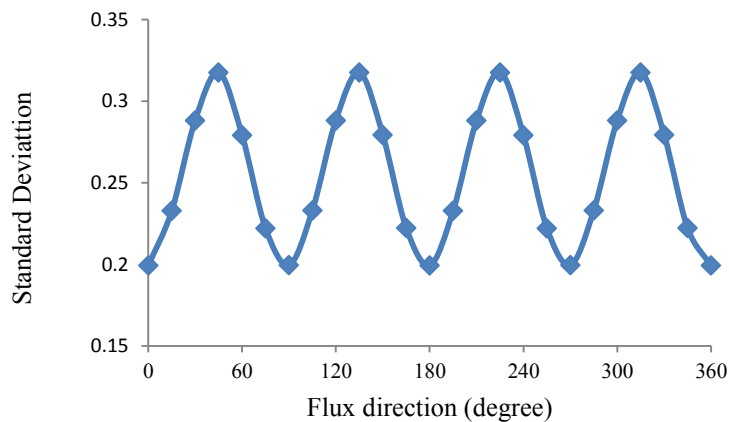


Fig. 2.17: Standard deviation profile of the flux density distribution for the square sample.

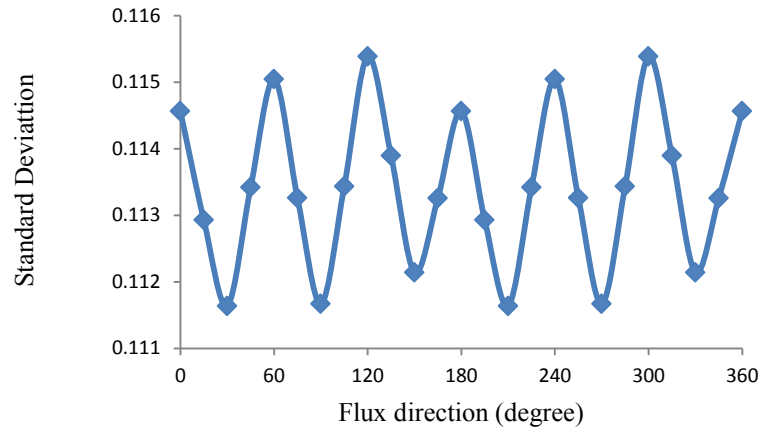


Fig. 2.18: Standard deviation profile of the flux density distribution for the hexagonal sample.

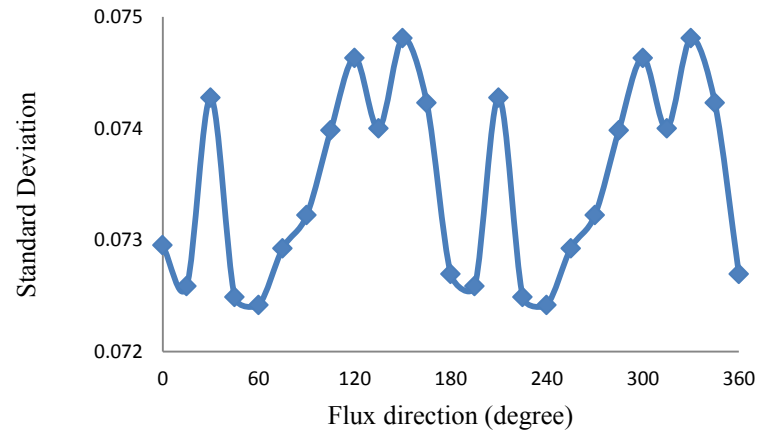


Fig. 2.19: Standard deviation profile of the flux density distribution for the circular sample using RRSST.

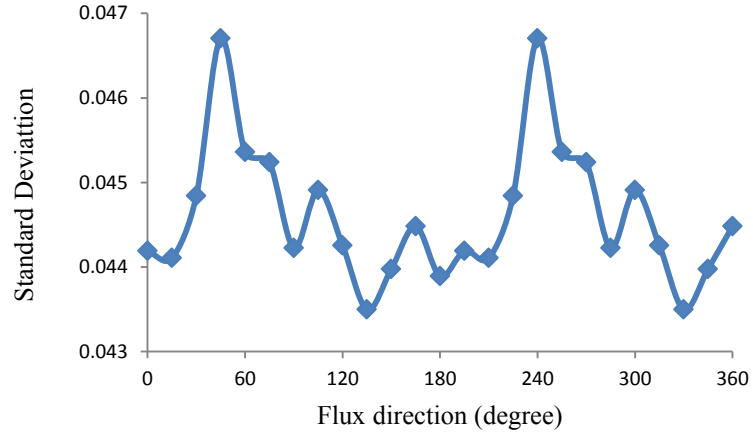


Fig. 2.20: Standard deviation profile of the flux density distribution for the circular sample using the Halbach array.

2.5 Simulation Results

A simulation was performed with DC excitation currents with equal amplitudes (in both the x and y arrays). To obtain the solution, the AC/DC module of COMSOL Multiphysics is used to perform the numerical simulations. A 20 cm diameter disc of M19 Silicon steel gauge 24 sample is used in this simulation. Fig. 2.21 shows the magnetic flux density profile in the x - z plane. The flux density increases once it leaves the air gap and enters the sample. The magnetic pole is around 30 times thicker than the sample. The flux density at the edges is smaller when compared with the entire sample area, and then increases to be nearly constant in the middle. Fig. 2.22 illustrates the color map of the magnetic flux distribution in a cross section of the sample in the x - z plane.

The sample thickness plays a role in reducing the variation of flux density at the edges, where a thinner sample concentrates the flux lines better than thicker sample. This implies a higher flux density not only at the edge, but also in the interior area. Fig. 2.23 compares three different samples of silicon steel M19 with same size (Diameter of 20 cm), and different gauges 20, 24, and 29. It is clearly noticed that in the case of the thinner sheet (gauge 29) the flux density is the highest at the edge and reaches a maximum value in a shorter distance than the other samples, which is more favorable to obtain field homogeneity. Moreover, the average flux density in the sample is higher, as shown in Table 2.3.

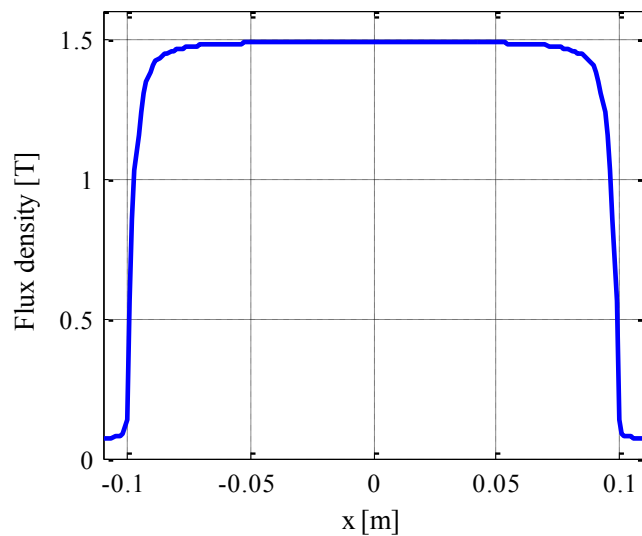


Fig. 2.21: The magnetic flux density profile in the x - z plane along the axis of the circuit, using M19 Silicon steel gauge 24.

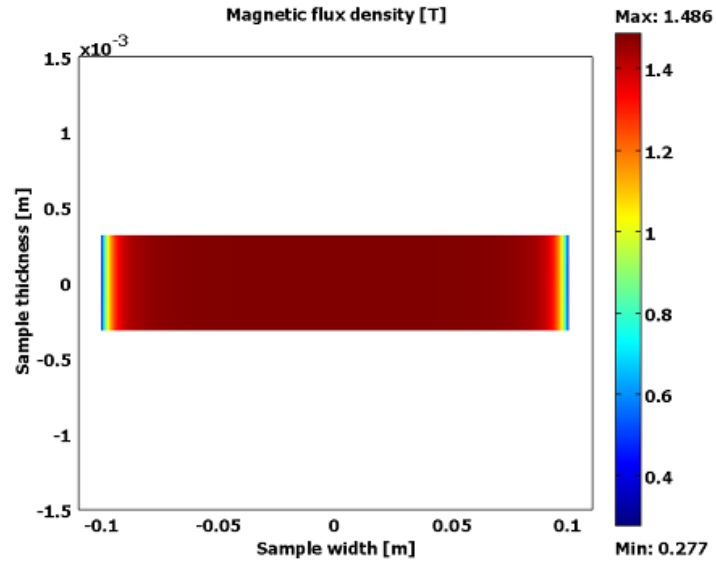


Fig. 2.22: The flux density distribution within the sample of M19 Silicon steel gauge 24 in x - z plane.

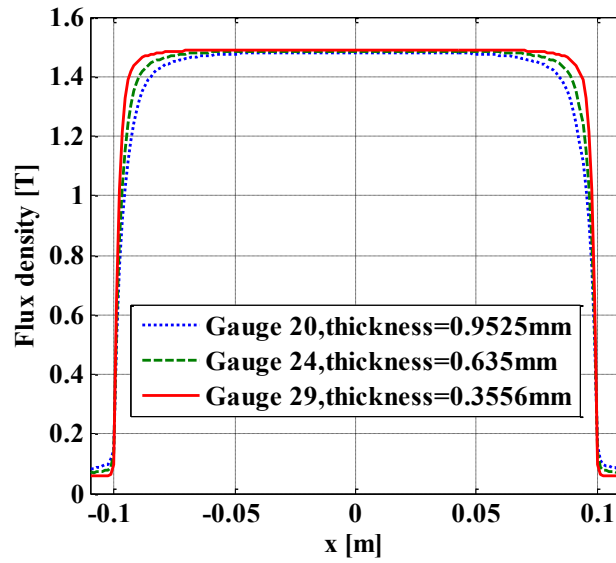


Fig. 2.23: The magnetic flux density profile in x - z plane along the axis of the circuit. Test of three samples with different gauges.

Table 2.3: The flux density in samples with different gauges.

Gauge	Flux density [T]
Gauge 20, thickness = 0.9525 mm	1.4809744
Gauge 24, thickness = 0.635 mm	1.4858800
Gauge 29, thickness = 0.3556 mm	1.4896961

2.6 The New Test Fixture Structure

This fixture is built of a frame, poles, and sensor coils for measuring the magnetic flux density (\mathbf{B}) and magnetic field strength (\mathbf{H}).

A. The magnetic circuit frame

The frame design is shown in Fig. 2.24 (a). The first component is a 20 mm thick, flat, circular frame-disc with 16 circular holes drilled around its perimeter. Each hole has a diameter of 51 mm. The frame inner radius is 100 mm, and the outer radius is 170 mm, as shown in Fig. 2.24 (b). The interior space of the frame is a circular indentation with a depth of 10 mm and a diameter of 200 mm. Its surface functions as a sample holder. This indentation is closed by a moveable cover with the same dimensions and provided with two handles as shown in Fig. 2.24 (c). The sample will be set between the sample holder and the cover in order to be fixed in the frame center, and in the middle of the frame height. This frame-disc is made from Cast Acrylic [Poly (methyl methacrylate)], which is a dielectric material (μ_r slightly less than 1), that gives the flexibility for the flux

to go out of the material to the air and then to the metallic sample. Other properties which encourage use of Acrylic are: its ability to withstand a high temperature (recommended continuous service temperature 85°C), cost effectiveness, superior dimensional stability, durability and ease of assembly [47] and [48].

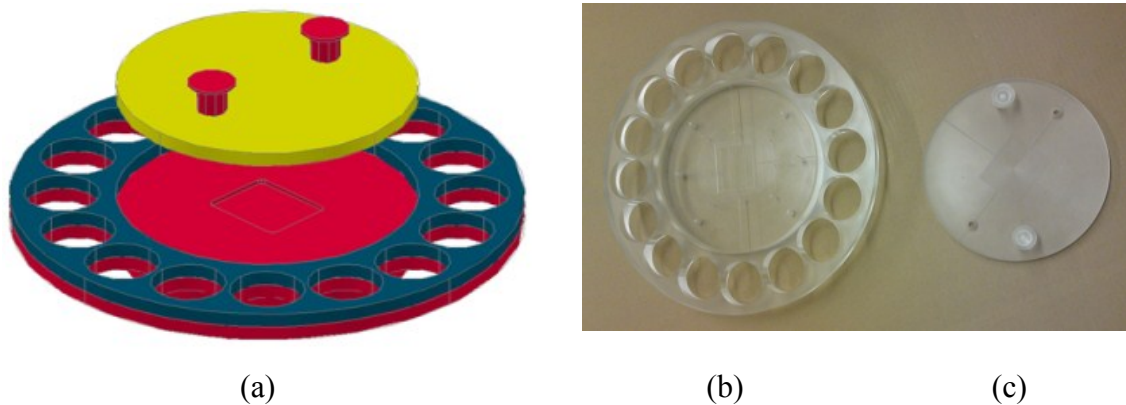


Fig. 2.24: (a) The 3D design of the circuit frame using *AutoCAD*. (b) The frame disc made of Cast Acrylic. (c) The Cover.

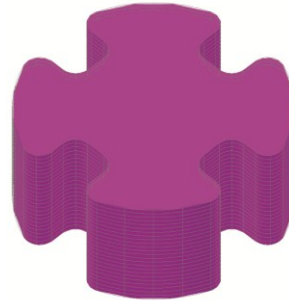
B. The poles

The assembly consists of 16-pole pairs. One such pole pair is shown in Fig. 2.25 (a). Each circular pole is composed of 56 thin laminations of non-oriented M19 Gauge 29 silicon steel and has a diameter of 50 mm. Four slots are laser cut into each lamination to accommodate the windings. Each slot is a square of 10 mm as shown in Fig. 2.25 (b). The interior and exterior corners of the slots are rounded in order to remove any sharp corners in the magnetic circuit. There are two orthogonal windings wrapped around the pole (x -direction coil, and y -direction coil). Each layer of the x -direction coil is wound so that it is placed on top of a corresponding layer of the y -direction coil where the coils

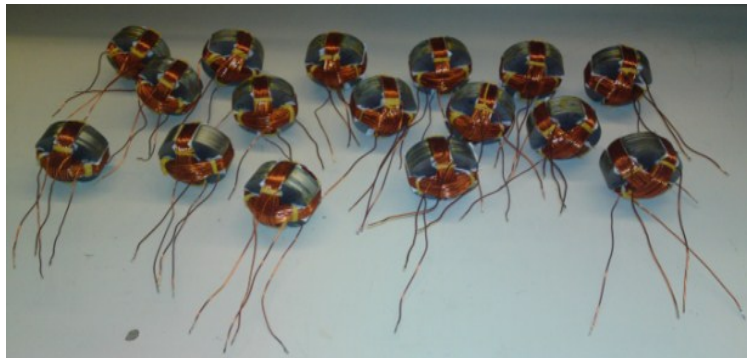
intersect at the center of the pole. Thus, the windings are interleaved. The interleaving between the windings increases the homogeneity, uniformity, and similarity between the produced fluxes from each winding.



(a)



(b)



(c)

Fig. 2.25: (a) Photograph of a pole with wound interleaved coils in x and y directions. (b) Laminations collected to form a pole designed by Auto Cad. (c) A complete set of 16 poles.

C. The sensor coils for measuring flux density (B)

There are at least two methods to measure the flux density in the sample under test. In the needle or tip method, the flux density is calculated by measuring the potential difference

between two points on the surface of a steel sheet to which the tips of needles are applied. Its problem appears in the low voltage produced between the needles and susceptibility to the surrounding noise. The other method is sensor coils which are placed within or around the sample [49]. In this design, two sensor coils are employed to measure the magnetic flux density \mathbf{B} , they are perpendicular to measure B_x and B_y , the x and y components, as shown in Fig. 2.26. One of the important contributions in improving the flux density distribution in the sample is to avoid drilling the sample for the purpose of measuring the flux density. Previously these coils were located on the middle of the sample, where holes are drilled and coils wrapped through the holes, to measure the uniform flux in the middle and to avoid the edges of the sample. But in the current design where the flux is more uniform and homogeneous, the coils are wrapped around the outside of the sample. The advantage is the absence of the drilled holes which reduces the magnetic quality of the material [19]. The authors believe that without drilling holes, the field distribution is more uniform, and more accurate measurements can be obtained. The middle area is empty where the tangential \mathbf{H} coils can be attached completely to the surface. The magnetic flux density in the sample can be calculated from Faraday's law, as in the following equation:

$$\mathbf{B} = \begin{cases} B_x = \int \frac{v_{Bx}}{N_B A_B} dt, & \text{in } x\text{-direction} \\ B_y = \int \frac{v_{By}}{N_B A_B} dt, & \text{in } y\text{-direction} \end{cases} \quad (2.5)$$

Where v_{Bx} and v_{By} are the terminal voltages of \mathbf{B} sensing coils in the x and y directions, respectively. N_B is the number of turns around the sample in each direction, and A_B is the cross sectional area of the coil.

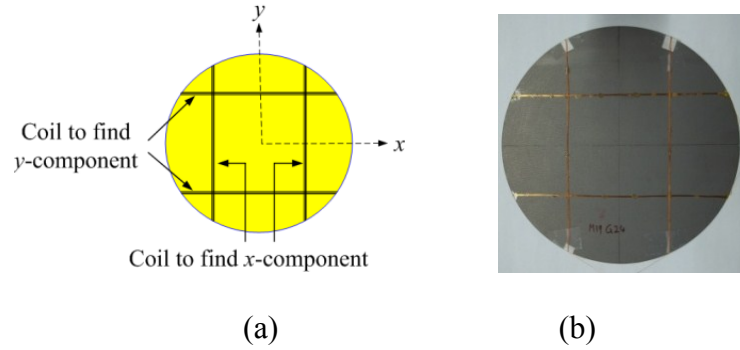


Fig. 2.26: The position of \mathbf{B} coils wound around the sample. (a) Drawing design. (b) Real picture.

D. The search coils for measuring magnetic field strength (\mathbf{H})

In general, determination of magnetic field strength \mathbf{H} at the surface of the electrical steel lamination can be achieved by using the measurement of the current, or using the coil method. In the current measurement method, which is also called the indirect method, \mathbf{H} is extracted from the measured magnetizing current by applying Ampere's law. This method lacks accuracy, since the magnetic flux path in the circuit is not well defined. It is used widely for pulsating core loss measurement devices, like toroids, Epstein frames, and single sheet testers. Nevertheless, it is not suitable for rotational loss apparatus where the flux path is less distinct [29]. On the other hand, the coil method measures the tangential component of the magnetic field strength at the surface of the sample and can be derived directly from the induced voltage v_H . Different types of sensors may be used to detect tangential magnetic field, such as Rogowski-Chattock potentiometer, tangential coil, Hall sensor, or magnetoresistive sensor [30], [33], and [31].

In this circuit design, two thin flat multi-turn coils wound on a Plexiglas former are used to measure the tangential components of magnetic field strength \mathbf{H} . To measure \mathbf{H} on the sample surface, the coils are situated perpendicularly in the sample's middle area, one over the sample for sensing H_x , and the other under it for H_y . Fig. 2.27 show these coils.

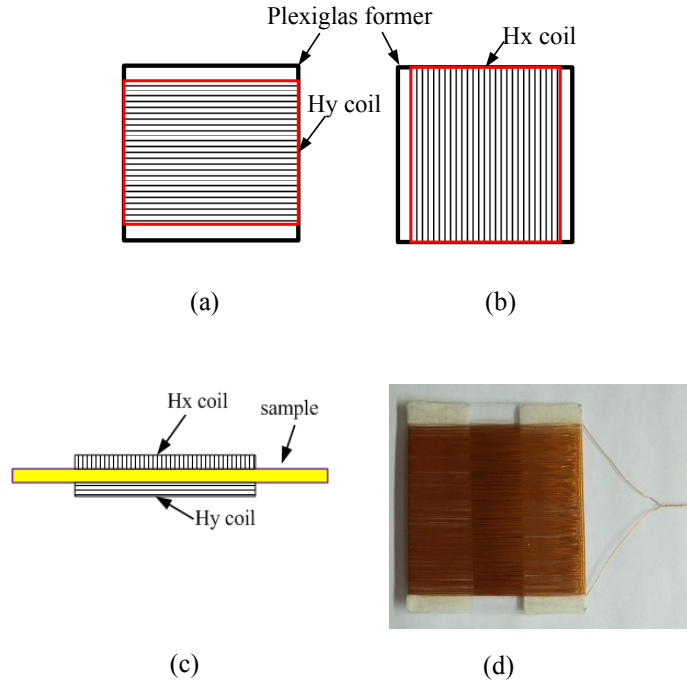


Fig. 2.27: (a) \mathbf{H} coil for measurement in y direction. (b) \mathbf{H} coil for measurement in x direction. (c) Positions of \mathbf{H} coil. (d) Real picture of tangential \mathbf{H} coil wound on Plexiglas former.

This coil is excited by the magnetic field on the sample surface, and since its former is a non-magnetic material, the magnetic field strength can be calculated by:

$$\mathbf{H} = \begin{cases} H_x = \int \frac{v_{Hx}}{\mu_o N_H A_H} dt, & \text{in } x\text{-direction} \\ H_y = \int \frac{v_{Hy}}{\mu_o N_H A_H} dt, & \text{in } y\text{-direction} \end{cases} \quad (2.6)$$

Where v_{Hx} and v_{Hy} are the terminal voltages of H sensing coils in the x and y directions, respectively. N_H is the number of turns on the former, and A_H is the cross sectional area of the coil. Noise affects the output induced voltage from the tangential sensor (V_H), since the obtained signal is in the range of a hundred millivolts; thus, any small error in the signal appears to be significant in the field strength H . To overcome the problem of error, the sensor terminals were twisted, which provides a magnetic field noise reduction. Fig. 2.28 shows the test fixture of the 16-pole electromagnetic Halbach array.

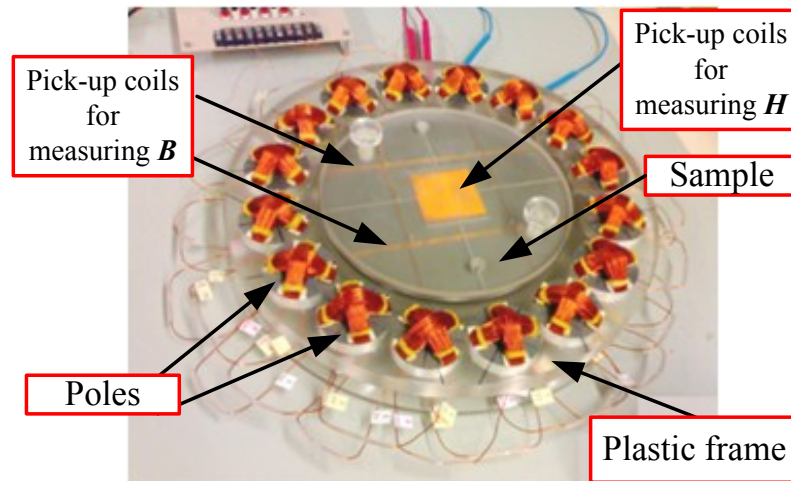
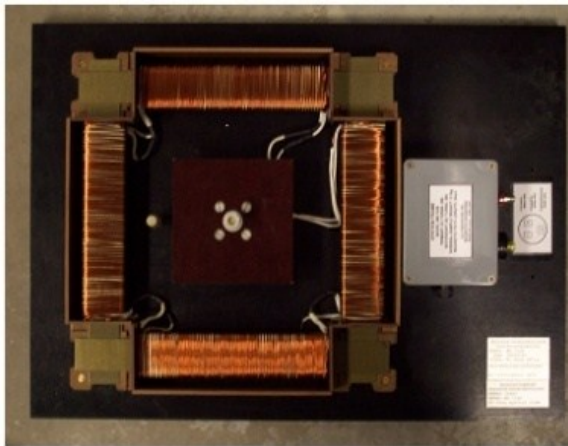


Fig. 2.28: Photograph of the Halbach magnetizing circuit.

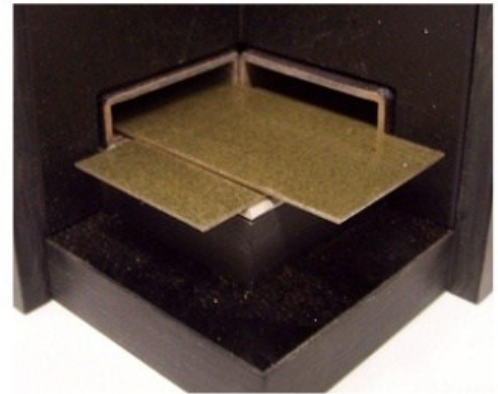
2.7 Validation

The validity of this circuit is tested by operating each array alone, measuring the corresponding pulsating core losses in the sample, and then comparing the loss between the x and y arrays (Ph_x and Ph_y). In addition these losses are benchmarked against the pulsating losses from two different Epstein frames. One of these Epstein frames has 352 turns, is part of a commercial measurement system for core loss. The other is a new

Epstein frame with 280 turns for high frequency testing, designed by KJS Magnetics to hold one Epstein strip in each leg of the frame. The 280-turn frame was specifically designed to reduce air flux by having very little space above the sample. The Epstein frames are shown in Fig. 2.29. Experimental tests were performed using non-oriented electrical steel M19 gauge 24 at 1 kHz. The pulsating core losses are illustrated in Fig. 2.30, where the results provide an acceptable correlation with each other with correlation coefficients shown in Table 2.4. The 352-turn Epstein frame is used as the reference. The pulsating core losses which are obtained with the x and y Halbach arrays match each other with a correlation coefficient of 0.99957.



(a)



(b)

Fig. 2.29: (a) 280 turns Epstein frame. (b) 352 turns Epstein frame.

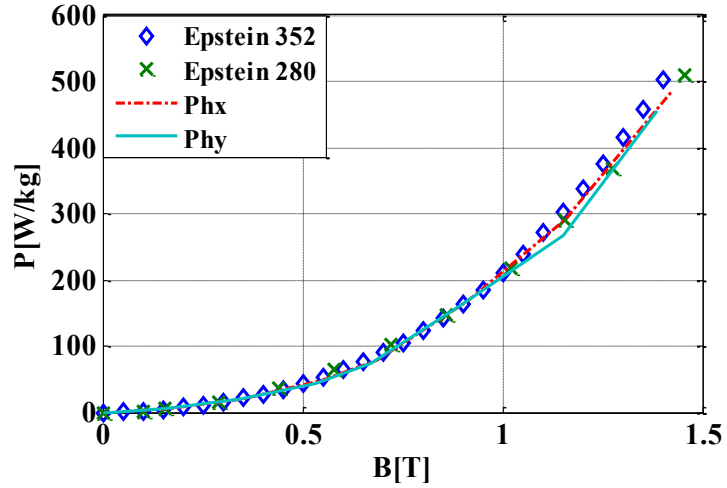


Fig. 2.30: The pulsating core losses in M19G24 at 1 kHz.

Table 2.4: Correlation coefficients of pulsating core losses.

	Halbach <i>x</i> -array	Halbach <i>y</i> -array	Epstein 280 turns
Epstein 352 turns	0.99982	0.99934	0.99941

2.8 Conclusion

In this chapter, a novel design of a magnetizing circuit based on an electromagnetic Halbach array is presented. The size of poles is determined by considering the sample dimensions, and the air gap in the fixture. Three designs of 8, 16, and 32 poles are considered, and simulations are performed to examine the most suitable number of poles for a circular sample of 20 cm diameter, and 1 cm air gap. As seen in the simulation results, the 16-pole circuit is considered as the best choice. The circuit structure is

designed using *AutoCAD*. The frame-disc is made from Cast Acrylic, which is a dielectric material, that gives the flexibility for the flux to go out of the material to the air and then to the metallic sample. Poles are prepared, and two orthogonal interleaved windings are wrapped around each pole. The search coils for measuring \mathbf{B} are wrapped around the sample, and tangential coils for measuring \mathbf{H} wound on Plexiglas formers.

Particular attention is paid to the specimen shape to allow accurate measurements. Simulation results show that the circular sample with the Halbach circuit has the lowest SD, which makes it the best shape to be tested since magnetic flux uniformity is the highest.

The validity of the circuit is tested by comparing its results with two different Epstein frames, where experimental results show a very good matching with high correlation coefficients.

3. BASIC MEASUREMENTS

3.1 Introduction

In this chapter, the new test fixture is used to perform the basic measurements which include pulsating losses, and rotational core losses under circular rotating field. The output voltage signals from coil sensors are shown for some measurements. The asymmetry in permeability under pulsating and rotating fields is also studied.

3.2 The Measurement Set-up

The test bench uses Matlab/Simulink[®] to generate two arbitrary waveforms. This allows the user the flexibility in choosing any physically realizable excitation waveform. These signals are sent through a digital to analogue converter and then isolated by an electronic buffer circuit. Then, two high bandwidth amplifiers receive the signals and amplify them to the required level. The output amplified signals are used to excite the Halbach magnetizing circuit; V_x excites the x -direction array, and V_y the y -direction array. Four output signals from the circuit can be obtained: v_{B_x} , v_{B_y} , v_{H_x} , and v_{H_y} , which are related to the flux density in the x -direction, flux density in the y -direction, magnetic field intensity in the x -direction, and magnetic field intensity in the y -direction, respectively. These signals are sent to dSPACE, which is linked with Matlab Simulink[®], thus allowing for digital monitoring and control of all generated and received signals. Fig. 3.1 and Fig. 3.2 illustrate the schematic diagram and the test bench of the measurement system, respectively.

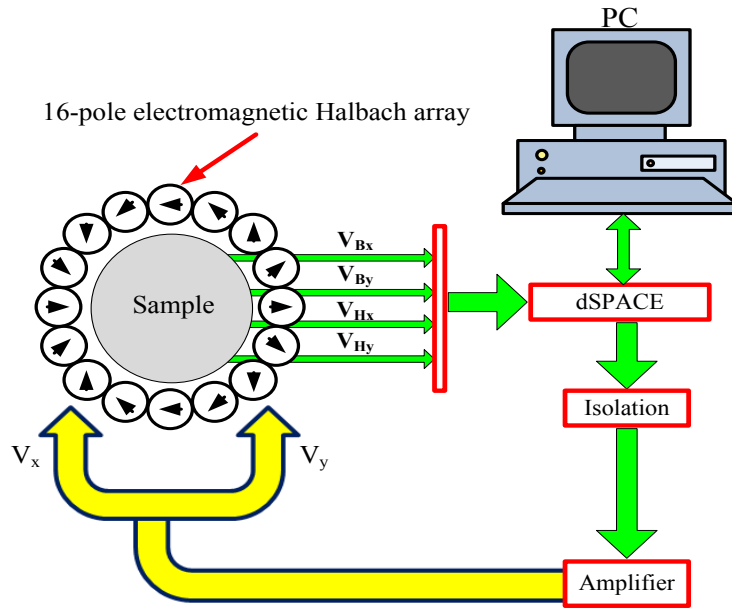


Fig. 3.1: The test bench schematic diagram.

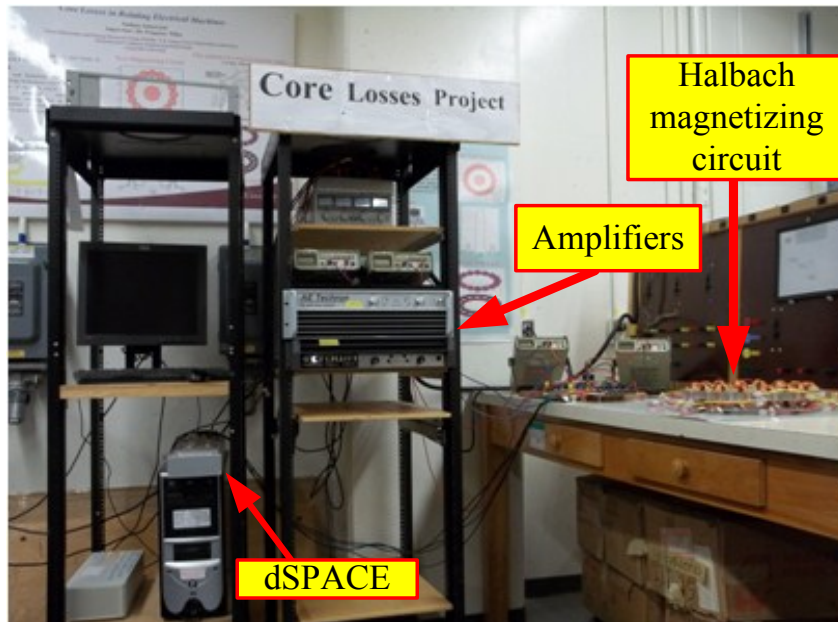


Fig. 3.2: The measurement system at Concordia University.

3.3 Data Extraction and Loss Evaluation

The field-metric method is used in this work, which is seen to be the most convenient and accurate method, plus the ability of providing the \mathbf{B} and \mathbf{H} waveforms in order to analyze the rotating field behavior along the measurement profile. This method is based on the measurements of the magnetic field strength \mathbf{H} at the sample surface and flux density \mathbf{B} inside the sample as explained in section 1.3.

The time dependent parameters H_x and H_y in equation (1.2) are extracted from the measured quantities as shown in equation (2.5), while the time derivatives of the magnetic flux density can be found as follows:

$$\frac{dB_x}{dt} = \frac{1}{N_B A_B} v_{Bx} \quad (3.1)$$

$$\frac{dB_y}{dt} = \frac{1}{N_B A_B} v_{By} \quad (3.2)$$

v_{Bx} and v_{By} are the terminal voltages of \mathbf{B} sensing coils in the x and y directions, respectively. N_B is the number of turns around the sample in each direction, and A_B is the cross sectional area of the \mathbf{B} coil.

The total loss expressed in equation (1.2) is calculated by numerical integration as:

$$P = \frac{1}{T\rho} \sum_{n=1}^N H_x(n) \frac{dB_x}{dt}(n) \Delta t(n) + H_y(n) \frac{dB_y}{dt}(n) \Delta t(n) \quad (3.3)$$

Since the sample rate is fixed during capturing data, the time intervals $\Delta t(n)$ are equal and defined as $\Delta t=T/N$, where N is the number of intervals, then equation (3.3) can be simplified as:

$$P = \frac{1}{N\rho} \sum_{n=1}^N H_x(n) \frac{dB_x}{dt}(n) + H_y(n) \frac{dB_y}{dt}(n) \quad (3.4)$$

The first part of the summation represents the rotational x -loss component and the second one is the rotational y -loss component.

On the other hand, to obtain pulsating loss measurements, each Halbach array is operated alone, measuring the corresponding magnetic field strength and magnetic flux density, and then evaluating the pulsating core losses in the sample as:

$$P_{puls.} = \begin{cases} P_{puls.x} = \frac{1}{T\rho} \int_{B_x} H_x . dB_x \\ P_{puls.y} = \frac{1}{T\rho} \int_{B_y} H_y . dB_y \end{cases} \quad (3.5)$$

Where $P_{puls.x}$ and $P_{puls.y}$ are the pulsating losses in x and y directions respectively.

3.4 Experimental Results

Measurements were carried out on five non oriented silicon steel circular specimen of 20 cm diameter. Theses samples are: M15 gauge 29, M19 gauge 29, M19 gauge 24, M36 gauge 29, and M36 gauge 26.

3.4.1 Signals Obtained from the Coil Sensors

The output voltage signals obtained from the coil sensors during testing of the M36G29 sample are presented at a flux density of 1.3 T, and with frequencies of 60 Hz and 1 kHz. At 60 Hz, the signals obtained from the surface coils v_{Hx} and v_{Hy} are seen in Fig. 3.3, these signals experience some distortion, but the integration reduces the distortion when they are used to construct the magnetic field strength signals H_x and H_y as shown in Fig. 3.4. Fig. 3.5 shows the signals obtained from the \mathbf{B} coils, used to evaluate the flux density signals B_x and B_y as shown in Fig. 3.6. The v_{Hx} and v_{Hy} at 1 kHz are shown in Fig. 3.7, which are used to construct the magnetic field strength signals H_x and H_y as in Fig. 3.8. Fig. 3.9 shows v_{Bx} and v_{By} which are used to construct the flux density signals B_x and B_y as shown in Fig. 3.10.

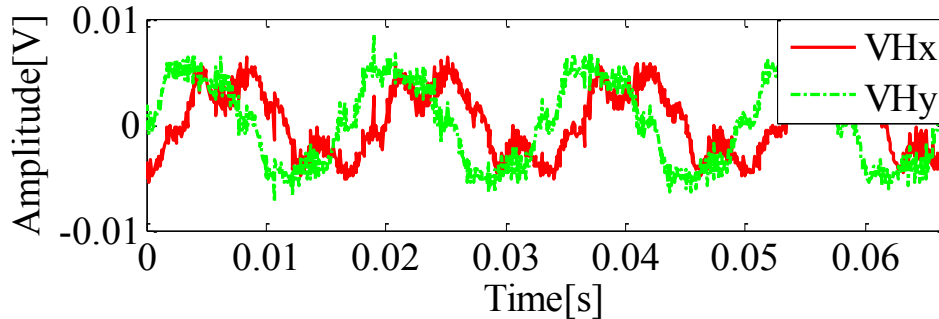


Fig. 3.3: The instantaneous output voltage signals at 60 Hz obtained from the surface coils in the x -direction (v_{Hx}), and y -direction (v_{Hy}).

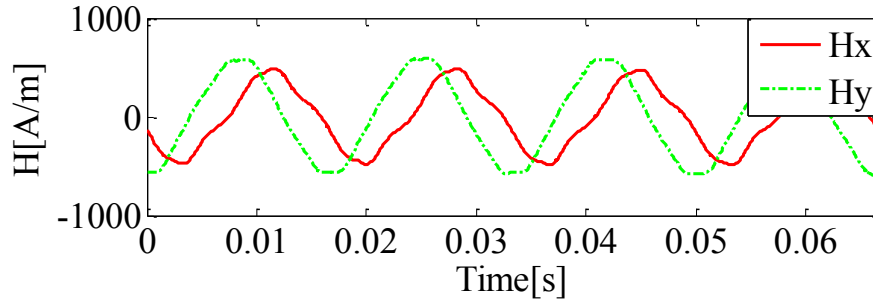


Fig. 3.4: The instantaneous values of the magnetic field strength at 60 Hz in the x -direction (H_x), and y -direction (H_y).

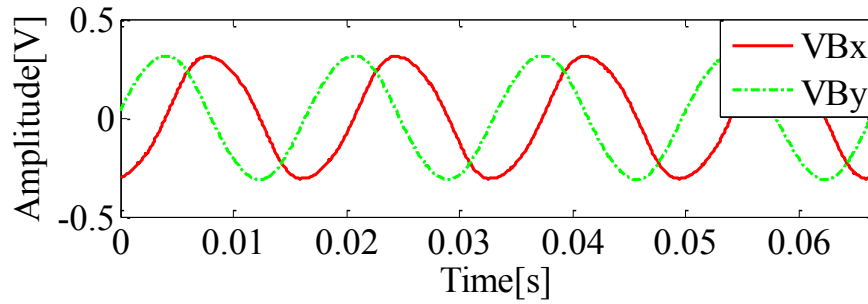


Fig. 3.5: The instantaneous output voltage signals at 60 Hz obtained from the B coils in the x -direction (v_{B_x}), and y -direction (v_{B_y}).

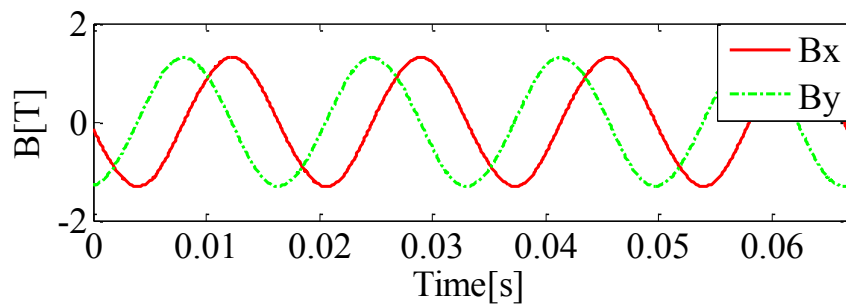


Fig. 3.6: The instantaneous values of the magnetic flux density at 60 Hz in the x -direction (B_x), and y -direction (B_y).

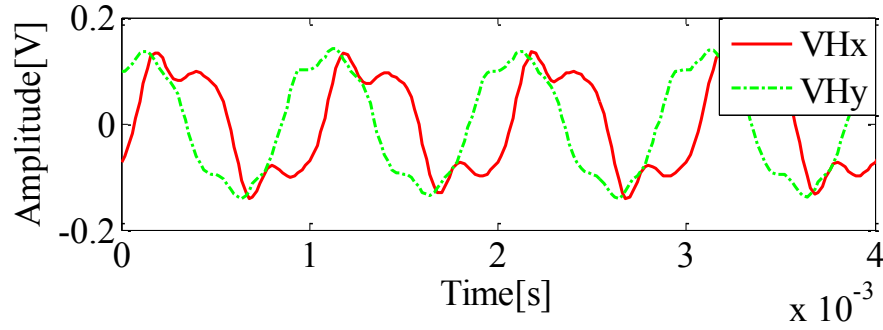


Fig. 3.7: The instantaneous output voltage signals at 1 kHz obtained from the surface coils in the x -direction (v_{Hx}), and y -direction (v_{Hy}).

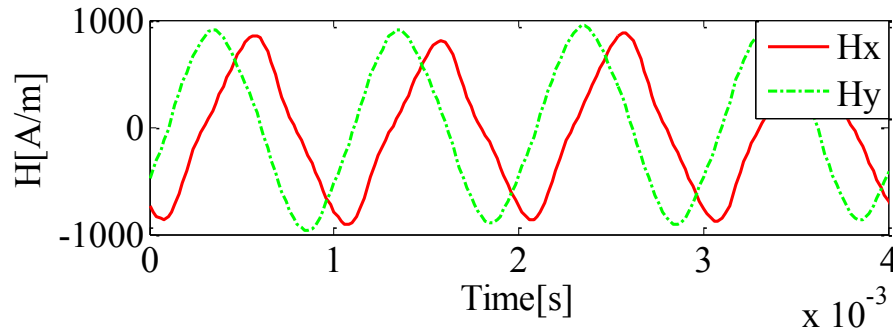


Fig. 3.8; The instantaneous values of the magnetic field strength at 1 kHz in the x -direction (Hx), and y -direction (Hy).

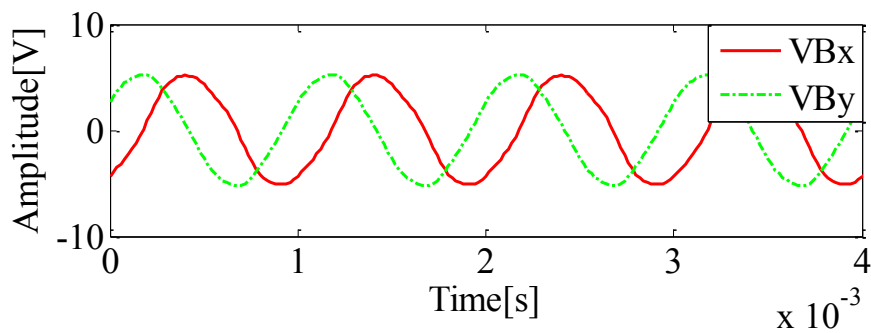


Fig. 3.9: The instantaneous output voltage signals at 1 kHz obtained from the \mathbf{B} coils in the x -direction (v_{Bx}), and y -direction (v_{By}).

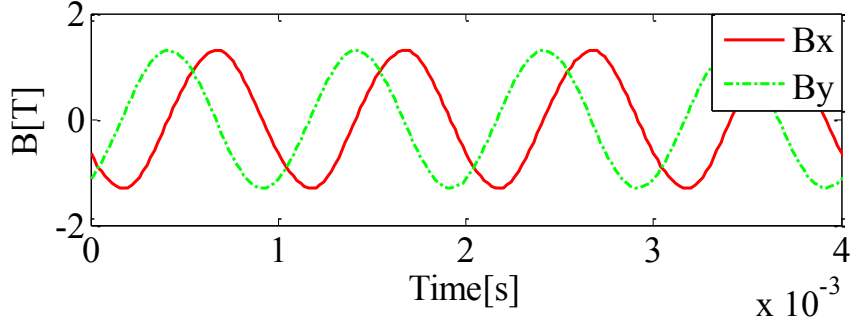


Fig. 3.10: The instantaneous values of the magnetic flux density at 1 kHz in the x -direction (B_x), and y -direction (B_y).

3.4.2 Rotational Core Losses under Circular Excitation

Both Halbach arrays are excited simultaneously by equal magnitude sinusoidal waveforms at three frequencies of interest to the industry (60 Hz, 400Hz, and 1 kHz), with a phase shift of $\varphi = 90^\circ$ between them, where this pattern of fluxes creates a clockwise circular rotating field in the specimen. Then the net flux density vector produced in the test specimen is:

$$\mathbf{B}_{net} = B_x \sin(\omega t) \vec{i} + B_y \sin(\omega t + \varphi) \vec{j} \quad (3.6)$$

Where, B_x and B_y are the flux density magnitudes generated by the x and y arrays, respectively, ω is the angular velocity, and φ is the phase shift angle. Notice that the angle of the \mathbf{B}_{net} changes continually in a clockwise direction at angular velocity ω .

Fig. 3.11 presents the rotational core losses at 1 kHz in the five samples, a comparison between these losses shows that the thickest sample M19 gauge 24 (its thickness is 0.635 mm) achieves the maximum loss. This is because of the eddy current loss component which is dominant in the case of high frequency. After that and for the same reason of eddy current loss, the M36 gauge 26 has the second highest loss, where its thickness (0.4699 mm) is less than gauge 24. This can be clarified if different gauges of the same material are compared to each other. As examples, M19 steel with two different gauges G24 and G29 is shown in Fig. 3.12. Once the samples have the same gauge, the divergence in core loss depends on the grade (the number follows the letter M), where the sample with higher number has a higher core loss. Fig. 3.13 shows the core loss of three different samples (M15, M19, and M36) of the same gauge 29 (thickness of 0.3556 mm), where the higher number (M36) produces a higher core loss.

By decreasing the frequency to 400 Hz, the core losses decrease in the samples, as seen in Fig. 3.14, and still in the same order as previously described. Fig. 3.15 shows grade comparison for three different samples of gauge 29, and Fig. 3.16 show gauge comparisons of M19.

At 60 Hz, the core losses decrease significantly, since the eddy current loss component is reduced and the hysteresis loss component is more dominant. The rotational core losses in the samples are shown in Fig. 3.17. The grade comparison is shown in Fig. 3.18, and the gauge comparison of M19 is shown in Fig. 3.19. The curves of loss start to go down after a certain flux density, since one loss component (let us say y-component) increases while the other one (x-component) decreases, and even becomes negative, as seen in Fig.

3.20. This negative power phenomenon has not so far been fully understood by the physicists.

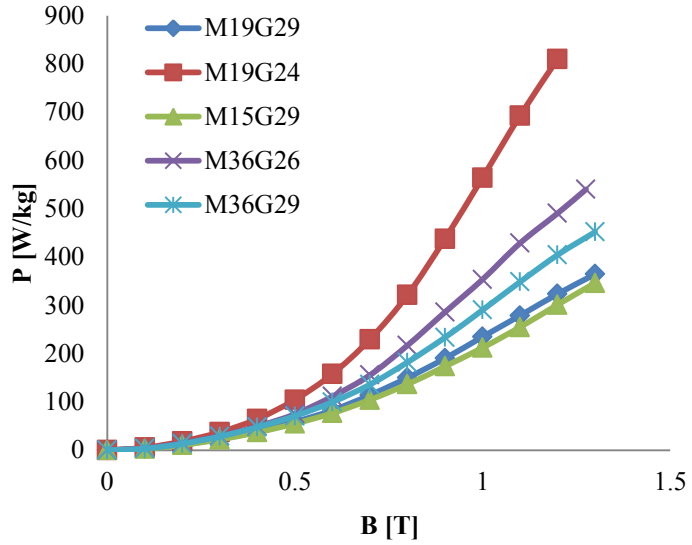


Fig. 3.11: Rotational core losses at 1 kHz in the five samples.

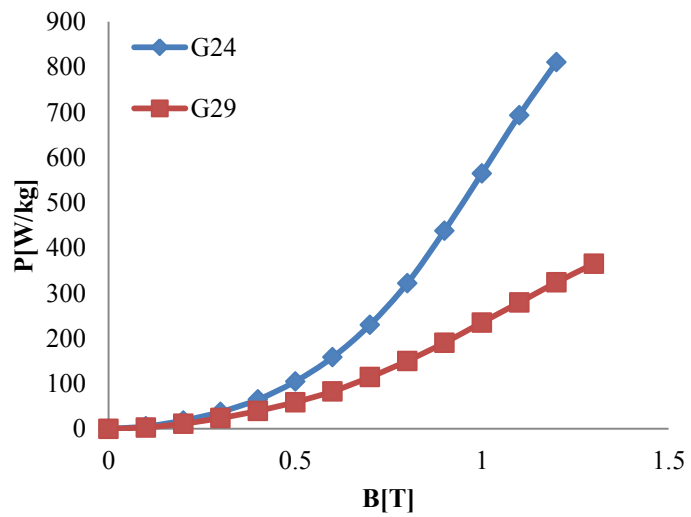


Fig. 3.12: A comparison of M19 steel with different gauges at 1 kHz.

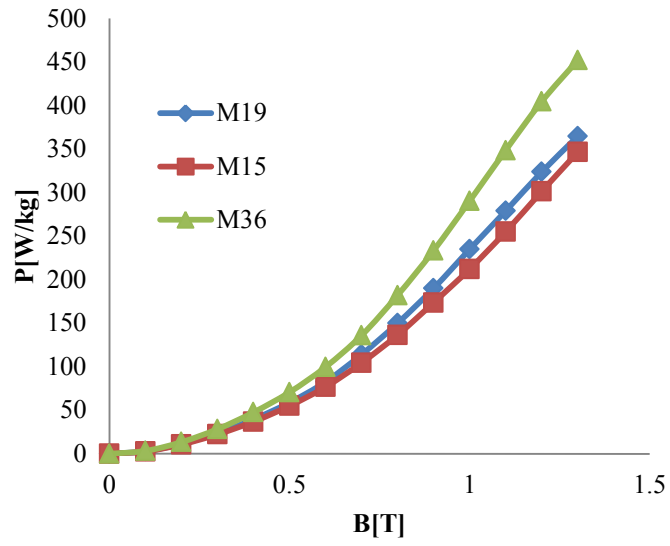


Fig. 3.13: The core losses at 1 kHz of three different samples (M15, M19, and M36) with the same gauge (Gauge 29).

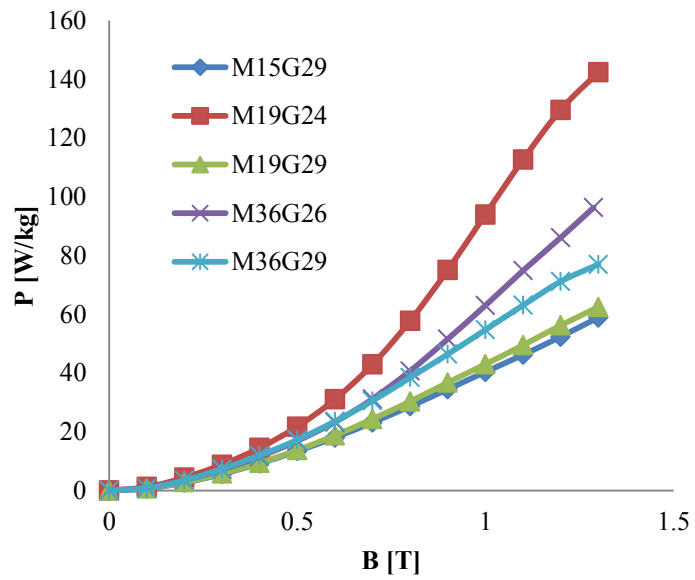


Fig. 3.14: Rotational core losses at 400 Hz in the five samples.

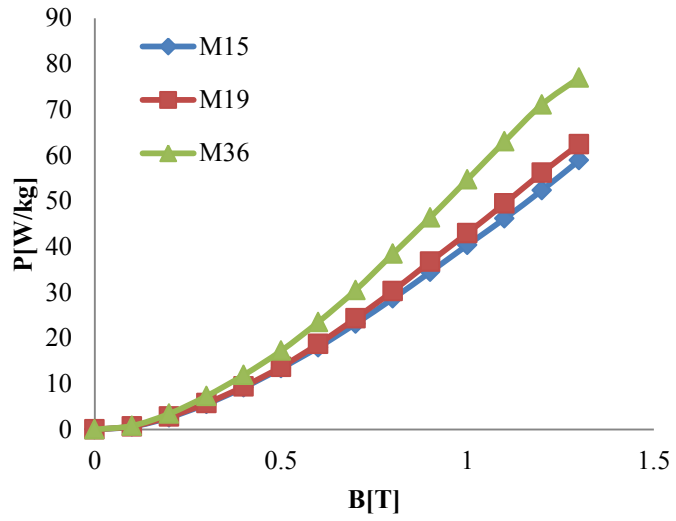


Fig. 3.15: The core losses at 400 Hz of three different samples (M15, M19, and M36) with the same gauge (Gauge 29)

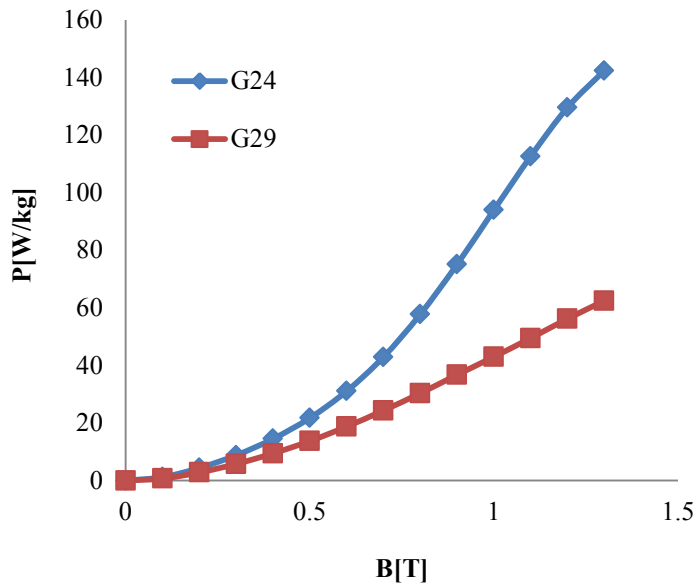


Fig. 3.16: A comparison of M19 steel with different gauges at 400 Hz.

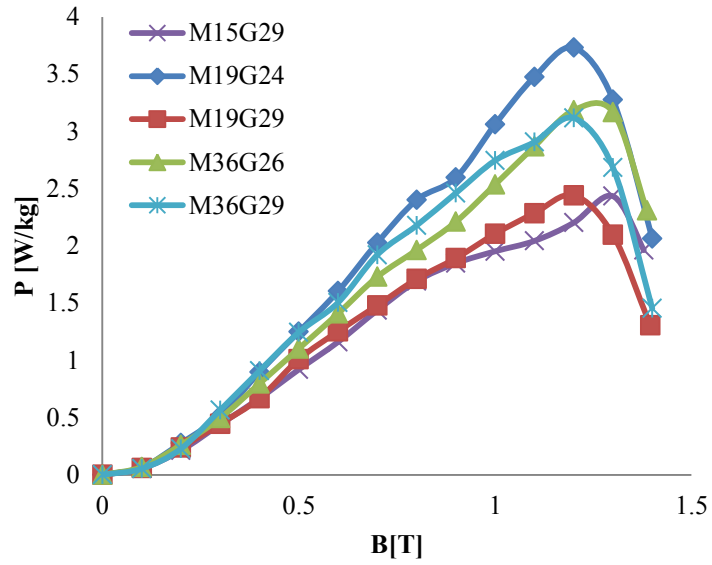


Fig. 3.17: Rotational core losses at 60 Hz in the five samples.

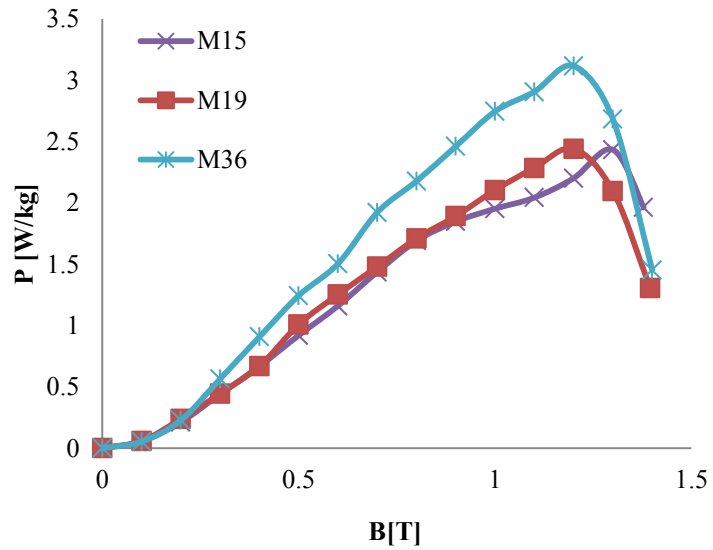


Fig. 3.18: The core losses at 60 Hz of three different samples (M15, M19, and M36) with the same gauge (Gauge 29).

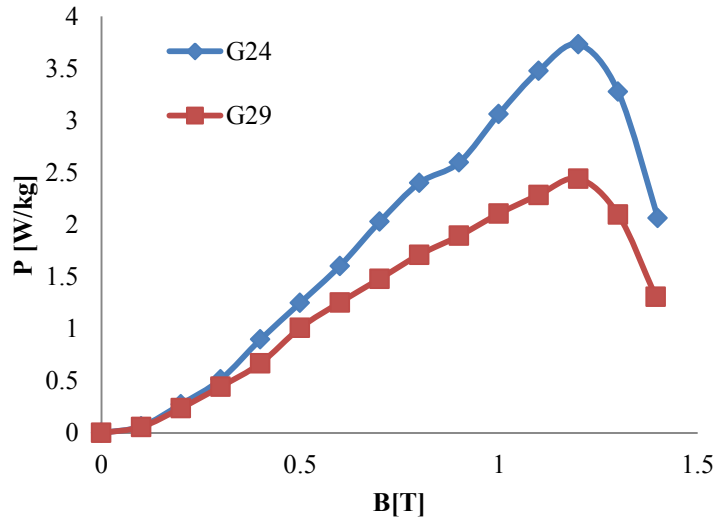


Fig. 3.19: A comparison of M19 steel with different gauges at 60 Hz.

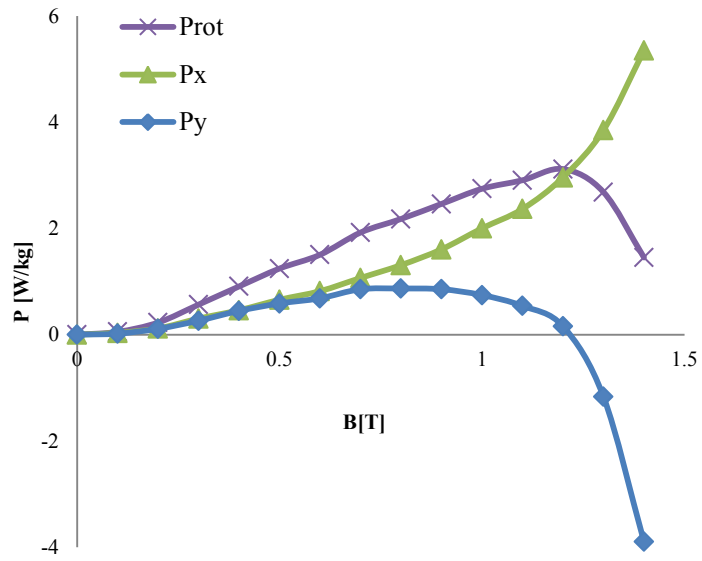


Fig. 3.20: The total rotational core loss at 60 Hz, in M36 steel Gauge 29, with the corresponding x and y components, P_x and P_y respectively.

3.4.3 Rotational Core Losses Compared with Pulsating Losses

Nowadays, the most common approach used to estimate core losses in electric machines is based on considering the effect of the flux densities in both x and y directions individually, *i.e.* the simulation by FEM gives the values of B_x and B_y in each mesh element, then the core loss due to each value is calculated using pulsating loss formulations, therefore the total core loss will be the sum of losses produced by the two components B_x and B_y [50], [51], [52], [53], and [54]. This method is consistent with the availability of only the pulsating loss data and the lack of standardized rotational core loss data. However, researchers agreed that the superposition of pulsating losses in x and y directions is not accurate [55].

A set of rotational losses (P_{rot}) data was obtained for these two samples with frequencies of 60 Hz, 400 Hz, and 1 kHz. In addition, when each one of the Halbach arrays operates alone, pulsating core losses are produced in the sample, *i.e.*, P_{hx} and P_{hy} , the pulsating core losses due to the x and y Halbach arrays, respectively. Results at these frequencies prove that it is not accurate to estimate the rotational core losses as suggested in [54] to avoid the complexity of rotational magnetizing measurements. Superposition gives acceptable estimation for the rotational core losses at low flux density, but as the material goes into saturation, the result becomes over estimated [55]. Fig. 3.21 shows the results for M19G24 at 60 Hz. The rotational core losses are compared with pulsating losses in the case of exciting both x and y arrays separately. In addition, the sum of (P_{hx} and P_{hy}) is benchmarked against these losses. Fig. 3.22 shows the results for M36G29 at 60 Hz, where in general losses are lower because of the thinner sample of (0.3556 mm)

compared to M19G24 (thickness of 0.635 mm). Fig. 3.23 depicts the difference between rotational core loss and the average of the pulsating core losses, where the rotational core loss is greater than the pulsating loss by a maximum of 60 %, and then rotational loss decreases in the saturation region at 1.3 T with percentage difference around -25% and -41% for M16G24 and M36G29, respectively. There is a clear difference between the rotational and pulsating core losses, not only in the value, but also in the characteristic behavior. The value of P_{rot} increases with the applied flux density until a peak value and then decreases, but pulsating loss increases steadily with flux density until the sample is saturated. The reason for this is that one loss component of rotating field (let us say x -component) increases while the other one (y -component) decreases, and even becomes negative, as shown previously in Fig. 3.20. This behavior is seen clearly at low frequency and is difficult to achieve at high frequencies, since it is mainly related to the rotational hysteresis loss which is dominant at low frequencies. Fig. 3.24 and Fig. 3.25 show the loss comparison results for the two samples with a frequency of 400 Hz, and Fig. 3.26 illustrates the difference between the rotational and average pulsating core losses. Fig. 3.27 and Fig. 3.28 provide the results under a frequency of 1 kHz, and Fig. 3.29 illustrates the difference between rotational and average pulsating core losses, which is around 50% on average. Here the eddy current loss is more dominant.

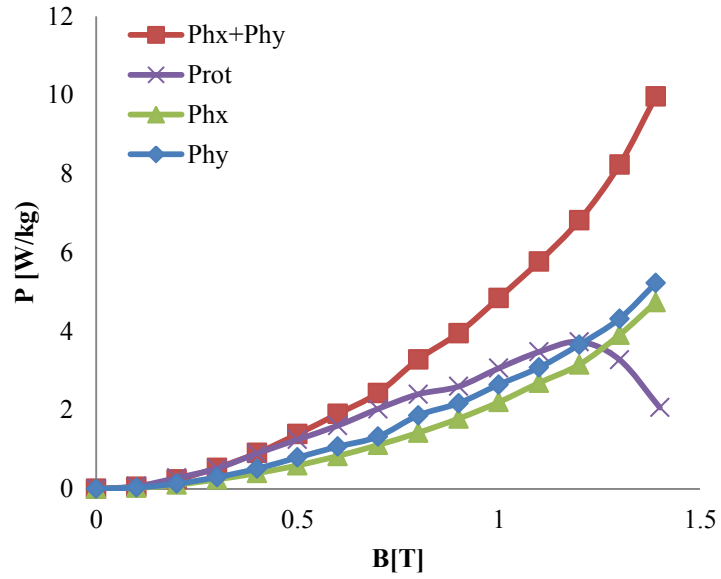


Fig. 3.21: The rotational core losses (P_{rot}) compared with pulsating losses in x and y directions, Phx and Phy , respectively. For M19G24 at 60 Hz.

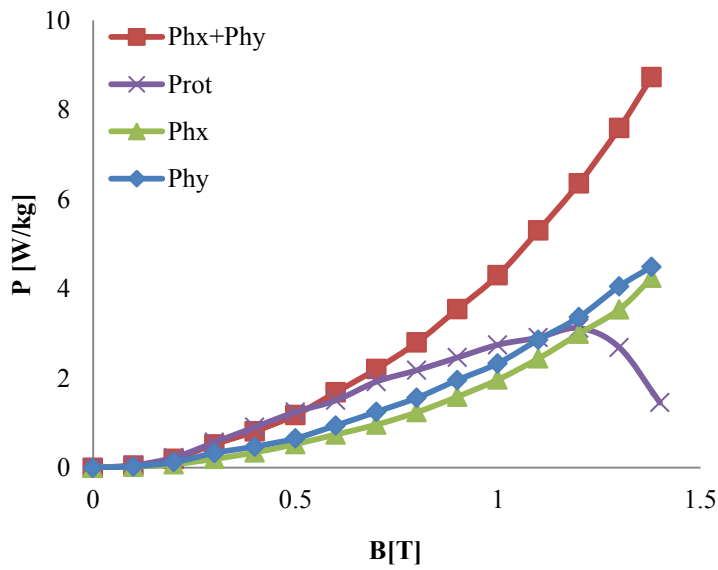


Fig. 3.22: The rotational core losses (P_{rot}) compared with pulsating losses in x and y directions, Phx and Phy , respectively. For M36G29 at 60 Hz.

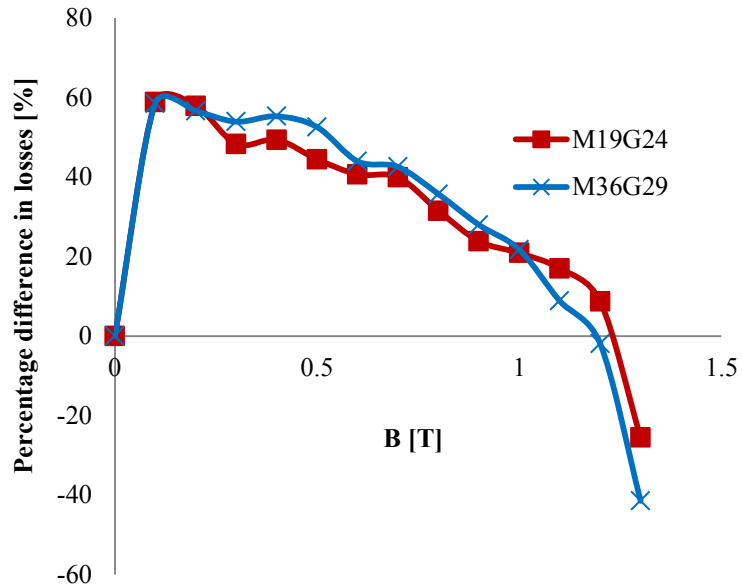


Fig. 3.23: The difference between rotational core loss and average pulsating core losses, for M19G24 and M36G29 at 60 Hz.

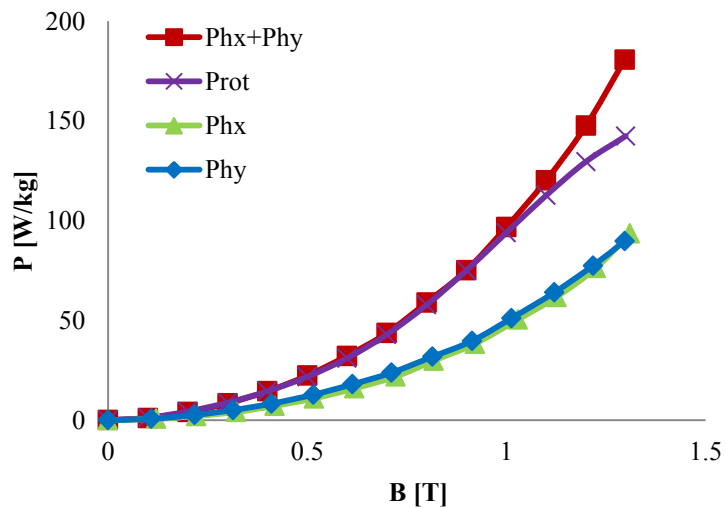


Fig. 3.24: The rotational core losses (P_{rot}) compared with pulsating losses in x and y directions, P_{phx} and P_{phy} , respectively. For M19G24 at 400 Hz.

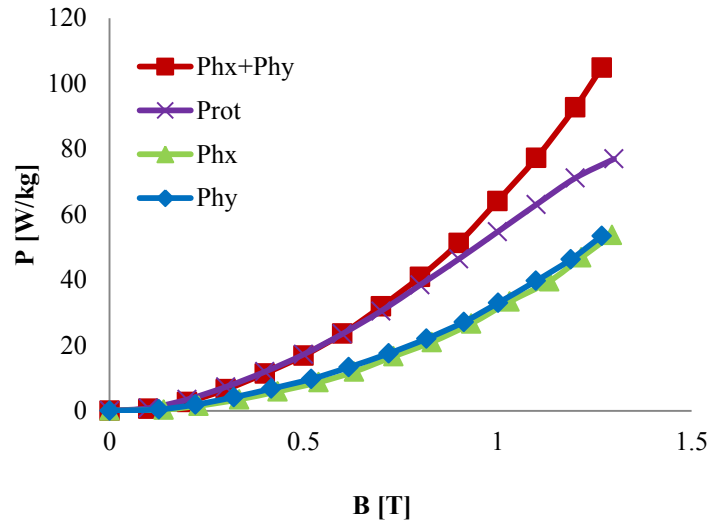


Fig. 3.25: The rotational core losses (P_{rot}) compared with pulsating losses in x and y directions, Phx and Phy , respectively. For M36G29 at 400 Hz.

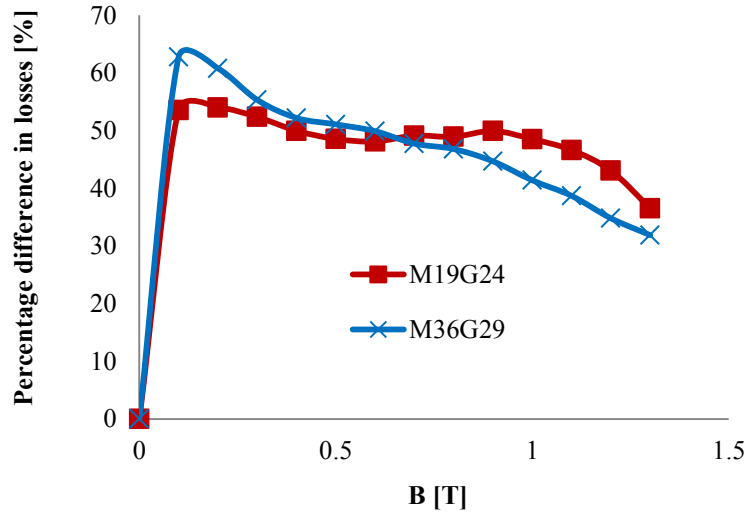


Fig. 3.26: The difference between rotational core loss and average pulsating core losses, for M19G24 and M136G29 at 400 Hz.

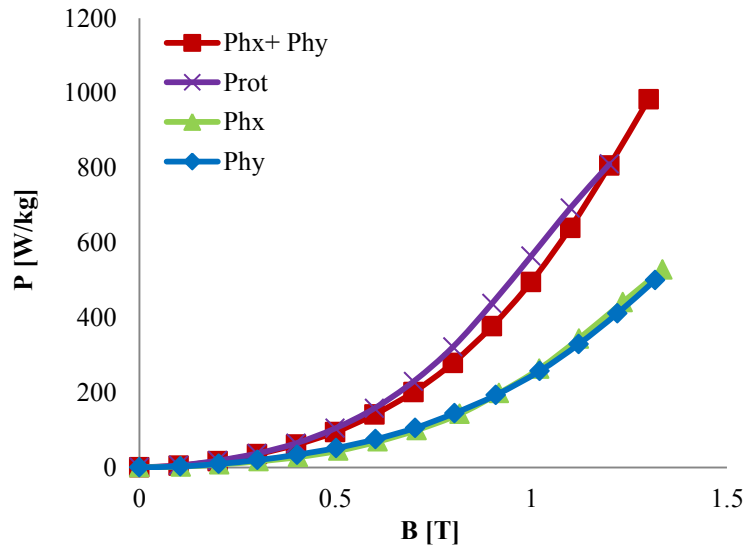


Fig. 3.27: The rotational core losses (P_{rot}) compared with pulsating losses in x and y directions, P_{hx} and P_{hy} , respectively. For M19G24 at 1 kHz.

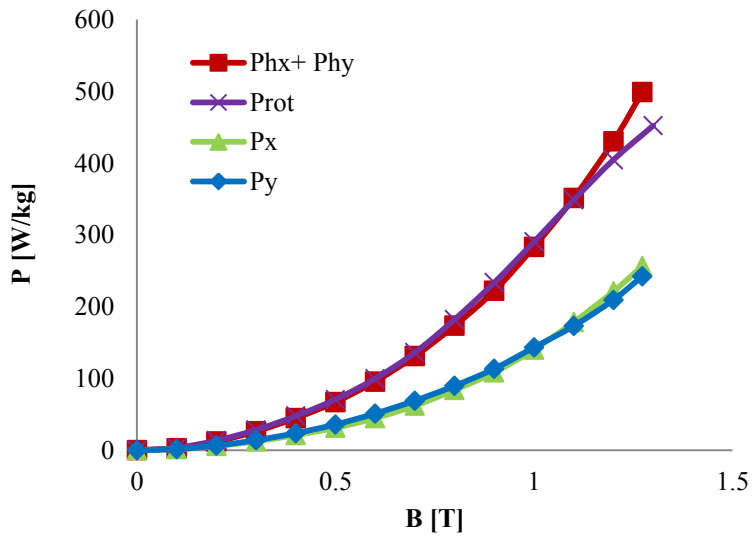


Fig. 3.28: The rotational core losses (P_{rot}) compared with pulsating losses in x and y directions, P_{hx} and P_{hy} , respectively. For M36G29 at 1 kHz.

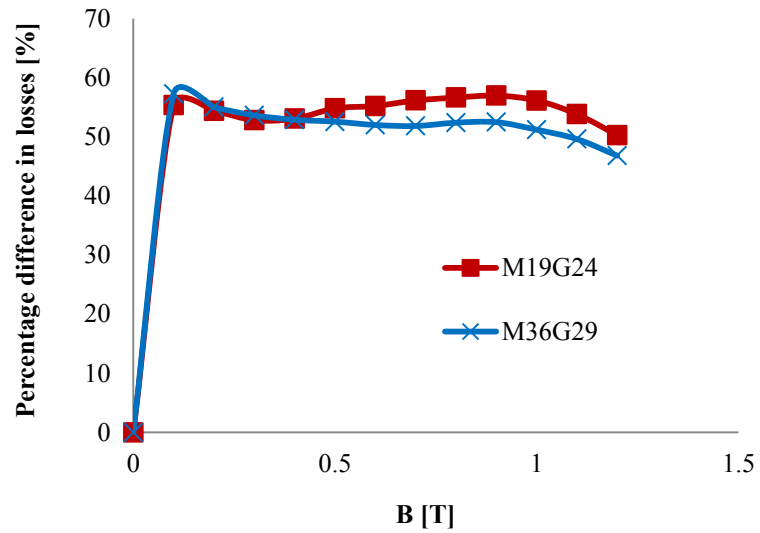


Fig. 3.29: The difference between rotational core loss and average pulsating core losses, for M19G24 and M136G29 at 1 kHz.

3.4.4 Rotational and Pulsating Core Loss Measurements with Reference to the Permeability Asymmetry

The total rotational core loss in electrical steel samples is evaluated by using the field-metric method which considers P_{xr} and P_{yr} , the rotational core loss components measured in x and y directions. During the measurement, a remarkable difference between P_{xr} and P_{yr} is noticed, which is mainly attributed to the asymmetry in the magnetic permeability. According to classical electromagnetic theory, the permeability of a magnetic material which is often expressed as the relative permeability μ_r is considered as a scalar quantity [56]; but in truth it is a vector affected by many factors such as the magnetic field strength \mathbf{H} , the field frequency, and the position in the medium [57]. The permeability is evaluated in the case of rotating field measurements in both x and y directions, μ_{xr} and μ_{yr}

respectively. This is benchmarked against the permeability obtained from exposing the sample to pulsating fields in the x and y directions, μ_{xp} and μ_{yp} respectively. This difference between the μ_{xr} and μ_{xp} , and also between μ_{yr} and μ_{yp} is related with a difference of the core losses between the rotational x -direction and the pulsating x -direction losses, in the other side, a difference between the rotational y -direction and the pulsating y -direction losses. These differences clarify why the rotational core loss in the lamination is not equivalent to the sum of pulsating losses in the x and y directions.

Measurements were performed on a non-oriented silicon steel M15 gauge 29 laser-cut circular specimen of 20 cm diameter. The measurements were carried out at three frequencies of interest to the industry (60 Hz, 400Hz, and 1 kHz). The x and y measuring directions are aligned 45° with respect to the rolling and transverse directions which increases the uniformity and similarity of the magnetic flux paths in the specimen, and reduces the influence of the crystalline anisotropy due to manufacturing process [58]. During the rotational core loss estimation, a noticeable difference can be seen between measurements in the x and y directions.

Fig. 3.30 shows the dynamic hysteresis loops in the x and y directions with a rotating field under 60 Hz, 400 Hz, and 1 kHz at 1.3 T. The enclosed areas by (B_x-H_x) and (B_y-H_y) loops represent the rotational iron losses in the x and y directions in the sample, P_{xr} and P_{yr} . The total rotational loss is considered to be the algebraic sum of P_{xr} and P_{yr} . The results show that the rotational core loss is greater than the pulsating loss as shown in Table3.1. In the case of pulsating loss measurements, the dynamic loops present more similarity and compatibility not only in the area, but also in the shape of the hysteresis

cycles as shown in Fig. 3.31. This difference between the pulsating losses in the x and y directions, and between the x and y directions in the case of rotational iron losses is attributed mainly to the difference in permeability which is affected by the direction of the applied field in addition to the status of pulsating or rotating condition, this effect gives an explanation for core loss errors during electric machine efficiency estimation. Fig. 3.32 shows the relative permeability as a function of magnetic flux density for M15G29 sample at 60 Hz, 400 Hz, and 1 kHz. Results of the measured permeability show that it differs in the x and y directions during pulsating field tests. A more noticeable difference can be seen when the sample is subjected to a rotating field. The percentage difference in permeability between the x and y directions in the case of pulsating field, and in the x and y directions in the case of rotating field are summarized in Table 3.2. It is clearly shown that the difference in permeability between the x and y directions in the case of rotating fields is larger than the difference between the x and y directions of permeability in the case of pulsating field excitation.

3.5 Conclusion

Basic measurements were carried out on different silicon steel samples, M15G29, M19G29, M19G24, M36G29, and M36G26. Rotational core losses under circular rotating field are obtained and compared with the pulsating core losses. Results show that it is not accurate to estimate the rotational core losses by the sum of pulsating losses in the x and y directions. The remarkable difference between the x and y loss components under rotating fields is mainly attributed to the asymmetry in the magnetic permeability.

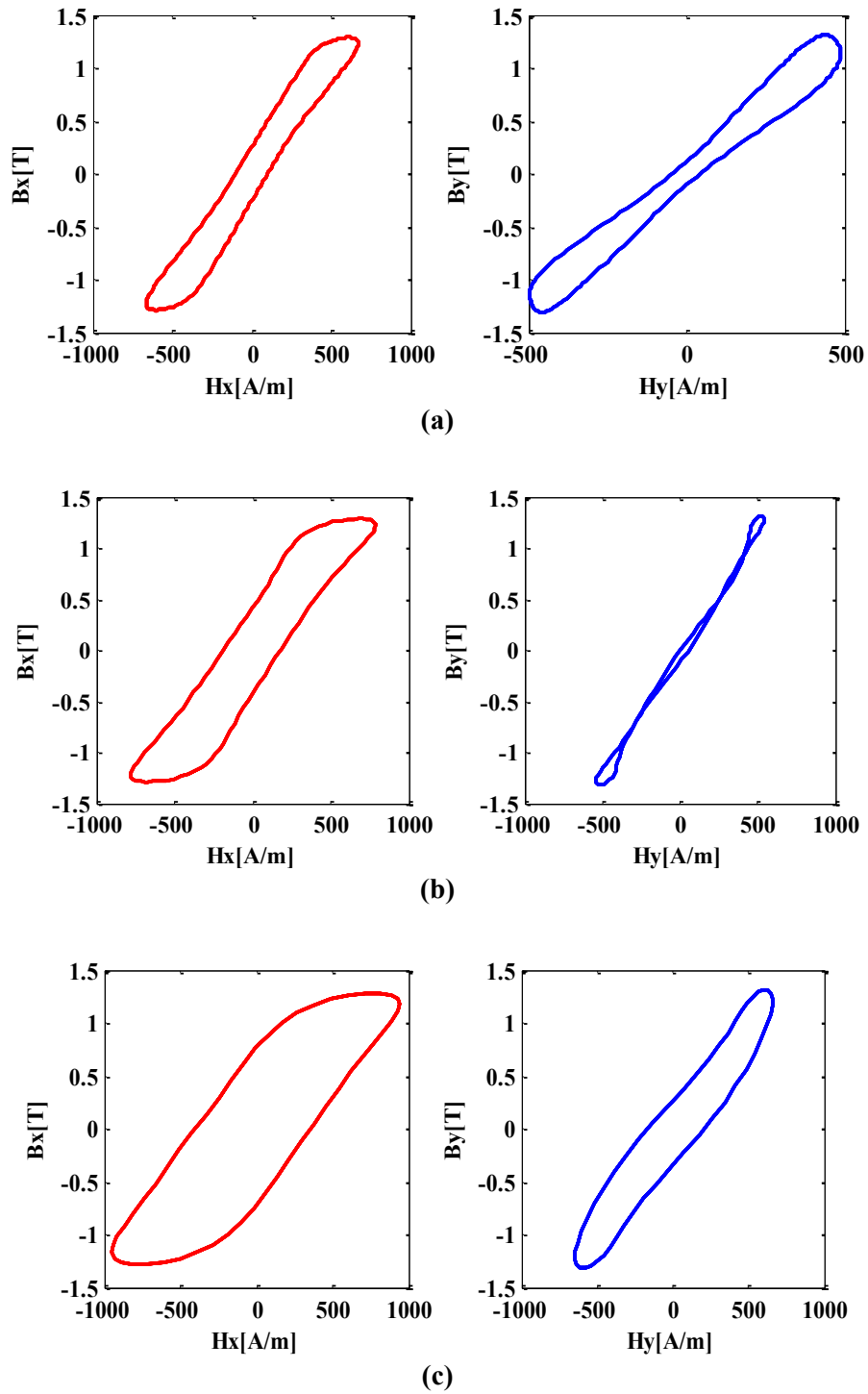


Fig. 3.30: The dynamic hysteresis loops in the x and y directions for M15G29 sample under 1.3T rotating field with (a) 60 Hz (b) 400 Hz (c) 1 kHz.

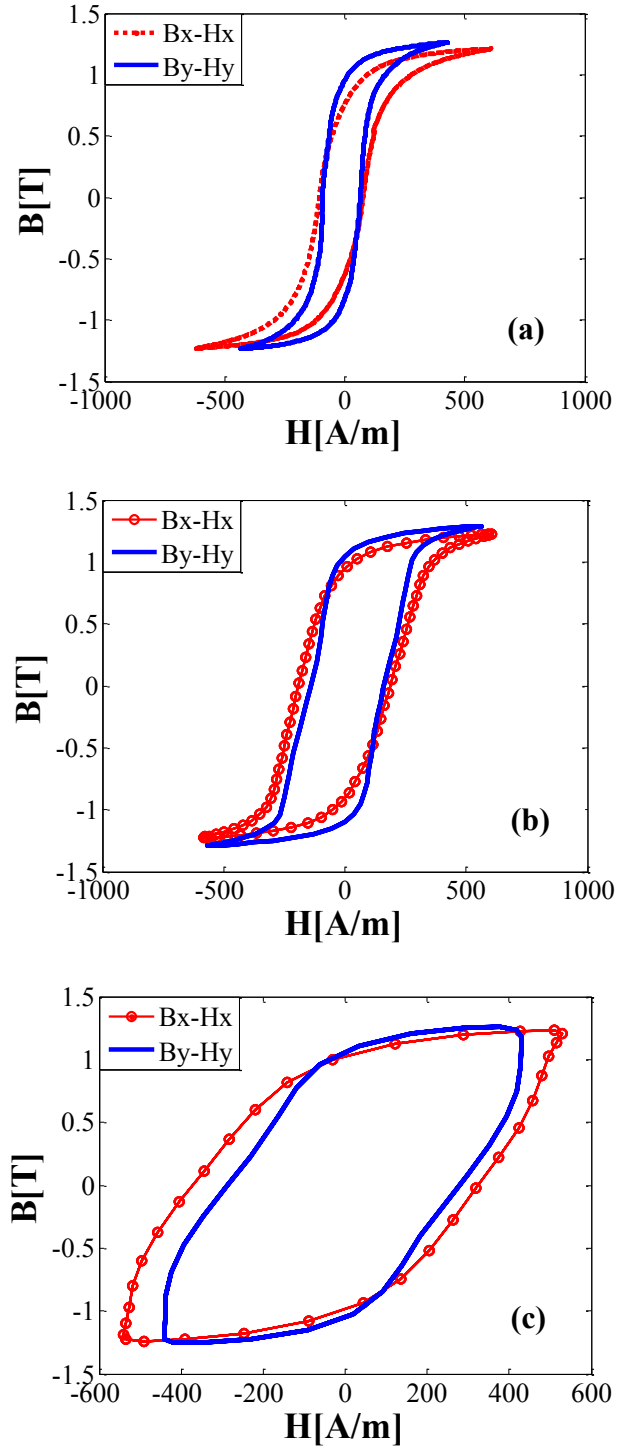


Fig. 3.31: The dynamic hysteresis loops B_x-H_x and B_y-H_y measured in the x and y directions, respectively, for M15G29 sample under 1.3T pulsating field, with (a) 60 Hz. (b) 400 Hz. (c) 1 kHz.

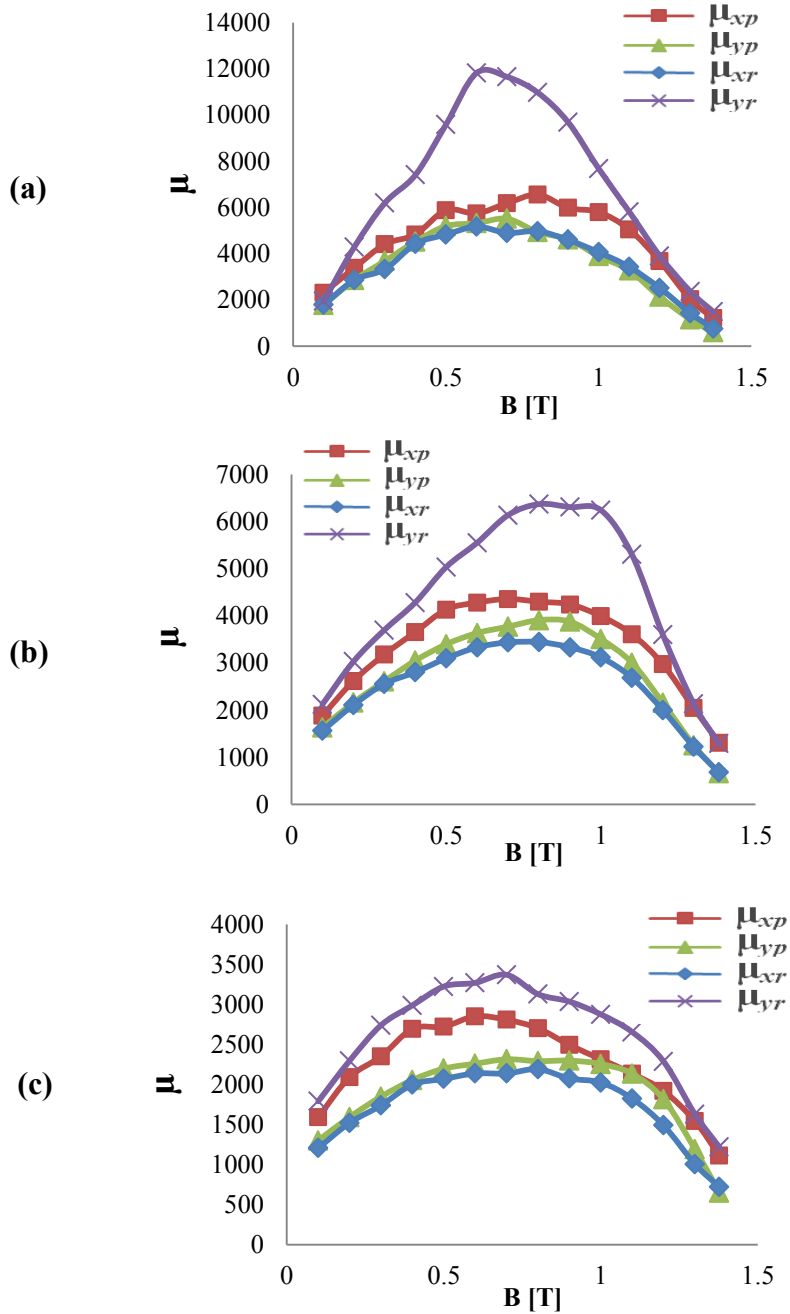


Fig. 3.32: The relative permeability as a function of magnetic flux density for M15G29 sample. Where μ_{xp} , μ_{yp} , μ_{xr} , and μ_{yr} refer to the relative permeability in the x -direction under pulsating field, y -direction under pulsating field, x -direction under rotating field, and y -direction under rotating field, respectively, with (a) 60 Hz. (b) 400 Hz. (c) 1 kHz.

Table3.1: A comparison between rotational and pulsating core losses in the x and y directions at different frequencies in [W/kg]

B[T]	60 Hz			400 Hz			1 kHz		
	Rot.	Puls.x	Puls.y	Rot.	Puls.x	Puls.y	Rot.	Puls.x	Puls.y
0.2	0.21	0.06	0.08	2.64	0.90	1.17	10.68	3.98	5.18
0.3	0.44	0.15	0.21	5.58	2.09	2.86	22.28	8.63	11.71
0.4	0.67	0.30	0.37	9.19	3.74	5.09	36.93	14.78	19.65
0.5	0.92	0.47	0.58	13.40	5.82	7.67	55.03	22.48	29.10
0.6	1.16	0.60	0.80	17.99	8.11	10.42	76.79	31.47	40.93
0.7	1.44	0.85	1.01	23.16	10.90	13.68	104.43	42.80	54.49
0.8	1.70	1.11	1.26	28.65	13.96	17.65	136.48	57.54	72.66
0.9	1.85	1.40	1.62	34.45	17.56	22.29	173.64	73.60	90.87
1.0	1.95	1.63	2.10	40.37	21.56	26.60	212.23	95.13	113.22
1.1	2.04	1.95	2.35	46.17	27.20	30.78	254.96	119.47	138.87
1.2	2.20	2.42	2.84	52.36	32.87	36.34	301.39	147.36	176.97
1.3	2.43	2.92	3.55	58.89	36.76	43.77	346.45	167.85	203.21

Table 3.2: The percentage permeability difference between the x and y directions

B[T]	60 Hz		400 Hz		1 kHz	
	Rot.[%]	Puls.[%]	Rot.[%]	Puls.[%]	Rot.[%]	Puls.[%]
0.2	33.22	16.94	30.43	16.63	33.81	25.54
0.3	46.21	20.43	30.94	18.49	36.52	25.97
0.4	40.28	20.95	34.52	24.39	33.13	25.77
0.5	49.60	23.29	38.47	22.99	35.80	31.69
0.6	56.24	27.45	39.99	20.87	34.63	29.80
0.7	57.92	28.88	44.01	13.91	36.60	27.09
0.8	54.69	28.28	45.98	8.06	29.97	24.45
0.9	52.51	31.72	47.18	8.68	31.67	21.99
1.0	47.08	30.97	50.09	8.60	29.61	18.24
1.1	41.03	33.01	49.35	16.16	31.35	15.06
1.2	35.54	35.72	44.50	20.64	34.91	16.24
1.3	39.58	45.39	42.74	17.37	38.26	20.87

4. THE IMPACT OF ROTATING FIELD ON CORE LOSS ESTIMATION

4.1 Introduction

At the present time, iron loss which is produced by pulsating flux only is considered, while the rotational core loss caused by the rotating field is ignored to simplify the calculation process. However, it is well known that a large portion of the stator in AC machines experiences rotational flux density with associated rotational core loss [59]. This chapter tries to answer the question of how much is the divergence in core loss estimation when calculated by the traditional machine design models where the whole flux is assumed pulsating compared with the reality of existence of the rotational flux with different loci in different parts of the stator. The answer to this question is obtained by application to three different types of machines, induction, BLDCM, and SRM. A methodology is presented to determine the trajectories of the rotating field in each mesh element in the machine stator.

4.2 Methodology to Determine Flux Patterns in Electrical Machines

Three types of machines, 2-pole induction machine (IM), 2-pole brushless DC machine (BLDC), and 6-4 switched reluctance motor (SRM) are modeled using the geometrical parameters given in Table 4.1, Table 4.2, and Table 4.3. A 2-D FE model was developed for each case. The flux density \mathbf{B} in each mesh element is resolved into two perpendicular components \mathbf{B}_x and \mathbf{B}_y . The flux distributions for the three machines are shown in Fig. 4.1. This solution is called the static solution where it is performed for a specific

time-independent input values at a certain rotor position. The dynamic solution can be obtained for a complete rotor rotation with the suitable input value according to the rotor position, in other words, the dynamic solution will be the sum of all static solutions. To attain complete flux density waveforms in each mesh element, 36 static models are solved while changing the rotor position. As a result, the mesh element contains two complete periodic waveforms referred to as B_x and B_y , the flux density waveforms in the x and y directions, respectively.

The flux density trajectory (B_x versus B_y) determines the flux density pattern, whether it is circular, elliptical, or pulsating. The detailed procedure can be described as follows: Fourier analysis is performed to find out the fundamental components of B_x and B_y . Then, the fundamental signals are drawn versus each others around the origin, which gives the flexibility to measure the distance between the origin and each point on the locus. The maximum value is considered to be the locus major axis (B_{max}), and the minimum value is the locus minor axis (B_{min}). An aspect ratio (or an axis ratio) is adopted by many researchers as a parameter to describe the locus of B_x, B_y , which is defined as the ratio of minor axis to major axis (B_{min}/B_{max}) [49], [60], and [61]. For a particular mesh element a value between 0 and 1 can be assigned which refers to the aspect ratio of the flux density vector locus, where the value 1 stands for a circular rotating field, value 0 for the pulsating field, and values between ($0 < B_{min}/B_{max} < 1$) for the elliptical rotating field, as seen in Fig. 4.2, the closer to 1 aspect ratio means nearer to the circular polarization. A flowchart that describes the methodology is shown in Fig. 4.3.

Table 4.1: Geometrical dimensions of the 2-pole induction machine in [mm].

	ROTOR	STATOR
Outer diameter	78.56	142.9
Inner diameter	22.23	79.38
Number of slots	24	24
Slot top radius	1.905	0.381
Slot bottom radius	1.194	4.267
Yoke width	NA	12.7

Table 4.2: Geometrical dimensions of the 2-pole BLDC machine in [mm].

	FIELD	ARMATURE
Outer diameter	30	70
Inner diameter	10	32
Yoke width	NA	7
Tooth width	NA	3
Magnet thickness	3	NA
Magnet arc	125	NA

Table 4.3: Geometrical dimensions of the 6-4 SRM in [mm].

	ROTOR	STATOR
Outer diameter	74.4	131.3
Inner diameter	20	77.8
Teeth number	4	6
Tooth width	22	18
Yoke diameter	44	NA
Yoke width	NA	9
Tooth arc	NA	36

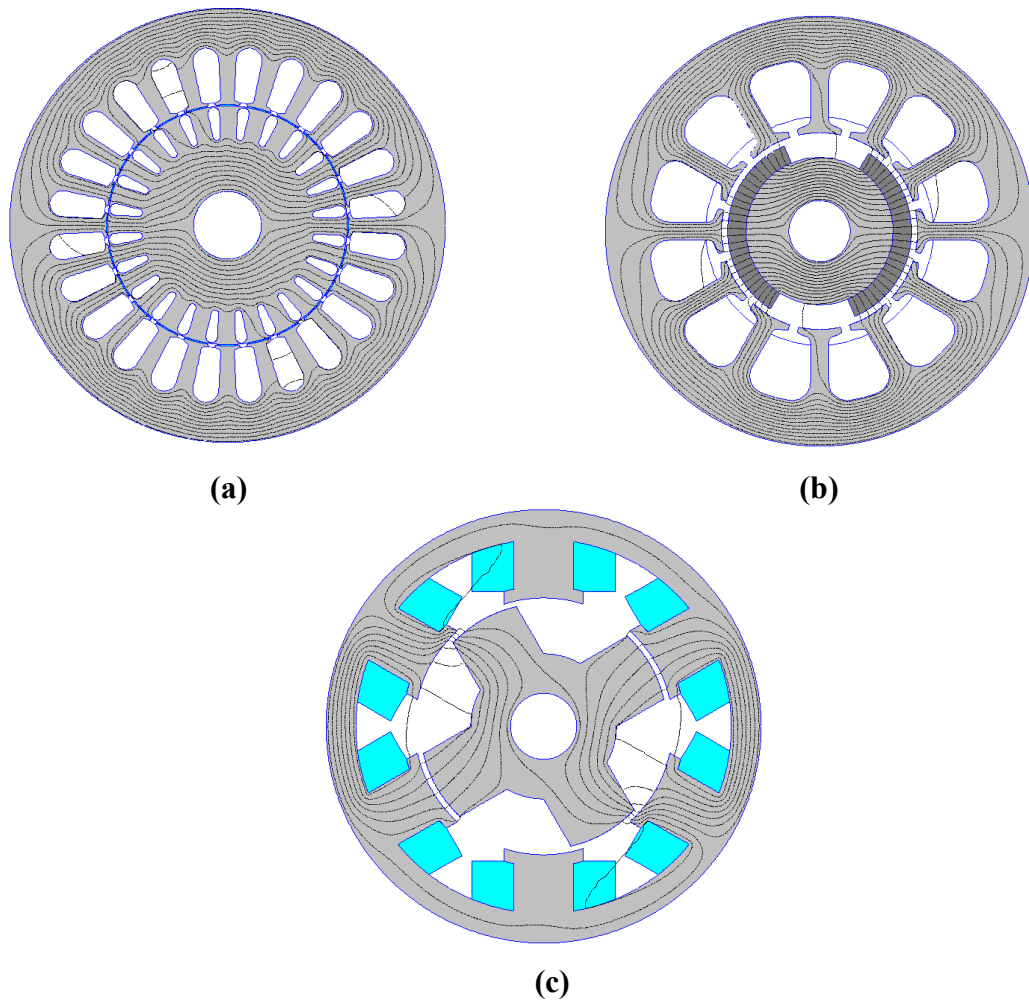


Fig. 4.1: Flux paths distributions in for FEA of (a) 2-pole IM (b) 2-pole BLDCM (c) 6-4 SRM.

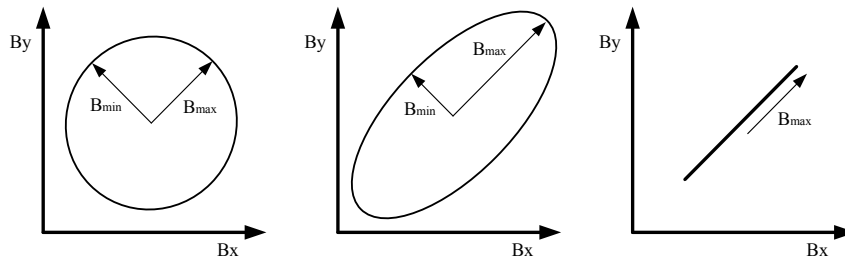


Fig. 4.2: Flux density locus of (a) Circular rotating field (b) Elliptical rotating field (c) Pulsating field.

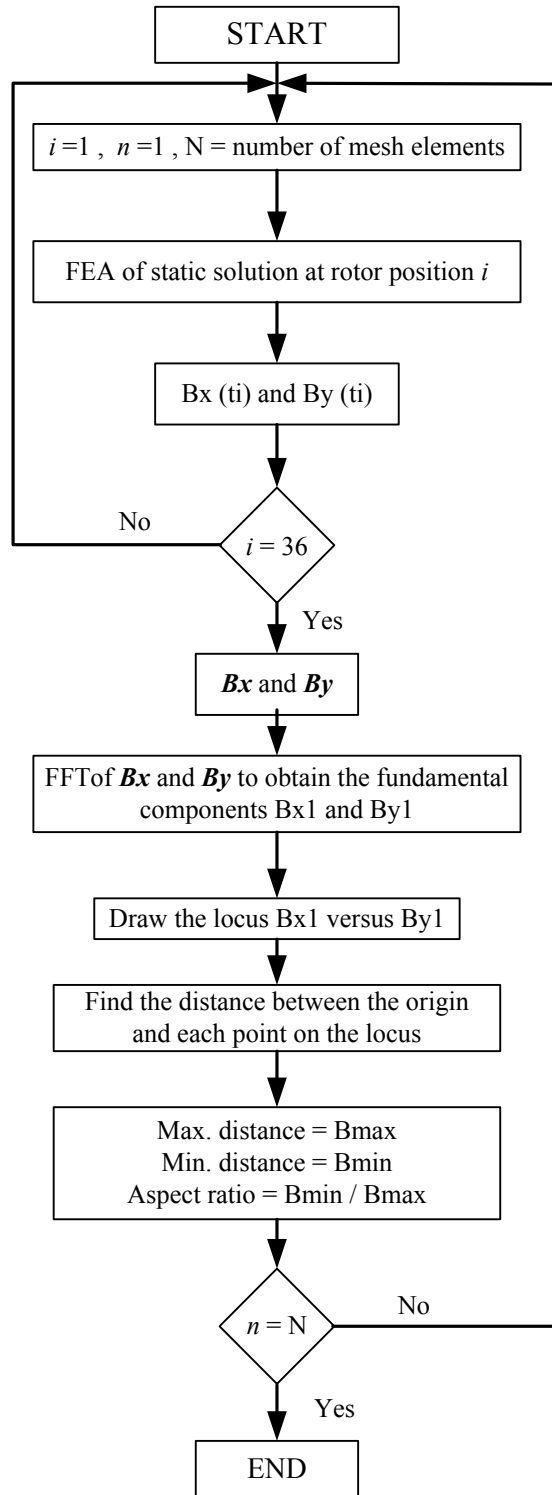


Fig. 4.3: Flowchart for determination of the flux patterns.

4.3 Simulation Results

After simulations and computation of the aspect ratios of the flux density loci, the mesh element can be described by position coordinates (x, y) , and its aspect ratio (B_{\min}/B_{\max}) , which gives the possibility of reconstruction of the stator 2-D image showing the distributions of magnetic flux density aspect ratio in the stators of the three machines as illustrated in Figs. 4.4, 4.5, and 4.6; where the x and y axes address the dimensions of the machines in [m], and the color map depicts the aspect ratio distribution from 0 to 1. The aspect ratio distribution offers an insight into the rotational core loss regions, which are mainly affected by the stator geometrical characteristics [62]. It is observed that the stators are mostly subjected to an elliptical rotating field with different aspect ratios, and it never finds a completely pulsating field (B_x and B_y waveforms without phase shift) or completely circular field (identical sinusoidal B_x and B_y waveforms with 90° phase shift) since usually there is a phase shift or difference in magnitudes between the B_x and B_y waveforms. Additionally, high aspect ratios are concentrated in the teeth roots where the flux subdivides and goes to the back of core in different directions during a complete rotation, this forms a rotating flux density vector in that area. The area percentages of the axis ratio out of the total area of the stator for the three machines are shown in Figs. 4.7, 4.8, and 4.9; where the ratios over 0.2 are higher in the SRM and lower in the IM, while the percentage ratio lower than 0.2 (closer to pulsating) is higher in the IM and lower in the SRM, which means the effect of rotating field will be more pronounced in the SRM, then in BLDCM, and the least in the IM. However, the stator portion covered with a

rotational component where the minor axis is at least 20% of the major axis is around 20% of the total.

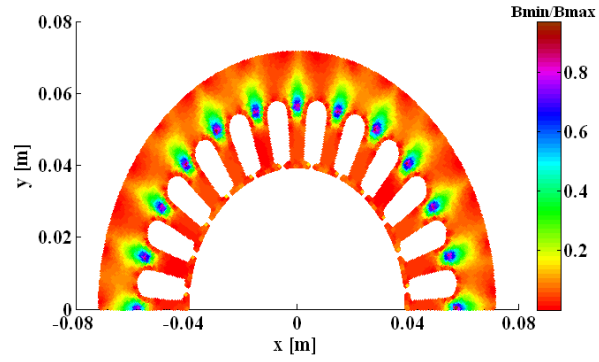


Fig. 4.4: The aspect ratio distribution in the stator of a 2-pole induction machine.

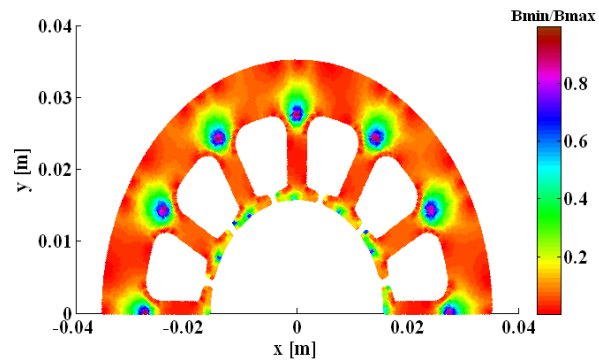


Fig. 4.5: The aspect ratio distribution in the stator of a 2-pole BLDCM.

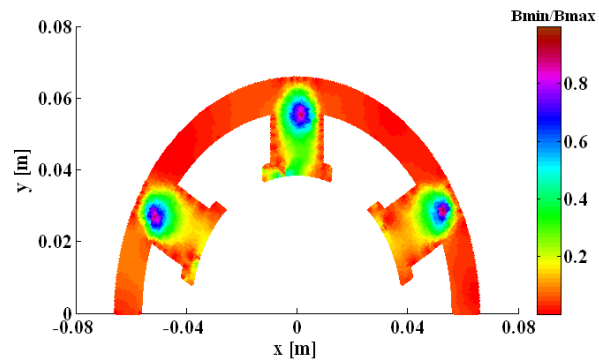


Fig. 4.6: The aspect ratio distribution in the stator of a 6-4 SRM.

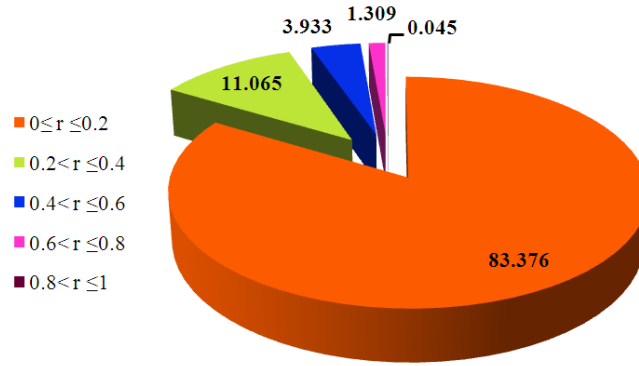


Fig. 4.7: Percentages of the aspect ratio out of the total area of the stator in a 2-pole induction machine.

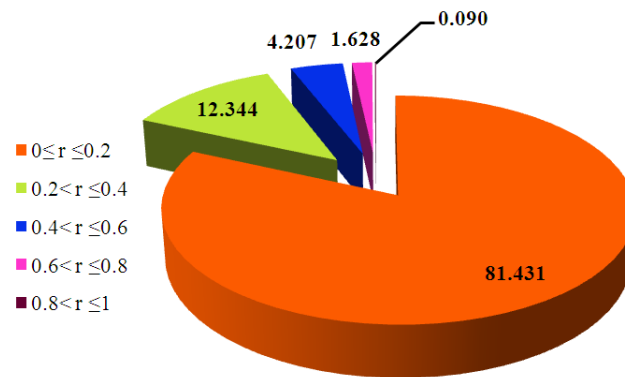


Fig. 4.8: Percentages of the aspect ratio out of the total area of the stator in a 2-pole BLDCM.

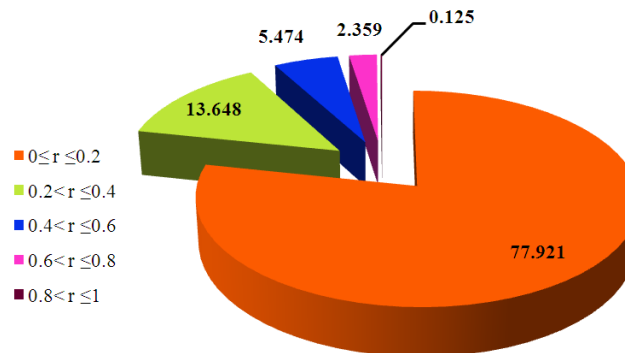


Fig. 4.9: Percentages of the aspect ratio out of the total area of the stator in a 6-4 SRM.

4.4 Experimental Results

The measurement system uses a novel design of a magnetizing circuit based on an electromagnetic Halbach array is capable of producing pulsating, circular, and elliptical fields with any aspect ratio within the sample under test. The desired flux density locus is achieved in the specimen by injecting both Halbach arrays simultaneously with equal magnitude sinusoidal waveforms V_x and V_y with some phase shift. Then, the net flux density vector is produced in the test specimen which can be presented mathematically as in equation (3.6). If $\varphi=90^\circ$ the flux will be completely rotating with constant amplitude. If $\varphi=0^\circ$ the flux will be pulsating, and an elliptical locus produced if $0^\circ < \varphi < 90^\circ$. The angle φ is pre-calculated for different aspect ratios through a subroutine written in MATLAB[®] and implemented to produce the input excitation waveforms. Here, we use the phase shift technique to generate the ellipse which is more flexible than changing the waveforms magnitudes. Table 4.4 shows the aspect ratios of flux density loci and the corresponding phase shift between the input signals. Verification tests are performed at three different frequencies on the M36G29 sample. The results at a vector magnitude of 1.4 T are presented in Figs. 4.10, 4.11, and 4.12.

Table 4.4: Aspect ratios of flux density loci and the corresponding phase shift between the input signals.

Aspect ratio	Phase shift (degree)
1.0	90
0.8	77.315
0.6	61.915
0.4	43.56
0.2	22.62
0.0	0

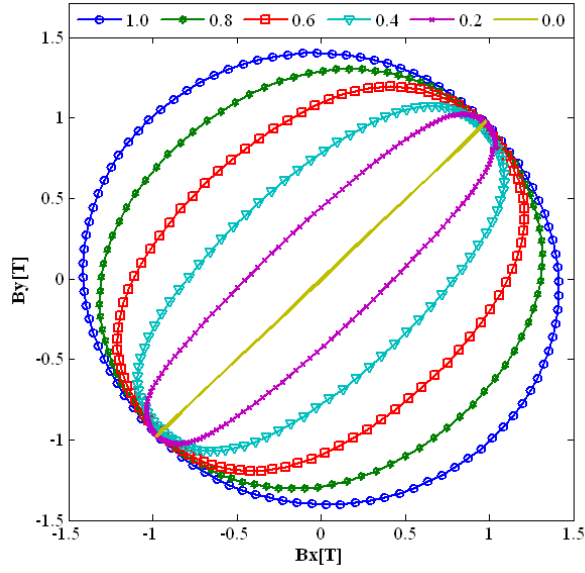


Fig. 4.10: The loci of flux density with different aspect ratios (From 0 to 1) at 60 Hz for M36G29.

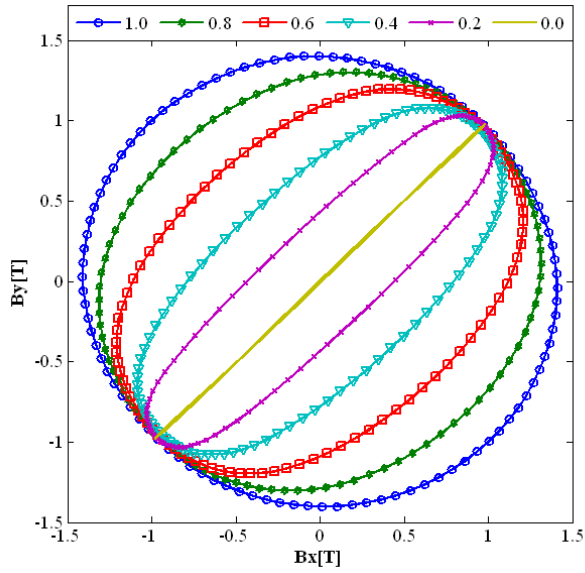


Fig. 4.11: The loci of flux density with different aspect ratios (From 0 to 1) at 400 Hz for M36G29.

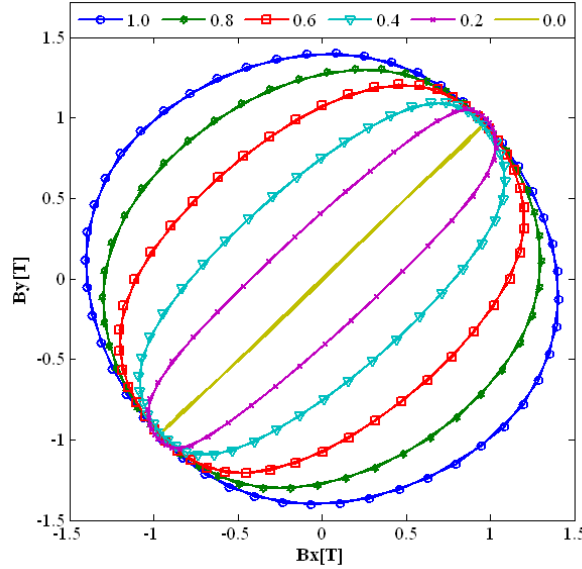


Fig. 4.12: The loci of flux density with different aspect ratios (From 0 to 1) at 1 kHz for M36G29.

Measurements were carried out on two circular samples of 20 cm diameter of electrical steel M36G29 and M19G24 at three different frequencies of interest to the industry (60 Hz, 400 Hz, and 1 kHz). A set of rotational losses (P_{rot}) data was obtained for each sample at each frequency with different aspect ratios (1, 0.8, 0.6, 0.4, and 0.2), in addition to the pulsating loss. Fig. 4.13 shows the loss curves at 60 Hz for M36G29, where circular rotational loss achieves higher magnitudes compared with pulsating loss until a certain value of flux density (around 1.2 T), then once it goes to saturation circular rotational curve decreases while pulsating curve keeps rising. This behavior states clearly that the material experiences higher core loss under rotating field before the intersection point (1.21 T, 3.262 W/kg) and after 1.21T the pulsating field produces higher loss. The elliptical rotating field with higher aspect ratio produces higher core loss compared with

rotating field with lower aspect ratio as noticed in a comparison of the power loss curves at ($r = 0.2, 0.4, 0.6,$ and 0.8), and the power loss curve due to elliptical rotating fields tend to start decreasing in the saturation region faster with higher aspect ratio, for example at 1.4 T the power loss curves at ratios 1.0, 0.8, and 0.6 amount to 1.9571, 2.8578, 3.1788 W/kg, respectively. Fig. 4.14 shows the loss curves at 60 Hz for M19G24, generally the losses are higher because of the effect of eddy currents where G24 thickness is 0.635 mm compared with G29 (thickness of 0.3556 mm). Similar observations as for the G29 material can be seen, but the curves at low aspect ratios (0.2 and 0.4) do not reach the turning point which needs a higher flux density which is difficult to be achieved with this magnetizing circuit. Fig. 4.15 and Fig. 4.16 depict the loss curves at 400 Hz for M36G29 and M19G24 respectively, where the losses increase with increase in frequency. When the frequency is increased to 1 kHz, higher losses are attained and become hard to see turning points of rotational loss curves even in the saturation region, since this decrease in loss is mainly related to the hysteresis rotational loss, and in the case of high frequencies the eddy loss component is dominant, as shown in Fig. 4.17 and Fig. 4.18.

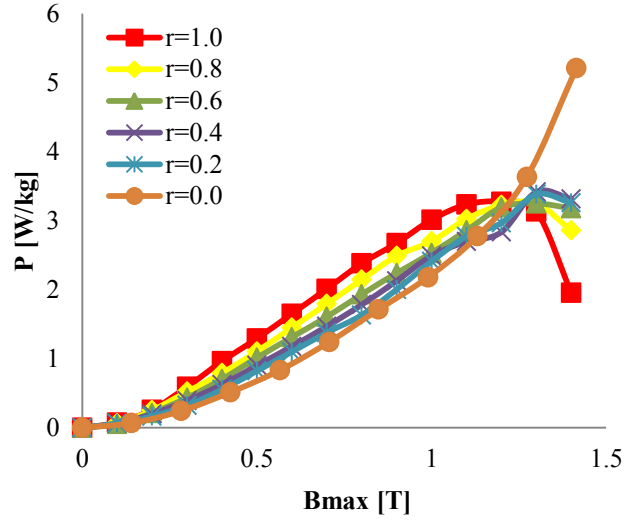


Fig. 4.13: The rotational core losses with different aspect ratios compared with pulsating loss (aspect ratio=0) at 60 Hz for M36G29.

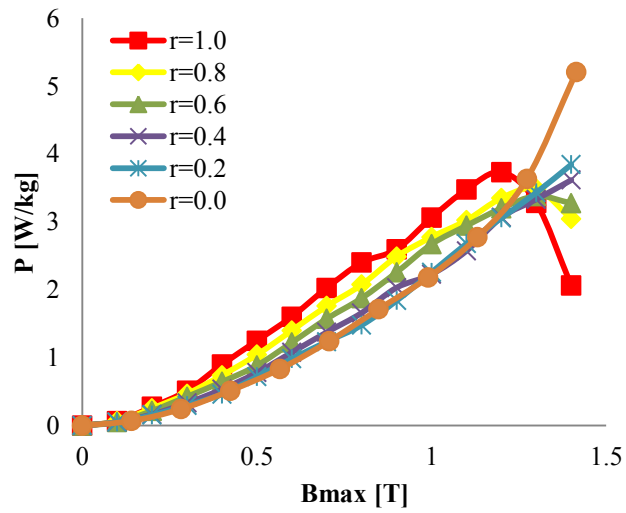


Fig. 4.14: The rotational core losses with different aspect ratios compared with pulsating loss (aspect ratio=0) at 60 Hz for M19G24.

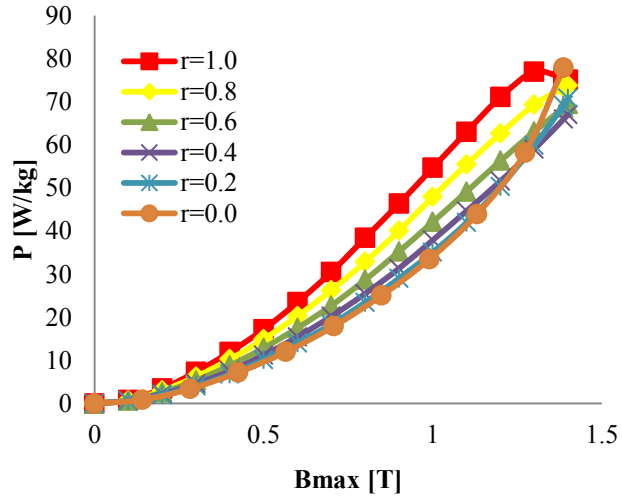


Fig. 4.15: The rotational core losses with different aspect ratios compared with pulsating loss (aspect ratio=0) at 400 Hz for M36G29.

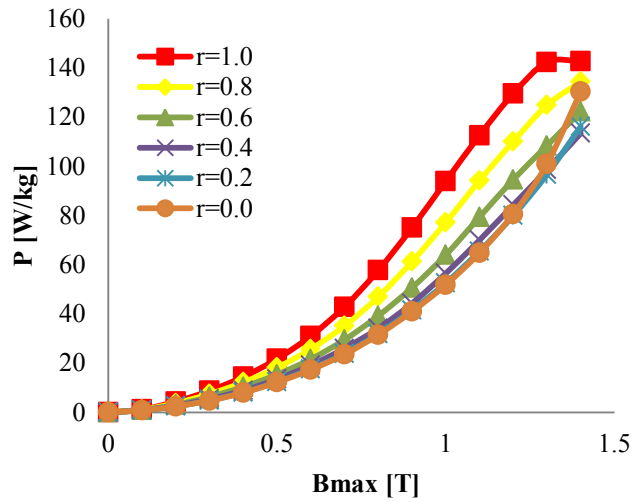


Fig. 4.16: The rotational core losses with different aspect ratios compared with pulsating loss (aspect ratio=0) at 400 Hz for M19G24.

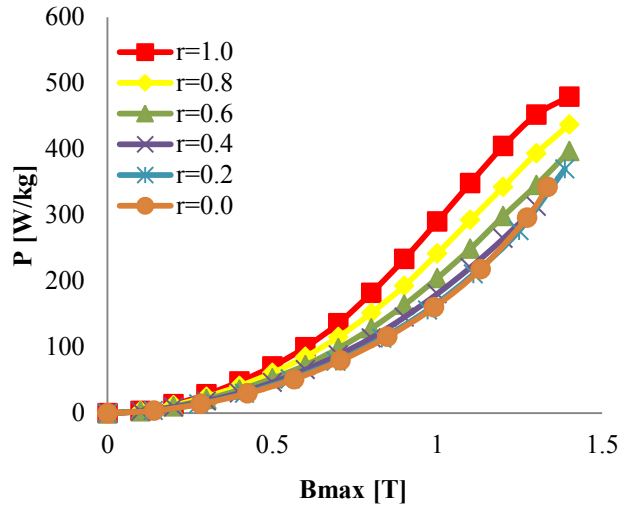


Fig. 4.17: The rotational core losses with different aspect ratios compared with pulsating loss (aspect ratio=0) at 1 kHz for M36G29.

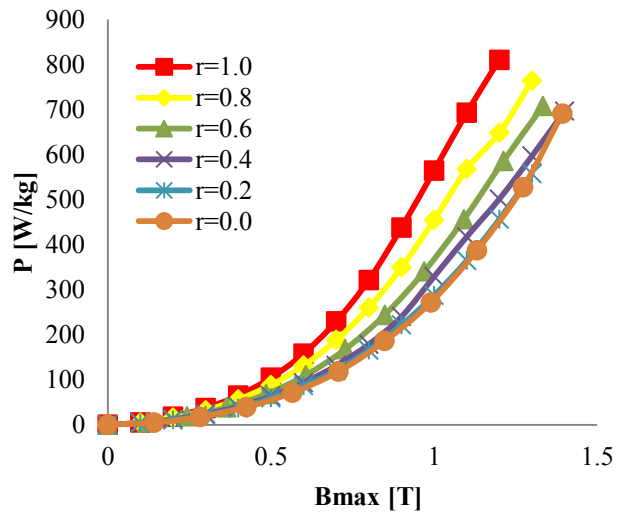


Fig. 4.18: The rotational core losses with different aspect ratios compared with pulsating loss (aspect ratio=0) at 1 kHz for M19G24.

4.5 Error Estimation

In this section, the error percentage along the flux density profile is calculated, where at a specific aspect ratio the difference between the rotational loss and pulsating loss is compared relative to the rotational loss as follows:

$$e = \frac{P_{rot} - P_{pul}}{P_{rot}} \times 100\% \quad (4.1)$$

Fig. 4.19 and Fig. 4.20 show the percentage of relative error in the rotational core losses at 60 Hz for M36G29 and M19G24, respectively. The highest difference can be noticed in the case of circular rotating field (higher aspect ratio) which is around 47 % and 51 % in M36G29 and M19G24, respectively. After the point of intersection between the pulsating loss curve and rotational loss curve, the error becomes negative which means the loss produced due to the pulsating field is higher than the loss produced by the rotating field. This negative error is higher in the case of circular rotating field as well and reaches around -158 % and -129 % in M36G29 and M19G24, respectively. Fig. 4.21 and Fig. 4.22 show the relative error in the rotational core losses at 400 Hz for M36G29 and M19G24, respectively. The variation in error becomes lower compared with the 60Hz case, and more constancy can be seen in M19G24 because of the eddy current component which is dominant and does not decrease in the saturation region. Fig. 4.23 and Fig. 4.24 show the relative error in the rotational core losses at 1 kHz for M36G29 and M19G24, respectively. Here, the least variation in error can be noticed, and less negative errors can be seen which appeared only in low aspect ratio curves.

The error in the mesh element can be determined by considering two parameters: the aspect ratio and the magnitude of the flux density vector. Using a MATLAB[®] subroutine the aspect ratios of all mesh elements are classified into five regions from 0 to 1 in steps of 0.2. So, each mesh element can be corresponded to a curve of relative error at determined frequency and determined material. Then, according to the magnitude of the flux density vector in that mesh element the value of relative error on the related curve can be determined exactly. This error which is assigned to the mesh element represents the error in considering the flux completely pulsating compared with the reality of being a rotating field with such an aspect ratio. Figs. 4.25, 4.26, 4.27, 4.28, 4.29, and 4.30 show the percentage error in each mesh element associated with considering the rotational core losses in the stator of the 2-pole induction machine in M36G29 and M19G24 at the 60 Hz, 400 Hz, and 1 kHz. Figs. 4.31, 4.32, 4.33, 4.34, 4.35, and 4.36 show the percentage errors in the 2-pole BLDCM, and for the 6-4 SRM percentage errors are illustrated in Figs. 4.37, 4.38, 4.39, 4.40, 4.41, and 4.42.

This error estimation determined the error individually in each mesh element, and as noticed in some cases such as 2-pole induction machine using M36G29 at 60 Hz, some areas experience positive error and others negative error which varies between 43.5517 % and -55.0574 %. This means that core losses are over estimated in some areas and under estimated in others. To clarify the results, the overall error is a stringent need to be estimated, which can be performed by considering the weight of each mesh element and the effect of its error in the whole stator area using the following equation:

$$Error = \frac{1}{A} \sum_{n=1}^N e_n A_n \quad (4.2)$$

Where,

A is total area of the stator and is $\sum_{n=1}^N A_n$, e_n is the error in mesh element n , A_n is the area of mesh element n , and N is the total number of mesh elements.

The flowchart in Fig. 4.43 clarifies the error estimation procedure, and Table 4.5 summarizes the maximum, minimum, and the all over error percentages in the three different machines at different frequencies for different materials.

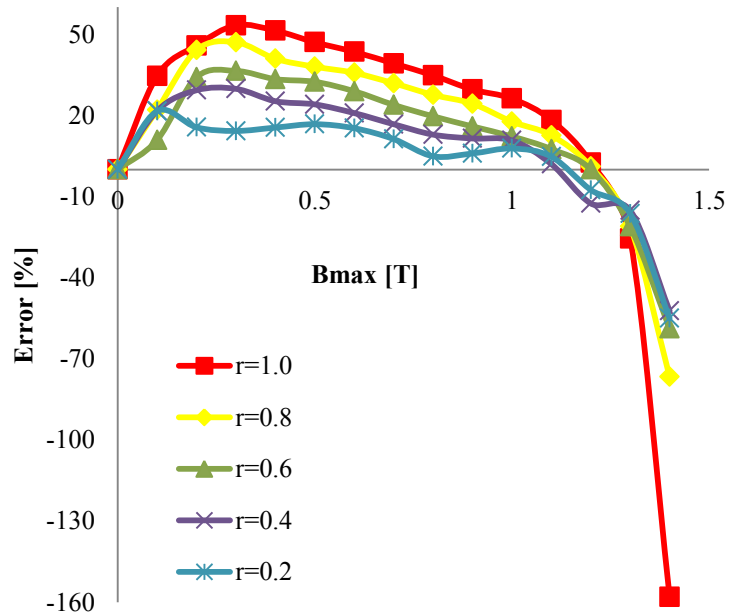


Fig. 4.19: The percentage of relative error in the rotational core losses at 60 Hz for M36G29.

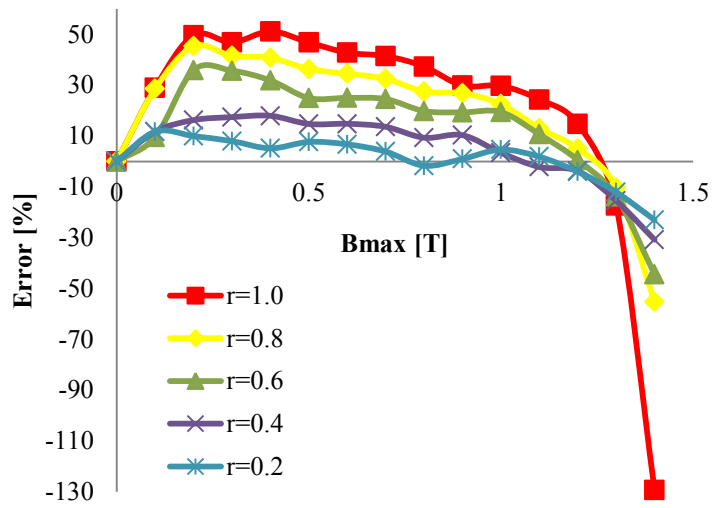


Fig. 4.20: The percentage of relative error in the rotational core losses at 60 Hz for M19G24.

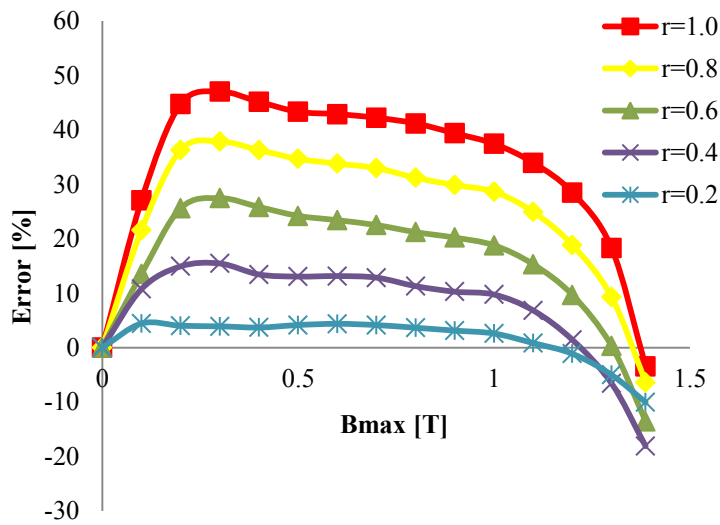


Fig. 4.21: The percentage of relative error in the rotational core losses at 400 Hz for M36G29.

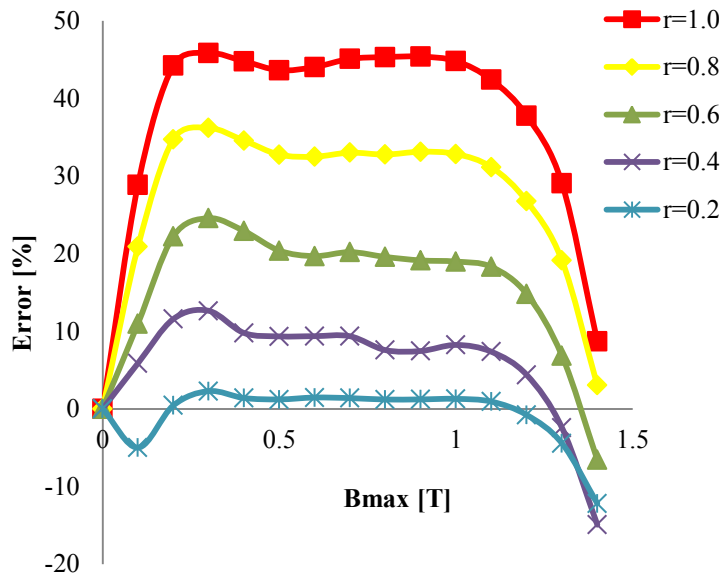


Fig. 4.22: The percentage of relative error in the rotational core losses at 400 Hz for M19G24.

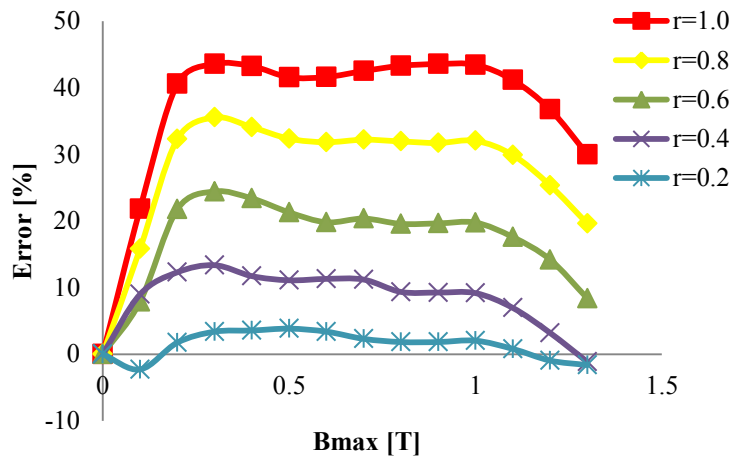


Fig. 4.23: The percentage of relative error in the rotational core losses at 1 kHz for M36G29.

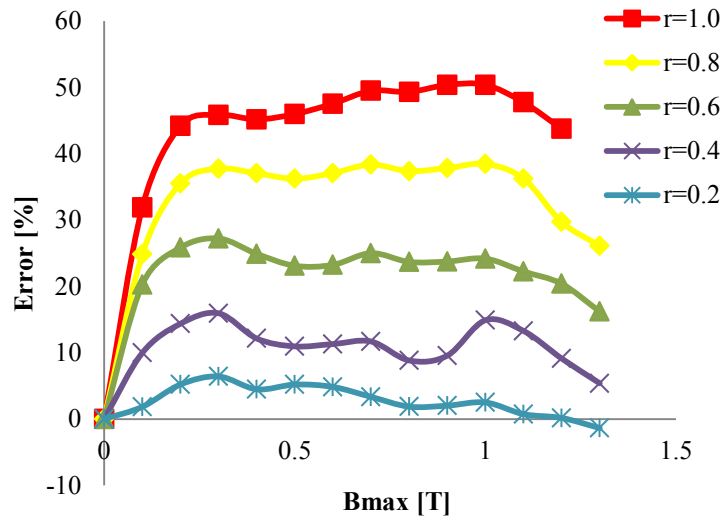


Fig. 4.24: The percentage of relative error in the rotational core losses at 1 kHz for M19G24.

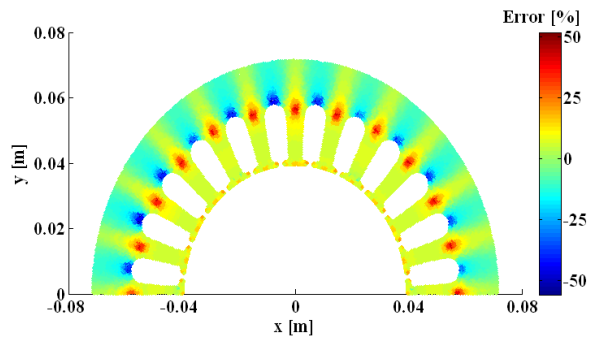


Fig. 4.25: The percentage errors associated with considering the rotational core losses in the stator of a 2-pole induction machine using M36G29 laminations at 60 Hz.

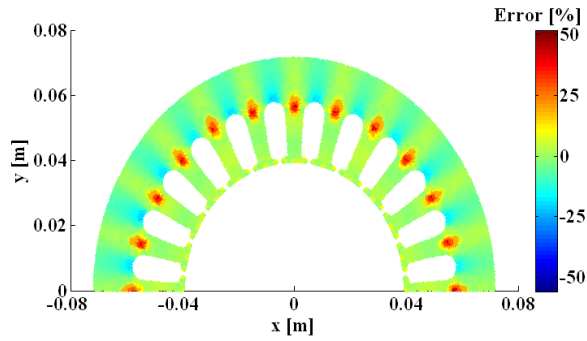


Fig. 4.26: The percentage errors associated with considering the rotational core losses in the stator of a 2-pole induction machine using M19G24 laminations at 60 Hz.

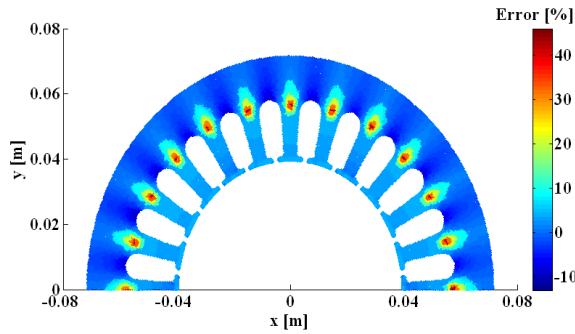


Fig. 4.27: The percentage errors associated with considering the rotational core losses in the stator of a 2-pole induction machine using M36G29 laminations at 400 Hz.

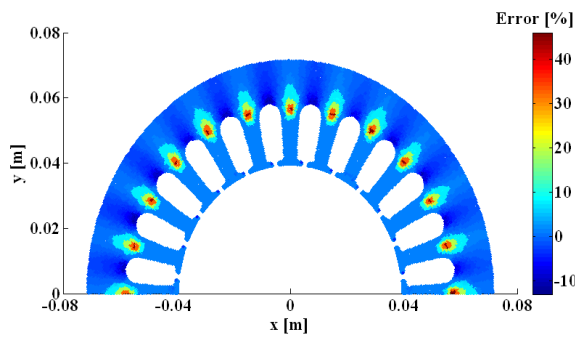


Fig. 4.28: The percentage errors associated with considering the rotational core losses in the stator of a 2-pole induction machine using M19G24 laminations at 400 Hz.

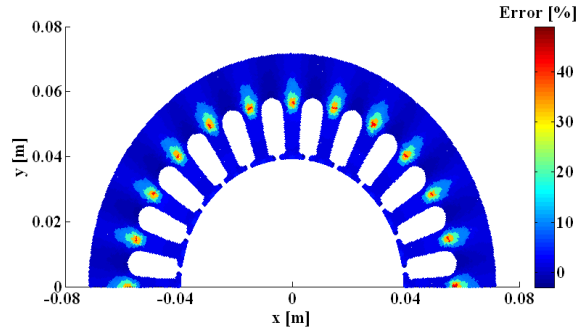


Fig. 4.29: The percentage errors associated with considering the rotational core losses in the stator of a 2-pole induction machine using M36G29 laminations at 1 kHz.

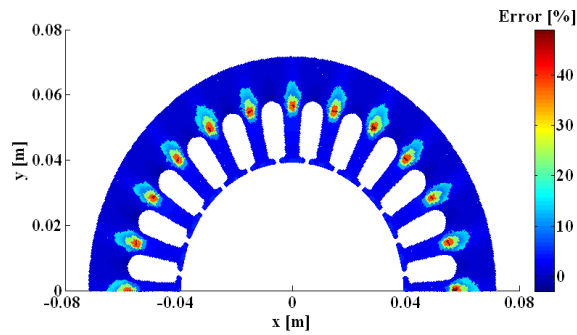


Fig. 4.30: The percentage errors associated with considering the rotational core losses in the stator of a 2-pole induction machine using M19G24 laminations at 1 kHz.

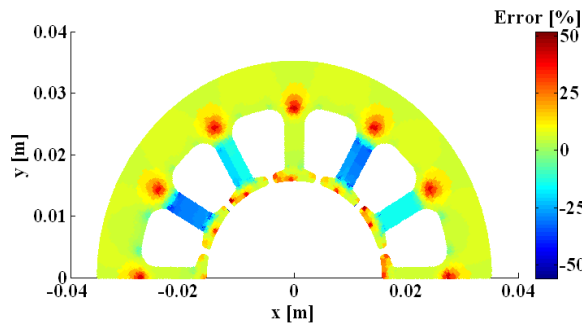


Fig. 4.31: The percentage errors associated with considering the rotational core losses in the stator of a 2-pole BLDCM using M36G29 laminations at 60 Hz.

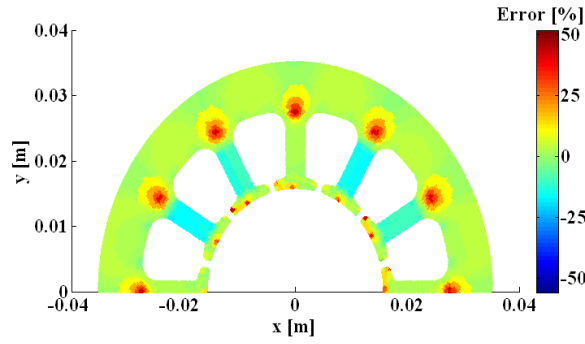


Fig. 4.32: The percentage errors associated with considering the rotational core losses in the stator of a 2-pole BLDCM using M19G24 laminations at 60 Hz.

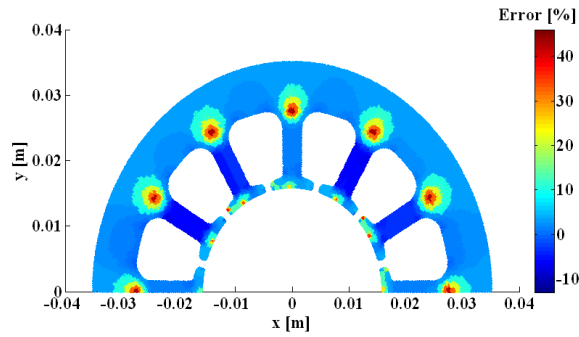


Fig. 4.33: The percentage errors associated with considering the rotational core losses in the stator of a 2-pole BLDCM using M36G29 laminations at 400 Hz.

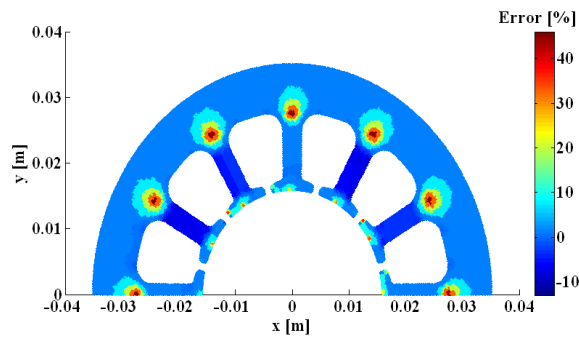


Fig. 4.34: The percentage errors associated with considering the rotational core losses in the stator of a 2-pole BLDCM using M19G24 laminations at 400 Hz.

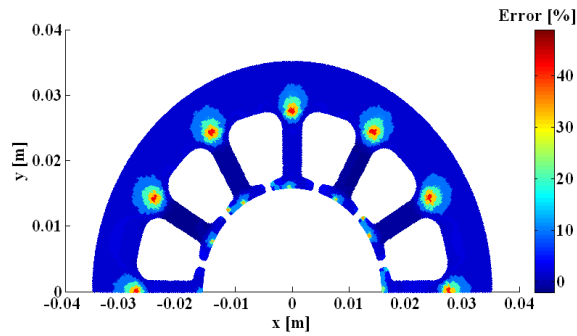


Fig. 4.35: The percentage errors associated with considering the rotational core losses in the stator of a 2-pole BLDCM using M36G29 laminations at 1 kHz.

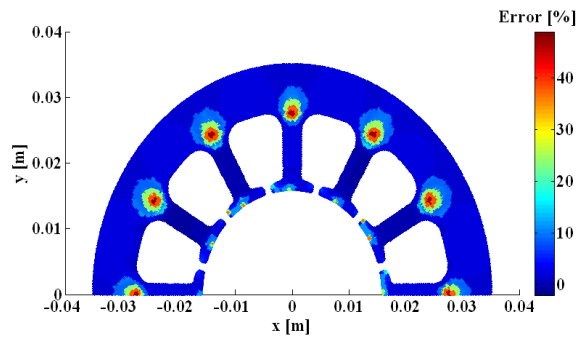


Fig. 4.36: The percentage errors associated with considering the rotational core losses in the stator of a 2-pole BLDCM using M19G24 laminations at 1 kHz.

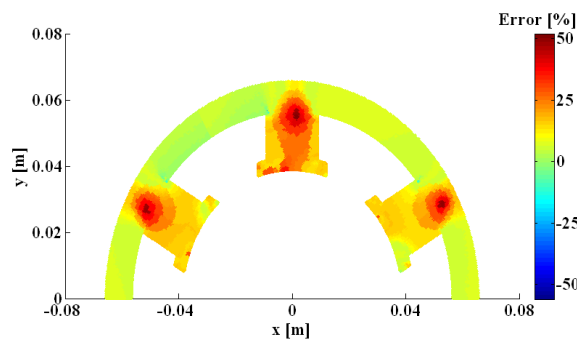


Fig. 4.37: The percentage errors associated with considering the rotational core losses in the stator of a 6-4 SRM using M36G29 laminations at 60 Hz.

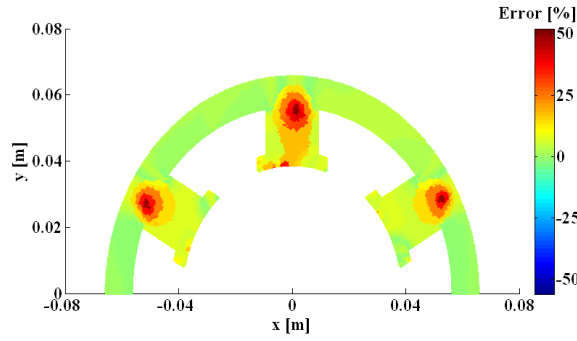


Fig. 4.38: The percentage errors associated with considering the rotational core losses in the stator of a 6-4 SRM using M19G24 laminations at 60 Hz.

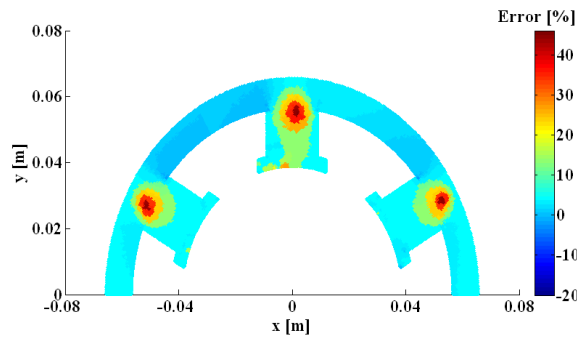


Fig. 4.39: The percentage errors associated with considering the rotational core losses in the stator of a 6-4 SRM using M36G29 laminations at 400 Hz.

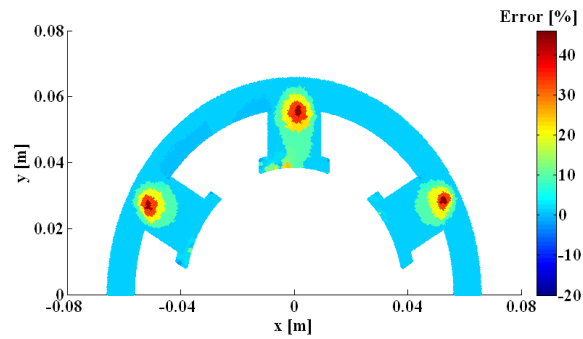


Fig. 4.40: The percentage errors associated with considering the rotational core losses in the stator of a 6-4 SRM using M19G24 laminations at 400 Hz.

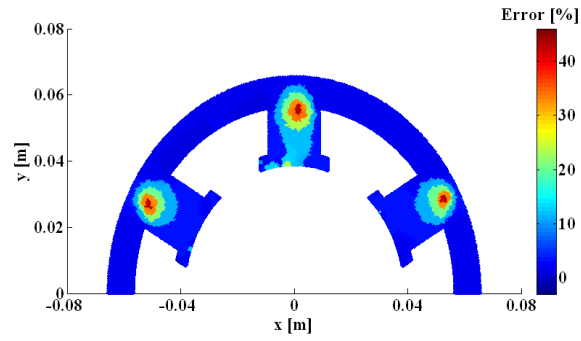


Fig. 4.41: The percentage errors associated with considering the rotational core losses in the stator of a 6-4 SRM using M36G29 laminations at 1 kHz.

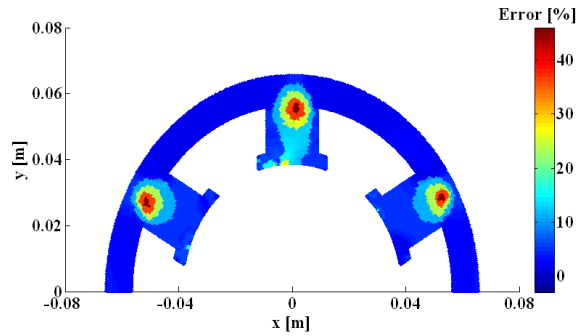


Fig. 4.42: The percentage errors associated with considering the rotational core losses in the stator of a 6-4 SRM using M19G24 laminations at 1 kHz.

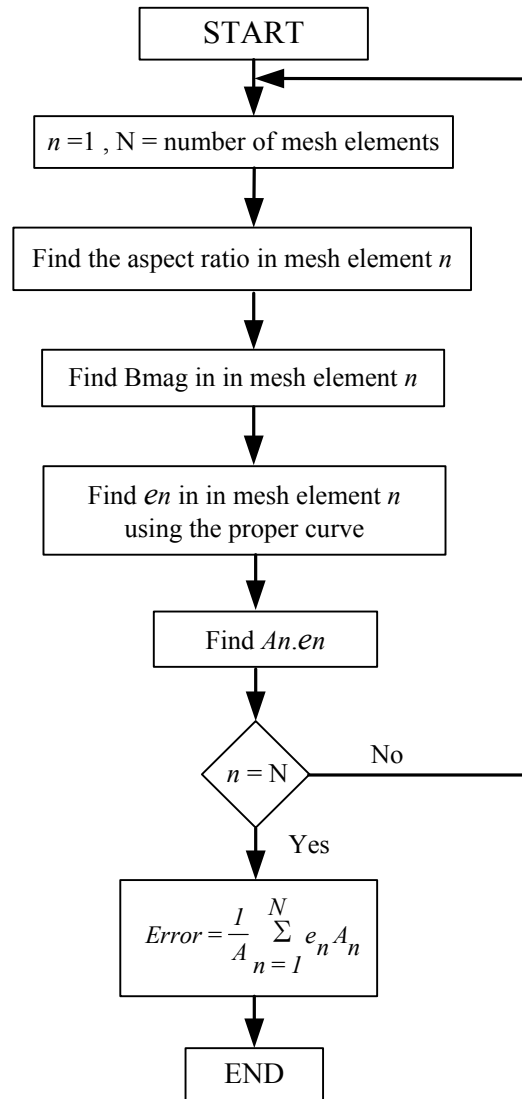


Fig. 4.43: Flowchart of determination the all over error in the machine when considering the effect of rotating field compared with considering the whole flux pulsating.

Table 4.5: Error percentages in the three different types of machines.

Machine	f [Hz]	Lamination	Error [%]		Over all
			Max.	Min.	
Induction	60	M36G29	43.5517	-55.0574	-0.1888
		M19G24	42.8405	-23.0287	-0.5818
	400	M36G29	42.9051	-10.0549	2.4834
		M19G24	45.2036	-12.1948	1.7527
	1000	M36G29	42.4504	-2.2803	3.1778
		M19G24	48.3576	-1.3670	4.0772
BLDC	60	M36G29	46.979	-55.0574	5.2923
		M19G24	43.2881	-23.0287	3.1917
	400	M36G29	42.8936	-10.0549	4.1396
		M19G24	45.1984	-12.1948	2.7878
	1000	M36G29	42.4311	-1.6358	3.9452
		M19G24	48.3193	-1.3670	4.5354
SRM	60	M36G29	51.3703	-55.0574	12.4243
		M19G24	51.1143	-23.0287	7.1452
	400	M36G29	45.2280	-10.0549	6.3929
		M19G24	44.8251	-12.1948	4.3880
	1000	M36G29	43.3291	-2.2128	5.5972
		M19G24	47.2141	-1.3670	6.4873

4.6 Discussion

The errors in some parts of the core of rotating machine prove that the rotating field can be responsible for extra losses of up to 51 % as obtained in SRM using M36G29 at 60 Hz. Sometimes, once the machine is saturated and its core is subjected to high flux density levels, the losses produced by the rotating field effect underestimates the total loss and the percentage errors become negative as seen for the induction machine at 60 Hz. Since the losses are overestimated in some areas and underestimated in other areas, the total error may only be around 12%. The machine geometrical shape plays an important role in determination of the field loci within the machine, which motivates researchers to investigate the field loci distribution in other types of machines and even for other designs of the same simulated machines in this work. The underestimated error in the induction machine at 60 Hz may give the opportunity for the machine designers to start thinking of increasing the areas of rotating field and operate the machine at high flux level to end up with lower core loss. The rotating field produces a high discrepancy in power loss from point to point in the stator as being 51.3703 % to -55% in the SRM using M36G29 at 60 Hz which will have an effect on the heat distribution and produce high temperature spots in the core. Performing measurements under elliptical rotating field with additional aspect ratios increases the accuracy of the error estimation, in this work it has been done only for (0.2, 0.4, 0.6, and 0.8).

4.7 Conclusion

This chapter has introduced a comprehensive study showing the influence of rotating field on core loss estimation. The investigation is implemented on three different types of machines, 2-pole IM, 2-pole BLDCM, and 6-4 SRM, where the FEA is used to determine flux patterns in the stators of these machines. Simulation results disclose the distribution of flux loci as an aspect ratio and show that the stators are completely subjected to rotating field with different aspect ratios. It can be seen that around 80 % of stator is subjected to a rotating field with an aspect ratio less than 0.2. The measurement system uses a novel design of a magnetizing circuit based on an electromagnetic Halbach array which is capable of producing pulsating, circular, and elliptical fields with any aspect ratio within the sample under test. The rotational and pulsating core losses are measured for two circular samples of non-oriented M19 gauge 24 and M36 gauge 29 silicon steel, at three frequencies of industrial interest (60 Hz, 400Hz, and 1 kHz). Elliptical core losses are measured at four different aspect ratios 0.2, 0.4, 0.6 and 0.8.

The error in different parts of the machine that neglects the rotational field effect can be around 50 % obtained in the SRM using M36G29 at 60 Hz.

Future work and research trends are concentrated towards building an accurate model of rotational core loss. In addition, more materials with different gauges should be investigated in order to build a rotational core loss database.

5. ROTATIONAL CORE LOSS MEASUREMENTS IN CLOCKWISE AND COUNTERCLOCKWISE DIRECTIONS

5.1 Introduction

The interest in measurement and characterization of rotational core losses in electrical machine laminations has increased. This interest includes developing measurement instrumentation, modeling, and efforts to explain physical phenomena in the magnetic materials under rotating fields [63] and [64]. One of the problems which was reported during the measurement of rotational core loss is a difference in loss characteristics obtained under CW and CCW rotating field directions. The need for rotational core loss estimation in CW and CCW conditions rests on the fact that the stators of many AC machines are subjected to a reverse rotating magnetic field when the machine changes its rotating direction. An understanding of the losses as a function of direction can provide important insight on machine design.

5.2 The Inconsistency between the CW and CCW Rotational Core Losses

From the literature it is hypothesized that the inconsistency between the CW and CCW rotational core losses is attributed to many reasons (a) Sensors misalignment installation (b) Cross talk voltage between the Hx and Hy sensors (c) Distortion on the connecting wires and (d) the crystal anisotropy effects of the magnetic material.

A. Sensor misalignment installation

The possibility of misalignment between the excitation axis and the sensor axis, or the

sensors are not being orthogonal to each other causes a measurement error. Two sensor pairs are used in the field-metric method, one pair for measuring \mathbf{B} and the other for measuring \mathbf{H} .

A.1 Misalignments in \mathbf{H} sensors

Using the 2-D Rogowski-Chattock potentiometer requires special attention to the structural installation, because it is difficult to place them exactly perpendicular to each other. Attempts to compensate for the misalignment error are dissatisfactory at high fluxes where the problem of CW and CCW appears [65]. Measuring \mathbf{H} by using the tangential coil sensors wound around the same non-magnetic former guarantees better orthogonality between the sensors [66], but the problem of misalignment between the sensor axis and the field excitation axis is still there, in addition the inner wound coil does not touch the sample surface which causes another source of error.

In this new test fixture, two thin flat 240-turn coils wound on a Plexiglas former are used to measure the tangential components of magnetic field strength \mathbf{H} , one over the sample for sensing H_x , and the other under it for H_y . This separation of coils each on its own frame gives better placement of the coil on the sample surface. Two grooves are cut into the fixture frame using the CNC machine to place the formers in their correct places. Thus, axis alignment is confirmed.

A.2 Misalignments in \mathbf{B} sensors

There is a possibility of misalignments in \mathbf{B} coils during the process of threading the coils

through the holes, see Fig. 5.1. For a typical coil width of 20 mm, 0.3 mm hole diameter, and a wire of 0.1 mm diameter the worst misalignments angle ζ will be 0.573° [67]. The misalignments angle is given by:

$$\zeta = \tan^{-1}\left(\frac{h}{r}\right) \quad (5.1)$$

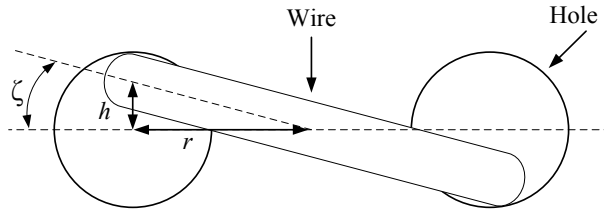


Fig. 5.1: The misalignment of **B** coil during the threading process.

In this novel design test fixture, the coil width is much higher (180 mm) and it is wrapped around the sample into two blocks as shown in chapter 2, where the simulation results prove high uniformity of flux density distribution within the sample and there is no need to drill holes in the middle area [68]. This provides three advantages (a) The tangential coils can be attached directly to the surface, but in prior designs the **B** coils were in between the **H** coil and the sample. (b) Avoidance of drilling holes maintains better magnetic characteristic of the sample. (c) Higher coil width decreases the chance of misalignments, where the worst case becomes ineffective (0.178°).

B. Cross talk voltage between Hx and Hy sensors

As many fixture designs use both **H** coils wound on the same plastic former, cross talk voltage may affect the accuracy of measurements [67]. This design does not have this

problem since H coils are separate and placed far from each others.

C. Distortion on the connecting wires

Noise affects the output induced voltage from the tangential sensor (V_H), since the obtained signal is in the range of a hundred milli volts and the connecting wires environment is highly magnetized, thus any small error in the signal appears to be significant in the field strength H . To reduce the noise influence, the sensor terminals were twisted carefully and uniformly as seen in Fig. 5.2, which provides a magnetic field noise reduction. Even this problem is not effective on B coils, their terminals are twisted as well.

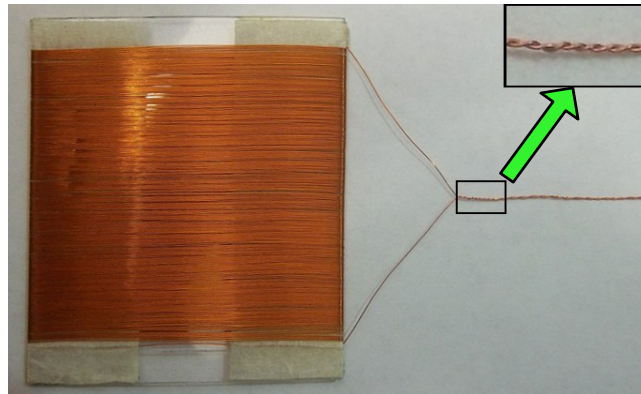


Fig. 5.2: Twisting terminals of H coil sensor.

D. The crystal anisotropy effect

The crystal anisotropy of the magnetic material contributes to the originating difference in the core loss based on the flux direction and the chemical composition of the material [69]. This difference becomes higher in grain oriented silicon steel material and still

considerable in non oriented samples [70]. The working mechanism has not been fully understood.

5.3 Results and Discussion

Measurements are performed under a circular rotating field, where both Halbach arrays are excited simultaneously by sinusoidal waveforms with a phase shift of 90° between them. The flux direction can be executed using many techniques, such as:

- (a) Turn over the sample, so the field is reversed inside the sample relative to the original placement, keeping the field rotating in the same direction inside the fixture gap.
- (b) Reversal of the current direction in one array is capable of changing the flux rotating direction.
- (c) Change the phase shift between the excitation input signals from 90° to -90° (or 270°).

Control the phase shift seems to be the most efficient way to change the direction of rotating field since it can be performed through the dSPACE software without any physical change in the circuit connection or sample replacement. Three non-oriented silicon steel samples have been employed in this study, which are referred to as M36G29, M19G24, and M15G29. Figs. 5.3, 5.4, and 5.5 show the rotational core losses in M36G29 sample at 1 kHz, 400 Hz, and 60 Hz respectively, where measured results present a comparison between losses in CW and CCW directions of rotating field. In general, the difference in CW and CCW losses becomes higher at high flux densities. By increasing the frequency the difference becomes less since the eddy current loss component which is

not affected by the field direction dominates at high frequencies. The percentage difference in rotational core losses in the CW and CCW directions for M36G29 sample can be seen in Fig. 5.6, where at the maximum possible flux density 1.4T the tests under 60 Hz, 400 Hz, and 1 kHz show differences of 80 % , 35 % , and 19 % respectively. The percentage difference curves tend to have a jump of variation at low flux density such as 0.1T. This jump can be clearly realized at 60 Hz where it reaches up to 39 %, and can be ascribed to the effect of distortion on the low level H coil voltage signal. Figs. 5.7, 5.8, and 5.9 show the rotational core losses in M19G24 silicon steel sample at 1 kHz, 400 Hz, and 60 Hz respectively, with a comparison between CW and CCW directions. The test with 1 kHz was limited to a maximum of 1.2T, where we could not go further because of power source limitations. Fig. 5.10 clarifies the percentage of error between rotational core losses in CW and CCW directions for the M19G24 sample. The difference in losses at 1 kHz is around 10 %, at 400 Hz is almost 9 % and then goes up to 29 %, and at 60 Hz the difference reaches 78 % at 1.4 T. It is noticed again an asymmetry in the percentage difference curve of 60 Hz at 0.1 T, where the difference is negative (-1.6 %) which means that the loss in the CW direction is higher than the loss in CCW direction at this point, this irregularity is caused by the high distortion on the voltage signal produced by the H coils. Figs. 5.11, 5.12, and 5.13 show the rotational core losses in M15G29 silicon steel sample in CW and CCW directions at 1 kHz, 400 Hz, and 60 Hz respectively. The percentage of error between rotational core losses in CW and CCW directions is presented in Fig. 5.14, where the difference at 1 kHz is around 7 %, and almost 10 % on average at 400 Hz. With 60 Hz, the difference reaches up to 59 % at 1.4T. The jumps in the error percentage curves at 0.1 T can be noticed.

To understand the magnetization behavior under rotating fields with different rotating directions, the measured dynamic hysteresis loops in the x and y directions are presented, where the loop enclosed area indicates the loss magnitude. Figs. 5.15, 5.16, 5.17, 5.18, 5.19, and 5.20 show the loops in the CW and CCW rotating field for M36G29 in the x and y directions under 1 kHz, 400 Hz, and 60 Hz respectively. It is seen that the difference is not only in the area but also in the cycle shape which becomes more noticeable at 60 Hz, where the loops experience an overlapping behavior. The mathematical evaluation of the enclosed area by the loop is affected by the function direction, *i.e.* the integration of the overlapped function results in a negative area. For example, in Fig. 5.19 the B_x-H_x loop in the CW direction at 60 Hz has a loss of 4.1247 W/kg, while the B_x-H_x loop in CCW is 0.0949 W/kg, this significant decrease in loss is attributed to the overlapping in the loop. The more interesting behavior can be seen in the B_y-H_y loop in the CW direction in Fig. 5.20, where the overlapping increases and the cycle changes its direction, thus the two overlapped small enclosed areas on the edges exhibit positive power and the inside closed part exhibits negative power, as a result the total area is negative and equal to -1.1672 W/kg. Figs. 5.21, 5.22, 5.23, 5.24, 5.25, and 5.26 show the loops in the CW and CCW rotating field for M19G24 in the x and y directions under 1 kHz, 400 Hz, and 60 Hz respectively. The loops at 1 kHz and 400 Hz offer more similarity in the CW and CCW directions, which means lower difference in CW and CCW losses. The difference in core loss is lower in thicker samples at high frequency (thickness of M19G24 is 0.635 mm, and M36G29 thickness is 0.3556 mm) because of the effect of eddy currents, which means greater similarity between the dynamic hysteresis loops in the CW and CCW directions.

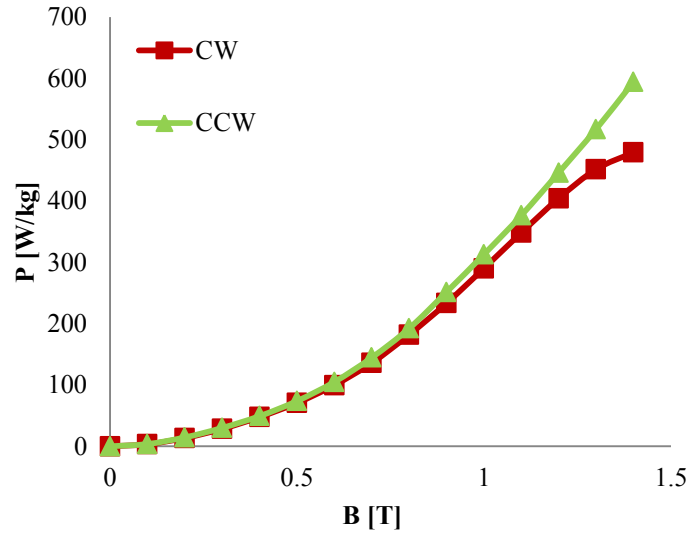


Fig. 5.3: Rotational core losses in M36G29 sample at 1 kHz, in CW and CCW directions.

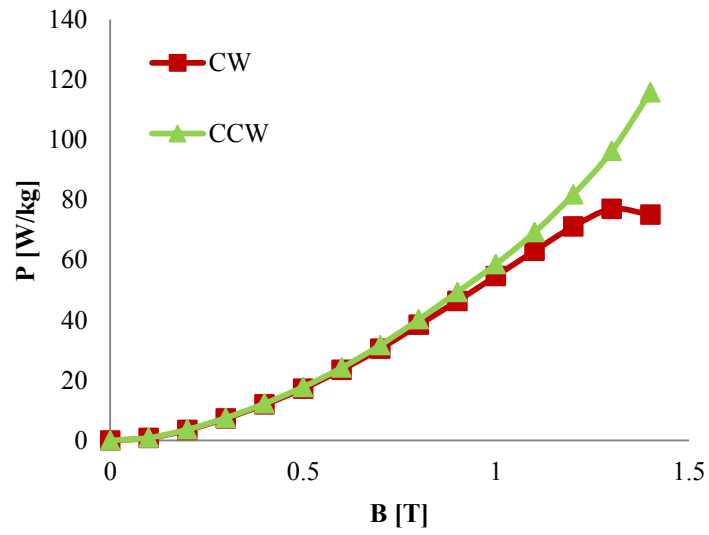


Fig. 5.4: Rotational core losses in M36G29 sample at 400 Hz, in CW and CCW directions.

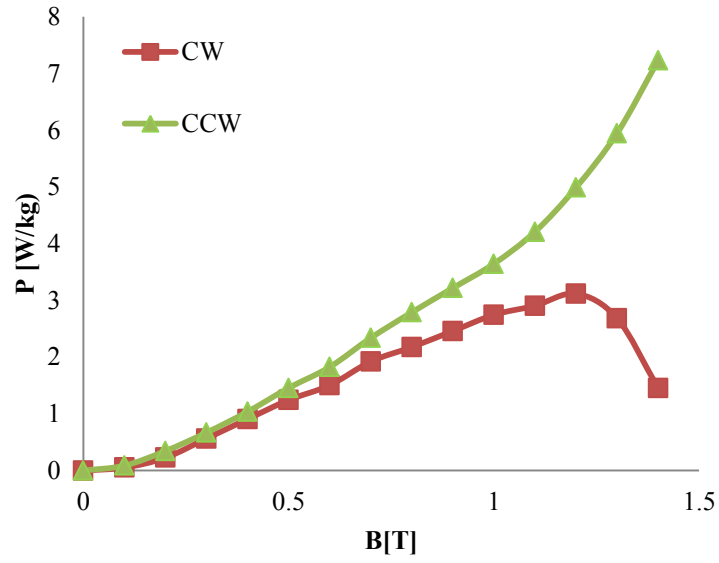


Fig. 5.5: Rotational core losses in M36G29 sample at 60 Hz, in CW and CCW directions.

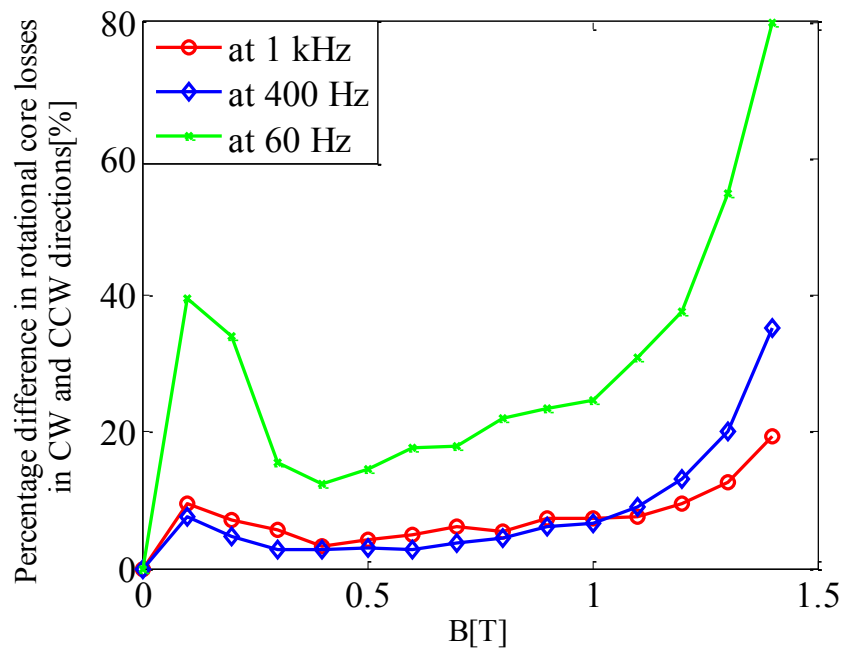


Fig. 5.6: Percentage of error between rotational core losses in CW and CCW directions for M36G29 sample.

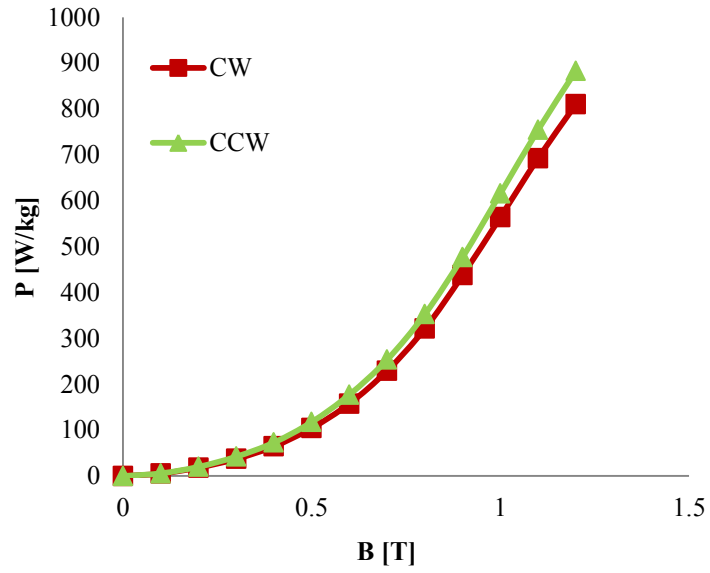


Fig. 5.7: Rotational core losses in M19G24 sample at 1 kHz, in CW and CCW directions.

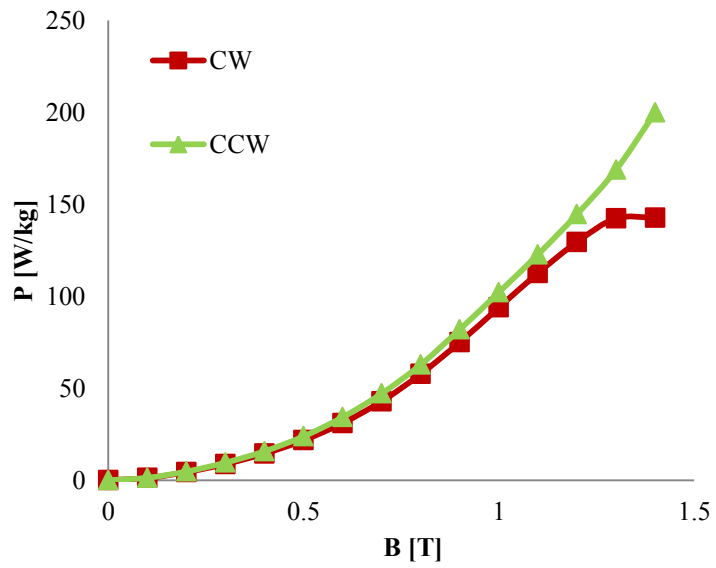


Fig. 5.8: Rotational core losses in M19G24 sample at 400 Hz, in CW and CCW directions.

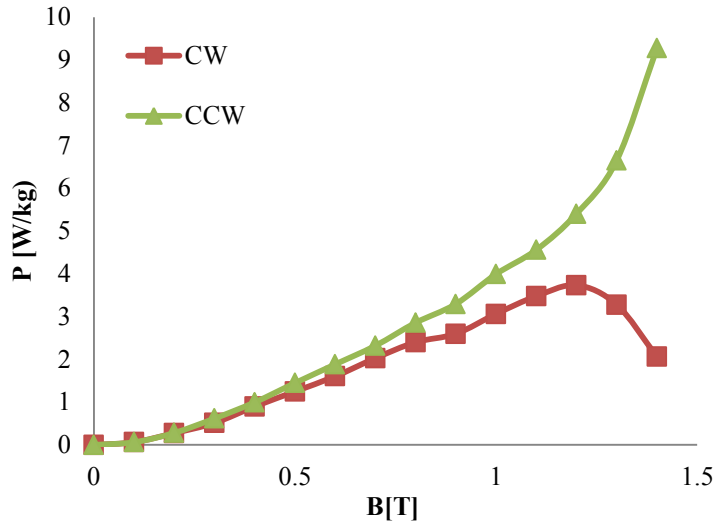


Fig. 5.9: Rotational core losses in M19G24 sample at 60 Hz, in CW and CCW directions.

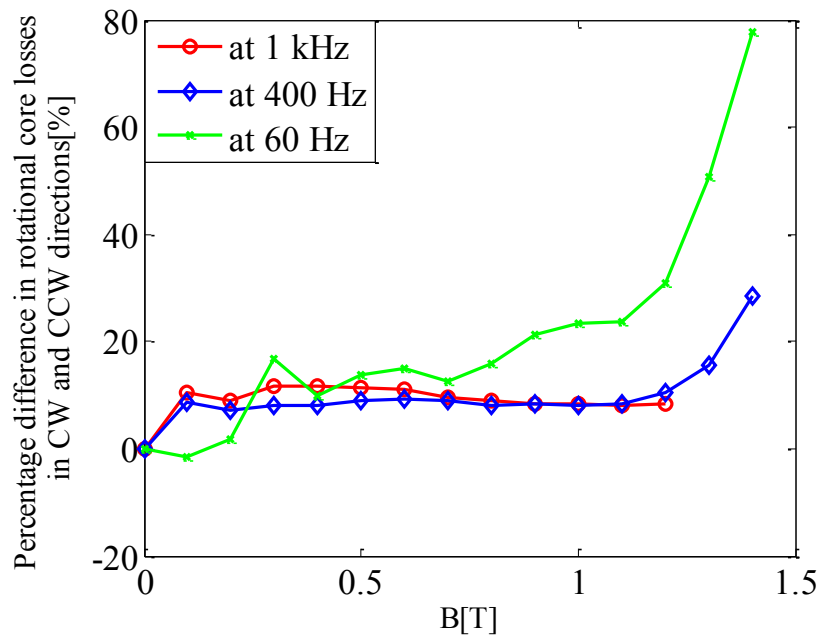


Fig. 5.10: Percentage of error between rotational core losses in CW and CCW directions for M19G24 sample.

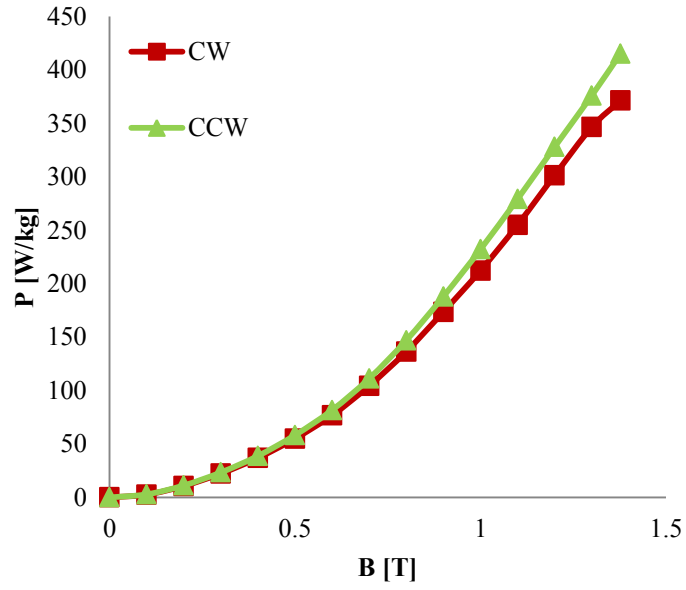


Fig. 5.11: Rotational core losses in M15G29 sample at 1 kHz, in CW and CCW directions.

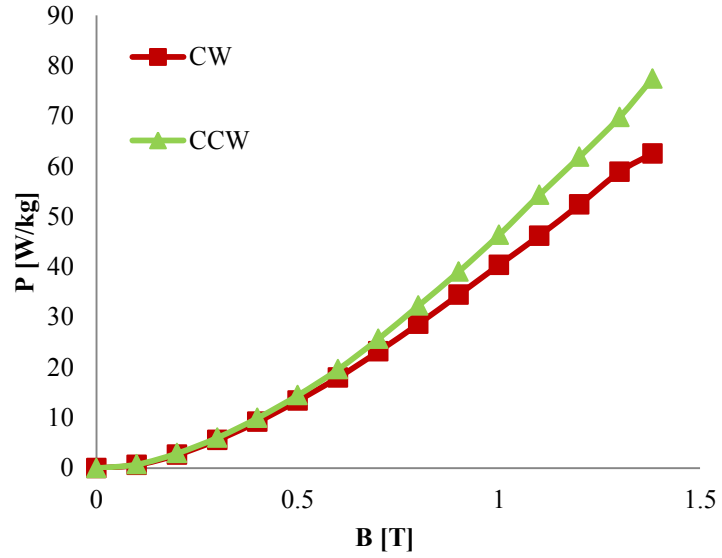


Fig. 5.12: Rotational core losses in M15G29 sample at 400 Hz, in CW and CCW directions.

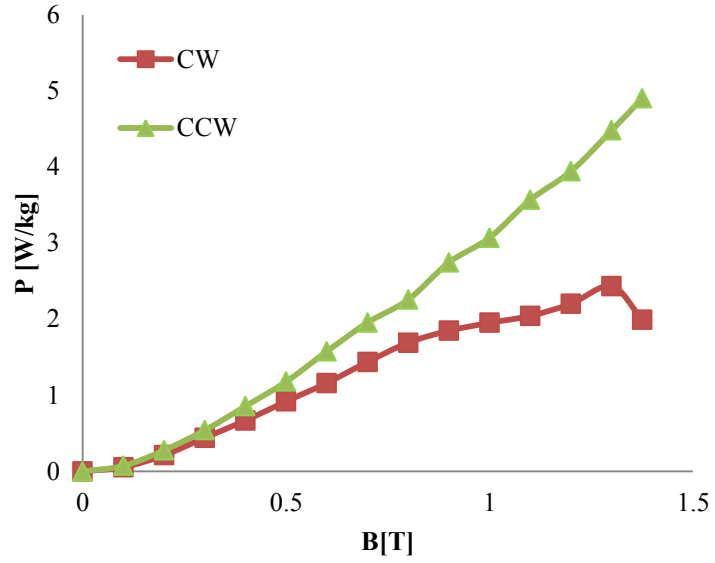


Fig. 5.13: Rotational core losses in M15G29 sample at 60 Hz, in CW and CCW directions.

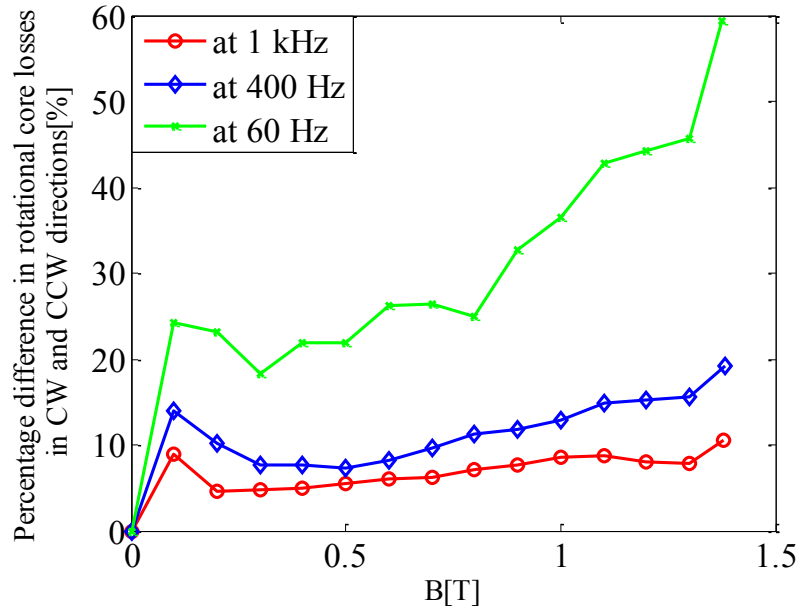


Fig. 5.14: Percentage of error between rotational core losses in CW and CCW directions for M15G29 sample.

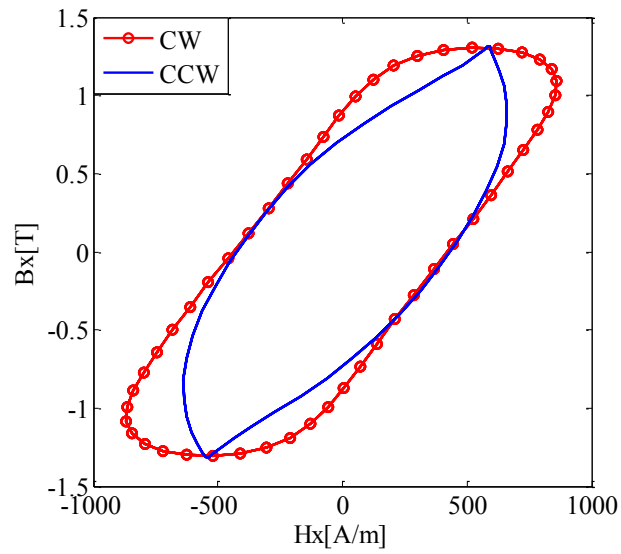


Fig. 5.15: The x -component measured dynamic hysteresis loops in CW and CCW directions for M36G29 sample under 1.3T rotating field with 1 kHz.

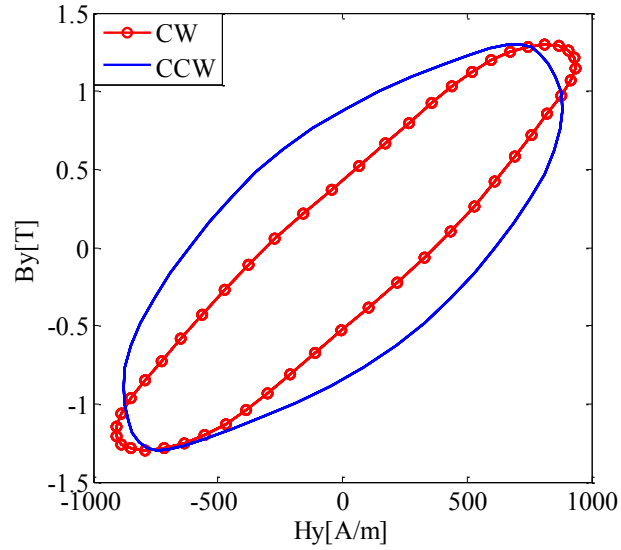


Fig. 5.16: The y -component measured dynamic hysteresis loops in CW and CCW directions for M36G29 sample under 1.3T rotating field with 1 kHz.

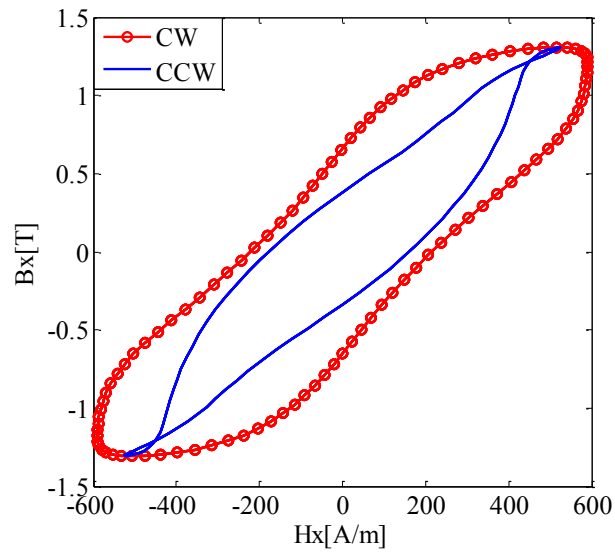


Fig. 5.17: The x -component measured dynamic hysteresis loops in CW and CCW directions for M36G29 sample under 1.3T rotating field with 400 Hz.

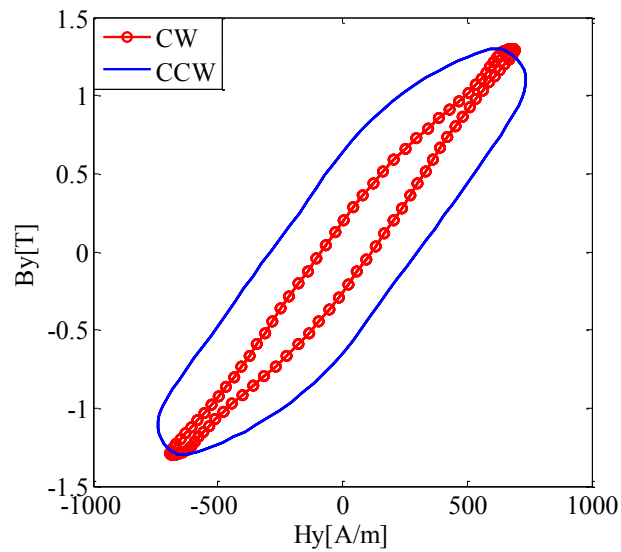


Fig. 5.18: The y -component measured dynamic hysteresis loops in CW and CCW directions for M36G29 sample under 1.3T rotating field with 400 Hz.

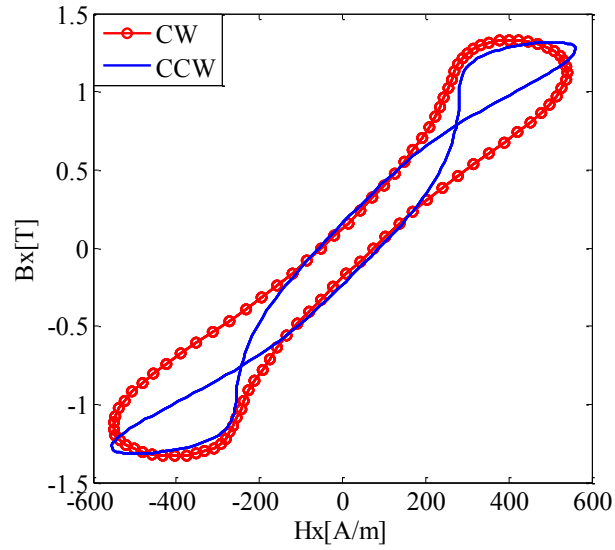


Fig. 5.19: The x -component measured dynamic hysteresis loops in CW and CCW directions for M36G29 sample under 1.3T rotating field with 60 Hz.

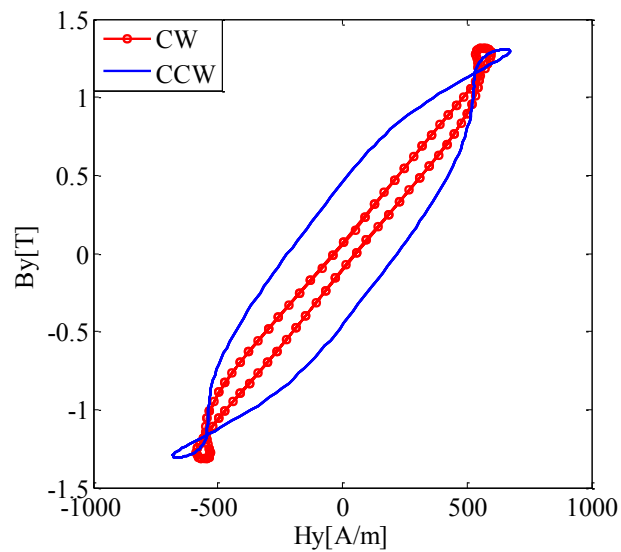


Fig. 5.20: The y -component measured dynamic hysteresis loops in CW and CCW directions for M36G29 sample under 1.3T rotating field with 60 Hz.

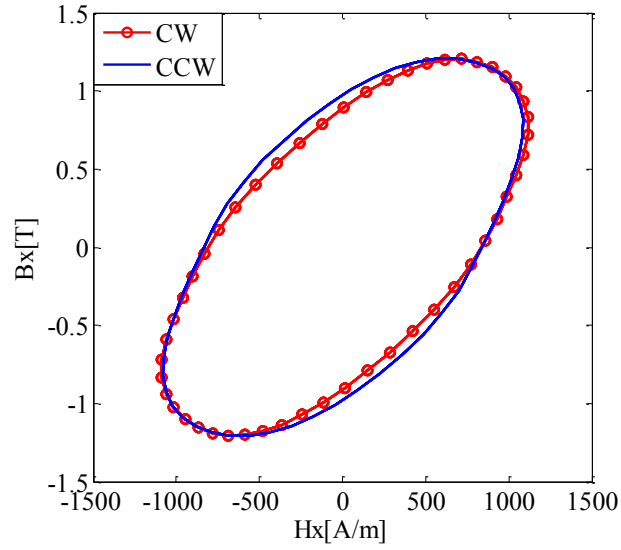


Fig. 5.21: The x -component measured dynamic hysteresis loops in CW and CCW directions for M19G24 sample under 1.2T rotating field with 1 kHz.

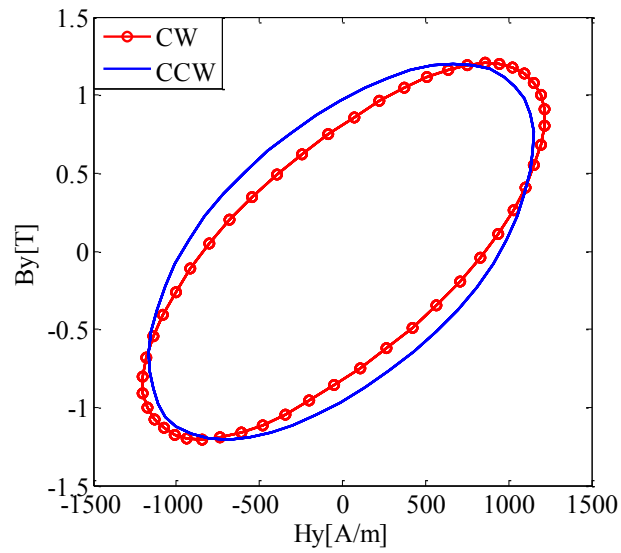


Fig. 5.22: The y -component measured dynamic hysteresis loops in CW and CCW directions for M19G24 sample under 1.2T rotating field with 1 kHz.

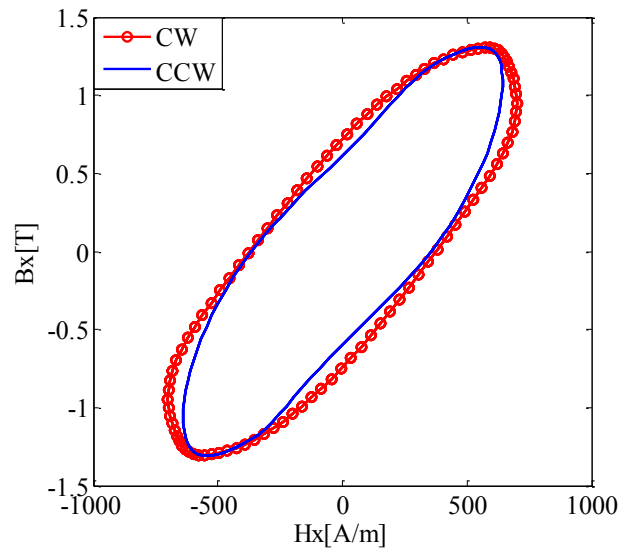


Fig. 5.23: The x -component measured dynamic hysteresis loops in CW and CCW directions for M19G24 sample under 1.3T rotating field with 400 Hz.

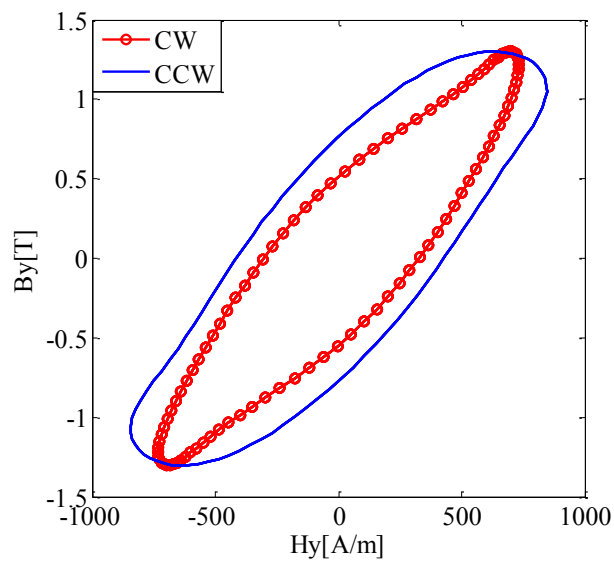


Fig. 5.24: The y -component measured dynamic hysteresis loops in CW and CCW directions for M19G24 sample under 1.3T rotating field with 400 Hz.

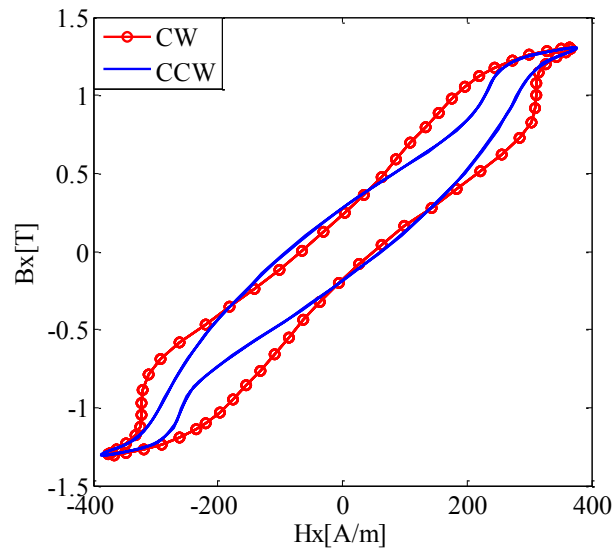


Fig. 5.25: The x -component measured dynamic hysteresis loops in CW and CCW directions for M19G24 sample under 1.3T rotating field with 60 Hz.

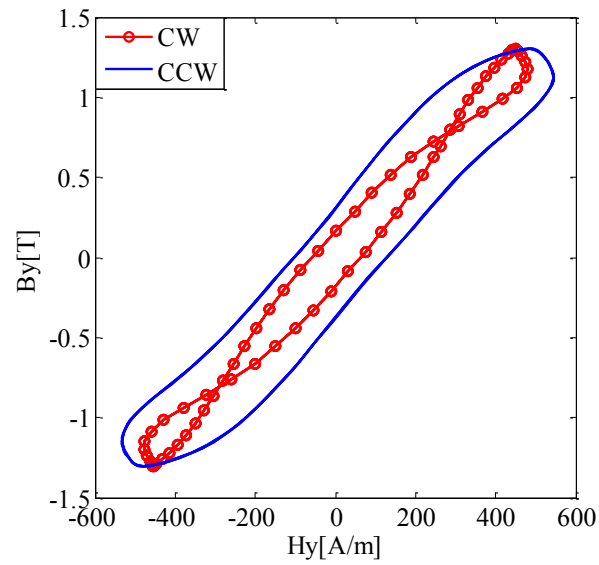


Fig. 5.26: The y -component measured dynamic hysteresis loops in CW and CCW directions for M19G24 sample under 1.3T rotating field with 60 Hz.

5.4 Permeability Asymmetry in CW and CCW Directions

An interpretation of the difference between core losses under CW and CCW rotating field is the asymmetry in the material permeability, where the permeability of the magnetic material tends to vary with changing the flux direction. In chapter 3, the study disclosed that the permeability depends strongly on the direction of pulsating field, and on the status of the flux whether it is pulsating or rotating. This variation in the permeability is reflected on the core loss value, whereas the x -component loss in the rotating field differs from the x -direction pulsating field, and also the y -component loss in the rotating field differs from the y -direction pulsating field, at the same flux density level. The more interesting phenomenon occurred in the sample under test is the difference between the x - loss components (and y -component as well) of rotating field when the field changes its rotation direction. For example, Fig. 5.27 and Fig. 5.28 show the rotational core losses at 60 Hz for M15G29 sample in the CW and CCW directions respectively, with the corresponding x and y components. This difference between losses on the same components is ascribed to the differences in the permeability, where a new permeability notation should be defined with reference to the rotating field direction. The x -component permeability under CW rotating field is μ_{xrcw} , and the y -component permeability under CW rotating field is μ_{yrcw} . The percentage differences in permeability between x and y components are calculated for the M15G29 sample in CW and CCW rotating field directions at three different frequencies 60 Hz, 400 Hz, and 1 kHz, as presented in Table 5.1. Results show that the percentage permeability difference between the x and y directions in the case of CW is mostly higher than CCW rotating field.

The relative permeability under rotating field can be evaluated as:

$$\mu = \begin{cases} \mu_x = \frac{B_x}{\mu_o H_x}, \text{in } x\text{-direction} \\ \mu_y = \frac{B_y}{\mu_o H_y}, \text{in } y\text{-direction} \end{cases} \quad (5.2)$$

Where, the μ_x is the permeability in the x direction, and μ_y is the permeability in the y direction. Figs. 5.29, 5.30, 5.31, 5.32, 5.33, and 5.34 show the relative permeability under CW and CCW rotating fields in the x and y directions for M15G29 sample with 60 Hz, 400 Hz, and 1 kHz respectively. It is noticed clearly that the permeability in the x direction is always lower at CW direction compared with the permeability at CCW direction, while in the y direction the permeability is always higher at CW direction compared with the permeability at CCW direction. By increasing the frequency the permeability becomes lower, and also the difference in permeability in CW and CCW directions tends to be lower as shown in Table 5.1. Higher permeability produces lower core loss. The above results manifest that the anisotropy of the magnetic material is responsible for the asymmetry in the CW and CCW rotational core losses, where the permeability varies significantly when the direction of rotating field is reversed.

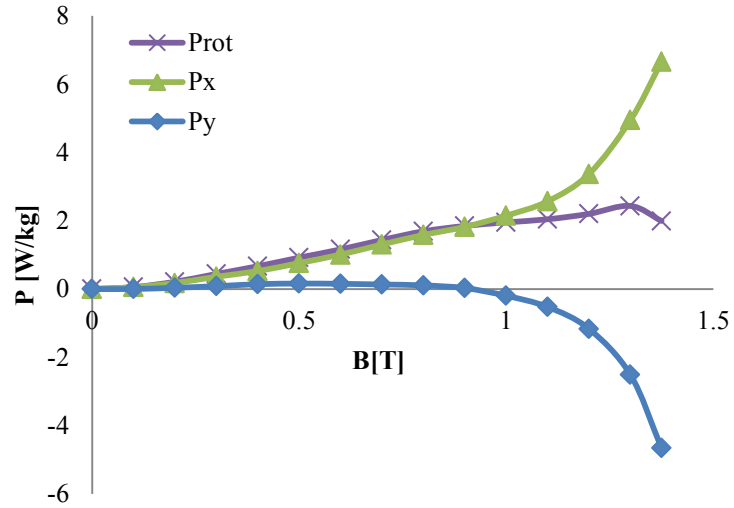


Fig. 5.27: The total rotational core loss under CW rotating field at 60 Hz, in M15 steel Gauge 29, with the corresponding x and y components, Px and Py respectively.

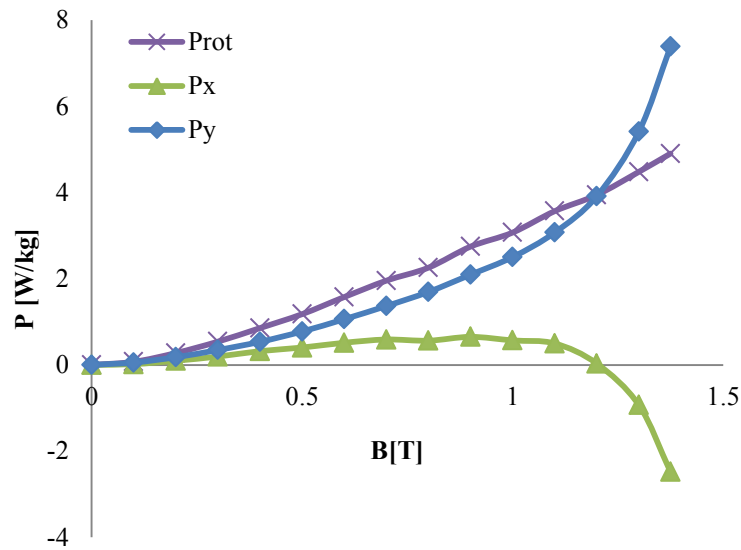


Fig. 5.28: The total rotational core loss under CCW rotating field at 60 Hz, in M15 steel Gauge 29, with the corresponding x and y components, Px and Py respectively.

Table 5.1: The percentage permeability difference between the x and y directions in the case of CW and CCW rotating field

B [T]	60 Hz		400 Hz		1 kHz	
	CW [%]	CCW [%]	CW [%]	CCW [%]	CW [%]	CCW [%]
0.2	33.22	15.44	30.43	17.48	33.81	23.82
0.3	46.21	16.46	30.94	17.81	36.52	21.35
0.4	40.28	6.35	34.52	16.59	33.13	23.71
0.5	49.60	11.73	38.47	17.85	35.80	19.29
0.6	56.24	7.43	39.99	15.10	34.63	20.77
0.7	57.92	10.86	44.01	13.47	36.60	17.62
0.8	54.69	24.72	45.98	9.08	29.97	15.19
0.9	52.51	22.74	47.18	8.61	31.67	7.87
1.0	47.08	32.77	50.09	12.13	29.61	2.63
1.1	41.03	35.15	49.35	16.73	31.35	0.075
1.2	35.54	41.87	44.50	27.59	34.91	5.42
1.3	39.58	42.74	42.74	38.68	38.26	22.75

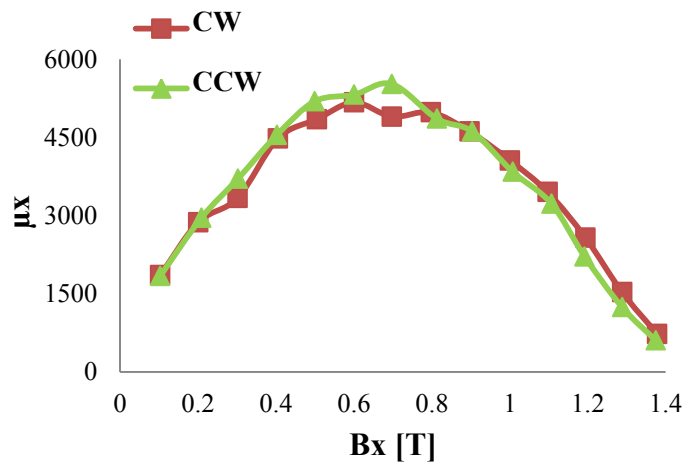


Fig. 5.29: The relative permeability in the x direction as a function of magnetic flux density for M15G29 sample under CW and CCW rotating field with 60 Hz.

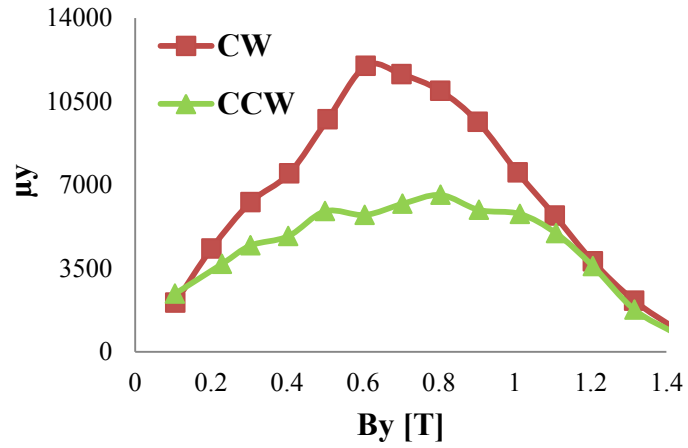


Fig. 5.30: The relative permeability in the y direction as a function of magnetic flux density for M15G29 sample under CW and CCW rotating field with 60 Hz.

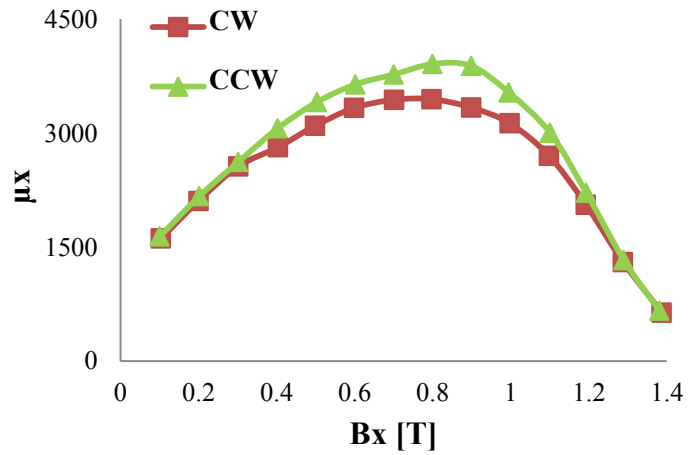


Fig. 5.31: The relative permeability in the x direction as a function of magnetic flux density for M15G29 sample under CW and CCW rotating field with 400 Hz.

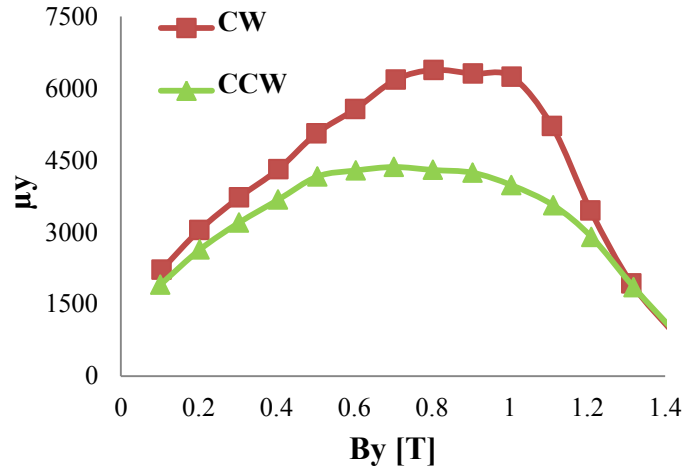


Fig. 5.32: The relative permeability in the y direction as a function of magnetic flux density for M15G29 sample under CW and CCW rotating field with 400 Hz.

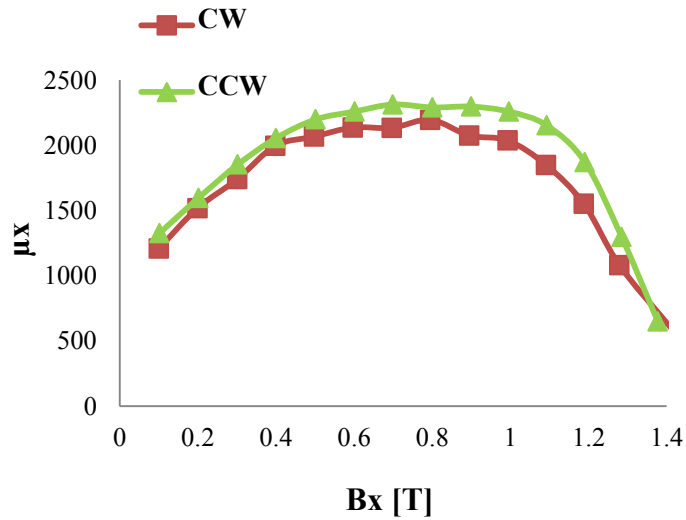


Fig. 5.33: The relative permeability in the x direction as a function of magnetic flux density for M15G29 sample under CW and CCW rotating field with 1 kHz.

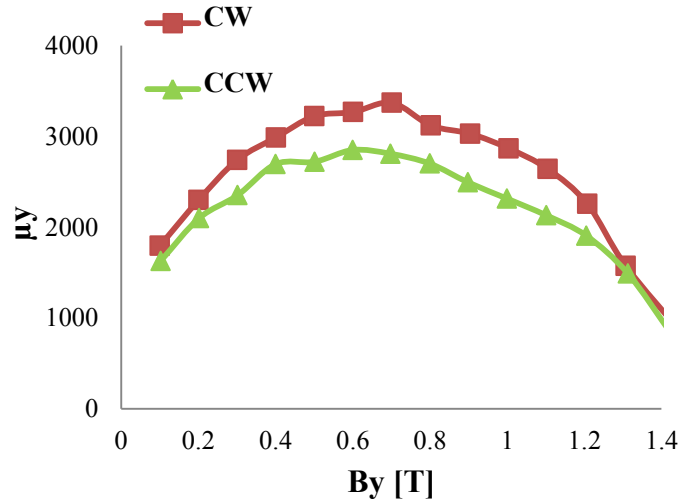


Fig. 5.34: The relative permeability in the y direction as a function of magnetic flux density for M15G29 sample under CW and CCW rotating field with 1 kHz.

5.5 The Influence on Rotating Machines

5.5.1 Simulations

Three types of machines, 2-pole induction machine (IM), 6-4 switched reluctance motor (SRM), and 2-pole brush less DC machine (BLDC) are chosen to investigate the effect of reversing the rotating field direction on the delivered core loss in the stator. The methodology of characterizing the flux density distribution and flux density patterns is explained in chapter 4. Unfortunately, the simulations under different direction of fields give the same distribution results in the machine core, where the anisotropy effect is not considered in current software. Simulation results show that the rotating field with high aspect ratio is concentrated mostly at the tooth roots, which means higher core losses are produced in these regions. During the machine operation, the flux rotates in the same

direction in all parts of the stator. To confirm the agreement of rotation direction of the flux density vectors, rotation directions are explored in all mesh elements located exactly at the tooth roots of BLDCM. Results in two mesh elements facing each other (points a and b) are seen in Fig. 5.35. Since B_x lags B_y in both points, the flux density vector rotates in CW direction.

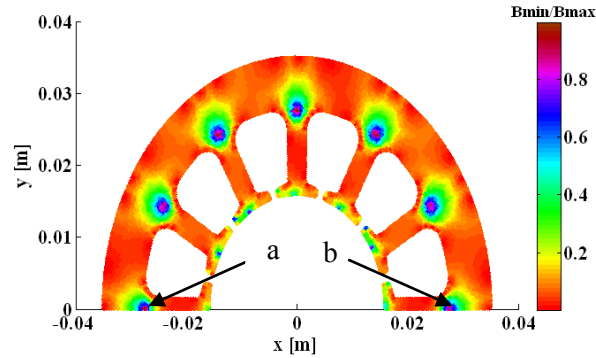


Fig. 5.35: The aspect ratio distribution in the stator of a 2-pole BLDCM, where the two mesh elements facing each other are shown at points (a) and (b)

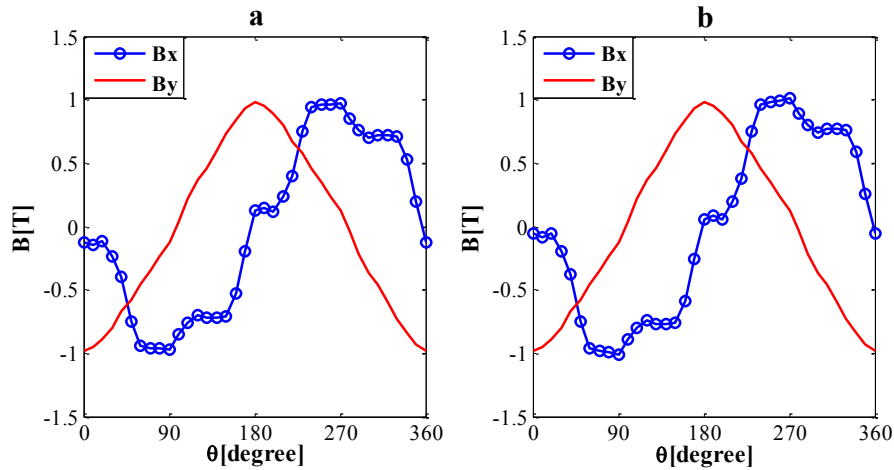


Fig. 5.36: The flux density waveforms (B_x and B_y) in two mesh elements located exactly at the tooth roots of BLDCM. (a) At mesh element located at point a. (b) At mesh element located at point b. Referral points are depicted in Fig. 5.35.

5.5.2 Experimental Results

Tests were performed on a M36G29 sample at three different frequencies 60 Hz, 400 Hz, and 1 kHz. The sample was subjected to CW and CCW rotating fields with aspect ratios of 0.2, 0.4, 0.6, 0.8, and 1, in addition to the pulsating field with aspect ratio of 0. Two sets of data were obtained, one is the losses under CW rotating field, as seen before in Figs. 4.13, 4.15, and 4.17, and the other is losses under CCW rotating field, as seen in Figs. 5.37, 5.38, and 5.39. Each set is applied individually to the machine models. Two parameters can be addressed for each mesh element from the simulations results, the aspect ratio of the flux density locus and the maximum vector magnitude.

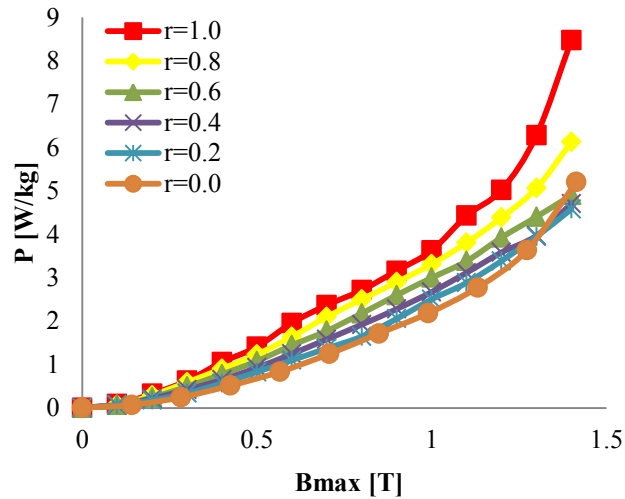


Fig. 5.37: The rotational core losses in the CCW direction with different aspect ratios compared with pulsating loss (aspect ratio=0) at 60 Hz for M36G29.

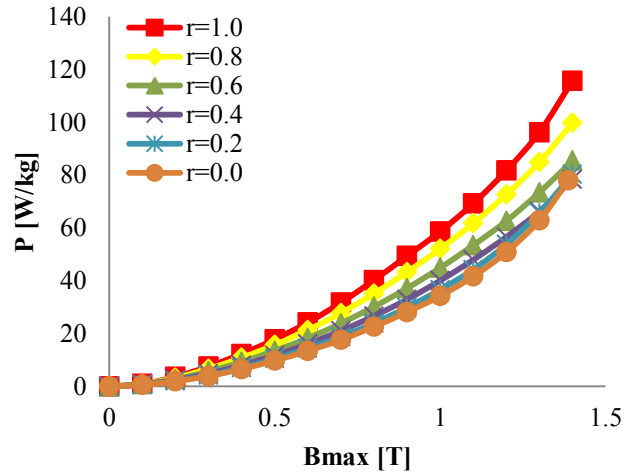


Fig. 5.38: The rotational core losses in the CCW direction with different aspect ratios compared with pulsating loss (aspect ratio=0) at 400 Hz for M36G29.

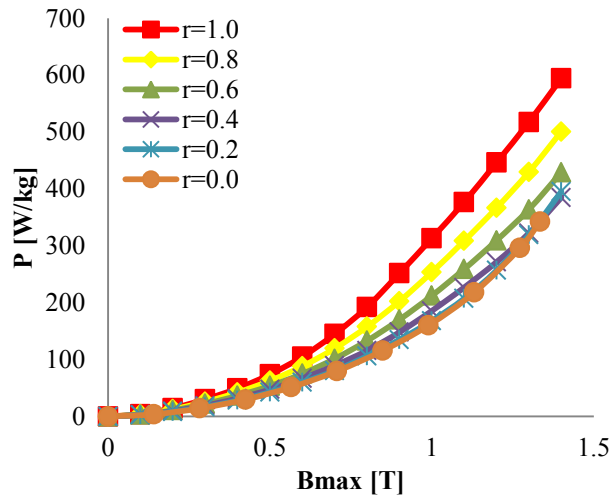


Fig. 5.39: The rotational core losses in the CCW direction with different aspect ratios compared with pulsating loss (aspect ratio=0) at 1 kHz for M36G29.

Using a MATLAB[®] subroutine the aspect ratios of all mesh elements are classified into five sets from 0 to 1 in steps of 0.2. The experimental loss curves can be fed to FE simulation map, where each mesh element belongs to a loss curve and the loss value can be determined on the curve by the maximum value of flux density vector. As a consequence, an experimental loss value which is picked up from the loss curve can be assigned to the mesh element.

The overall power loss in the stator lamination is estimated by considering the weight of each mesh element and the effect of its power loss in the whole stator area using the following equation:

$$Power = \frac{I}{A} \sum_{n=1}^N P_n A_n \quad (5.3)$$

Where, A is total area of the stator and is $\sum_{n=1}^N A_n$, P_n is the power loss in mesh element n , A_n is the area of the mesh element n , and N is the total number of mesh elements.

The flowchart in Fig. 5.40 summarizes the procedure of power loss estimation in the machine stator lamination. Fig. 5.41 shows the power loss distribution in [W/kg] considering the rotational core losses in the stator of a 2-pole induction machine using M36G29 laminations at 60 Hz, and under a CW rotating field. The high loss is concentrated at the back of the slots despite of the rotating field with high aspect ratios condenses at the teeth roots. A general view of the color map loss distribution shows higher loss produced in the stator yoke compared with the stator teeth. Fig. 5.42 shows the loss distribution under a CCW rotating field, where the loss reaches higher levels with a maximum of 4.581 W/kg compared with 3.3827 W/kg in the case of CW direction. By

increasing the frequency to 400 Hz, the loss levels increased within the stator and the CCW case remains handling a higher loss of a maximum of 70.8439 W/kg compared with 80.279 W/kg in the case of CW rotation, as seen in Fig. 5.43 and Fig. 5.44. At 1 kHz, the losses are increased significantly because of the domination of the eddy current loss component where the loss maximum is 395.397 W/kg and 381.01 W/kg in CCW and CW rotating fields, respectively, as seen in Fig. 5.45 and Fig. 5.46.

Figs. 5.47, 5.48, 5.49, 5.50, 5.51, and 5.52 illustrate the power loss distribution in [W/kg] considering the rotational core losses in the stator of a 2-pole BLDCM using M36G29 laminations at 60 Hz, 400 Hz, and 1 kHz, under CW and CCW rotating fields. Despite the high aspect ratios rotating field is appeared mainly in the teeth roots, the highest power loss is produced basically in some teeth because of the effects of the magnetic field generated by the permanent magnets of rotor. At higher frequencies, 400 Hz and 1 kHz, the losses become higher and the CCW rotating field case keeps achieving higher loss compared with CW rotating field case.

Figs. 5.53, 5.54, 5.55, 5.56, 5.57, and 5.58 show the power loss distribution in [W/kg] considering the rotational core losses in the stator of a 6-4 SRM using M36G29 laminations at 60 Hz, 400 Hz, and 1 kHz, under CW and CCW rotating field. The higher power loss in the stator laminations is found at the edges of the machine. These high loss spots are expected because of high magnetization at sharp corners which were avoided in the prior IM and BLDCM model designs. Moreover, the poles separate the yoke to four parts in terms of power loss distribution as can be distinguished in the color maps. The left upper part achieves the higher loss, followed by the upper right one. Both the left

lower and right lower parts have the same loss distribution with less loss values compared with the higher parts. This non uniformity in loss distribution between the yoke parts is related to the different flux density waveforms attained in the yoke parts. The same observations of higher loss in the CCW rotating field over the CW rotating field are revealed with lower difference compared in the case of IM and BLDCM. At 1 kHz, the overall power loss reaches 110.8762 W/kg with the CCW field compared with 110.2646 W/kg with the CW field.

Table 5.2 presents the power loss for the three different machine types using M36G29 lamination with CW and CCW rotating field, with three different frequencies, 60 Hz, 400 Hz, and 1 kHz. The percentage relative error is calculated between the overall losses produced in the machine lamination in the CW and CCW rotating field direction. A comparison between the machine types show that the IM experiences the highest effect of field reversal followed by the BLDCM, and then the SRM is least affected. Results show a noticeable difference in loss between CW and CCW cases at low frequency, where the difference in loss between the CW and CCW cases in the IM at 60 Hz comes up with an error of 9.66 %. At high frequencies, the difference becomes smaller and is 1.44 %, 1.06 %, and 0.55 % in IM, BLDCM, and SRM respectively.

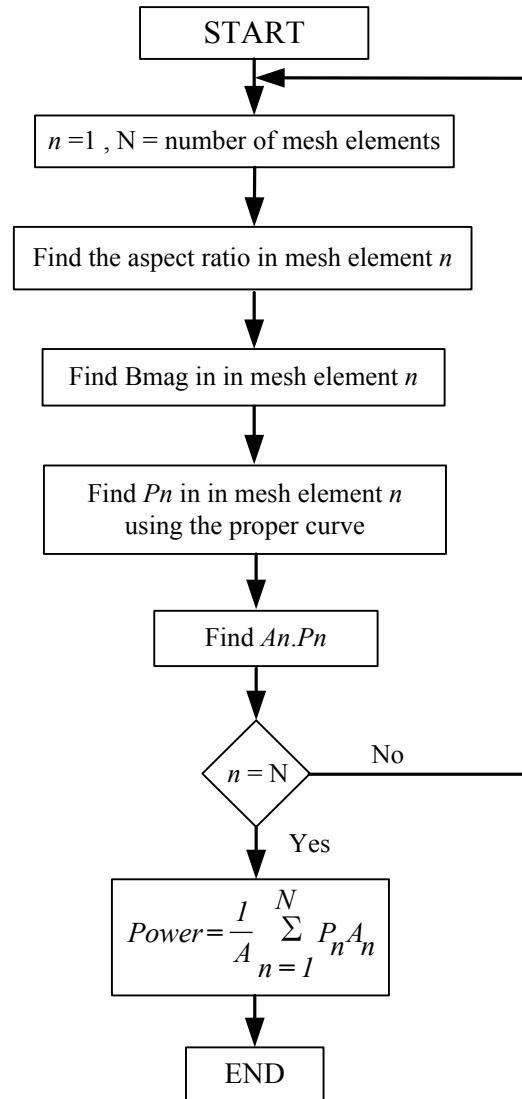


Fig. 5.40: Flowchart of determination the all over error in the machine when considering the effect of rotating field compared with considering the whole flux pulsating.

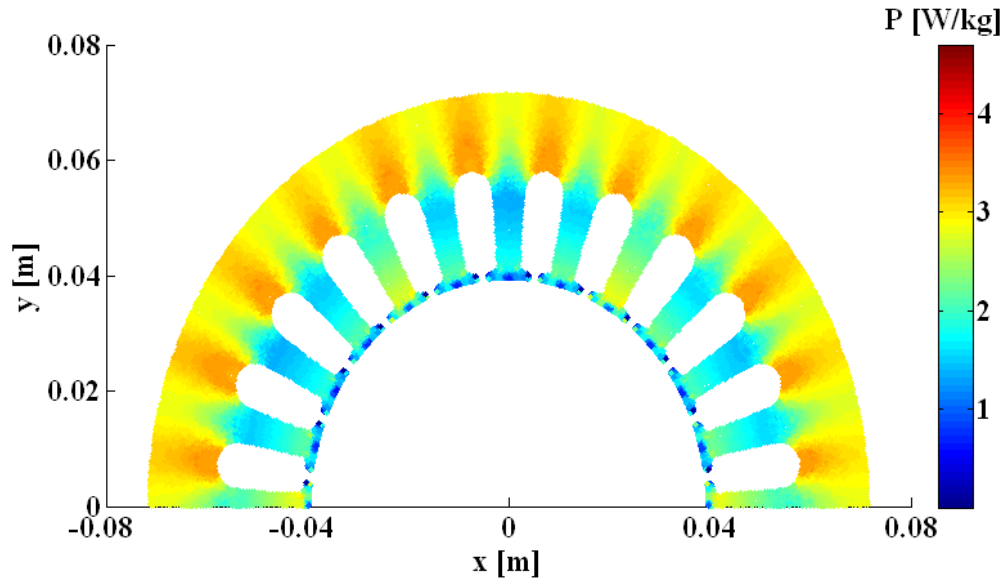


Fig. 5.41: The power loss distribution in $[W/kg]$ considering the rotational core losses in the stator of a 2-pole IM using M36G29 laminations at 60 Hz, and under a CW rotating field.

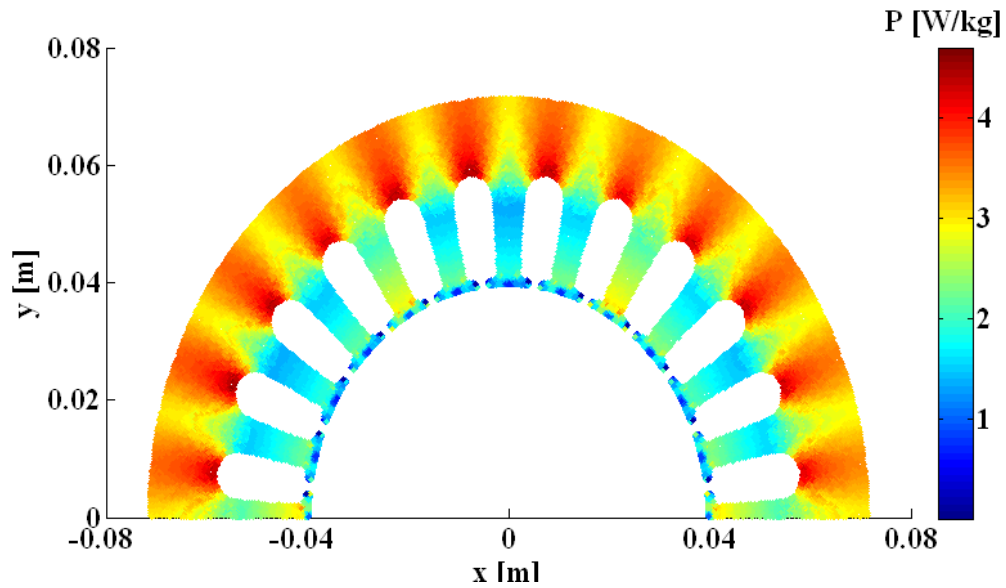


Fig. 5.42: The power loss distribution in $[W/kg]$ considering the rotational core losses in the stator of a 2-pole IM using M36G29 laminations at 60 Hz, and under a CCW rotating field.

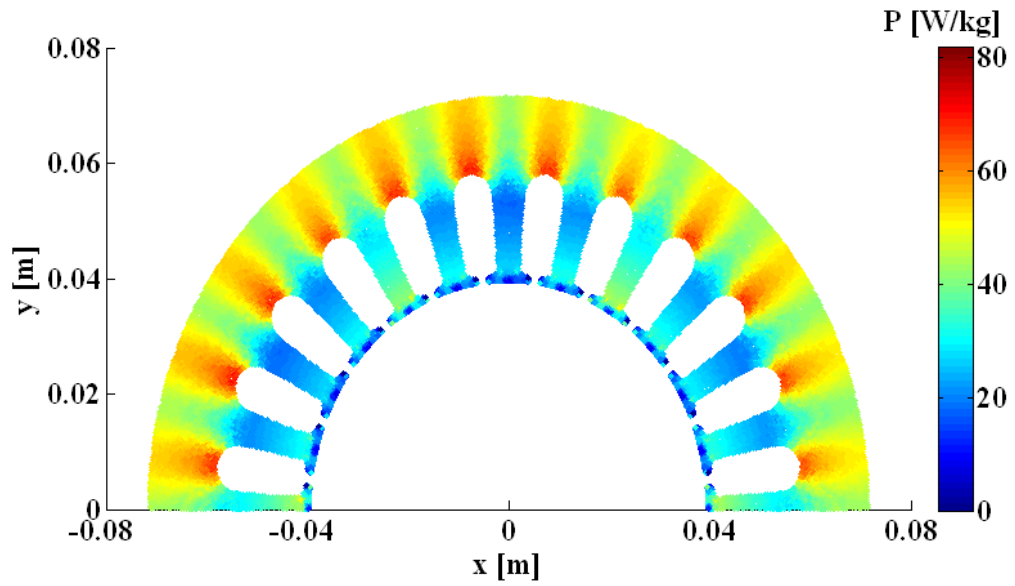


Fig. 5.43: The power loss distribution in [W/kg] considering the rotational core losses in the stator of a 2-pole IM using M36G29 laminations at 400 Hz, and under a CW rotating field.

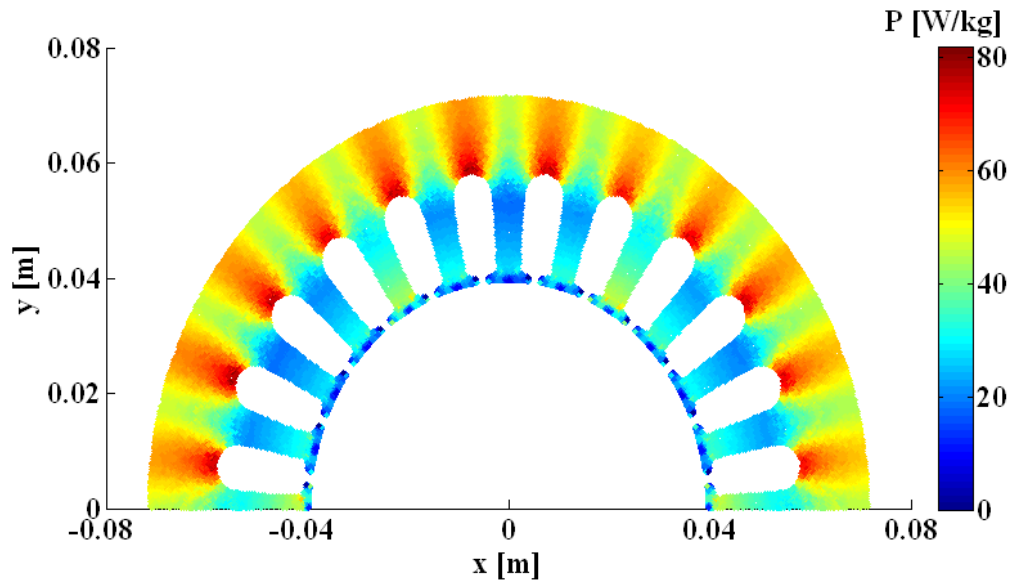


Fig. 5.44: The power loss distribution in [W/kg] considering the rotational core losses in the stator of a 2-pole IM using M36G29 laminations at 400 Hz, and under a CCW rotating field.

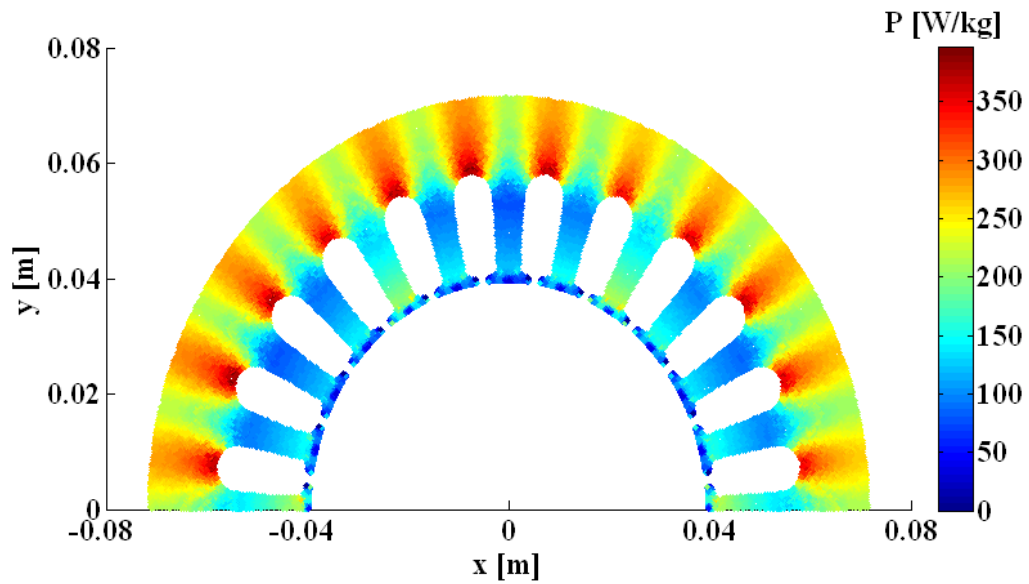


Fig. 5.45: The power loss distribution in $[W/kg]$ considering the rotational core losses in the stator of a 2-pole IM using M36G29 laminations at 1 kHz, and under a CW rotating field.

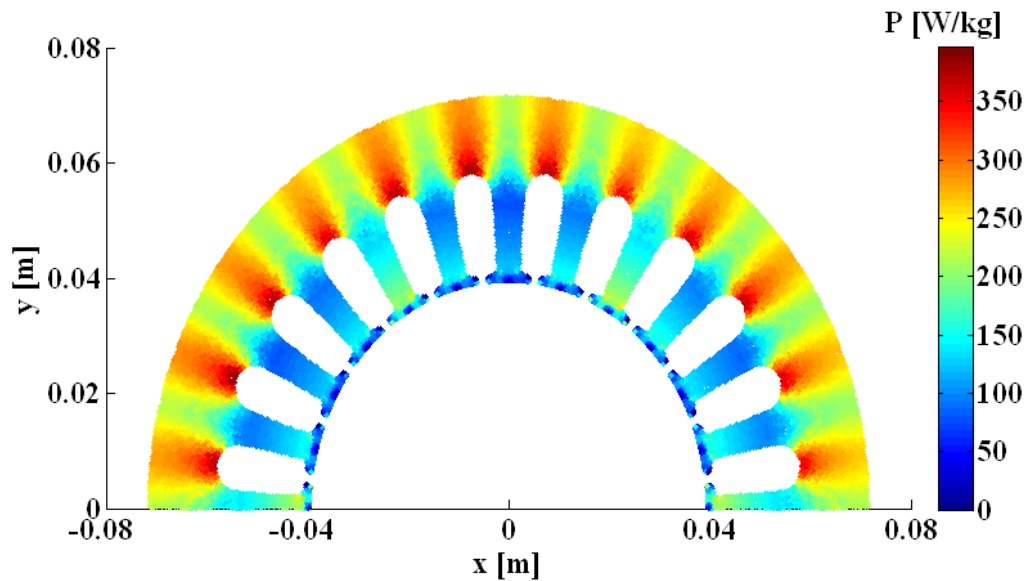


Fig. 5.46: The power loss distribution in $[W/kg]$ considering the rotational core losses in the stator of a 2-pole IM using M36G29 laminations at 1 kHz, and under a CCW rotating field.

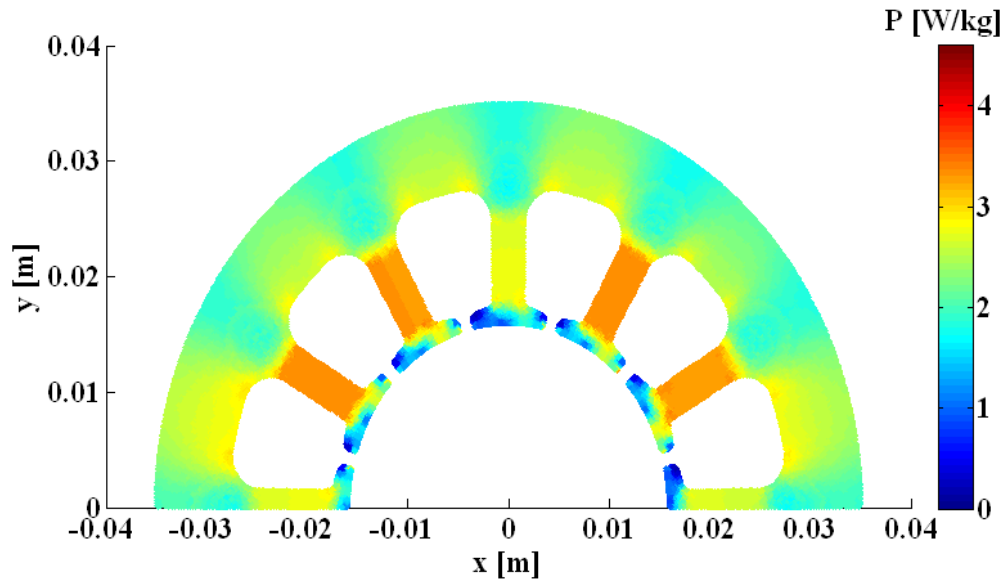


Fig. 5.47: The power loss distribution in [W/kg] considering the rotational core losses in the stator of a 2-pole BLDCM using M36G29 laminations at 60 Hz, and under a CW rotating field.

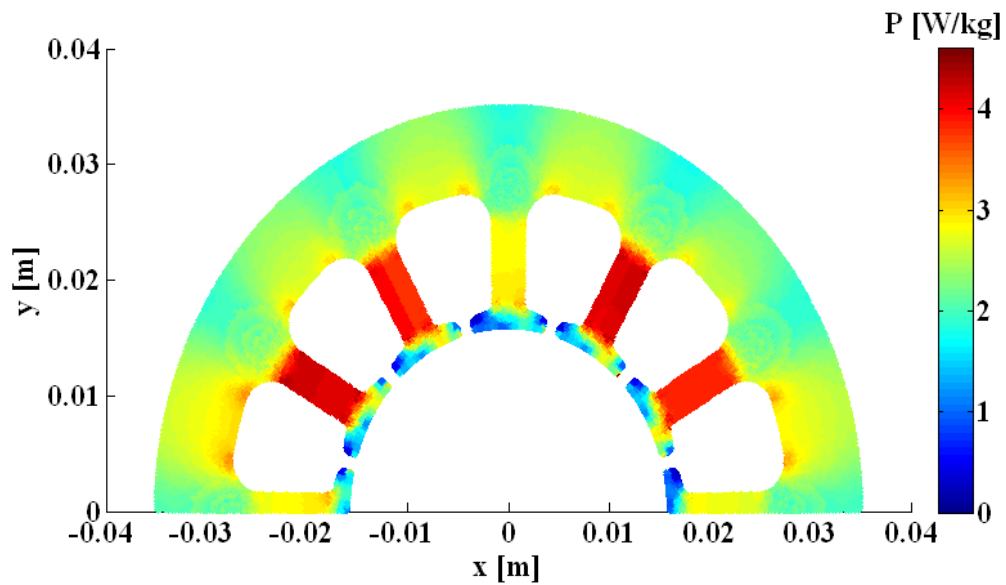


Fig. 5.48: The power loss distribution in [W/kg] considering the rotational core losses in the stator of a 2-pole BLDCM using M36G29 laminations at 60 Hz, and under a CCW rotating field.

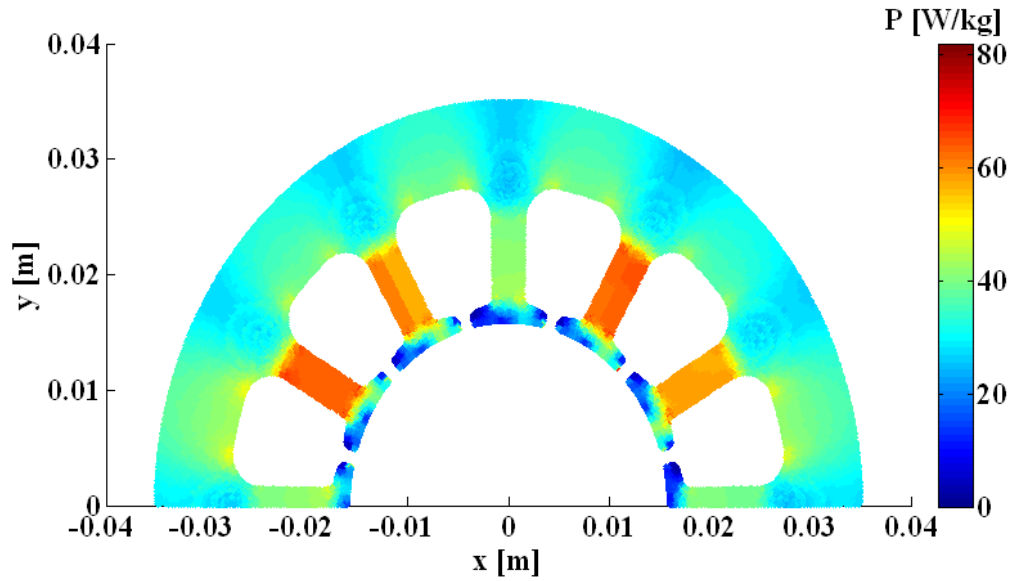


Fig. 5.49: The power loss distribution in [W/kg] considering the rotational core losses in the stator of a 2-pole BLDCM using M36G29 laminations at 400 Hz, and under a CW rotating field.

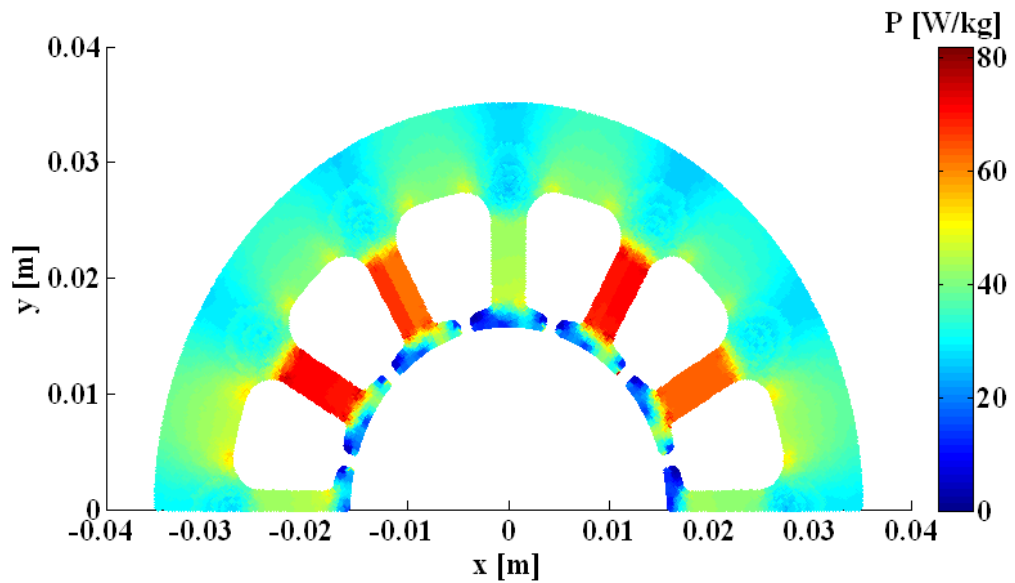


Fig. 5.50: The power loss distribution in [W/kg] considering the rotational core losses in the stator of a 2-pole BLDCM using M36G29 laminations at 400 Hz, and under a CCW rotating field.

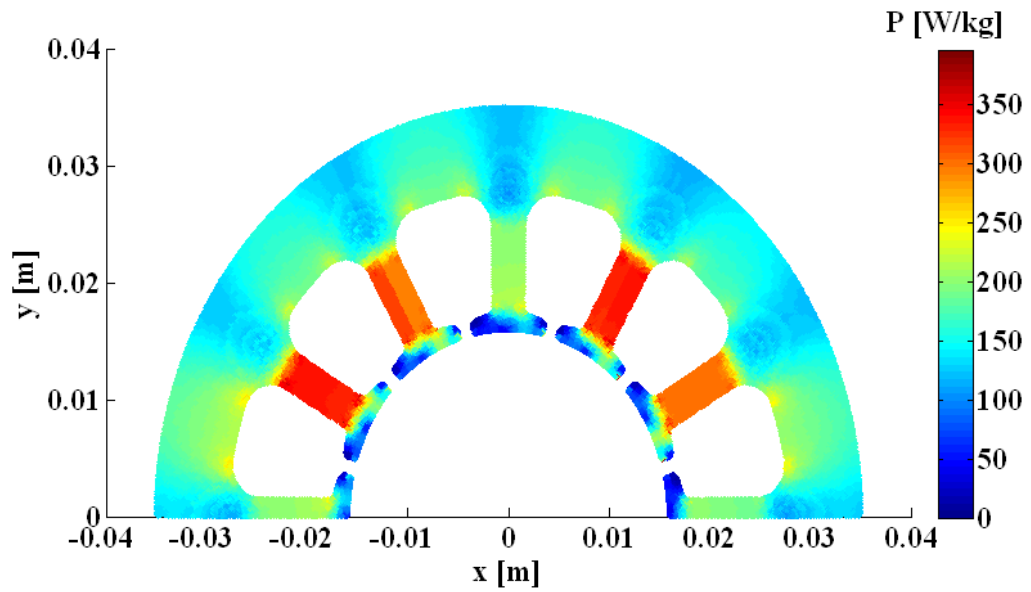


Fig. 5.51: The power loss distribution in [W/kg] considering the rotational core losses in the stator of a 2-pole BLDCM using M36G29 laminations at 1 kHz, and under a CW rotating field.

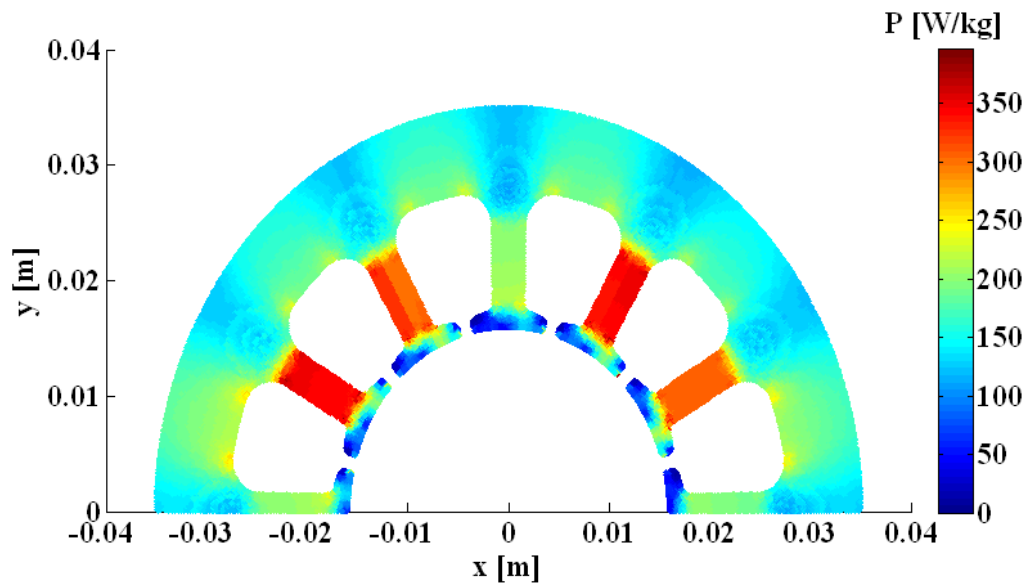


Fig. 5.52: The power loss distribution in [W/kg] considering the rotational core losses in the stator of a 2-pole BLDCM using M36G29 laminations at 1 kHz, and under a CCW rotating field.

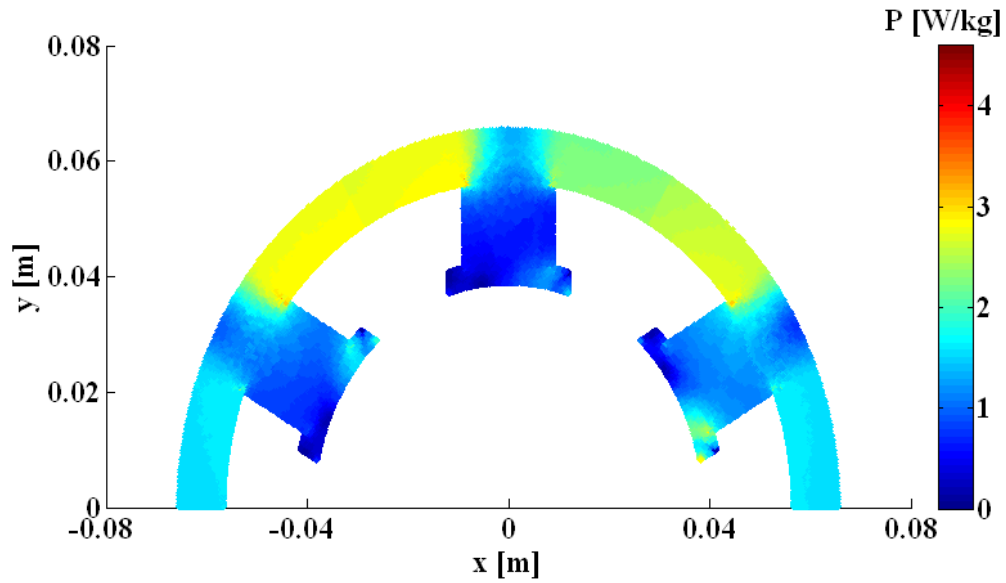


Fig. 5.53: The power loss distribution in $[W/kg]$ considering the rotational core losses in the stator of a 6-4 SRM using M36G29 laminations at 60 Hz, and under a CW rotating field.

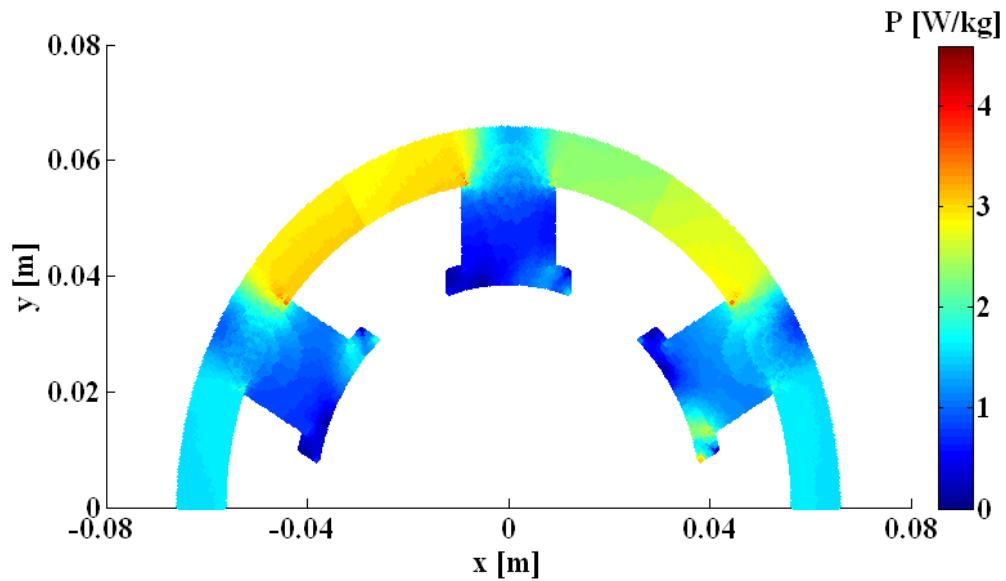


Fig. 5.54: The power loss distribution in $[W/kg]$ considering the rotational core losses in the stator of a 6-4 SRM using M36G29 laminations at 60 Hz, and under a CCW rotating field.

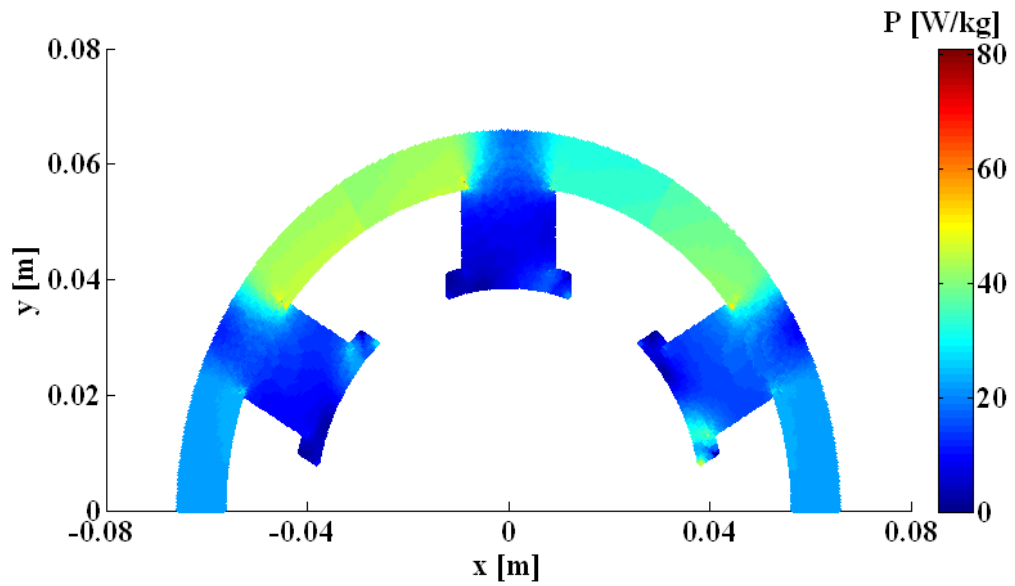


Fig. 5.55: The power loss distribution in $[W/kg]$ considering the rotational core losses in the stator of a 6-4 SRM using M36G29 laminations at 400 Hz, and under a CW rotating field.

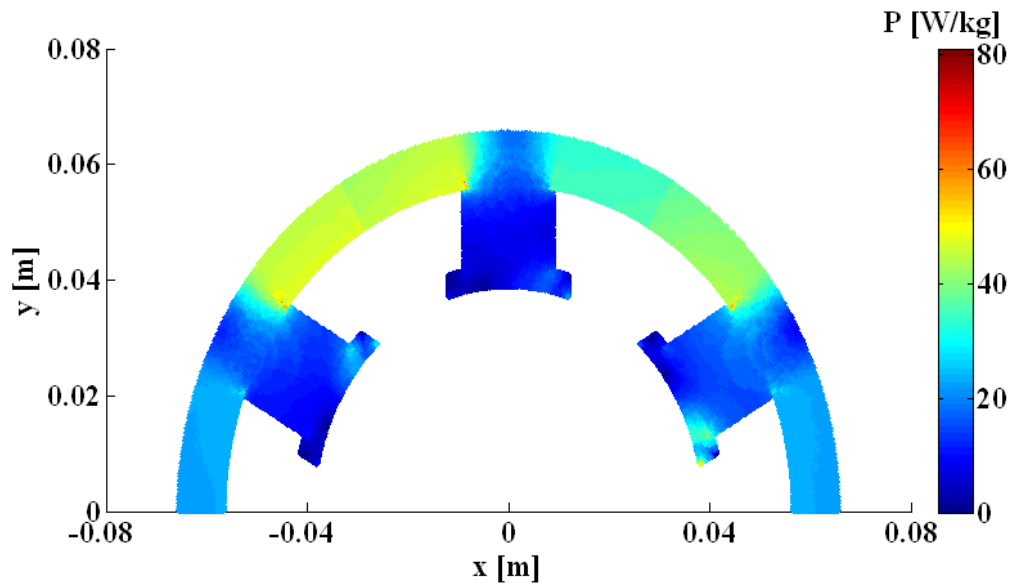


Fig. 5.56: The power loss distribution in $[W/kg]$ considering the rotational core losses in the stator of a 6-4 SRM using M36G29 laminations at 400 Hz, and under a CCW rotating field.

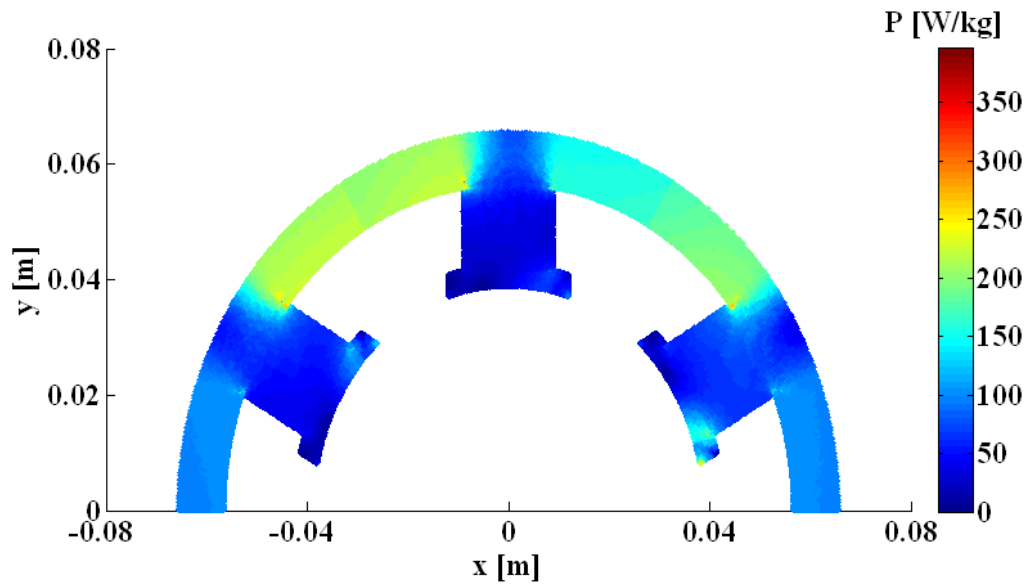


Fig. 5.57: The power loss distribution in $[W/kg]$ considering the rotational core losses in the stator of a 6-4 SRM using M36G29 laminations at 1 kHz, and under a CW rotating field.

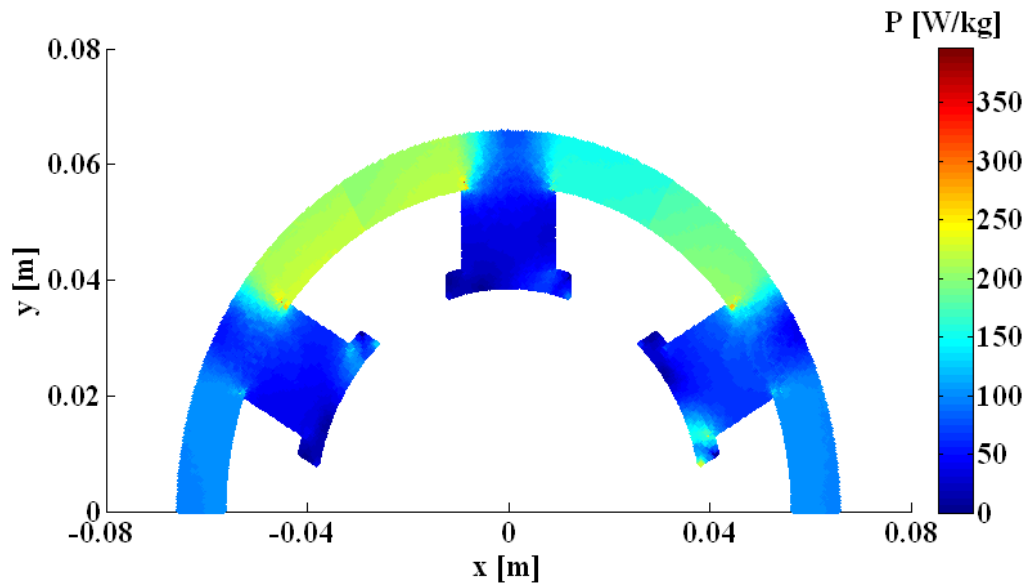


Fig. 5.58: The power loss distribution in $[W/kg]$ considering the rotational core losses in the stator of a 6-4 SRM using M36G29 laminations at 1 kHz, and under a CCW rotating field.

Table 5.2: Power loss in the three different machine types using M36G29 laminations
with CW and CCW rotating field

Machine	f [Hz]	Field Direction	Power loss [W/kg]			Error [%]
			Max.	Min.	Overall	
Induction	60	CW	3.3827	0.0653	2.6052	9.66
		CCW	4.5810	0.0772	2.8837	
	400	CW	70.8439	0.6964	42.0985	6.14
		CCW	80.279	0.7261	44.8518	
	1000	CW	381.01	2.8287	208.0818	1.44
		CCW	395.397	2.9948	211.1221	
BLDC	60	CW	3.3825	0.1561	2.3769	6.48
		CCW	4.5810	0.1757	2.5417	
	400	CW	70.8439	1.8803	36.2567	5.10
		CCW	80.279	2.0471	38.2060	
	1000	CW	381.01	7.492	174.7433	1.06
		CCW	395.397	7.984	176.6146	
SRM	60	CW	3.3607	0.0713	1.6635	4.29
		CCW	4.5810	0.0774	1.738	
	400	CW	70.8439	0.7742	23.8180	3.93
		CCW	80.279	0.8076	24.7911	
	1000	CW	381.01	3.1467	110.2646	0.55
		CCW	395.397	3.3185	110.8762	

5.6 Conclusion

Rotational core loss measurements under CW and CCW directions show noticeable differences. In the literature, this difference is attributed to many reasons such as misalignment in sensors which is avoided in this work where a novel design of a new magnetizing test fixture is used to perform the measurements. It is concluded that the anisotropy is the most important source of power loss difference in machine laminations when the sample is exposed to rotating fields in the CW and CCW direction. Three samples of non oriented M36G29, M15G29, and M19G24 silicon steel are tested under CW and CCW circular rotating fields with three different frequencies 1 kHz, 400 Hz, and 60 Hz. Results disclose a high difference in rotational core loss at high flux densities reaching up to 80% in M36G29 at 60 Hz. The eddy current loss is not affected by the direction of the rotating field, where a thicker sample at high frequency shows that the difference in losses in the CW and CCW directions becomes less, and the dynamic hysteresis loops become more similar in area and cycle shape. Three types of machines, 2-pole IM, 6-4 SRM, and 2-pole BLDCM are chosen to investigate the effect of reversing the rotating field direction on the delivered core loss in the stator. FEA determines the rotating flux zones within the stator lamination, and experimental loss data are applied to the machine models. A comparison between the machine types show that the IM experiences the highest effect of field reversing followed by the BLDCM, and then the SRM is the least affected. Results show a noticeable difference in loss between CW and CCW cases at low frequency. At high frequency, the difference becomes smaller and is 1.44 %, 1.06 %, and 0.55 % in IM, BLDCM, and SRM respectively.

6. SPECIFIC PHENOMENA ASSOCIATED WITH ROTATIONAL CORE LOSS MEASUREMENTS

6.1 The Negative Power in the Rotational Core Loss Measurements

6.1.1 Introduction

The increasing interest in magnetic measurements in machine laminations under rotating fields requires better interpretations for many unclear phenomena which have been observed experimentally. One of these phenomena is the negative power which is reported during the measurement of rotational core losses. This negative power can be noticed only when using the field metric method which provides more detailed information when compared with other methods of rotational core loss estimation. In particular, the negative power appears in one loss component in low frequency measurements, in addition, it has been observed in total power loss in the lamination [71]. This section addresses the problem of negative power and gives a descriptive picture for the field behavior by presenting the experimental dynamic hysteresis loops.

6.1.2 Results and Discussion

A circular rotating field is generated in the sample by exciting both Halbach arrays by sinusoidal waveforms with a phase shift of 90° between them, thus allowing the flux density vector to rotate in a clockwise direction. A non oriented silicon steel sample of M36G26 is tested at three different frequencies of interest to the industry, 60 Hz, 400 Hz, and 1 kHz.

Figs. 6.1, 6.2, and 6.3 show the rotational core losses in M36G26 silicon steel sample at 60 Hz, 400 Hz, and 1 kHz respectively. The corresponding x and y loss components, P_x and P_y are posed against the total loss P_{rot} . Generally, the performance of P_x and P_y can be described in the saturation region as P_x keeps rising up gradually, P_y decreases and sometimes attains negative values, as seen in Fig. 6.1. The y loss component at 400 Hz and 1 kHz could not reach negative values because the eddy current loss is dominant at high frequencies which is not affected directly by rotating field. The hysteresis loss component is basically responsible for the difference in loss behavior between the rotating and pulsating fields, and it is noticed that the magnetic materials show a clear different response to the rotating field compared with pulsating fields at lower frequencies. At this point, detailed eddy current loss model under rotating field seems to be an imperative need. Therefore, this study will focus on experiments under 60 Hz, where the negative power can be recognized and recorded.

When the magnetic material is subjected to a pulsating field, the core loss is expected to increase steadily. This phenomenon has been reported, agreed, and modeled mathematically as a function of frequency and flux density. The same sample M36G26 is exposed to a pulsating field by exciting one Halbach array, the x -array and later on the y -array. Using the same measuring techniques with the same sensors, the pulsating core losses produced in each direction are depicted in Fig. 6.4. The main difference between core losses produced by pulsating and rotating fields in the saturation region is that the loss under a rotating field decreases while the pulsating loss keeps rising.

The ***B-H*** curve for a cyclic magnetization is considered key for expressing the relation between the applied field and the domains alignment direction, in addition the enclosed area by the loop is directly proportional to the loss in the material [27] and [72]. Accordingly, the ***B-H*** loops are considered, and their evolution is studied to investigate the change in the material response to the applied field. Fig. 6.5 and Fig. 6.6 show the dynamic hysteresis loops in *x* and *y* directions respectively at 60 Hz for M36G29, which correspond to the pulsating losses presented in Fig. 6.4. The loops are drawn at flux density levels of 1T, 1.1T, 1.2T, and 1.3T. The loops offer systematic evolution, where the curves rise rapidly at the beginning, and then the slope decreases significantly because of the larger ***H*** required to orient the material domains.

On the other hand, for the *y* loss component presented in Fig. 6.1, the dynamic hysteresis loops are tracked consecutively. The dynamic hysteresis loop at 1.1 T is shown in Fig. 6.7, which seems to be consistent with the ordinary hysteresis loop. At 1.2 T, the loop starts to narrow and interfere at the tips as an introduction to the overlapping, as shown in Fig. 6.8. At, 1.3 T, the overlapping is continued and increased, where the loop is divided into three loops, as seen in Fig. 6.9. The upper and lower loops have a different direction from the middle loop, which means that the mathematical integration used to calculate the area of the loop will be negative for the upper and lower loops, and positive for the middle loop. As a result, the overall area of the loop is decreased. Fig. 6.10 shows the loop at 1.39 T, where the overlapping is done, and the loop's direction is completely

reversed. In this case, the enclosed area by the loop exhibits negative area, in other words, the loss is negative due to changing the flux direction. Figs. 6.11, 6.12, 6.13 and 6.14 show the dynamic hysteresis loops corresponding to the x loss component in Fig. 6.1 measured at 60 Hz for M36G29. Despite the loops become narrower at the middle being different from the normal shape of the hysteresis loops, the loops keep the same direction of the flux and no overlapping appears. The loop behavior agrees with the x loss component curve in Fig. 6.1 where it rises along the flux density profile. This negative power loss appears in one loss component and is considered to be acceptable mathematically and physically, where the total rotational core loss in the lamination after summing both components becomes positive.

The total rotational core loss with the negative values has been reported in [73] and [74]. Practically, we could not obtain a negative value under a circular rotating field until a change performed on the measuring system, where the \mathbf{B} coils are moved physically by around 10 degrees relative to the field excitation axis, as depicted in Fig. 6.15. Results show a significant and rapid decreasing in loss curve toward the negative values, as seen in Fig. 6.16. A more detailed comparison between losses before and after the movement of the sensors can be seen through presenting the x and y loss components as shown in Fig. 6.17. After moving the sensors, the loss components are decreased, and the y loss component has a more noticeable difference compared with the corresponding component before the sensor deflection. To investigate the effect of the coil

misalignments on the $\mathbf{B-H}$ loop behavior, the dynamic hysteresis loops for the y loss component after the \mathbf{B} coils deflection are presented in Figs. 6.18, 6.19, 6.20 and 6.21. Fig. 6.18 shows the dynamic hysteresis loop of M36G26 sample at 1.1T with rotating field in the CW direction. Compared to Fig. 6.7, the loop keeps the same shape as before the deflection with lower enclosed area. Fig. 6.19 depicts the loop at 1.2 T, where the loop shows an entangle in the upper tip, and tighter lower tip compared with the loop in Fig. 6.8. At 1.3 T, the dynamic hysteresis loop continues the overlapping and has larger upper and lower loops and a smaller middle loop, as seen in Fig. 6.20. This means that the loop tends to increase the negative power and achieves a higher negative power value compared with the loop in Fig. 6.9. In Fig. 6.21, the loop reverses its direction completely, and becomes wider in the middle, *i.e.* higher enclosed area and then higher negative power compared with the loop in Fig. 6.10.

In [73] and [74], it was suggested to measure the rotational core losses under a rotating field in the counterclockwise direction and then taking the average of losses in the CW and CCW directions in order to remove the negative values. However, it was shown in [73] and [74] that the negative power in the total loss comes from the sensor misalignments and attention should be paid to improving the sense coil system. In this new test fixture, the \mathbf{H} coil sensors are placed in grooves which are cut into the fixture frame using the CNC machine to place the sensors in their correct positions. Thus, axis alignment is confirmed. The possibility of misalignments in \mathbf{B} coils is very low, where the coil width is much higher (180 mm) compared with the typical coil width (20 mm). A higher \mathbf{B} coil width decreases the chance of misalignments, where the worst

misalignment angle becomes ineffective (0.178°). The sensors should maintain the orthogonality between each others, and aligned exactly to the field excitation axis.

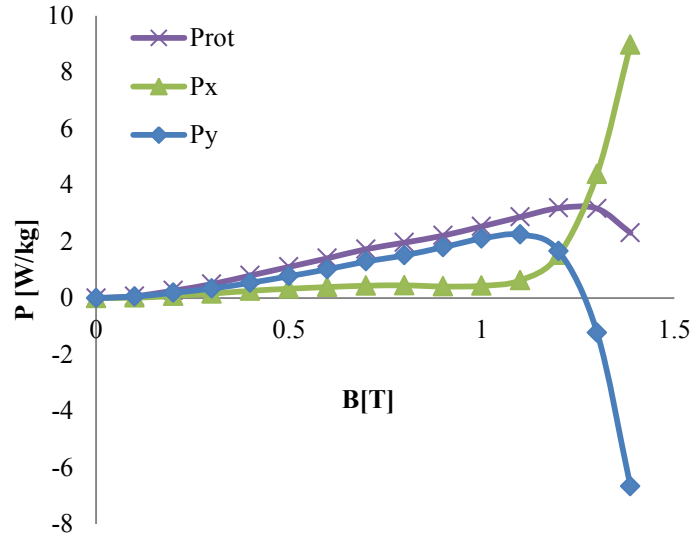


Fig. 6.1: The total rotational core loss at 60 Hz, in M36 steel Gauge 26, with the corresponding x and y components, P_x and P_y respectively.

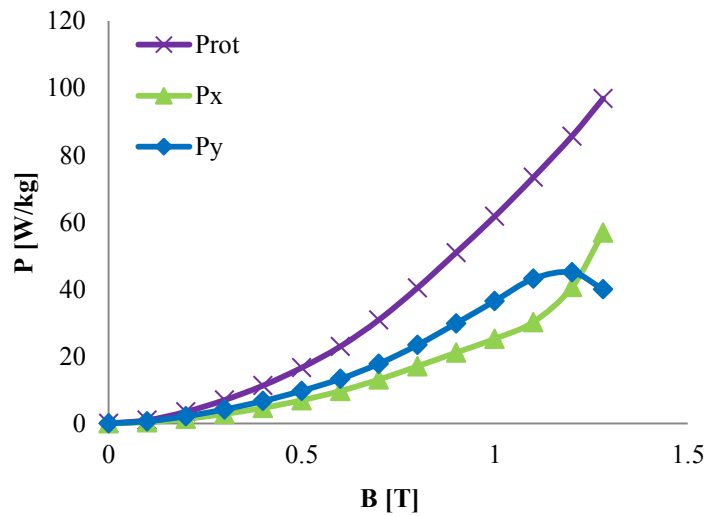


Fig. 6.2: The total rotational core loss at 400 Hz, in M36 steel Gauge 26, with the corresponding x and y components, P_x and P_y respectively.

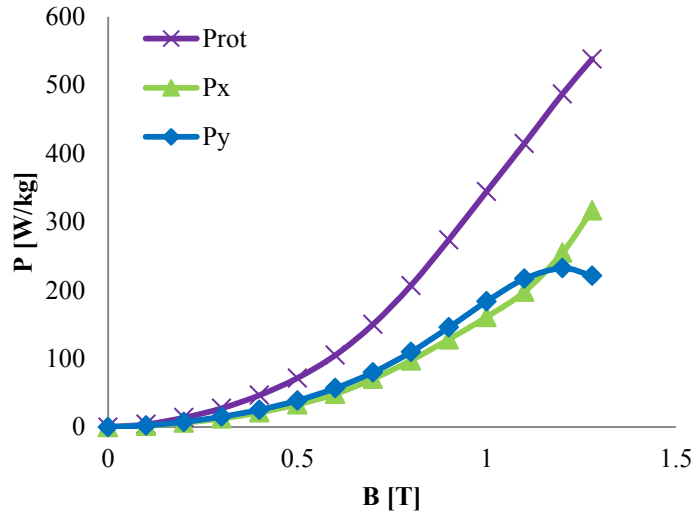


Fig. 6.3: The total rotational core loss at 1 kHz, in M36 steel Gauge 26, with the corresponding x and y components, P_x and P_y respectively.

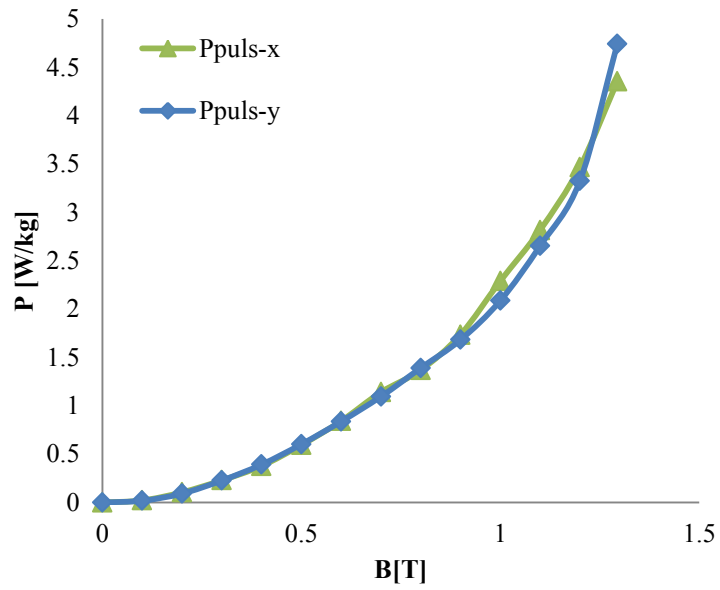


Fig. 6.4: The pulsating losses in x and y directions at 60 Hz for M36G26.

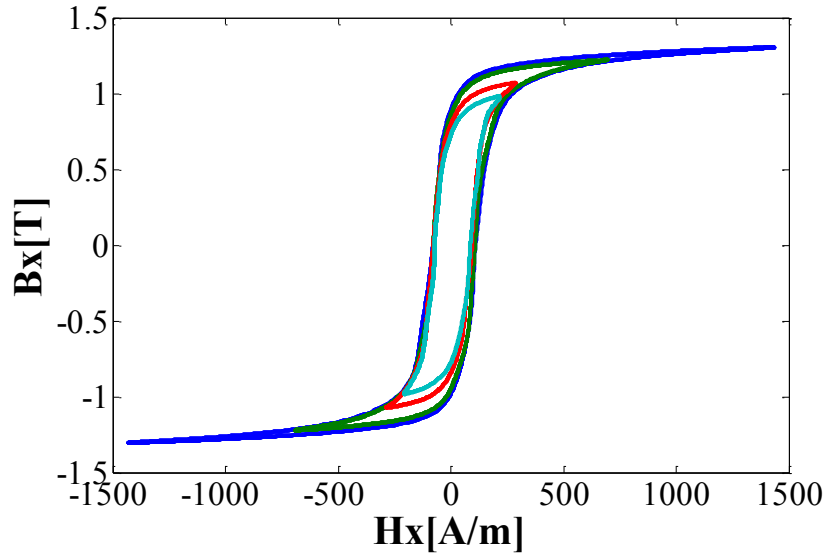


Fig. 6.5: The dynamic hysteresis loops (B_x - H_x) for the pulsating loss component in y direction at 60 Hz for M36G26. The loops are drawn at flux density level of 1T, 1.1T, 1.2T, and 1.3T.

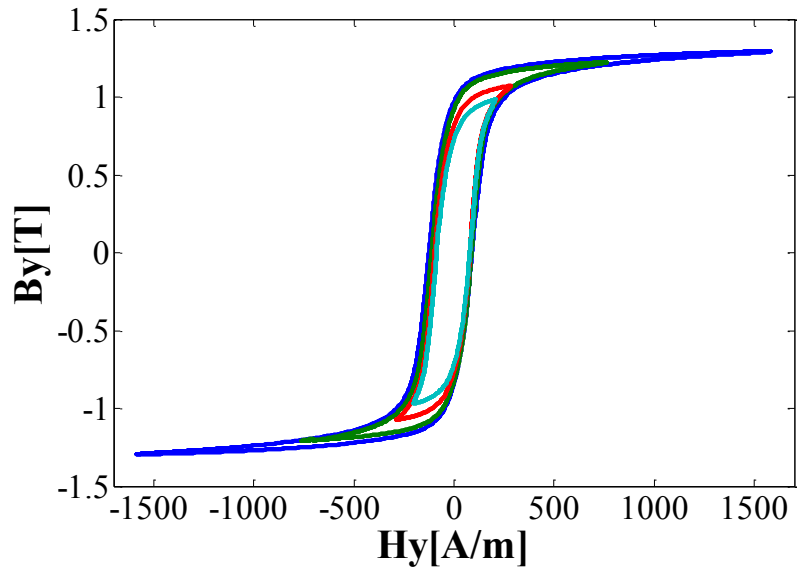


Fig. 6.6: The dynamic hysteresis loops (B_y - H_y) for the pulsating loss component in y direction at 60 Hz for M36G26. The loops are drawn at flux density level of 1T, 1.1T, 1.2T, and 1.3T.

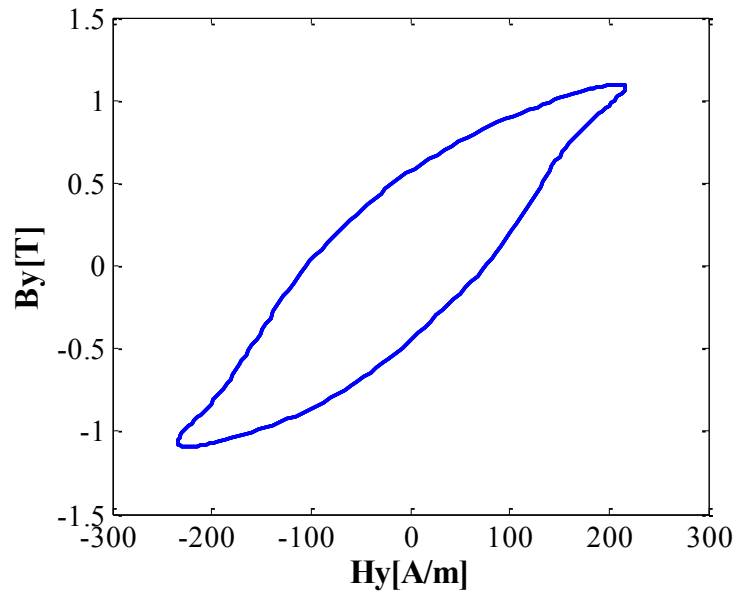


Fig. 6.7: The dynamic hysteresis loop for the y -component measured in the CW direction for M36G26 sample under 1.1T rotating field with 60 Hz.

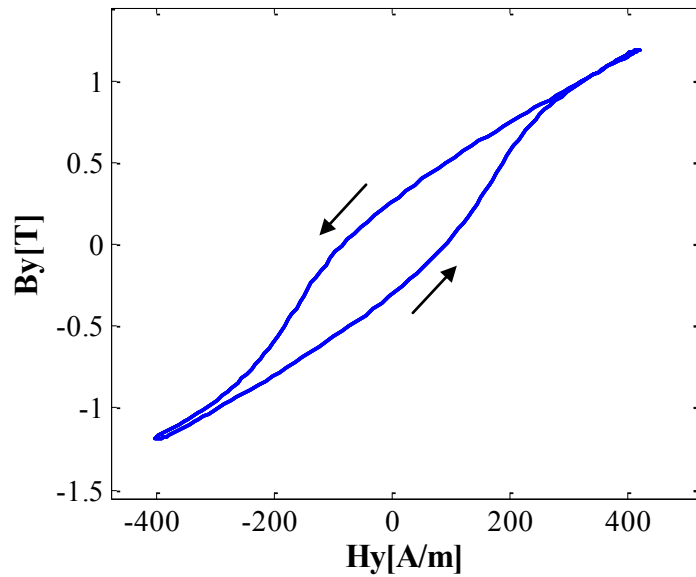


Fig. 6.8: The dynamic hysteresis loop for the y -component measured in the CW direction for M36G26 sample under 1.2T rotating field with 60 Hz.

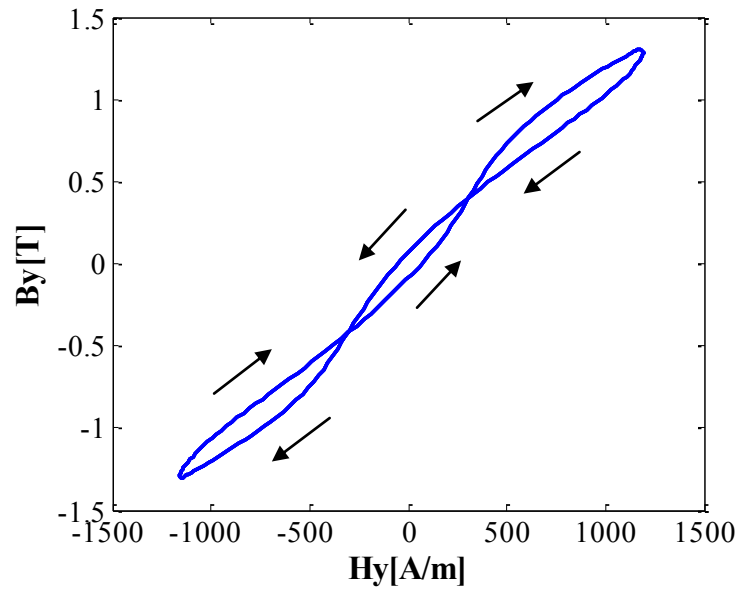


Fig. 6.9: The dynamic hysteresis loop for the y -component measured in the CW direction for M36G26 sample under 1.3T rotating field with 60 Hz.

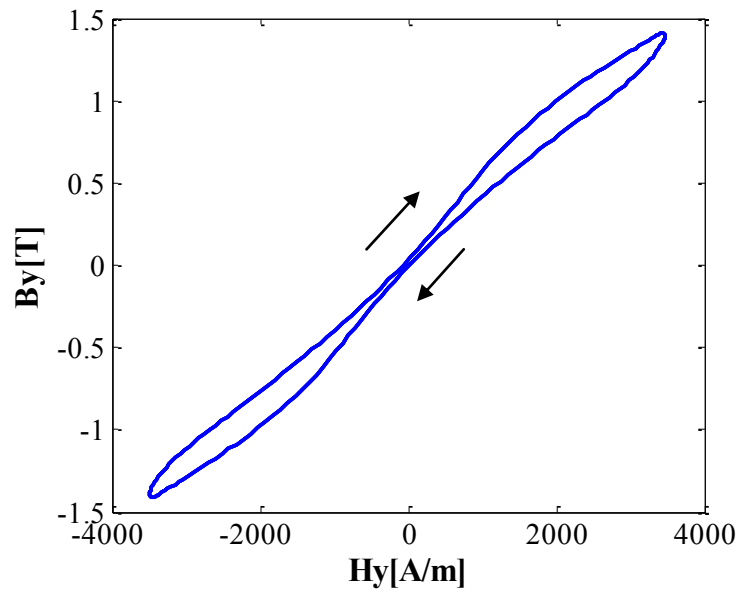


Fig. 6.10: The dynamic hysteresis loop for the y -component measured in the CW direction for M36G26 sample under 1.4T rotating field with 60 Hz.

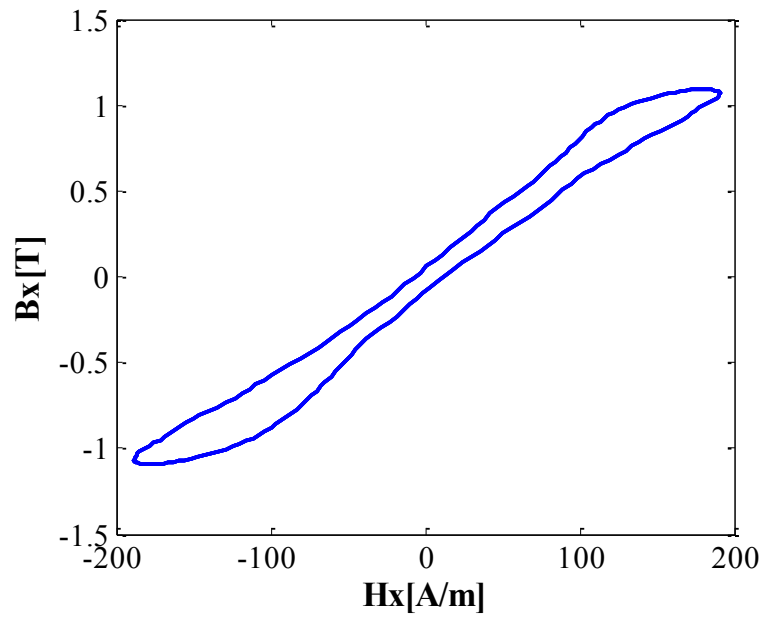


Fig. 6.11: The dynamic hysteresis loop for the x -component measured in the CW direction for M36G26 sample under 1.1T rotating field with 60 Hz.

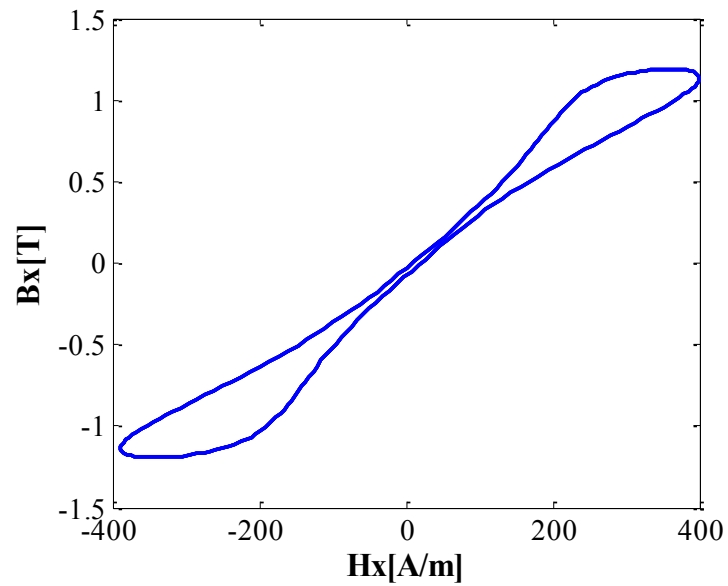


Fig. 6.12: The dynamic hysteresis loop for the x -component measured in the CW direction for M36G26 sample under 1.2T rotating field with 60 Hz.

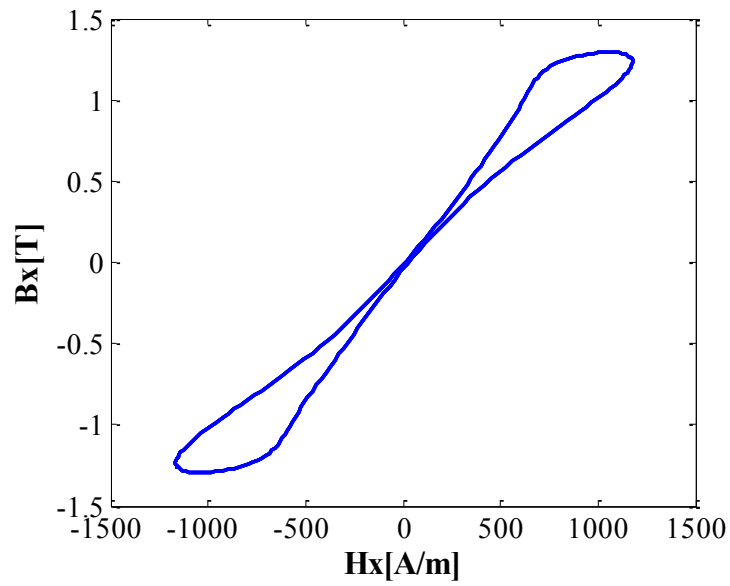


Fig. 6.13: The dynamic hysteresis loop for the x -component measured in the CW direction for M36G26 sample under 1.3T rotating field with 60 Hz.

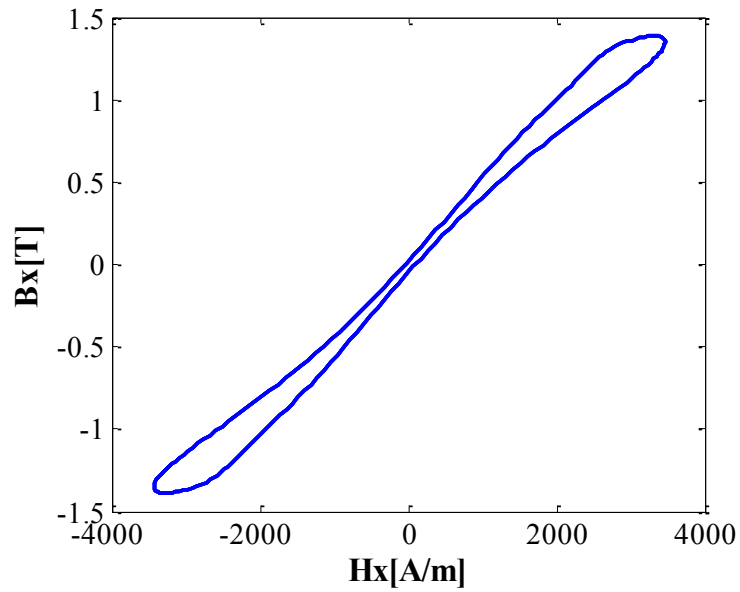


Fig. 6.14: The dynamic hysteresis loop for the x -component measured in the CW direction for M36G26 sample under 1.4T rotating field with 60 Hz.

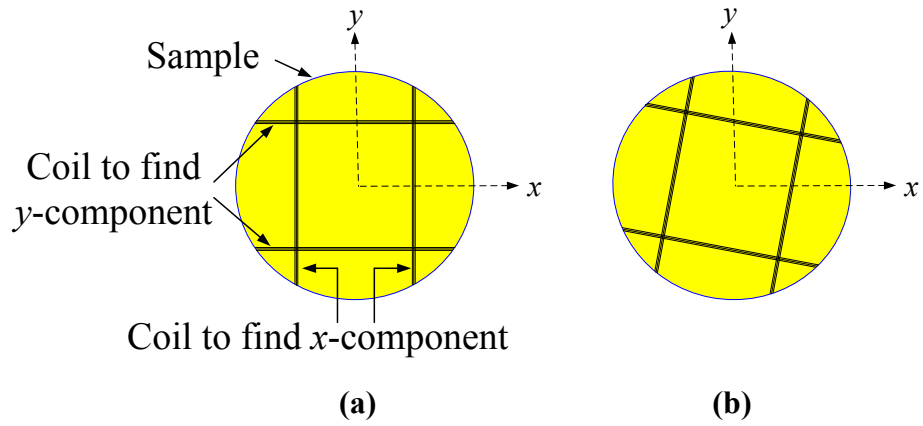


Fig. 6.15: The position of B coils wound around the sample. (a) The original position. (b) The position after a deflection of 10° in the CW direction.

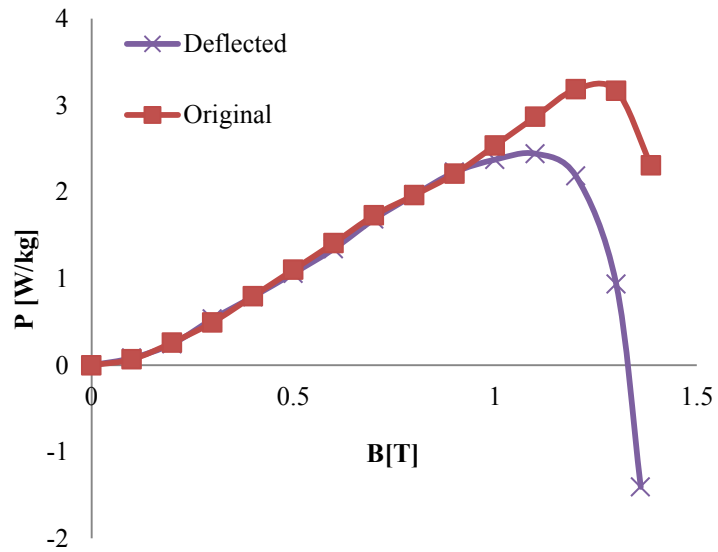


Fig. 6.16: Rotational core losses in M36G26 sample before and after the B coil deflection. Measurements are under the CW rotating field at 60 Hz.

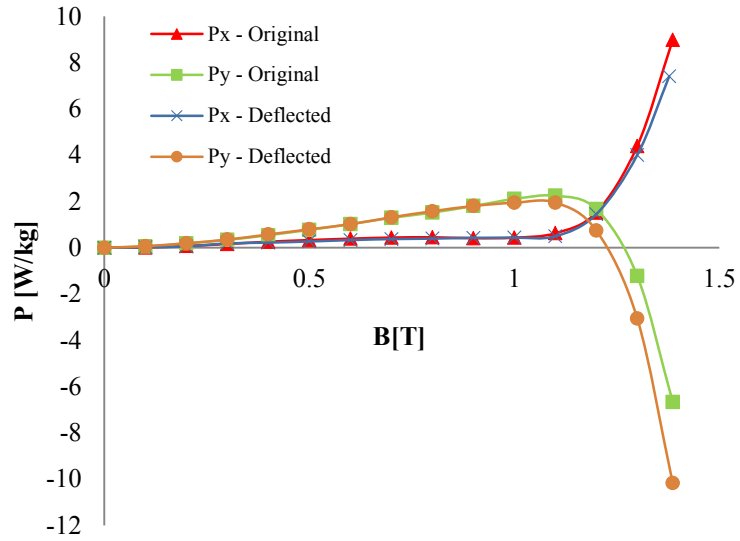


Fig. 6.17: The measured x and y loss components of rotational core losses in the CW direction for M36G26 sample with 60 Hz. The loss components at which \mathbf{B} coils were in their original right position P_x -Original and P_y -Original are compared with loss components after the deflection of the \mathbf{B} coil.

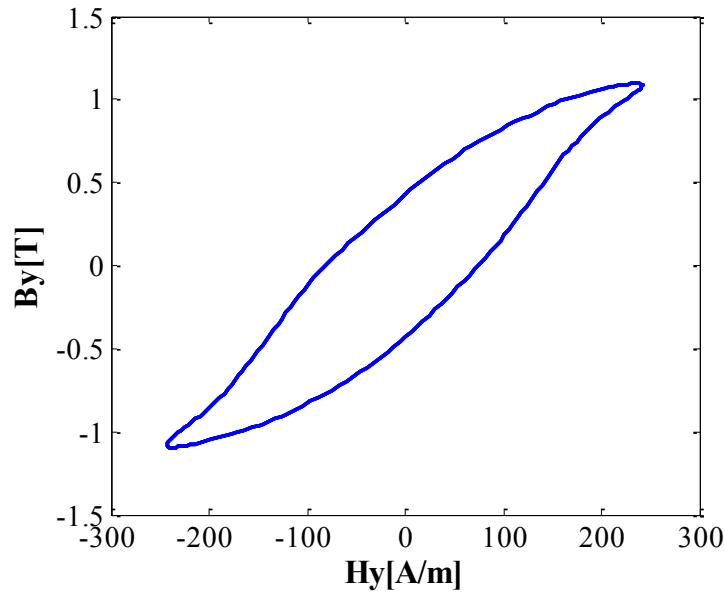


Fig. 6.18: The dynamic hysteresis loop for the y -component measured in the CW direction for M36G26 sample under 1.1T rotating field with 60 Hz after the \mathbf{B} coils deflection.

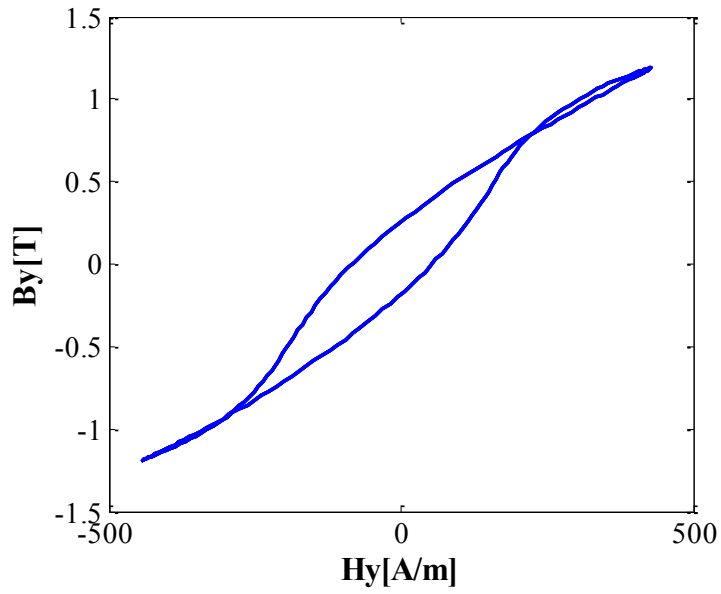


Fig. 6.19: The dynamic hysteresis loop for the y -component measured in the CW direction for M36G26 sample under 1.2T rotating field with 60 Hz after the \mathbf{B} coils deflection.

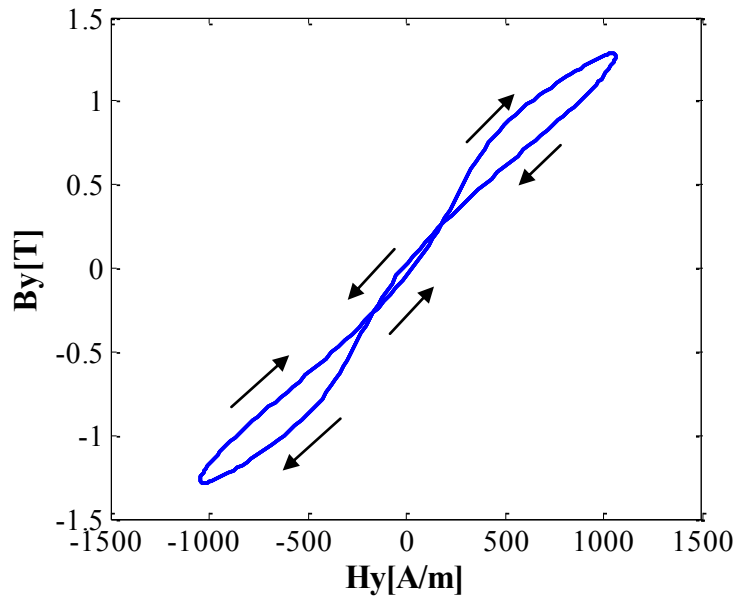


Fig. 6.20: The dynamic hysteresis loop for the y -component measured in the CW direction for M36G26 sample under 1.3T rotating field with 60 Hz after the \mathbf{B} coils deflection.

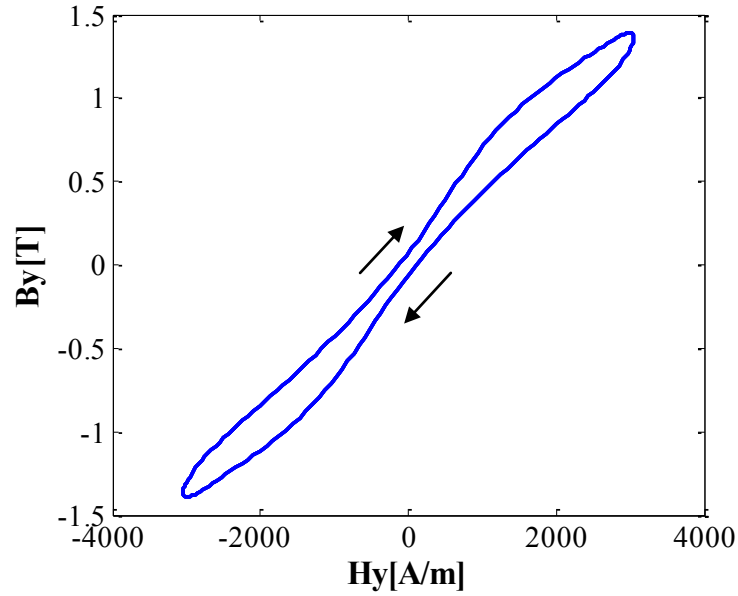


Fig. 6.21: The dynamic hysteresis loop for the y -component measured in the CW direction for M36G26 sample under 1.4T rotating field with 60 Hz after the \mathbf{B} coils deflection.

6.1.3 Conclusion

During the measurements of rotational core loss in magnetic materials using the field metric method, a negative power was observed. This negative power may be in one loss component, or be the net value of the total rotational core loss. The negative power that appears in one loss component is caused by the reversal of the field direction which can be realized from the dynamic hysteresis loop. The negative value in one loss component is acceptable as long as the total loss is positive. The negative value in total rotational loss is caused by sensor misalignment. The novel test fixture design used in this work offers an accurate alignment of the sensor systems; therefore, the negative values at the total loss could not be realized until the \mathbf{B} coils are physically moved. The dynamic

hysteresis loops are presented for loss components in both the pulsating and rotating fields. Loop behaviors are described and compared with each others.

6.2 The Minor Hysteresis Loop under Rotating Magnetic Fields

6.2.1 Introduction

In rotating AC machines, the saturated flux density waveforms contain harmonics, which create minor hysteresis loops. The minor hysteresis loop in machine laminations causes a serious challenge in core loss estimation, especially under rotating magnetic fields. Fourier series analysis can extract harmonics from the distorted saturated flux density signal of which the third harmonic is the most dominant component. This section highlights the problem of harmonics in rotating fields and its effect on core loss estimation. In addition, the behavior of minor loops under rotating fields is compared with the minor loop under pulsating fields.

6.2.2 Fundamentals of Minor Loop Generation

Typically, the magnetic material excited by a sinusoidal source has a saturated flux density waveform of a shape ends up with a square wave at complete saturation. Higher saturation leads to closer form of square waveform. The saturated square signal can be expanded using Fourier series as [75]:

$$B(t) = \frac{-2B_m}{\pi} \sum_{k=1}^{\infty} \frac{(-1)^k - 1}{k} \sin(k\omega t) \quad (6.1)$$

Note that the even harmonics vanish, and the signal contains only odd harmonics. The

maximum possible magnitude of the k^{th} harmonic component compared with the fundamental is given by:

$$\left| B_k \right| = \frac{(-1)^k - 1}{-2k} \left| B_1 \right| \quad k=1,2,3,\dots \quad (6.2)$$

Equation (6.2) shows that the third harmonic has the highest magnitude among all harmonics with a value of 1/3 of the fundamental. The phase shift between the harmonic and the fundamental component is considered a primary factor in minor loop generation, and has a direct influence on core losses due to the change in the peak flux value [76], [77], and [78]. If only the third harmonic is considered with a peak of 1/3 of the fundamental and a fundamental of unity [T] peak, there are three possible cases: (a) In-phase, (b) 180° phase shift, and (c) a phase of angle between 0° and 180°. When the fundamental and the third harmonic are in-phase, the resultant flux has two symmetric peaks of 0.9428 T which is lower than the fundamental peak, as shown in Fig. 6.22. In the case of 180° phase shift, the resultant is higher than the fundamental with a value of 1.3333 T, as seen in Fig. 6.23. The last case when the phase varies between 0° and 180°, the peaks are not symmetric. One case at 90° phase shift is shown in Fig. 6.24. Minor loops appear when the flux density waveform reverses its direction within the half cycle, as in case (a) and (c), and the existence of harmonics does not mean that the minor loops should appear, as can be recognized in case (b) where the third harmonic is shifted 180° and no reversal in the flux density occurs in the half cycle.

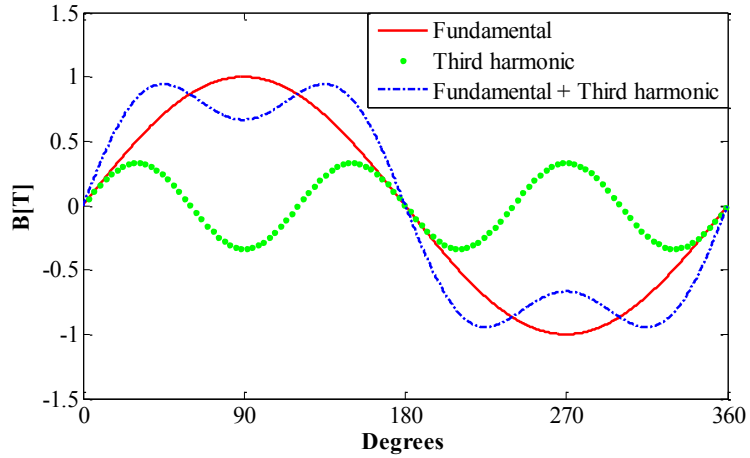


Fig. 6.22: The result of the flux density from the addition of the fundamental of 1T peak value and a third harmonic of a peak of 0.3 T, where both the fundamental and the harmonic are in-phase.

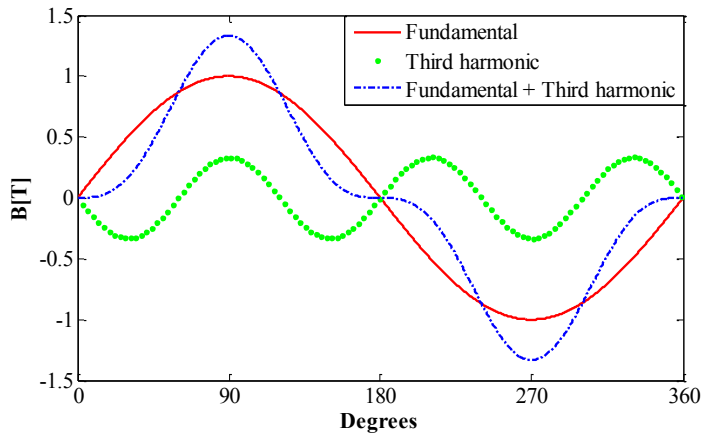


Fig. 6.23: The result of the flux density from the addition of the fundamental of 1T peak value and a third harmonic of a peak of 0.3 T, where the third harmonic is 180° lagging.

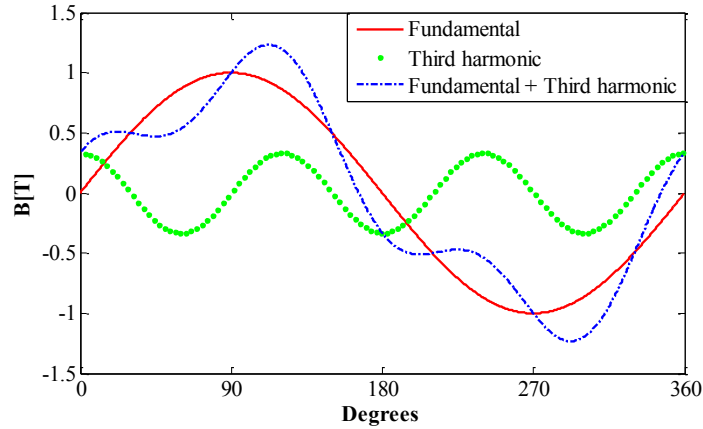


Fig. 6.24: The result of the flux density from the addition of the fundamental of 1 T peak value and a third harmonic of a peak of 0.3 T, where the third harmonic is 90° leading.

6.2.3 Measurements and Results

Measurements were carried out on a non oriented silicon steel sample of M36G29 with different fundamental frequencies of interest to the industry, 60 Hz and 400 Hz, with consideration of the third harmonic at each frequency. The pulsating field can be produced by exciting only one array, and a circular rotating field is established in the sample by injecting both arrays simultaneously with sinusoidal waveforms with a 90° phase shift. Practically, the Matlab Simulink[®] is used to generate waveforms which can be injected into the magnetic circuit in order to generate flux density waveforms with reversal peaks. The target is to test the sample under purely pulsating field, purely circular rotating field, and then under distorted pulsating fields and distorted rotating fields, where only the third harmonic is considered since it is the most significant one.

A. Harmonics in pulsating field

The Halbach arrays are excited separately by sinusoidal fundamental signals of 1.0, 1.1, 1.2 and 1.3 T with harmonics of 0.3 of the fundamentals. The fundamental and the harmonic are in-phase. The measured flux density waveforms of 60 Hz and 1.3T fundamental component, and their corresponding magnetic field strength waveforms in the x and y directions are shown in Fig. 6.25 and Fig. 6.26 respectively. The dynamic hysteresis loops under pulsating fields obtained in Fig. 6.25 and Fig. 6.26 are depicted in Fig. 6.27. The minor loops appear symmetric in the upper and lower parts of the major loop and confined entirely within the major loop borders. The dynamic hysteresis loops under pulsating fields of 1.3T and 400 Hz fundamental component with the third harmonic in the x and y directions are shown in Fig. 6.28. By increasing the frequency, the loop size is increased which reflects an increase in power loss, and the minor loops are remained inside the major loops. The core loss results in the sample reveal an increase in loss when the harmonic is added to the fundamental. These losses are benchmarked against a pulsating field without harmonics, as illustrated in Table 6.1.

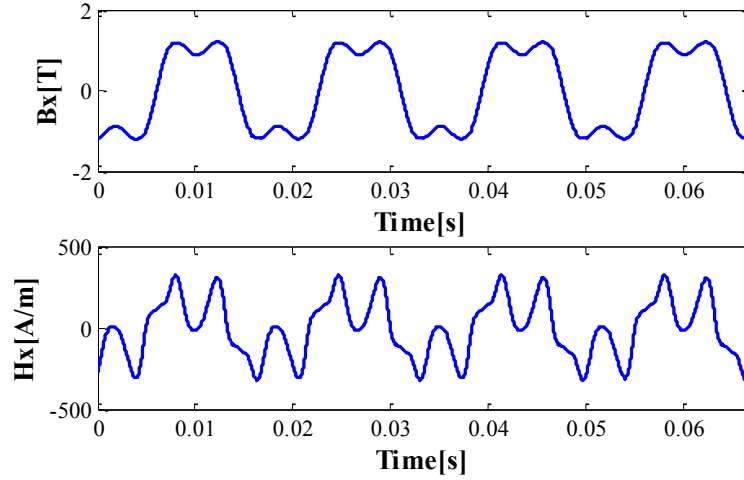


Fig. 6.25: The flux density waveform of 1.3T and 60 Hz fundamental component with a third harmonic B_x , and the corresponding magnetic field strength waveform H_x for a M36G29 sample under a pulsating field.

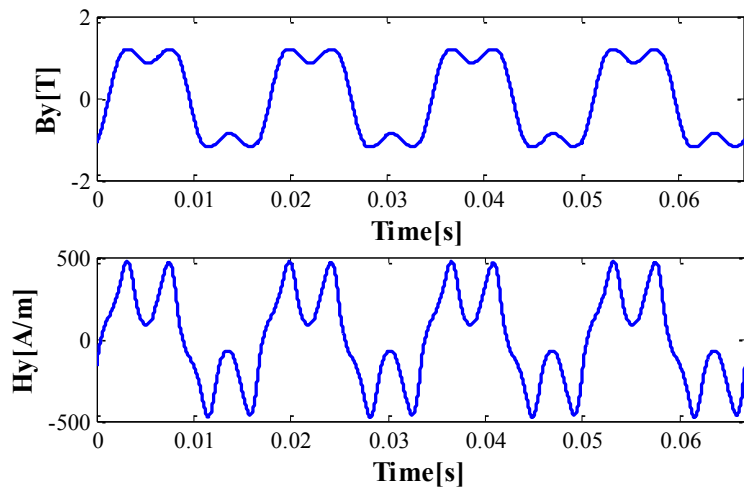


Fig. 6.26: The flux density waveform of 1.3T and 60 Hz fundamental component with a third harmonic B_y , and the corresponding magnetic field strength waveform H_y for a M36G29 sample under a pulsating field.

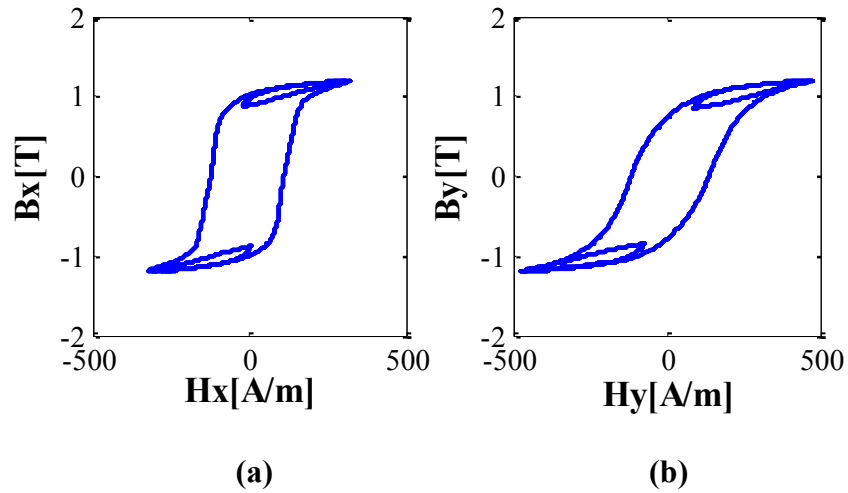


Fig. 6.27: The dynamic hysteresis loops for a M36G29 sample under a pulsating field of 1.3T and 60 Hz fundamental component with a third harmonic. (a) In the x -direction. (b) In the y -direction.

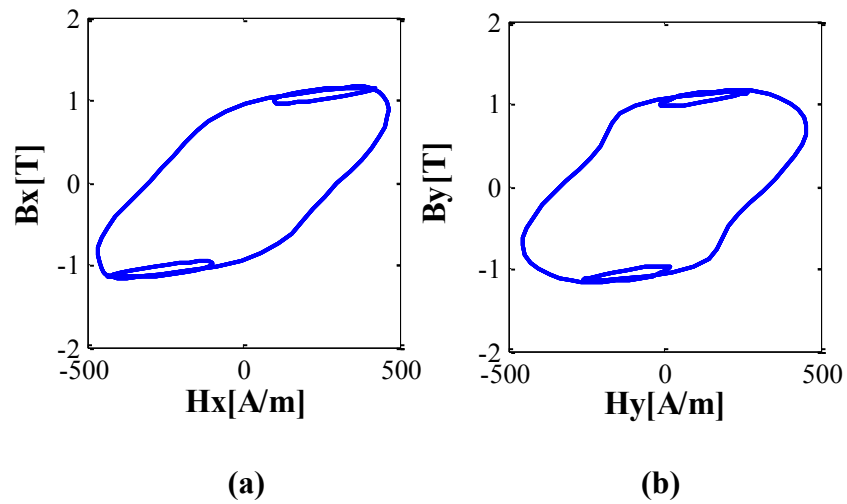


Fig. 6.28: The dynamic hysteresis loops for a M36G29 sample under a pulsating field of 1.3T and 400 Hz fundamental component with a third harmonic. (a) In the x -direction. (b) In the y -direction.

Table 6.1: Power loss in the M36G29 lamination at 60 Hz and 400 Hz produced by pulsating fields with and without the third harmonic component.

FREQ. [Hz]	THE PEAK OF FUNDAMENTAL FLUX DENSITY COMPONENT [T]	WITH HARMONIC P [W/KG]	WITHOUT HARMONIC P [W/KG]
60	1	5.8008	4.2989
	1.1	6.7875	5.3004
	1.2	7.9126	6.3544
	1.3	9.2064	7.5942
400	1	81.9856	64.1364
	1.1	99.9839	77.3171
	1.2	119.5156	92.7451
	1.3	140.6289	104.8889

B. Harmonics in rotating field

Both Halbach arrays are excited simultaneously by sinusoidal fundamental signals of 1.0, 1.1, 1.2 and 1.3 T with harmonics of 0.3 of the fundamental. A phase shift of 90° is applied to the waveform injected to the y -array. This pattern of input waveforms creates a circular rotating flux density vector with harmonics, and has a mathematical expression as:

$$\mathbf{B}_{net} = [B_x \sin(\omega t) + 0.3B_x \sin(3\omega t)]\vec{i} + [B_y \sin(\omega t + 90^\circ) + 0.3B_y \sin(3\omega t + 90^\circ)]\vec{j} \quad (6.3)$$

The measured flux density waveforms in the x and y directions \mathbf{B}_x and \mathbf{B}_y of 60 Hz and 1.0T fundamental component, and their corresponding magnetic field strength waveforms \mathbf{H}_x and \mathbf{H}_y are shown in Fig. 6.29 and Fig. 6.30. The loci of magnetic field strength (H_x - H_y) and magnetic flux density (B_x - B_y) are shown in Fig. 6.31. The dynamic hysteresis loops in the x and y directions for M36G29 sample under a rotating field of 1T and 60 Hz fundamental component with a third harmonic are shown in Fig. 6.32 and Fig. 6.33

respectively. In the x direction, the minor loops expand outside the major loop, and in the y direction, the major loop bifurcates in the upper and lower ends. The evolution of the dynamic hysteresis loops under rotating fields at higher flux density levels of 1.1, 1.2, and 1.3 T fundamentals associated with the third harmonic can be seen in Figs. 6.34, 6.35, 6.36, 6.37, 6.38, and 6.39. Ultimately, at 1.3 T, the minor loops settle outside the major loops' borders with some overlapping, as seen in Fig. 6.38 and Fig. 6.39.

When the fundamental frequency is increased to 400 Hz, the dynamic hysteresis loops become wider. Fig. 6.40 shows the dynamic hysteresis loop in the x -direction under a rotating field of 1T fundamental component with a third harmonic, where the minor loops are almost confined inside the major loop. On the contrary, in the y direction, the minor loops are outside the major loop, as seen in Fig. 6.41. Following the evolution of the dynamic hysteresis loops at higher flux density levels of 1.1, 1.2, and 1.3 T show that the major loop releases the minor loops, and then the minor loops continue rotating in clockwise direction, as noticed in Figs. 6.42, 6.43, 6.44, 6.45, 6.46, and 6.47. Previously, these shapes of dynamic hysteresis have appeared in some studies and described as unusual hysteresis loops, as seen in Fig. 6.48. This inconsistency with the traditional loop under pulsating fields was attributed to the interactions between the x and y field components [3], [22], [79], and [80]. This study reveals the fact that the harmonics under rotating fields formalize these shapes of dynamic hysteresis loops, and could only be recognized when the magnetizing circuit is injected by fundamentals with harmonics or at high flux density where harmonics naturally exist in the saturated flux density waveform. The core loss results in the sample produced by a circular rotating field with the third

harmonic compared with losses under pure sinusoidal rotating field are shown in Table 6.2.

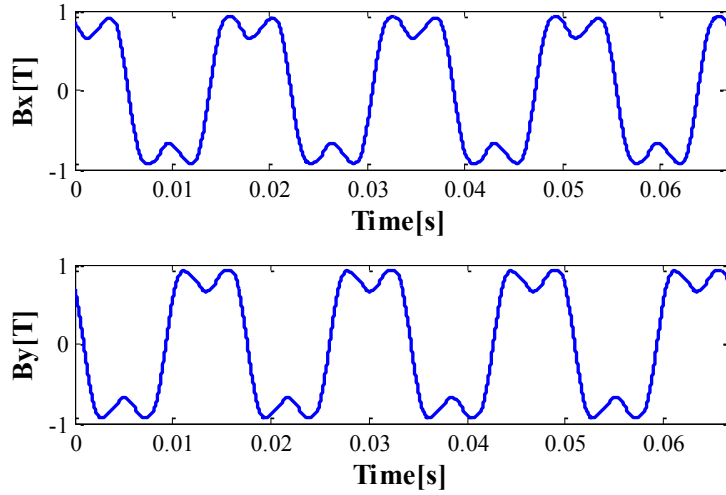


Fig. 6.29: The flux density waveforms B_x and B_y of 1.0T and 60 Hz fundamental component with a third harmonic for a M36G29 sample under rotating field.

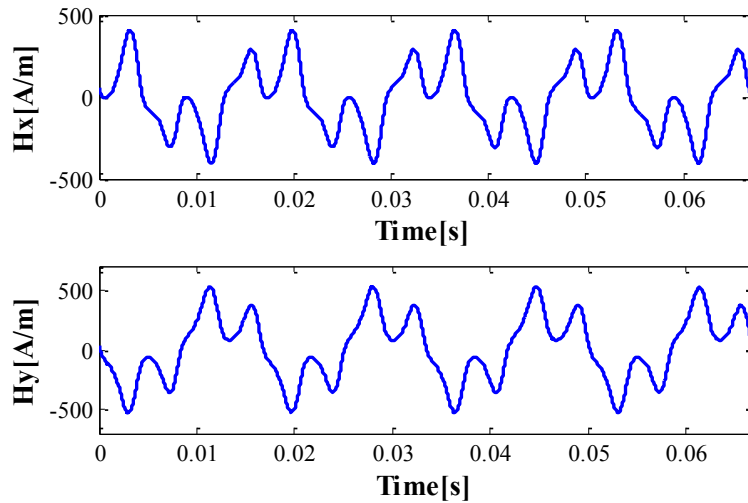


Fig. 6.30: The magnetic field strength waveforms H_x and H_y associated with the flux density waveforms B_x and B_y in Fig. 6.29 for a M36G29 sample under rotating field.

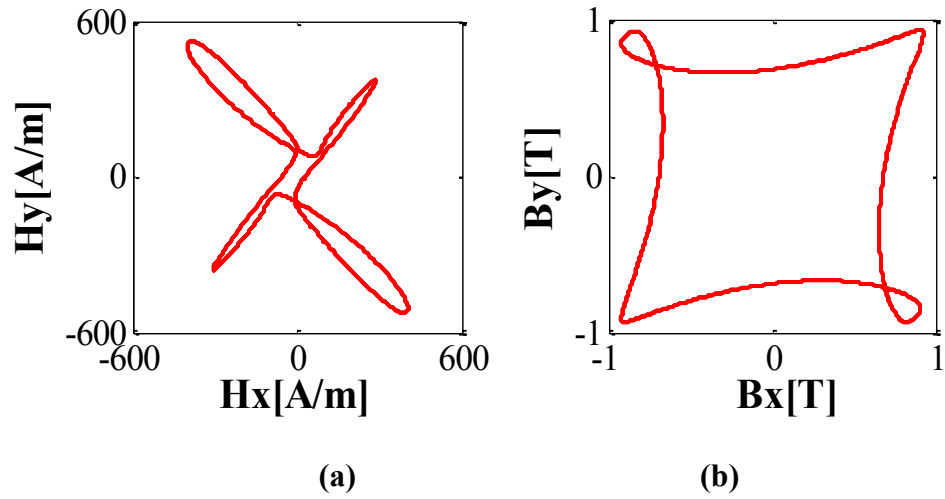


Fig. 6.31: (a) Locus of magnetic field strength for H_x and H_y waveforms in Fig. 6.30.
 (b) Locus of magnetic flux density for B_x and B_y waveforms in Fig. 6.29.

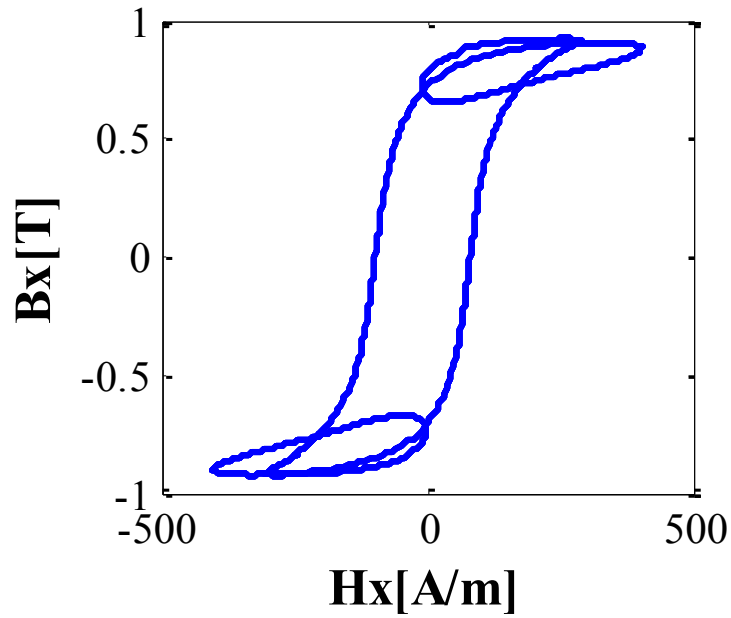


Fig. 6.32: The dynamic hysteresis loop in the x -direction for a M36G29 sample under a rotating field of 1T and 60 Hz fundamental component with a third harmonic.

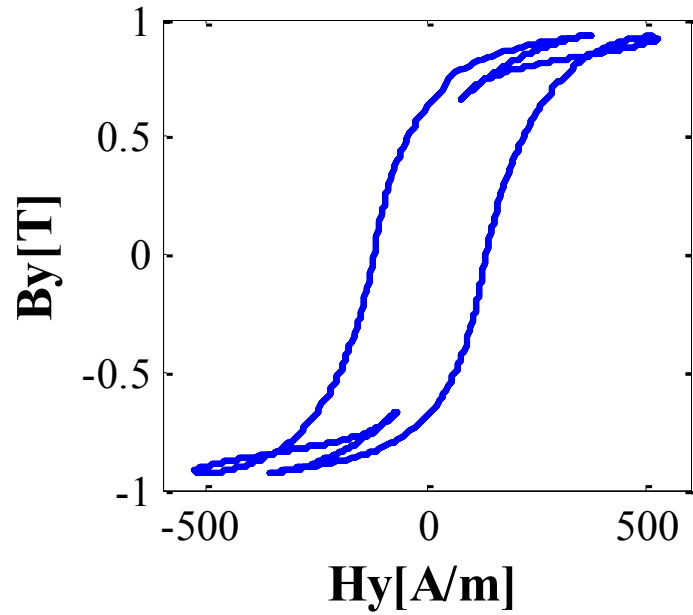


Fig. 6.33: The dynamic hysteresis loop in the y -direction for a M36G29 sample under a rotating field of 1T and 60 Hz fundamental component with a third harmonic.

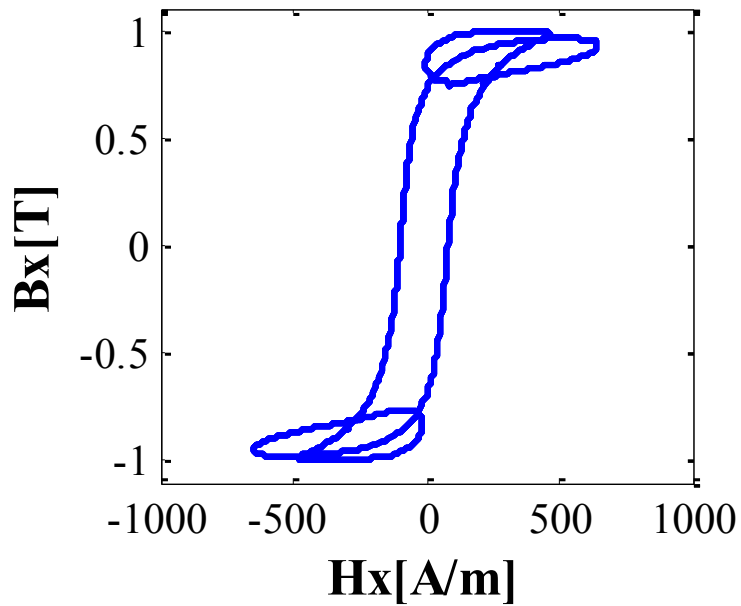


Fig. 6.34: The dynamic hysteresis loop in the x -direction for a M36G29 sample under a rotating field of 1.1T and 60 Hz fundamental component with a third harmonic.

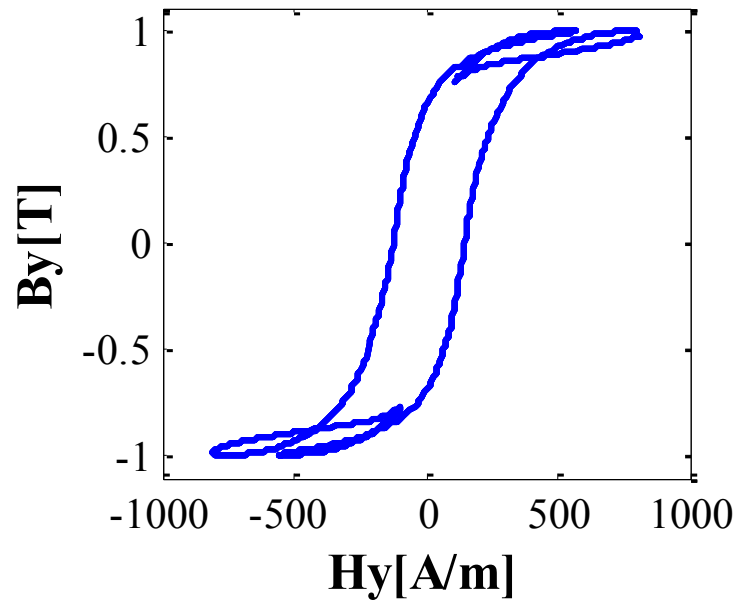


Fig. 6.35: The dynamic hysteresis loop in the y -direction for a M36G29 sample under a rotating field of 1.1T and 60 Hz fundamental component with a third harmonic.

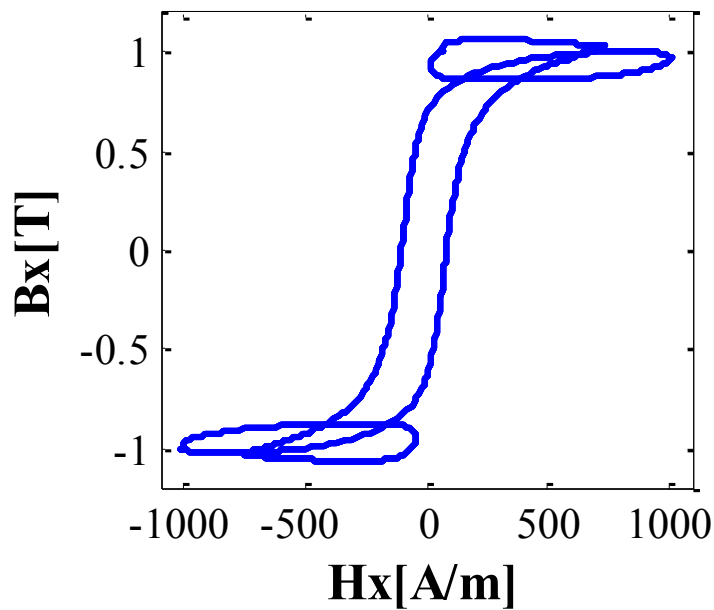


Fig. 6.36: The dynamic hysteresis loop in the x -direction for a M36G29 sample under a rotating field of 1.2T and 60 Hz fundamental component with a third harmonic.

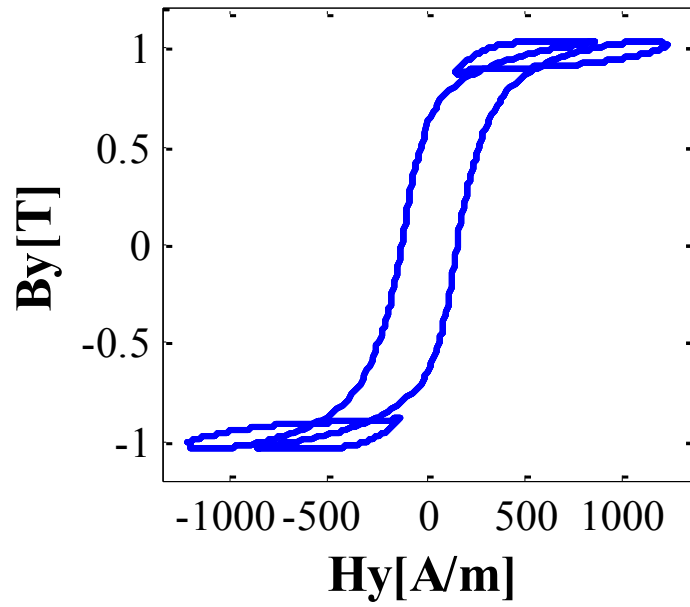


Fig. 6.37: The dynamic hysteresis loop in the y -direction for a M36G29 sample under a rotating field of 1.2T and 60 Hz fundamental component with a third harmonic.

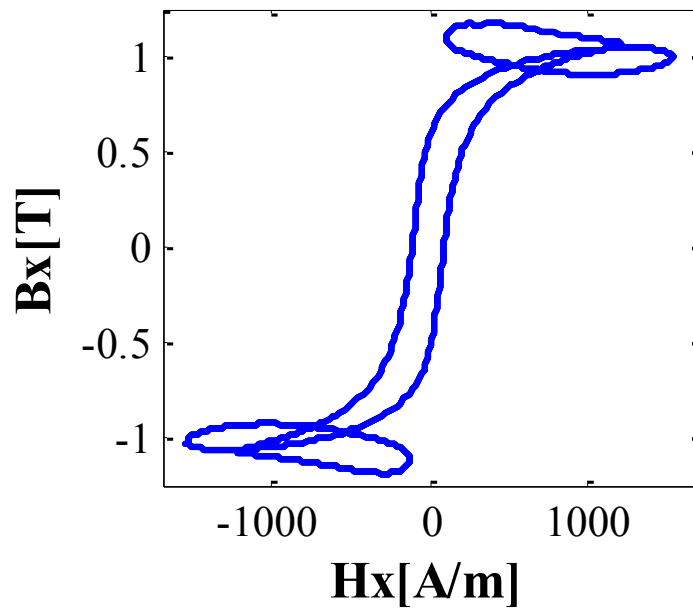


Fig. 6.38: The dynamic hysteresis loop in the x -direction for a M36G29 sample under a rotating field of 1.3T and 60 Hz fundamental component with a third harmonic.

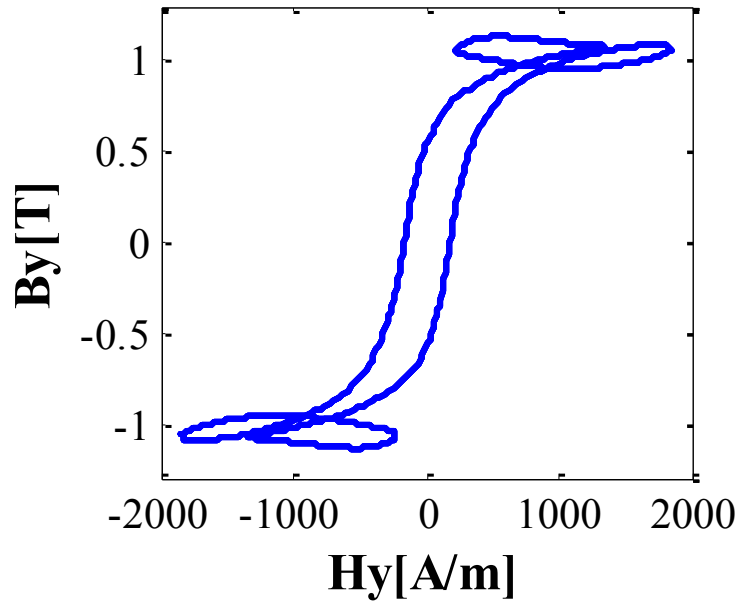


Fig. 6.39: The dynamic hysteresis loop in the y -direction for a M36G29 sample under a rotating field of 1.3T and 60 Hz fundamental component with a third harmonic.

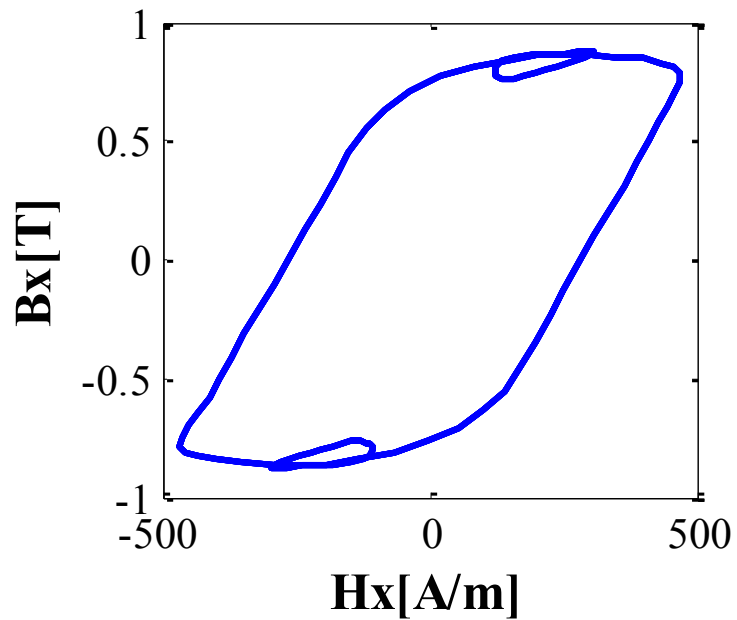


Fig. 6.40: The dynamic hysteresis loop in the x -direction for a M36G29 sample under a rotating field of 1T and 400 Hz fundamental component with a third harmonic.

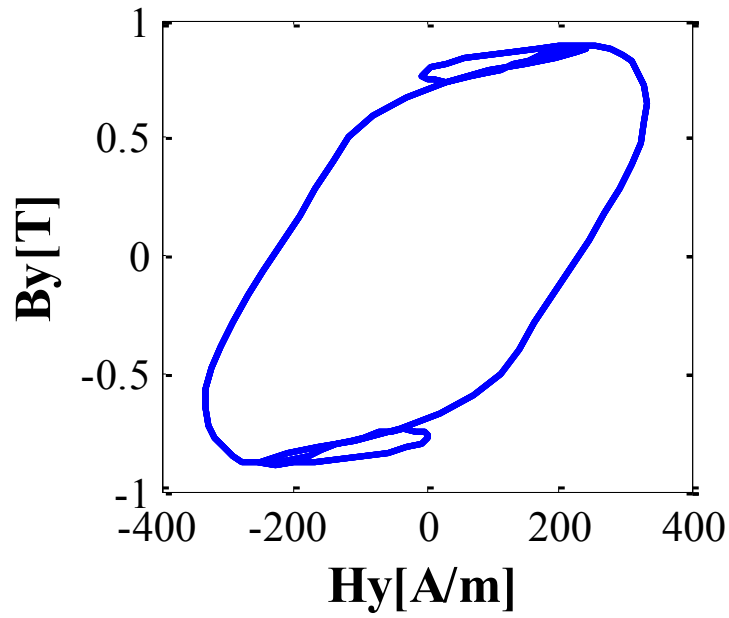


Fig. 6.41: The dynamic hysteresis loop in the y -direction for a M36G29 sample under a rotating field of 1T and 60 Hz fundamental component with a third harmonic.

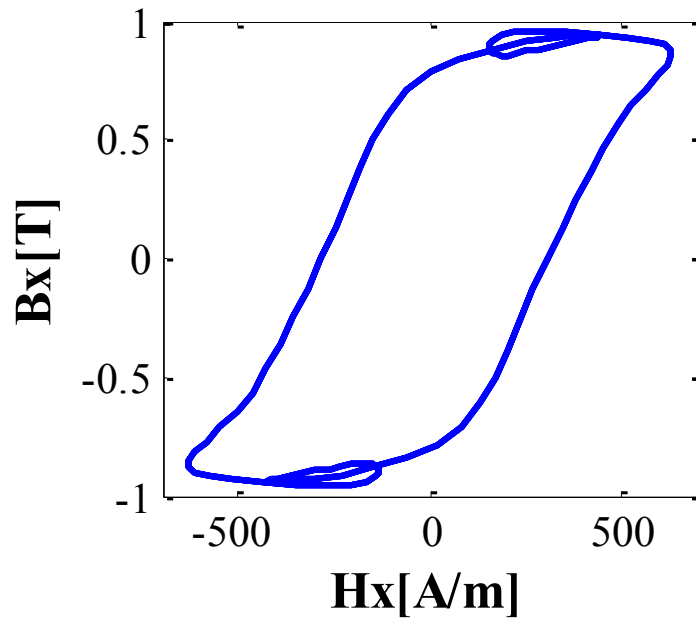


Fig. 6.42: The dynamic hysteresis loop in the x -direction for a M36G29 sample under a rotating field of 1.1T and 400 Hz fundamental component with a third harmonic.

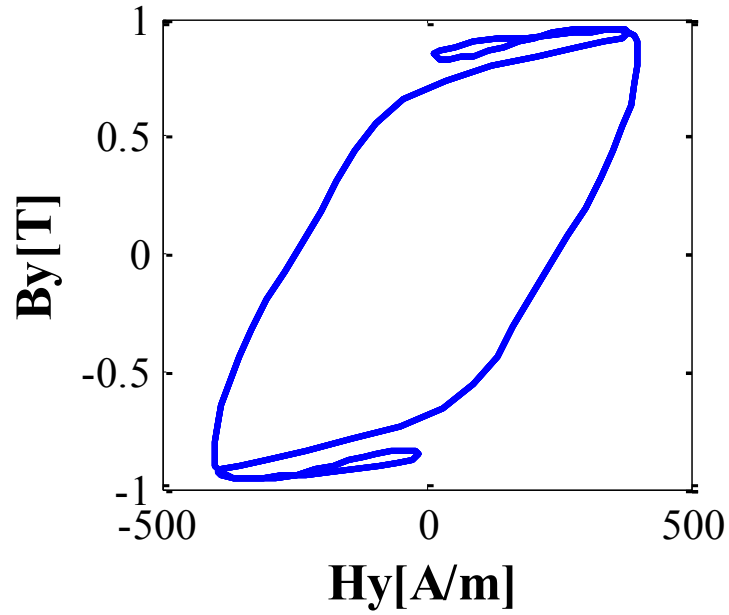


Fig. 6.43: The dynamic hysteresis loop in the y -direction for a M36G29 sample under a rotating field of 1.1T and 400 Hz fundamental component with a third harmonic.

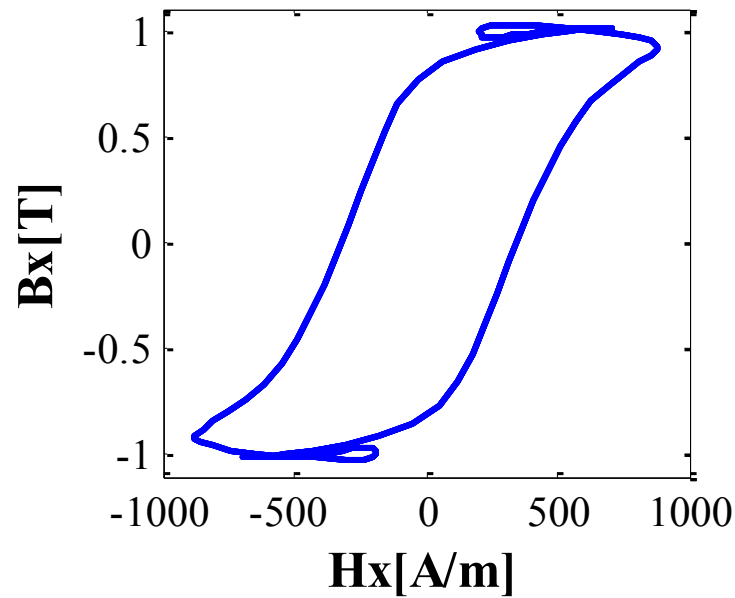


Fig. 6.44: The dynamic hysteresis loop in the x -direction for a M36G29 sample under a rotating field of 1.2T and 400 Hz fundamental component with a third harmonic.

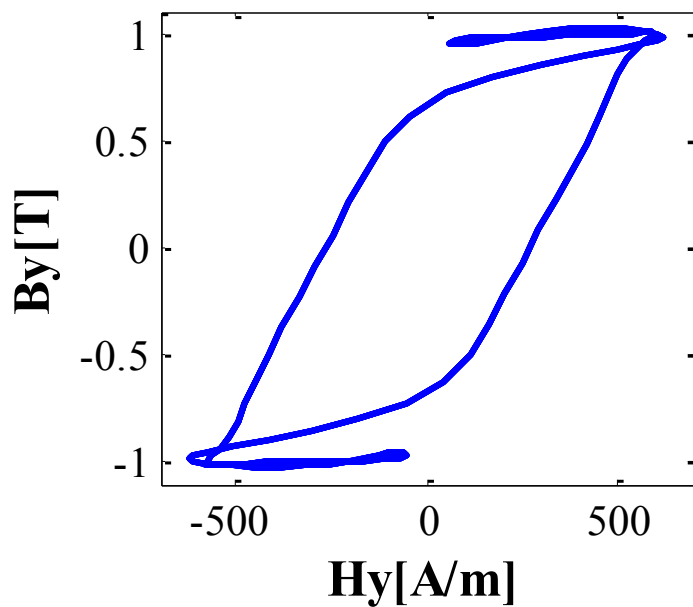


Fig. 6.45: The dynamic hysteresis loop in the y -direction for a M36G29 sample under a rotating field of 1.2T and 400 Hz fundamental component with a third harmonic.

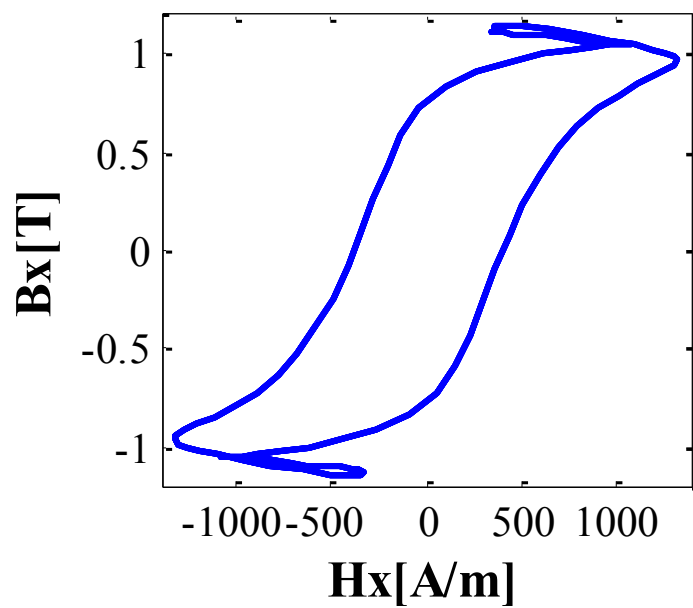


Fig. 6.46: The dynamic hysteresis loop in the x -direction for a M36G29 sample under a rotating field of 1.3T and 400 Hz fundamental component with a third harmonic.

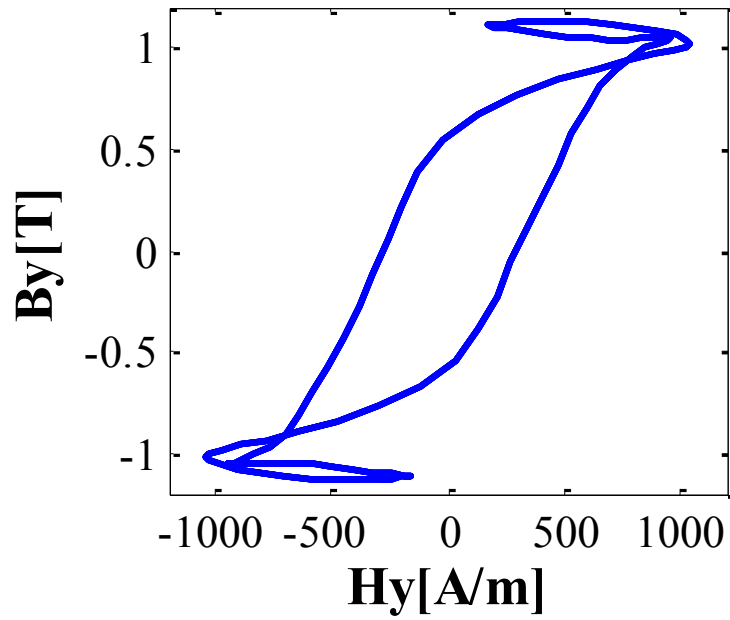


Fig. 6.47: The dynamic hysteresis loop in the y -direction for a M36G29 sample under a rotating field of 1.3T and 400 Hz fundamental component with a third harmonic.

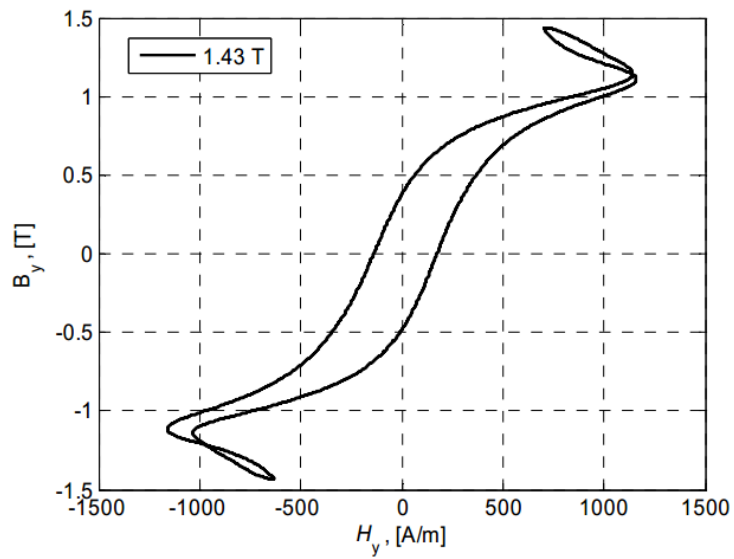


Fig. 6.48: The dynamic hysteresis loop in the y -direction under a rotating field of 1.43T peak [22].

Table 6.2: Power loss in the M36G29 lamination at 60 Hz and 400 Hz produced by rotating fields with and without the third harmonic component.

FREQ. [Hz]	THE PEAK OF FUNDAMENTAL FLUX DENSITY COMPONENT [T]	WITH HARMONIC P [W/KG]	WITHOUT HARMONIC P [W/KG]
60	1	6.6791	3.0125
	1.1	7.6816	3.2337
	1.2	8.5559	3.2738
	1.3	10.0067	3.1337
400	1	84.5364	54.7058
	1.1	100.1527	63.0516
	1.2	116.3949	71.1229
	1.3	135.4699	76.9782

C. Loss Comparison

The influence of harmonics on the total core loss under pulsating field has been studied, where empirical formulas and correction factors for the difference in loss due to the minor loops are set successfully [81], [82], and [83]. The effect of harmonics in rotating fields is still to be studied, and no relevant significant work has appeared in literature. In this work, power losses obtained in the sample under a rotating flux density with the third harmonic are compared with losses due to purely sinusoidal circular rotating field. Then, the power loss caused by exposing the sample to a rotating field created by the third harmonics only is calculated. Superposition is applied by summing the powers due to the harmonics and that of the purely rotating field. Differences in power losses at 60 Hz and 400 Hz are illustrated in Fig. 6.49 and Fig. 6.50, respectively. Another comparison between power losses obtained under rotating flux densities with the third harmonic, benchmarked against power losses obtained under pulsating fields with harmonics in x

and y directions. Power loss comparisons at 60 Hz and 400 Hz are illustrated in Fig. 6.51 and Fig. 6.52, respectively.

It is concluded that the power loss caused by rotating fields with harmonics can be estimated better by the sum of losses due to pulsating fields with harmonics. However, the sum of losses due to the purely sinusoidal rotating field and the loss due to the harmonics gives higher error.

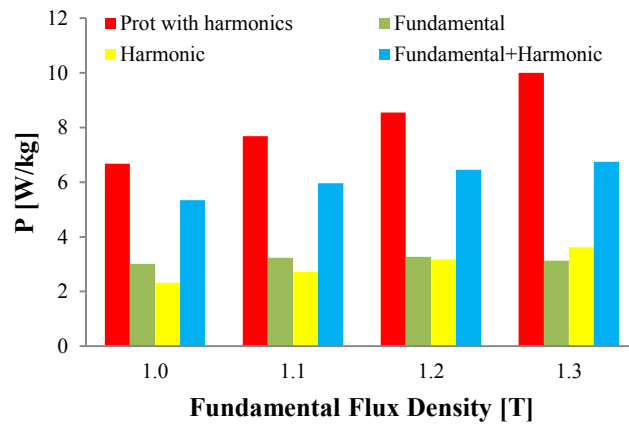


Fig. 6.49: A comparison between core losses obtained by: (a) Rotating field with a third harmonic. (b) Purely circular rotating field created by fundamentals. (c) Circular rotating field created by only third harmonics. (d) The algebraic sum of losses obtained in (b) and (c). Tests performed under fundamental frequency of 60 Hz for a M36G29 sample.

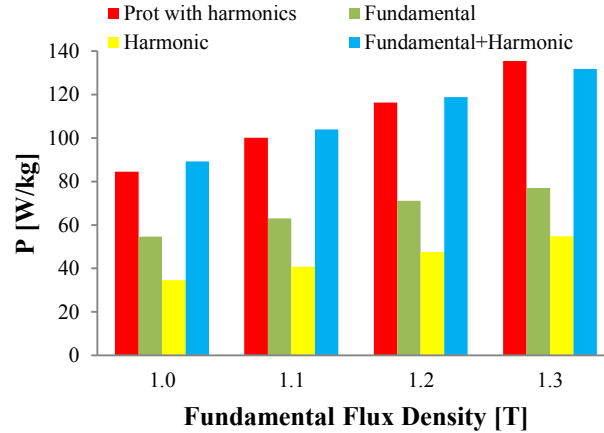


Fig. 6.50: A comparison between core losses obtained by: (a) Rotating field with a third harmonic. (b) Purely circular rotating field created by fundamentals. (c) Circular rotating field created by only third harmonics. (d) The algebraic sum of losses obtained in (b) and (c). Tests performed under fundamental frequency of 400 Hz for a M36G29 sample.

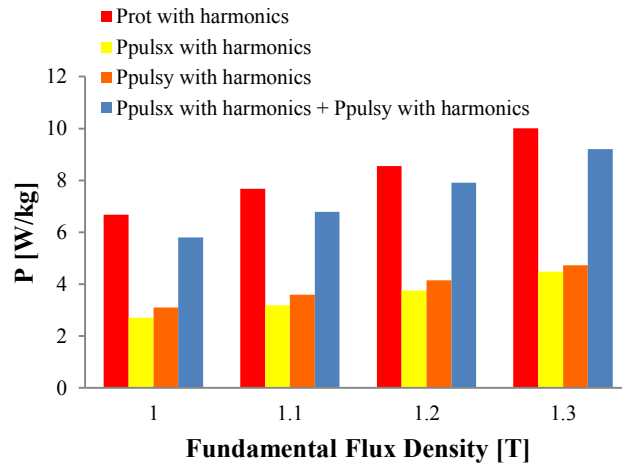


Fig. 6.51: A comparison between core losses obtained by: (a) Rotating field with a third harmonic. (b) Pulsating field with a third harmonic in x -direction. (c) Pulsating field with a third harmonic in y -direction. (d) The algebraic sum of losses obtained in (b) and (c). Tests performed under fundamental frequency of 60 Hz for a M36G29 sample.

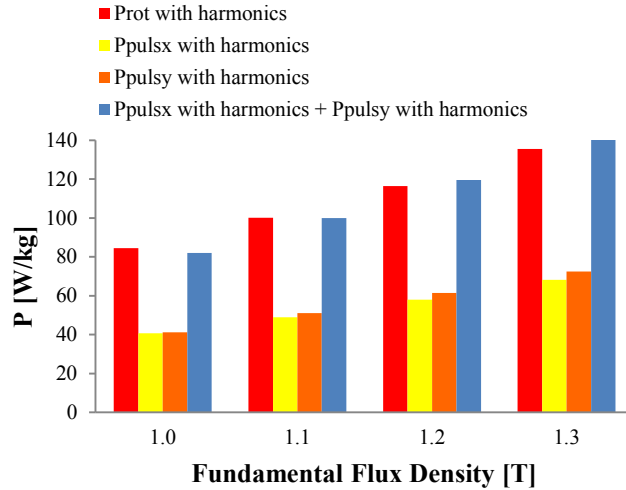


Fig. 6.52: A comparison between core losses obtained by: (a) Rotating field with a third harmonic. (b) Pulsating field with a third harmonic in x -direction. (c) Pulsating field with a third harmonic in y -direction. (d) The algebraic sum of losses obtained in (b) and (c). Tests performed under fundamental frequency of 400 Hz for a M36G29 sample.

6.2.4 Further Discussion

Since 1905, Madelung's rules are considered as a basic reference for modeling theories of hysteresis. These rules govern the hysteresis loop path behavior in magnetic materials, and state of being the minor loop nested inside the major loop borders. The observations of Madelung were formulated based on experimental studies using different alloys of steel [84] and [85]. Madelung's rules are valid under pulsating field, but when the material is subjected to a rotating field with harmonics, the minor loops leave outside the major loop borders and rotate in clockwise direction. More attention should be paid to generalize Madelung's rules under rotating fields.

6.2.5 Conclusion

The saturated flux density waveforms in machine laminations contain harmonics of which the third one is the most dominant. Minor hysteresis loop in machine laminations causes a serious challenge in core loss estimation, especially under rotating magnetic field. The unusual behavior of the hysteresis loop under rotating fields which appeared in literature is attributed to the harmonics in the saturated flux density waveforms. The minor loop under pulsating fields is confined entirely within the major loop which is consistent with Madelung's rules, while under rotating field the minor loop leaves the major loop.

Measurements were carried out on a non oriented silicon steel sample of M36G29 with different fundamental frequencies of interest to the industry, 60 Hz and 400 Hz, with consideration of a third harmonic at each frequency. Results are presented and discussed.

7. CONCLUSIONS AND RECOMMENDATIONS

7.1 Conclusions

Methods and devices for the measurement of rotational core losses have been reviewed. The field-metric method is seen to be the most convenient and reliable method, which is used in this work. Techniques for measuring components of the magnetic flux density (\mathbf{B}) and the magnetic field strength (\mathbf{H}) are presented.

A novel design of a magnetizing circuit based on an electromagnetic Halbach array is proposed, which generates uniform and homogeneous flux densities inside the sample; this uniformity gives the researchers the opportunity to improve the test conditions, where measuring techniques of \mathbf{B} and \mathbf{H} became better. Using electromagnets to establish the Halbach pattern; provides more flexibility in control (controllability in field magnitude and in signal shape). This magnetizing array is capable of producing pulsating, circular, and elliptical fields with any aspect ratio within the sample under test.

Extensive simulations of different magnetizing circuits used in rotational loss measurements are performed. Results show that the circular sample with the Halbach circuit has the lowest standard deviation, which makes it the best shape to be tested since magnetic flux uniformity is the highest.

The new test fixture is prototyped and operated successfully using dSPACE. The validity of this fixture is tested by comparing its results with two different Epstein frames, where experimental results show a very good matching with high correlation coefficients. Measurements were carried out on five silicon steel circular samples of 20 cm diameter.

These samples are: M15 gauge 29, M19 gauge 29, M19 gauge 24, M36 gauge 29, and M36 gauge 26.

Basic measurements show that it is not accurate to estimate the rotational core losses by the sum of pulsating losses produced in x and y directions, and the difference between the x and y loss components under rotating field is mainly attributed to the asymmetry in the magnetic permeability.

A comprehensive study been conducted to understand the influence of rotating fields on core loss estimation. The investigation is implemented on three different types of machines, 2-pole IM, 2-pole BLDCM, and 6-4 SRM. Simulations show that around 80 % of stator is subjected to a rotating field with an aspect ratio less than 0.2, and the rotational core losses with high aspect ratios are concentrated mostly at the tooth roots. The error in different parts of the machine that neglects the rotational field effect can be around 50 % obtained in the SRM using M36G29 at 60 Hz.

Rotational core loss measurements under CW and CCW directions show noticeable differences. Results manifest that the anisotropy of the magnetic material is responsible for the asymmetry in the CW and CCW rotational core losses, where the permeability varies significantly when the direction of rotating field is reversed. A comparison between the machine types show that the IM experiences the highest effect of field reversing follows by BLDCM, and then the SRM is the least affected.

The negative power observed during the measurement of rotational core losses using the field metric method has been studied. The negative power appears in one loss component

is caused by the reversal of the field direction, and considered to be acceptable as long as the total loss is positive. The negative value in the total rotational loss is caused by sensor misalignment, and could not be recognized in the new test fixture until the \mathbf{B} coils were physically misaligned.

Minor hysteresis loops in machine laminations causes a serious challenge in core loss estimation, especially under rotating magnetic fields. The unusual behavior of the hysteresis loop under rotating fields which has appeared in literature is attributed to the harmonics in the saturated flux density waveforms. The minor loop under pulsating fields is confined entirely within the major loop which is consistent with Madelung's rules, while under rotating field the minor loop leaves the major loop.

7.2 Recommendations and Proposed Future Research

In this section, some recommendations are proposed as suggested future research:

- Build an accurate mathematical model which will be able to predict the total core losses in machine laminations.
- Improve the sensing system for the test fixture, especially the tangential coils. A multi-coil sensor for tangential magnetic field is suggested to be examined [33]. A commercial Rogowski-Chattock potentiometer with high accuracy and low noise effect might be worthwhile to try [86]. Shielding the sample during the measurement is recommended to achieve more homogeneous magnetization, thus decreasing in stray flux, and better magnetic field strength waveform will be obtained from the sensor [87].

- Build other designs of magnetizing circuits producing rotating field. This could benefit the research area by providing the researchers with comparable results from different test apparatus. This will be an important step toward identifying standard techniques for the measurement of rotational core losses.
- Power amplifier with higher capability is needed, where the power restrictions of the current amplifier limit the test to 1.4 T with a highest frequency of 1 kHz. More powerful power amplifier allows for higher frequency tests, and higher flux density levels in the saturation region.
- To get precise results, the magnetic flux density has to be kept sinusoidal as much as possible without exceeding an acceptable form factor (FF). Results with FF below 10% are considered to be acceptable by the ASTM standard [88]. A feedback control system to the magnetizing circuit is recommended to guarantee a sinusoidal signal along the measurement profile especially in the saturation region [89] and [90].
- More materials with different gauges and under a wide range of frequencies should be investigated in order to build a rotational core loss database. This will be of benefit to start providing researchers and machine designers with core loss data under rotating field.
- Loss separation under rotating field is required, where detailed eddy current loss model under rotating field seems to be an imperative need to understand the behavior of rotational eddy currents [91].
- Many attempts are accomplished to improve the core loss formulations in order to compensate the additional losses due to the harmonics in pulsating field. The

effect of harmonics on core losses under rotating fields is still to be investigated and no relevant work has appeared in literature. It is recommended to perform tests under rotating fields with different orders of harmonics to find out the influence of harmonics on the total loss, and try to present that mathematically through a correction factor.

- Particular attention should be paid to generalize Madelung's rules under rotating fields.
- Simulations of different types and designs of machines should be performed to study the effect of geometrical shapes on rotational core loss production. The expected outcome of this suggestion is to end up with an optimized geometrical shape of electric machine with lower core losses.

7.3 Contribution

This thesis contributes to date to the topic of rotational core losses through the following publications:

7.3.1 Journal Papers

1. **N. Alatawneh** and P. Pillay, "Design of a novel test fixture to measure rotational core losses in machine laminations," accepted for publication in the *IEEE Transactions on Industry Applications*.
2. **N. Alatawneh** and P. Pillay, "Rotational Core Loss and Permeability Measurements in Machine Laminations with Reference to Permeability Asymmetry," *IEEE Transactions on Magnetics*, vol. 48, pp. 1445-1448, 2012.

3. **N. Alatawneh** and P. Pillay, "Test Specimen Shape Considerations for the Measurement of Rotational Core Losses," *IEEE Transactions on Energy Conversion*, vol. 27, pp. 151-159, 2012.

7.3.2 Conference Papers

1. **N. Alatawneh** and P. Pillay, " The Impact of Rotating Field on Core Loss Estimation in Electrical Machine Laminations," in Energy Conversion Congress and Exposition (ECCE), Raleigh, North Carolina, USA, Sep., 2012.
2. **N. Alatawneh** and P. Pillay, "Rotational Core Loss Measurements in Clockwise and Counterclockwise Directions," Submitted to the International Conference on Electrical Machines (ICEM), Marseille, France, Sep., 2012.
3. **N. Alatawneh** and P. Pillay, "Design of a novel test fixture to measure rotational core losses in machine laminations," in Energy Conversion Congress and Exposition (ECCE), Phoenix, Arizona, USA, Sep., 2011.
4. **N. Alatawneh** and P. Pillay, "Rotational Core Loss Measurements in Machine Laminations with Reference to Permeability Asymmetry," 20th Soft Magnetic Materials Conference, (SMM. 20), Kos Island, Greece, Sep., 2011.
5. **N. Alatawneh** and P. Pillay, "Test Specimen Shape Considerations for the Measurement of Rotational Core Losses," *IEEE International Electric Machines and Drives (IEMDC)*, Toronto, ON, Canada, May, 2011.
6. Z. Yu, **N. Alatawneh**, M. C. Cheng, and P. Pillay, "Magnetic core losses measurement instrumentations and a dynamic hysteresis loss model," *IEEE Electrical Power & Energy Conference (EPEC)*, Montreal, Canada, 2009.

REFERENCES

- [1] J. Pyrhönen, *et al.*, *Design of Rotating Electrical Machines*, 1st ed. Chippingham: John Wiley & Sons, 2009.
- [2] A. Moses, "Importance of rotational losses in rotating machines and transformers," *Journal of Materials Engineering and Performance*, vol. 1, pp. 235-244, 1992.
- [3] T. Sasaki, *et al.*, "Measurement of rotational power losses in silicon-Iron sheets using wattmeter method," *IEEE Transactions on Magnetics*, vol. 21, pp. 1918-1920, 1985.
- [4] F. Fiorillo and A. M. Rietto, "Extended induction range analysis of rotational losses in soft magnetic materials," *IEEE Transactions on Magnetics*, vol. 24, pp. 1960-1962, 1988.
- [5] M. Enokizono and J. D. Sievert, "Magnetic field and loss analysis in an apparatus for the determination of rotational loss," *Physica Scripta*, vol. 39, pp. 356-359, 1989.
- [6] J. Sievert, *et al.*, "European intercomparison of measurements of rotational power loss in electrical sheet steel," *Journal of Magnetism and Magnetic Materials*, vol. 160, pp. 115-118, 1996.
- [7] G. A. McCoy, *et al.*, *Energy-Efficient Electric Motor Selection Handbook*, Revision 3, January, 1993.
- [8] C. Gonzalez-Moran, *et al.*, "Classification of rotational losses zones in stator cores of induction motors using fuzzy-clustering," in *18th International Conference on Electrical Machines, 2008. ICEM 2008.*, 2008, pp. 1-4.
- [9] G. Diaz, *et al.*, "Characterization of Flux Rotation and of the Ensuing Core Losses in the Stator of Induction Motors," *IEEE Transactions on Energy Conversion* vol. 23, pp. 34-41, 2008.
- [10] H. V. Sande, *et al.*, "Simulation of a three-phase transformer using an improved anisotropy model," *IEEE Transactions on Magnetics*, vol. 40, pp. 850-855, 2004.
- [11] F. G. Bailey, "The Hysteresis of Iron and Steel in a Rotating Magnetic Field," *Philosophical Transactions of the Royal Society of London*, vol. 107, pp. 715-746, 1896.
- [12] J. G. Zhu, "Numerical modelling of magnetic materials for computer aided design of electromagnetic devices," PhD, Sydney, 1994.
- [13] F. Brailsford, "Rotational hysteresis loss in electrical sheet steels," *Journal of the Institution of Electrical Engineers*, vol. 83, pp. 566-575, 1938.

- [14] G. Youguang, *et al.*, "Measurement and Modeling of Rotational Core Losses of Soft Magnetic Materials Used in Electrical Machines: A Review," *IEEE Transactions on Magnetics*, vol. 44, pp. 279-291, 2008.
- [15] C. R. Boon and J. E. Thompson, "Alternating and rotational power loss at 50 c/s in 3% silicon-iron sheets," *Proceedings of the Institution of Electrical Engineers*, vol. 112, pp. 2147-2151, 1965.
- [16] F. Fiorillo, *Characterization and Measurement of Magnetic Materials*, 1st ed. Torino: Academic Press, 2004.
- [17] A. Moses and B. Thomas, "The spatial variation of localized power loss in two practical transformer T-joints," *IEEE Transactions on Magnetics*, vol. 9, pp. 655-659, 1973.
- [18] K. Atallah and D. Howe, "Calculation of the rotational power loss in electrical steel laminations from measured H and B ," *IEEE Transactions on Magnetics*, vol. 29, pp. 3547-3549, 1993.
- [19] M. Enokizono, *et al.*, "Rotational power loss of silicon steel sheet," *IEEE Transactions on Magnetics*, vol. 26, pp. 2562-2564, 1990.
- [20] J. Sievert, *et al.*, "The measurement of rotational power loss in electrical sheet steel using a vertical yoke system," *Journal of Magnetism and Magnetic Materials*, vol. 112, pp. 91-94, 1992.
- [21] M. Enokizono and I. Tanabe, "Studies on a new simplified rotational loss tester," *IEEE Transactions on Magnetics*, vol. 33, pp. 4020-4022, 1997.
- [22] M. Belkasim, "Identification of Loss Models from Measurements of the Magnetic Properties of Electrical Steel Sheets," MSc Thesis, Helsinki University of Technology, 2008.
- [23] S. Tumanski, *Handbook of Magnetic Measurements*. Boca Raton: Taylor & Francis Group, 2011.
- [24] M. A. Plonus, *Applied Electromagnetics*, 1st ed. New York: McGraw-Hill, 1978.
- [25] H. Pfutzner and G. Krismanic, "The needle method for induction tests: sources of error," *IEEE Transactions on Magnetics*, vol. 40, pp. 1610-1616, 2004.
- [26] G. Krismanic, *et al.*, "A hand-held sensor for analyses of local distributions of magnetic fields and losses," *Journal of Magnetism and Magnetic Materials*, vol. 215-216, pp. 720-722, 2000.
- [27] R. P. Winch., *Electricity and magnetism*, 2nd ed. Englewood Cliffs, New Jersey: Prentice-Hall, 1963.

- [28] P. Flanders, "A hall sensing magnetometer for measuring magnetization, anisotropy, rotational loss and time effects," *IEEE Transactions on Magnetics*, vol. 21, pp. 1584-1589, 1985.
- [29] H. Pftzner and P. Schonhuber, "On the problem of the field detection for single sheet testers," *IEEE Transactions on Magnetics*, vol. 27, pp. 778-785, 1991.
- [30] S. Tumanski, "Induction coil sensors - a review," *Measurement Science and Technology* vol. 18, pp. 31-46, 2007.
- [31] H. Zijlstra, *Experimental methods in magnetism, Vol. 2 : measurement of magnetic quantities*. Amsterdam: North-Holland Pub. Co., 1967.
- [32] Z. Jin Jiang, *et al.*, "Improved measurement with 2-D rotating fluxes considering the effect of internal field," *IEEE Transactions on Magnetics*, vol. 41, pp. 3709-3711, 2005.
- [33] S. Tumanski, "A multi-coil sensor for tangential magnetic field investigations," *Journal of Magnetism and Magnetic Materials*, vol. 242-245, pp. 1153-1156, 2002.
- [34] M. Enokizono, *et al.*, "Measurement of Iron Loss Using Rotational Magnetic Loss Measurement Apparatus," *IEEE Translation Journal on Magnetics in Japan*, vol. 6, pp. 508-514, 1991.
- [35] T. Nakata, *et al.*, "Improvement of measuring accuracy of magnetic field strength in single sheet testers by using two H coils," *IEEE Transactions on Magnetics*, vol. 23, pp. 2596-2598, 1987.
- [36] J. J. Zhong, *et al.*, "Techniques and Apparatus for Measuring Rotational Core Losses of Soft Magnetic Materials," *Journal of Electronic Science and Technology*, vol. 5, pp. 218-225, 2007.
- [37] S. Tumanski, "New Design of the Magnetising Circuit for 2-D testing of Electrical Steel," *Przegląd Elektrotechniczny*, vol. 5, pp. 32-34, 2005.
- [38] N. Nencib, *et al.*, "2D analysis of rotational loss tester," *IEEE Transactions on Magnetics*, vol. 31, pp. 3388-3390, 1995.
- [39] J. Mallinson, "One-sided fluxes - A magnetic curiosity?," *IEEE Transactions on Magnetics*, vol. 9, pp. 678-682, 1973.
- [40] C. Jae-Seok and Y. Jeonghoon, "Design of a Halbach Magnet Array Based on Optimization Techniques," *IEEE Transactions on Magnetics*, vol. 44, pp. 2361-2366, 2008.
- [41] H. Raich, P. Blümler, "Design and construction of a dipolar Halbach array with a homogeneous field from identical bar magnets: NMR Mandhalas," *Concepts in Magnetic Resonance Part B-Magnetic Resonance Engineering*, vol. 23B, pp. 16-25, 2004.

- [42] K. Halbach, "Physical and Optical Properties of Rare Earth Cobalt Magnets," *Nuclear Instruments and Methods*, vol. 187, pp. 109-117, 1981.
- [43] Z. Q. Zhu and D. Howe, "Halbach permanent magnet machines and applications: a review," *IEE Proceedings-Electric Power Applications*, vol. 148, pp. 299-308, 2001.
- [44] A. Hasenzagl, *et al.*, "Novel 3-phase excited single sheet tester for rotational magnetization," *Journal of Magnetism and Magnetic Materials*, vol. 160, pp. 180-182, 1996.
- [45] V. Gorican, *et al.*, "Unreliable determination of vector B in 2-D SST," *Journal of Magnetism and Magnetic Materials*, vol. 254-255, pp. 130-132, 2003.
- [46] C. Ragusa and F. Fiorillo, "A three-phase single sheet tester with digital control of flux loci based on the contraction mapping principle," *Journal of Magnetism and Magnetic Materials*, vol. 304, pp. e568-e570, 2006.
- [47] M. F. Ashby, *Materials Selection in Mechanical Design* 3rd ed.: Elsevier Butterworth-Heinemann, 2005.
- [48] Physical Properties of Acrylic Sheets, Data sheet. Available: <http://www.kaysons.in>
- [49] N. Stranges, "An investigation of iron losses due to rotating flux in three phase induction motor core," PhD, McMaster University, Hamilton, 2000.
- [50] Z. Gmyrek, *et al.*, "Estimation of Iron Losses in Induction Motors: Calculation Method, Results, and Analysis," *IEEE Transactions on Industrial Electronics*, vol. 57, pp. 161-171, 2010.
- [51] C. A. Hernandez-Aramburo, *et al.*, "Estimating rotational iron losses in an induction machine," *IEEE Transactions on Magnetics*, vol. 39, pp. 3527-3533, 2003.
- [52] P. Hudak, *et al.*, "Core Loss Analysis of the Reluctance Synchronous Motor with Barrier Rotors," *Journal of Electrical Engineering*, vol. 55, pp. 273-276, 2004.
- [53] N. Takahashi, *et al.*, "Analysis of iron loss under distorted elliptical rotating flux of SPM motor," *The International Journal for Computation and Mathematics in Electrical and Electronic Engineering*, vol. 24, no. 2, pp. 385-395, 2005.
- [54] A. J. Moses, "Rotational magnetization-problems in experimental and theoretical studies of electrical steels and amorphous magnetic materials," *IEEE Transactions on Magnetics*, vol. 30, pp. 902-906, 1994.
- [55] N. Stranges and R. D. Findlay, "Measurement of rotational iron losses in electrical sheet," *IEEE Transactions on Magnetics*, vol. 36, pp. 3457-3459, 2000.
- [56] K. H. J. Buschow and F. R. d. Boer, *Physics of Magnetism and Magnetic Materials*, 1st ed. New York: Kluwer Academic Publishers, 2003.

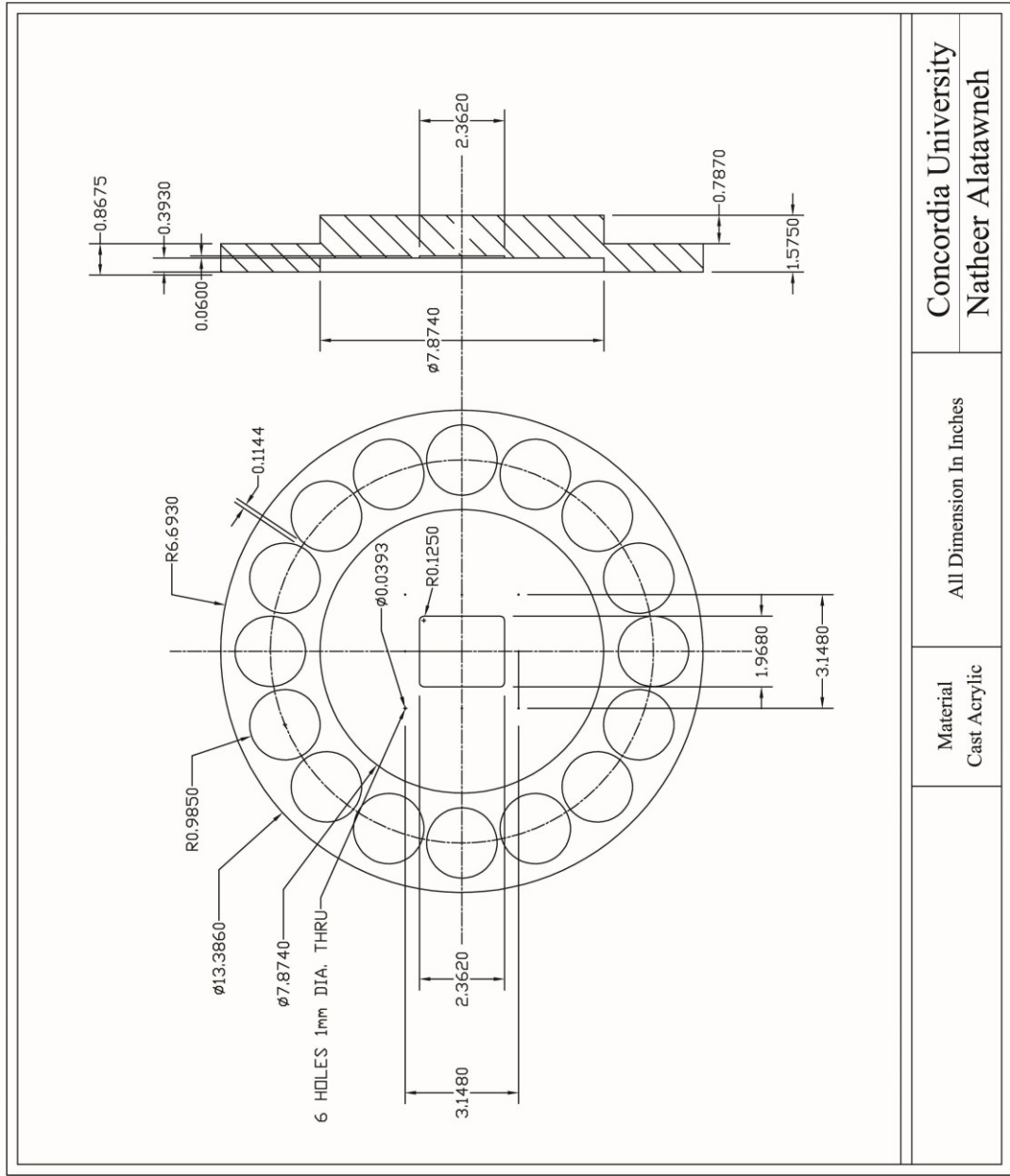
- [57] J. Franklin, *Classical electromagnetism*, 1st ed. San Francisco: Addison Wesley Longman, 2005.
- [58] M. S. Lancarotte and A. de Arruda Penteado, "Improving the magnetizing device design of the single sheet tester of two-dimensional properties," *Journal of Magnetism and Magnetic Materials*, vol. 269, pp. 346-351, 2004.
- [59] L. Yang, *et al.*, "Analysis of magnetic field in three-phase induction motor core considering two-dimensional vector magnetic properties," in *International Conference on Electrical Machines and Systems (ICEMS)*, 2010, pp. 1822-1825.
- [60] W. Salz and K. A. Hempel, "Power loss in electrical steel under elliptically rotating flux conditions," *IEEE Transactions on Magnetics*, vol. 32, pp. 567-571, 1996.
- [61] P. Arboleya, *et al.*, "Fuzzy-clustering as a tool for magnetic losses analysis in induction machines," in *18th International Conference on Electrical Machines, ICEM 2008.*, 2008, pp. 1-5.
- [62] G. Diaz, *et al.*, "Analytical Interpretation and Quantification of Rotational Losses in Stator Cores of Induction Motors," *IEEE Transactions on Magnetics*, vol. 43, pp. 3861-3867, 2007.
- [63] J. Sievert, "Two-dimensional magnetic measurements – History and achievements of the workshop," *Journal of Electrical Review*, vol. 87, pp. 1-10, 2011.
- [64] A. J. Moses, "Possible Future Trends and Research Challenges related to 1 & 2 D Magnetic Properties of Soft Magnetic Materials," *Journal of Electrical Review*, vol. 87, pp. 11-16, 2011.
- [65] Z. Jin Jiang, *et al.*, "Improved measurement with 2-D rotating fluxes considering the effect of internal field," *IEEE Transactions on Magnetics*, vol. 41, pp. 3709-3711, 2005.
- [66] N. Stranges, *et al.*, "Iron losses in AC machines due to rotational flux conditions," in *Canadian Conference on Electrical and Computer Engineering*, , 14-17 Sep, 1993, pp. 1049-1052.
- [67] S. Zurek and T. Meydan, "Errors in the power loss measured in clockwise and anticlockwise rotational magnetisation. Part 2: Physical phenomena," *IEE Proceedings Science, Measurement and Technology*, vol. 153, pp. 152-157, 2006.
- [68] N. Alatawneh and P. Pillay, "Test Specimen Shape Considerations for the Measurement of Rotational Core Losses," *IEEE Transactions on Energy Conversion*, vol. PP, pp. 1-9, 2011.
- [69] K. E. Blazek and C. Riviello, "New magnetic parameters to characterize cold-rolled motor lamination steels and predict motor performance," *IEEE Transactions on Magnetics*, vol. 40, pp. 1833-1838, 2004.
- [70] N. Nencib, *et al.*, "Macroscopic anisotropy characterization of SiFe using a rotational single sheet tester," *IEEE Transactions on Magnetics*, vol. 31, pp. 4047-4049, 1995.

- [71] G. Krismanic, "Recent developments and trends in measurements of two-dimensional magnetic properties," *Journal of Electrical Engineering*, vol. 55, pp. 45-48, 2004.
- [72] R. P. Ward, *Introduction to electrical engineering*, 3rd ed. Englewood Cliffs, New Jersey: Prentice-Hall, 1960.
- [73] J. J. Zhong, *et al.*, "Characteristics of soft magnetic composite material under rotating magnetic fluxes," *Journal of Magnetism and Magnetic Materials*, vol. 299, pp. 29-34, 2006.
- [74] Y. Maeda, *et al.*, "Rotational power loss of magnetic steel sheets in a circular rotational magnetic field in CCW/CW directions," *Journal of Magnetism and Magnetic Materials*, vol. 320, pp. e567-e570, 2008.
- [75] D. Zill and M. Cullen, *Advanced Engineering Mathematics*, 3rd ed. Sudbury, Massachusetts, 2006.
- [76] P. Rupanagunta, *et al.*, "Determination of iron core losses under influence of third-harmonic flux component," *IEEE Transactions on Magnetics*, vol. 27, pp. 768-777, 1991.
- [77] J. S. Hsu, *et al.*, "Losses influenced by third-harmonic flux in induction motors," *IEEE Transactions on Energy Conversion*, vol. 6, pp. 461-468, 1991.
- [78] J. S. Hsu, *et al.*, "Potential for loss reductions in transformers through utilization of third-harmonic flux," in *Industry Applications Society Annual Meeting, 1988., Conference Record of the 1988 IEEE*, 1988, pp. 1443-1450 vol.2.
- [79] T. Tanaka, *et al.*, "Measurement of AC Magnetic Properties in a Single Strip Sample," presented at the The Second International Workshop on Two-Dimensional Magnetic Measurement and its Properties, Oita, Japan, pp. 43-55, 1992.
- [80] K. Alkar, "Measuring Power Losses of Electrical Steel Sheets in One- and Two-Dimensional Magnetic Fields," MSc Thesis, Helsinki University of Technology, 2009.
- [81] J. Lavers and P. Biringer, "Prediction of core losses for high flux densities and distorted flux waveforms," *IEEE Transactions on Magnetics*, vol. 12, pp. 1053-1055, 1976.
- [82] J. Lavers, *et al.*, "Estimation of core losses when the flux waveform contains the fundamental plus a single odd harmonic component," *IEEE Transactions on Magnetics*, vol. 13, pp. 1128-1130, 1977.
- [83] J. Lavers, *et al.*, "A simple method of estimating the minor loop hysteresis loss in thin laminations," *IEEE Transactions on Magnetics*, vol. 14, pp. 386-388, 1978.
- [84] M. Brokate and J. Sprekels, *Hysteresis and Phase Transitions*. New York, 1996.
- [85] M. S. Pierce, *et al.*, "Disorder-induced magnetic memory: Experiments and theories," *Physical Review B*, vol. 75, pp. 1-23, 2007.

- [86] <http://www.rocoil.co.uk>.
- [87] D. Makaveev, *et al.*, "Accurate field strength measurement in rotational single sheet testers," *Journal of Magnetism and Magnetic Materials*, vol. 215–216, pp. 673-676, 2000.
- [88] M. J. Manyage and P. Pillay, "New Epstein Frame for Core Loss Measurements at High Frequencies and High Flux Densities," in *IEEE Industry Applications Society Annual Meeting (IAS)*, 2008, pp. 1-6.
- [89] S. Baranowski, *et al.*, "Comparison of various methods of the control of flux density waveform," *Journal of Magnetism and Magnetic Materials*, vol. 0, pp. 1-3, 2005.
- [90] S. Zurek, *et al.*, "Use of novel adaptive digital feedback for magnetic measurements under controlled magnetizing conditions," *IEEE Transactions on Magnetics*, vol. 41, pp. 4242-4249, 2005.
- [91] W. Salz, *et al.*, "Loss separation under elliptically rotating B-field with bias field in electrical steel," *Journal of Magnetism and Magnetic Materials*, vol. 133, pp. 144-146, 1994.

APPENDIX

AutoCAD Drawings



Concordia University
Natheer Alatawneh

All Dimension In Inches

Material
Cast Acrylic